Biomass-derived carbon as a precursor for bipolar plate in vanadium redox flow battery

A thesis submitted for the Degree of Doctor of Philosophy

Ha Huu Phan

Supervisors

Dr Anh N. Phan

Prof Mark K. Thomas

School of Engineering

Newcastle University, United Kingdom

January 2021

Abstract

In vanadium redox flow battery (VRFB), electrodes comprise of carbon/graphite felt and composite bipolar plate. The felt provides reaction sites for vanadium redox reactions and controls mass transport of electrolyte flows throughout VRFB electrodes, while the bipolar plate provides electrical conductivity and connects adjacent cells in VRFB. However, current studies have focused mainly on the carbon/graphite felt, giving few attention to bipolar plates. In chemistry, a heteroatom is an atom that is not carbon or hydrogen, such as oxygen, nitrogen and phosphorus. Bipolar plates lack heteroatom functional groups and porous structures, which have been shown to improve kinetics of vanadium redox reactions and energy efficiency. Both heteroatom functional groups and porous structures are prominent properties of biomass-derived carbon, which is renewable and abundant. Therefore, the aim of the PhD study is to examine the ability of applying biomass-derived carbon as a precursor for bipolar plate in VRFB, in order to simultaneously leverage the strengths of biomass-derived carbon in vanadium redox reactions and reduce the price of bipolar plates. To achieve this aim, walnut shell-derived carbon was obtained via heat treatment in various environments *i.e.* N_2 and CO_2 at 600-1000°C, and hydrothermal carbonisation (HTC – 200-290°C). Walnut shell-derived carbon was functionalised through a combination of chemical and thermochemical treatments *e.g.* NH_3, HNO_3, K_2CO_3 and H_3PO_4, and dielectric barrier discharge (DBD) cold plasma in NH_3. Properties of walnut shell-derived carbon were characterised to understand the effects of operating conditions on functional groups, surface morphology and carbonaceous structures.

DBD cold plasma is a novel method to incorporate nitrogen into walnut shell-derived carbon, in which DBD cold plasma power is a dominating factor controlling nitrogen surface contents and nitrogen surface species with surface nitrogen contents varying in 3.9-8.7 at%. Low cold plasma power 20 W favours the formation of amide-N groups (2.8-5.1 at%), but increasing cold plasma power to 40 and 80 W creates more amine-N groups (2.8-3.5 at%). The ratio of amine-N/amide-N group increases from ~0.4 to ~2.5 with increasing DBD cold plasma power from 20 W to 80 W. This is significantly different to heat treatment in NH_3 at 800°C with pyridinic-N, pyrrolic-N and quaternary-N being main nitrogen species. The total surface nitrogen contents of carbons obtained from NH_3 heat treatment are 3.1-5.6 at% with the ratio of pyridinic-N and pyrrolic-N being ~2:1. Furthermore, DBD cold plasma has negligible influence on porous structure and carbonaceous structure of both biochar (obtained from pyrolysis) and hydrochar (obtained from HTC) with BET N_2 surface area remaining

< 10 m^2 g^{-1}. It is recommended to use different analysis techniques such as temperature programmed desorption to examine nitrogen functional groups besides X-ray photoelectron spectroscopy due to overlapping binding energies of amine, amide, and pyridinic-N, pyrrolic-N and quaternary-N.

Regarding H_3PO_4 treatment, although phosphorus incorporation using H_3PO_4 did not significantly increase the phosphorus contents in walnut shell-derived carbon (1-2 wt%), it is proved that both heat treatment temperatures (in the range of 600-1000°C) and concentration of H_3PO_4 solution (0.5-5 M) govern the relative contents of C-P groups ($C-PO_3/C_2-PO_2/C_3-PO$) and C-O groups ($C-O-PO_3/(C-O)_3PO$). At H_3PO_4 0.5 M, temperature ≥ 1000°C is required to transform $C-O-PO_3/(C-O)_3PO$ to $C-PO_3/C_2PO_2$, but most phosphorus functional groups are shifted to $C-PO_3/C_2PO_2$ in the whole temperature range of 600-1000°C when using H_3PO_4 0.5 M.

It has been found that micropores account up to 57-78% of total pore volumes in most walnut shell-derived carbon samples, and ultramicropores and micropores do not play any significant role in contributing to reaction kinetics of vanadium redox reactions, due to diffusion limitations. Although the total pore volumes vary in the range of 0.013-0.380 cm^3 g^{-1}, the domination of ultramicropores and micropores in most samples suggested that the porosity and surface area do not involve in the conversions of vanadium redox reactions. The oxidation of VO^{2+} to VO_2^+ was affected by differences in molecular structures as characterized by Raman spectroscopy and PXRD between 600-800°C with I_D/I_G ration increasing from 0.69 to 0.94 and L_a increasing from 18.33 Å to 23.15 Å, respectively. With the significant increase of total oxygen content from 7.54 wt% to 23.84 wt% through HNO_3 treatment, it has been found that the presence of oxygen functional groups improves the conversion of V^{2+}/V^{3+} and V^{3+}/VO^{2+}. NH_3 heat treatment at 800°C increased the nitrogen contents markedly leading to the improvement of both the kinetic transfer of V^{2+}/V^{3+} and V^{3+}/VO^{2+} couples. Surface oxygen functional groups does not enhance the conversion of VO^{2+}/VO_2^+ couple, but they contribute to the reversibility of the oxidation and reduction processes of VO^{2+} and VO_2^+.

Acknowledgement

First and foremost, I want to express my deepest gratitude to my supervisory team, Dr Anh Phan, Prof Mark Thomas, Dr Yuen Ling Ng, and Dr Tuti Mariana Lim (NTU, Singapore) for keeping challenging my ideas so I can reflect and sharpen my understanding about my PhD project. Your support, guidance, and advice during my PhD helped me to understand research environment, strengthen my skills, and complete my PhD thesis. Dr Yuen Ling Ng, and Dr Tuti Mariana Lim supported me during my time in Singapore in summer 2018. My gratitude extends to Newcastle University and School of Engineering for my Research Excellence Award PhD studentship. I would like to thank Prof Ulrich Stimming and other research colleagues for allowing me to use the equipment in Outreach Laboratory for electrochemical experiment. Without your support, I could not complete my research on time.

I want to offer my special thanks to other research students in the research group, Jonathan Harris, Laura Diaz-Silvarrey, Phuet Prasertcharoensuk, Long Duong and other colleagues for your practical advice in lab techniques. Without your advice, it would be difficult for me to visualise how things got done and prepare the experiment system by myself.

Furthermore, my research could not be fulfilled without the assistance from Dr Greg Mutch in carrying out Raman spectroscopy experiment and your explanation on Raman result, Mrs Maggie White from ACMA in XRD analysis and other technicians in School of Engineering and IT team in Newcastle University for your support in technical and IT problems. I also want to say thank you to School of Engineering administrative staffs for your support.

Last but not least, it would be more difficult for me to continue and complete this PhD without the support from my parents and my little sister. Thank you for keeping caring for me, and always being happy, safe, and happy even without the presence of myself in the hometown. Thank the people, who I consider as my best friends, my sisters and brothers, Uyen Minh, Quang Trieu, Hong Yen, Thanh Luong, Minh Thong, and Huyen Trang for spending your times with me through ups and downs and giving me valuable advices during my time here.

Table of content

List of Figures

List of Tables

Nomenclature

β_{002}	Full width at half maximum of the (002) peak in X-ray diffraction pattern
β_{100}	Full width at half maximum of the (100) peak in X-ray diffraction pattern
λ	Wavelength (nm)
θ_{002}	Positions of the (002) peak in X-ray diffraction pattern
θ_{100}	Positions of the (100) peak in X-ray diffraction pattern
ΔEp	Separation between two peak potential in cyclic voltammetry test (V, or mV)
A_D	Area of D peak (~1350-1360 cm^{-1}) in Raman spectroscopy
A_G	Area of G peak (~1580-1590 cm^{-1}) in Raman spectroscopy
C_{ads}	Capacitance of adsorption (Ω)
C_{dl0}	Capacitance of double layer (Ω)
d_{002}	Interlayer spacing between different two carbon layers (nm or)
E_{pa}	Peak anodic potential (V, or mV)
E_{pc}	Peak cathodic potential (V, or mV)
HY250-H80W2	Dielectric barrier discharge cold plasma-treated hydrochar treated at 80 W for 2 h using hydrochar HY250 (treated at 250°C) as the precursor
I_{2D}	Intensity of 2D peak (~2700cm^{-1}) in Raman spectroscopy
I_D	Intensity of D peak (~1350-1360 cm^{-1}) in Raman spectroscopy
I_G	Intensity of G peak (~1580-1590 cm^{-1}) in Raman spectroscopy
I_{pc}	Peak cathodic current (A, or mA)
I_{pa}	Peak anodic current (A, or mA)
L_a	Stack width of the graphite crystal
L_c	Stack height of graphite crystal
M	Moles per litre (mol L^{-1})

N_2/800-1-H40W2	Dielectric barrier discharge cold plasma-treated biochar treated at 40 W for 2 h using biochar N_2/800-1 (pyrolysed at 800°C in N_2) as the precursor
N-5	Pyrrolic-N
N-6	Pyridinic-N
N-Q	Quaternary-N
R_{ads}	Resistance of adsorption (Ω)
R_{ct}	Charge transfer resistance (Ω)
R_{dl0}, R_{dl}	Double layer capacitance (Ω)
S_{BET}	BET N_2 surface area from N_2 adsorption-desorption isotherm at -196°C ($m^2 g^{-1}$)
S_{CO2}	DR CO_2 surface area from CO_2 adsorption-desorption isotherm at 0°C (m^2 g^{-1})
r^2	Coefficient of determination
t	Holding time (min, or h)
T	Temperature (°C)
V_{CO2}	DR micropore volume from CO_2 adsorption-desorption isotherm at 0°C (cm^3 g^{-1})
V_{micro}	DR micropore volume from N_2 adsorption-desorption isotherm at -196°C (cm^3 g^{-1})
V_{N2}	Total pore volume from N_2 adsorption-desorption isotherm at -196°C (cm^3 g^{-1})

Abbreviations

AC	Activated carbon
ATR	Attenuated total reflectance
BET	Brunauer-Emmett-Teller
CE	Counter electrode
CNT	Carbon nanotube
CPE	Constant phase element
CV	Cyclic voltammetry
DBD	Dielectric barrier discharge
DI	Deionised
DTA	Differential thermal analysis
DTG	Differential thermogravimetry
EIS	Electrochemical impedance spectroscopy
FT-IR	Fourier transform infrared spectroscopy
GC	Gas chromatography
GC-MS	Gas chromatography-Mass spectrometry
HTC	Hydrothermal carbonization
HTT	Heat treatment temperature
IGA	Intelligent gravimetric analyser
IUPAC	International Union of Pure and Applied Chemistry
MSE	Mercury saturated electrode in 1 M H_2SO_4 (MSE)
NASA	National Aeronautics and Space Administration
PAN	Polyacrylonitrile
PF	Phenolic resin
PP	Polypropylene

PVDF	Polyvinylidene fluoride
RE	Reference electrode
REN21	Renewable Energy Policy Network for the 21st Century
SAED	Selected area diffraction
SEM	Scanning electron microscope
SHE	Standard hydrogen electrode
TEM	Transmission electron microscopy
TEM-DF	Transmission electron microscopy – Dark field
TEM-BF	Transmission electron microscopy – Bright field
TGA	Thermogravimetric analysis
TPD	Temperature-programmed desorption
VRFB	Vanadium redox flow battery
XPS	X-ray photoelectron spectroscopy
XRD	X-ray powder diffraction

Chapter 1

Introduction

1.1 Background

The global total energy consumption around the world is expected to increase approximately 50% with respect to 2018 energy consumption level by 2050 (U.S. Energy Information Administration 2016). Overconsumption of non-renewable energy resources coupling with deterioration of the natural environment has led to the development of renewable sources (wind, tidal wave, solar energy, *etc.*) to replace fossil fuels. However, the intermittent nature and low dispatch ability of the renewables requires the use of more environmentally friendly energy storage systems for both grid energy and portable devices (*e.g.* smartphones, laptops, hybrid engine vehicles, and electric cars). Therefore, the use of energy storage equipment such as redox flow battery is emerging as an appropriate solution (Skyllas-Kazacos and McCann). The redox flow battery model was first introduced by the National Aeronautics and Space Administration (NASA) in the 1970s (NASA TM-79067 *et al.* 1979, 1980). More specifically, vanadium redox flow battery (VRFB) developed by the Skyllas-Kazacos has been receiving considerable attention (Yang *et al.* 2011, Saha *et al.* 2014) due to their safety, long lifecycles (over 10,000 charge and discharge cycles), flexibility in capacity and design, and low risk of cross-contamination between the positive and negative half-cells (Figure 1-1) (Skyllas-Kazacos *et al.* 2011, Saha *et al.* 2014). Since then, many efforts have been put into improving the performance of VRFB, including improving kinetic reaction rates on electrodes and electrode designs, conductivity and selectivity of battery membrane (Sha'rani *et al.* 2016, Wang *et al.* 2016, Zeng *et al.* 2016, Zhang *et al.* 2016, Aziz and Shanmugam 2017), and electrolyte solutions (Park *et al.* 2016, Wang *et al.* 2016, Li *et al.* 2017). Nevertheless, this device is facing some disadvantages preventing its widespread application. The energy density and specific energy of VRFB are lower than for other rechargeable batteries (*e.g.* 15-25 W h L^{-1} for VRFB compared to 250-329 W h L^{-1} of lithium ion battery (Doe 2007, Reddy 2010)), and large volume of aqueous electrolyte restricts their application in small scale systems and automobiles. Furthermore, capital, operational and maintenance costs remain a major obstacle hindering the popular use of this battery. In VRFB, electrodes include carbon/graphite felt and bipolar plate. Metallic bipolar plate is not suitable for VRFB due to high acidic concentrations of vanadium electrolytes, so composite bipolar plate is commonly used. The main components for composite bipolar plate are graphite and a polymer, in which graphite is normally non-renewable and costly, and accounts up to 80-86 wt% of the composite bipolar plate (Minke *et al.* 2016). This high graphite content in bipolar plate is crucial to electrical conductivity of VRFB, but it also increases the capital cost of VRFB.

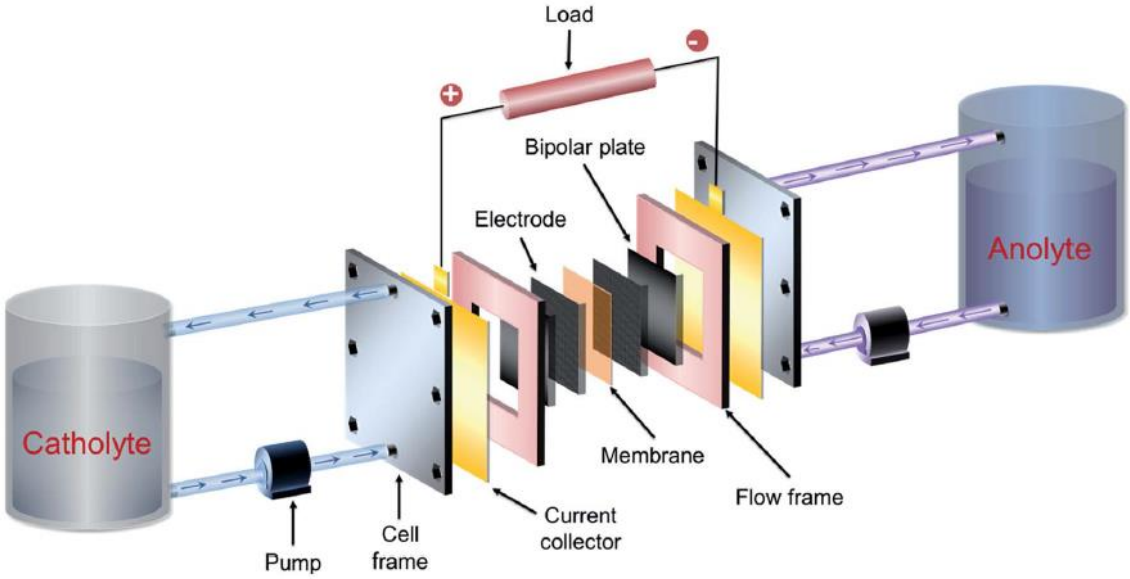

Figure 1-1 Schematic of a vanadium redox flow battery (Kim *et al.* 2015)

To reduce the cost of VRFB and make VRFB become more broadly used, the new carbon material that replaces graphite in composite bipolar plate needs to be abundant and low-cost but also needs to maintain or improve electrical conductivity of electrode. Biomass wastes (agricultural residues, food waste, *etc.*) are potential sources for carbon precursors because they are high in carbon contents (47-50% (Işıtan *et al.* 2016, Lee *et al.* 2017)) and mostly disposed into landfill (Tripathi *et al.* 2019). However, converting biomass into biomass-derived carbon remains as a critical challenge because it is difficult to control pore size, surface area, and functional groups, especially in pyrolysis and hydrothermal carbonization (HTC) – the two traditional thermal procedures to convert biomass into carbon materials.

Pyrolysis, a thermochemical process in inert/limited oxidation environment at temperature range of 250-900°C (Demirbas 2004, Uchimiya *et al.* 2011, Mašek *et al.* 2013, Windeatt *et al.* 2014, Cheng *et al.* 2015, Yu *et al.* 2017)) to convert biomass into carbon rich materials (known as biochar). Oxygen atoms in lignocellulosic materials are almost removed, so most carbon atoms inside biochar are in the form of C sp^2 (mainly aromatic carbon) and C sp^3 (aliphatic carbon) (Smith *et al.* 2017). Pyrolysis also does not favour the formation of porosity and surface area (Sharma *et al.* 2004, Chen *et al.* 2019). Hydrothermal carbonisation (HTC), on the other hand, is the process which treats biomass in sub-critical water conditions (up to 300°C and 90 bar). This process favours the development of functional groups (the solid product from HTC is denoted as “hydrochar” to distinguish solid product from pyrolysis). Hydrochar is often amorphous carbon (with carbon content in the range of 50-70 wt% (Guo *et al.* 2016)), which is not suitable for electrode material as it can reduce the conductivity of carbon electrode in VRFB. From these viewpoints, carbon products from these two aforementioned processes still have some drawbacks hindering their direct applications in VRFB. Therefore, functionalisation is required to enhance heteroatom functional groups, surface area and porosity.

The application of biomass-derived carbon into composite bipolar plate has been explored (Ulaganathan *et al.* 2015, Maharjan *et al.* 2017). In these studies, biomass-derived carbon was obtained through pyrolysis and then functionalised to enhance surface area, pore structure and oxygen groups. The obtained biomass-derived carbon (after activation and functionalisation) was mixed with a polymer such as polyvinylidene fluoride to formulate composite bipolar plate, and then applied on commercial bipolar plate for testing. It was found that that biomass-derived carbon required for bipolar plate is expected to have high ordered carbon structure to increase electrical conductivity, oxygen functional groups to act as active sites for redox reactions in VRFB (Figure 1-2), and high surface area and porous system (an optimal degree between micro, meso, and macropores) to allow sufficient contact between electrolyte ions and bipolar plate (Ulaganathan *et al.* 2015, Maharjan *et al.* 2017). Other studies in other types of carbon showed that introducing nitrogen and phosphorus into carbon can also enhance water interaction of the bipolar plate and electrolyte via density functional theory calculations (Xu *et al.* 2019). Despite these positive results, the application of biomass-derived carbon into composite bipolar plate has not received much attention compared to carbon/graphite felt, resulting in discrepancy in understanding how biomass-derived carbon function as a graphite replacement in bipolar plate. Until now, there have been only a handful of studies using biomass-derived carbon in bipolar plate in VRFB.

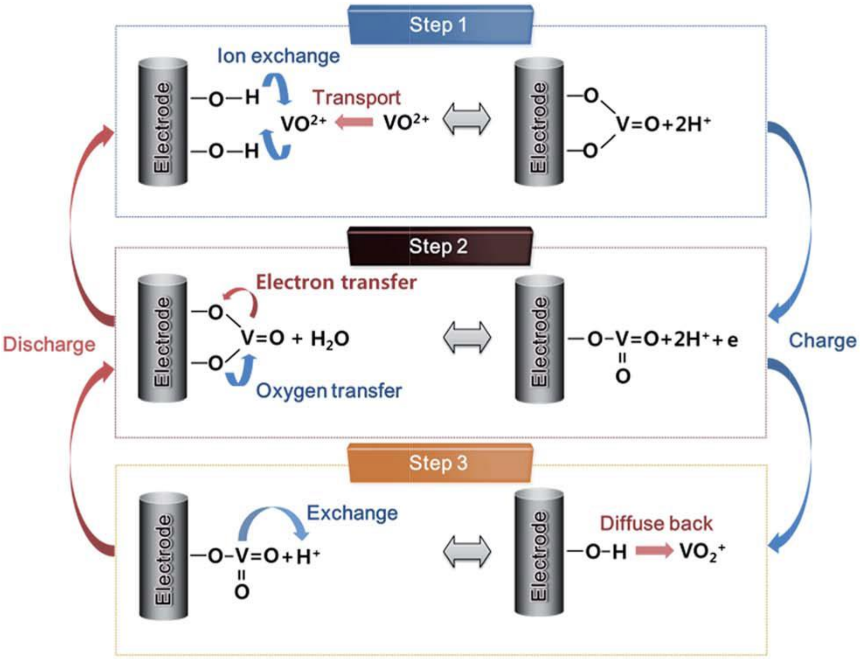

Figure 1-2 Schematic of reaction mechanism in which hydroxyl groups facilitate the conversion between ions VO_2^+ and VO^{2+} in VRFB cathode (Sun and Skyllas-Kazacos 1992)

As a result, it is difficult to have a clear understanding about the influence of carbonaceous structure, functional groups, surface area and pore structure on VRFB. As biomass-derived carbon characteristics are influenced by operating conditions in thermochemical procedures, it is important to understand how to control operating conditions to achieve a specific carbon property. Furthermore, to overcome the drawbacks of biomass-derived carbon obtained from pyrolysis and HTC, functionalised biomass-derived carbon (using different methods such as heat treatment in HNO_3 and metallic salts such as K_2CO_3) can increase oxygen functional groups and porosity.

Other heteroatoms such as nitrogen have been suggested to enhance the performance of VRFB (Xu *et al.* 2019). Nitrogen functional groups (up to 4.2 at%) were deemed to improve the reversibility of VO^{2+}/VO_2^+ couple and reduce the charge transfer resistance from 104 Ω to 78 Ω (Schnucklake *et al.* 2019). The conventional heat treatment in NH_3 can incorporate nitrogen into carbon structure, and this method has also been studied for a long time. However, this method uses intensive heat at high temperatures and heat-resistance materials for reactors, which is not economical and environmentally friendly. Cold plasma, on the other hand, can be a promising method to incorporate nitrogen into biomass-derived carbon. In cold plasma, electron temperature can increase up to 10,000-100,000 K (1-10 eV) without significantly affecting bulk temperatures. Electrons, being accelerated in electric field, ionise gas molecules to create a wide range of ions/radicals and/or excite gas molecules to result in chemical bond breakages. Therefore, in cold plasma, NH_3 can be transformed into radicals/ions without the need of using heat treatment. These radicals/ions can react with biomass-derived biochar to create nitrogen functional groups. Dielectric barrier discharge (DBD) is a type of cold plasma in which one or two electrodes are covered with dielectric barrier layers. DBD cold plasma is simple and economical because it can be operated in atmospheric pressure, and dielectric barrier layers can protect electrode from corrosive atmosphere like NH_3. However, there have not been many studies that explore the incorporation of nitrogen functional groups into biomass-derived carbon using cold plasma, so it is important to understand how operating conditions of cold plasma influence nitrogen functional groups and other physicochemical properties of biomass-derived carbon.

The phosphorus content on carbon felt using NH_4PF_6 2 M (activated at 800°C for 2 h in Ar) could reach 2.0 at%, and these oxygen-rich phosphate group benefited the conversion of V^{2+}/V^{3+} and VO^{2+}/VO_2^+ couples (Kim *et al.* 2016). Phosphorus groups lowered the activation energy of the vanadium couple reactions by acting as catalytic sites (Figure 1-3) and suppressed undesirable reactions such as hydrogen evolution. Phosphorus incorporation using H_3PO_4 on biomass has been studied (Lee and Reucroft 1999, Benaddi *et al.* 2000, Puziy *et al.* 2005), but there is no systematic study on how operating conditions influence phosphorus contents and other physicochemical properties of biomass-derived carbon. Therefore, this study will try to reveal the impact of operating conditions on phosphorus functional group contents and specific types of phosphorus functional groups.

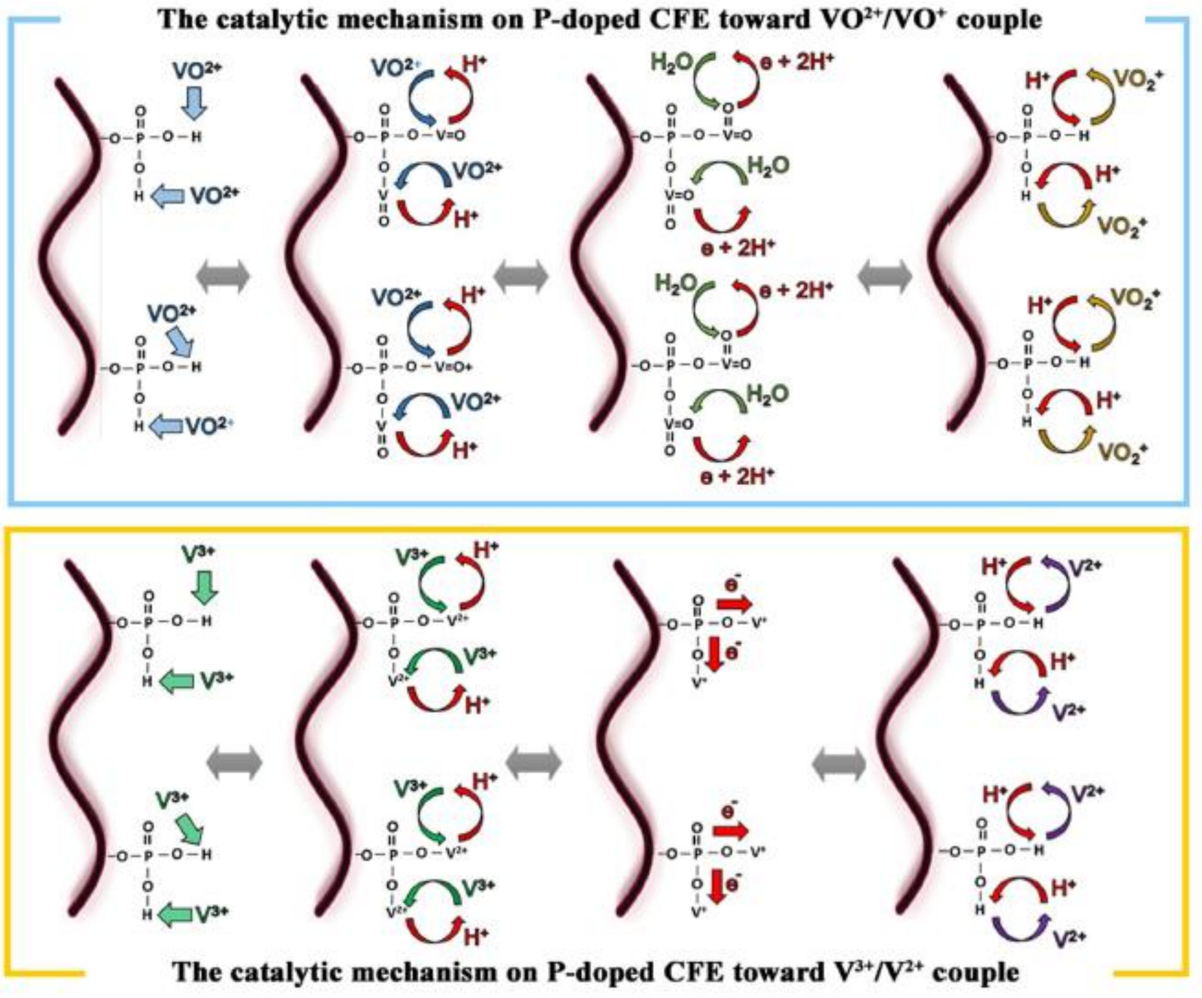

Figure 1-3 Suggested mechanisms for the catalytic effects of phosphorus functional groups to the conversion of V^{2+}/V^{3+} and VO^{2+}/VO_2^+ (Kim *et al.* 2016)

1.2 Objectives

Based on the afore mentioned viewpoints, it can be seen that the application of biomass-derived carbon in composite bipolar plate for VRFB is still in the early stage. It lacks understanding about how to obtain the optimal carbonaceous structure, functional groups, surface area and pore structure for carbon material in bipolar plate, and how these conditions can fundamentally influence vanadium redox reactions. Therefore, this PhD project aims to synthesize and functionalise biomass-derived carbon materials for bipolar plate in VRFB. To achieve the aim, three main objectives are set:

1. To convert biomass into carbon materials using pyrolysis and HTC and relate the physicochemical characteristics of carbon materials with operating conditions.
2. To explore the feasibility of incorporating nitrogen into biomass-derived carbon using heat treatment and dielectric barrier discharge cold plasma and incorporating phosphorus

using heat treatment, and to relate physicochemical characteristics of carbon materials with operating conditions.

3. To fundamentally define correlations between physicochemical properties (mainly surface area, porous structure, oxygen functional groups and carbonaceous structure) of biomass-derived carbon and kinetics of vanadium redox reactions.

1.3 Thesis outline

This thesis is divided into 7 chapters. **Chapter 1** is the introduction, providing the overview of the importance of VRFB in raising the use of renewable energy, and how biomass-derived carbon – the solid product from biomass wastes – could be used as a precursor for bipolar plate as a mean to enhance the performance of electrodes and reduce the price of bipolar plate. **Chapter 2** is literature review, providing detailed explanation on the conversion of biomass into biochar and functionalisation methods to increase surface area, porosity and functional groups. These functionalisation methods include heat treatment with K_2CO_3, HNO_3, NH_3 and H_3PO_4 and dielectric barrier discharge cold plasma in NH_3 environment. **Chapter 3** covers details about material, biomass conversion and functionalisation techniques, together with experimental setups and analytical techniques. **Chapter 4 – 6** cover the results and discussions in this thesis. **Chapter 4** concentrates on pyrolysis of biomass in N_2 and CO_2 environment, and functionalisation in K_2CO_3, HNO_3 and NH_3 environment. The influence of surface area and porosity, functional groups and carbonaceous structure from biomass-derived carbon obtained in different series of treatment/functionalisation on the performance of VRFB is discussed. **Chapter 5** focuses on dielectric barrier discharge cold plasma in NH_3 environment as a novel method to functionalise biomass-derived carbon, in comparison with conventional NH_3 heat treatment. **Chapter 6** explores systematic change in properties of biochar at different temperatures, holding times and H_3PO_4 concentration. Conclusions, further perspectives, and suggestion for future study are discussed in **Chapter 7**.

Chapter 2

Literature review

This chapter will first give an overview about the role of flow battery in general and vanadium redox flow battery in particular as an important factor in expanding the use of renewable energy worldwide, focusing on the potentials as well as challenges. The chapter will also discuss the potential of biomass-derived carbon for cost reduction and improvement of VRFB performance. The latter part of this chapter will discuss in detail the synthesis approaches of biomass-derived carbon, focusing mainly on pyrolysis and HTC, and other functionalisation/activation methods to enhance physicochemical properties of biomass-derived carbon.

2.1 Background: From energy crisis to renewable energy

According to the prediction of International Energy Outlook 2019, the total worldwide energy consumption would increase nearly 50% from 620 quadrillion British thermal units in 2018 to 910 quadrillion British thermal units in 2050 which equals to 41,400 million tons of coal or 157,400 million barrels of crude oil. This high energy requirement, coupling with degradation of non-renewable energy resources asks for more sustainable energy supplies *i.e.* renewable energies. Renewable energies comprise biomass, geothermal, concentrating solar thermal, solar photovoltaic, wind, and ocean power. In the Global Status Report 2020 of Renewable Energy Policy Network for the 21st Century (REN21) – the global renewable energy community of actors from science, governments, non-government organisations and industry, the total share of all modern renewable energy accounted for only 11% in total final energy consumption (Renewable Energy Policy Network for the 21st Century 2020). Traditional biomass such as wood and straw can be used traditionally for cooking and heating in small stoves that are usually energy inefficient, while modern renewable biomass in the form of bioenergy *i.e.* biofuel (mainly bioethanol from sugar cane and corn, and biodiesel from vegetable oils) can be used for transport. Geothermal energy utilises heat generated from Earth, and it is restricted to regions that demonstrate medium-to-high enthalpy resources, requiring hot rock is permeable and stable for heat extraction to be economical. Both solar photovoltaic, wind power, and ocean power are variable renewable energy sources, and they can directly convert other forms of energy including sunlight, wind, and ocean currents to electricity. Until now, both geothermal, solar photovoltaic, wind power and ocean power account for only 2.1% of total final energy consumption around the world, according to REN21.

In variable renewable energy sources, the solar photovoltaic and wind power are two main sources that contribute to 8.7% of total electricity production worldwide while the ocean power represents the smallest share in all renewable energy sources. The ocean power only started to move from pilot scale projects into permanent plants recently (Renewable Energy Policy Network for the 21st Century 2020). According to Skyllas-Kazacos *et al.*, any level of integration of variable renewable energy into grid network higher than 12-15% would cause significant instability to the whole system (Skyllas-Kazacos *et al.* 2013), so the development of energy storages, including pumped storage, mechanical storage and electrochemical storage, is important to support the integration of variable renewable energy resources into the conventional system for all end-use customers. The energy storages facilitate power system flexibility, reduce grid imbalances by mitigating the intermittent nature of renewable energy, and promote the link between supply from variable renewable energy sources and all end-use demands over larger areas. Until now, pumped hydroelectric energy storage is the main form of energy storage, accounting for 158 over 183 GW of global market for energy storage in 2019, but it is restricted by geography and loss of water from evaporation (Renewable Energy Policy Network for the 21st Century 2020). The mechanical storage such as compressed air is still at early development stage, with the first commercial compressed air storage site was installed by Hydrostor in Goderich, Ontario, Canada. The compressed air system uses surplus electricity to produce heated compressed air and store in an underground cavern, and during high-demand period, compressed air is released through a turbine to generate electricity. Other energy storages include thermal energy storage that is usually deployed with concentrating solar thermal system to store heat, and biofuel that is blended in gasoline and diesel for transport. They are, however, not suitable for direct energy storage for electricity.

On the other hand, electrochemical storage *i.e.* battery enables greater flexibility for solar photovoltaic and wind power and supports deployment into grid or a decentralised, stand-alone system without geographic constraints. Although lithium-ion battery is currently recognised as the leading electrochemical storage, non-lithium electrochemical storage such as flow battery is also recognised as a potential long-duration energy storage due to safety concerns and only short-duration storage ability of lithium-ion battery due to technical constraints (Skyllas-Kazacos *et al.* 2011, Saha *et al.* 2014, Doetsch and Burfeind 2016). Table 2-1 summaries critical features of some common batteries in the market.

Table 2-1 Comparison of some common rechargeable batteries (Linden 2010)

Battery type	**Specific energy (W h kg^{-1})**	**Energy density (W h L^{-1})**	**Cycle life**	**Specific power**	**Application**
Lead acid	30-40	60-75	500-800	180	Moderate energy density. Used in vehicles for automotive staring, lighting, and ignition. The use of lead acid battery can cause environmental hazard due to lead.
Lithium-ion	105-128	250-329	> 5,000	250-340	High energy density, suitable for electric vehicles and portable devices such as smartphones and laptops. This battery faces capacity loss over lifetime, and may cause explosion due to short circuiting
Sodium-sulphur (Na-S)	110	360	~2,500	180	High energy density. This battery is used for grids, but requires high temperatures (~300-350°C) for operation.
Vanadium redox flow battery	10-20	15-25	> 10,000		Energy density and specific power are independent. Long life cycle, and operate at ambient temperatures. This battery is used for grids.

2.2 Redox flow battery

2.2.1 Overview about redox flow battery

Flow battery was first invented in 1970s by NASA as iron-chromium redox battery. The fundamental difference between flow battery and conventional battery is that energy is stored in two separate redox couple solutions in external tanks, and an ion-exchange membrane is used to prevent mixing of solutions of these two redox couples. There are several flow batteries such as iron-chromium redox battery, polysulfide bromine flow battery, metal-halide flow battery and vanadium redox flow battery. Some main features regarding these batteries are as follows:

- Two redox couples of Fe^{3+}/Fe^{2+} (working as cathode) and Cr^{3+}/Cr^{2+} (working as anode) were chosen for iron-chromium battery after being tested by NASA for a wide range of suitable redox couples. Further attempt to commercialise this battery was relinquished due to high cross-contamination between anode and cathode, despite the success of pilot scale iron-chromium battery developed in 1980s and high energy efficiency of 80% during the first 300 cycles.
- Polysulfide bromine flow battery was also first developed in 1980s, using two redox couples Br_3^-/Br^- ($NaBr_3/NaBr$) and S_2^{2-}/ S_4^{2-} (Na_2S_2/Na_2S_4). This battery attracted early attention due to its low cost and availability of electrolyte solutions, and ambient temperatures for operation (20-40°C). However, similarly to iron-chromium battery, this battery also shows cross-contamination problem between anode and cathode, leading to imbalance between two half-cell and subsequently changes in electrolyte compositions. Furthermore, by-products including H_2S and Br_2 evolving from undesirable reactions also reduces this battery efficiency.
- The working mechanism of metal-halide flow battery, including Zn-Br and Zn-Cl, is different from the two aforementioned batteries. Instead of using an electrolyte redox couple, Zn-Br and Zn-Cl halide flow batteries use solid zinc depositing on the negative electrode during the charging process, so the capacity of Zn-Br and Zn-Cl battery is limited by the quantity of Zn. On the positive electrode, bromide ions react to form Br_2. The main advantages of this battery are similar with polysulfide bromine flow battery, besides high energy efficiency and ability to complete discharge. However, this battery can lose capacity due to self-discharge process because Br_2 can diffuse from positive side into negative side and self-oxidise Zn through reactions: $Br_2 + H_2O \rightarrow HBr + HBrO$ and $2HBr + Zn \rightarrow ZnBr_2 + H_2$. Zinc dendrites growing in the negative side also cause a short circuit in cell when it reaches

the positive electrode, so periodically complete discharge is required to remove all Zn on the negative electrode. Moreover, unbalanced kinetics between Zn^{2+}/Zn and Br_2/Br^- couples can cause polarisation in battery, resulting in a drop in energy efficiency. Despite these drawbacks, Zn-Br battery has been tested in small scale demonstration for electric vehicles.

- Vanadium redox flow battery (VRFB) deploys two redox couples of the same metal (V^{2+}/V^{3+} and VO^{2+}/VO_2^+) for negative and positive sides. VRFB was first developed in New South Wales, Australia by Prof Skyllas-Kazacos in 1988 (Skyllas-Kazacos *et al.* 1988). Compared to other types of redox flow batteries, VRFB eliminates the cross-contamination between cathode and anode due to one metal species being employed in electrolyte solutions, resulting in long-life cycles (up to 20,000 cycles compared to 5,000-15,000 cycles of lithium ion batteries and 3,000-7,000 cycles of sodium ion batteries) (Skyllas-Kazacos *et al.* 2011, Saha *et al.* 2014, Doetsch and Burfeind 2016). VRFB also operates at ambient temperatures between 10-40°C, and the use of electrolyte solutions also removes the risk of thermal runaway from solid electrodes like lithium-ion battery. Lower temperatures (*i.e.* sub-zero temperatures) results in precipitates from V^{2+}, V^{3+}, while higher temperature than 40°C results in the precipitate of V^{5+} into undissolved V_2O_5 (Xiao *et al.* 2016). Among these flow batteries, VRFB becomes the most popular and widespread, and available in a commercial scale. Many VRFB plants have been constructed in recent years in several countries (*i.e.* Japan, USA, and Thailand) for storing the energy produced from renewable energy plants (Holzman 2007, Leung *et al.* 2012).

Despite many advantages over other types of batteries such as lithium-ion battery, VRFB uses high concentration of acidic solutions which requires high power pump. The vanadium species can easily precipitate temperatures higher than 40°C or lower than 10°C, and this leads to blockage of pipe systems. All these factors increase the capital, operational and maintenance costs of VRFB.

The capital cost of VRFB can be varied significantly due to the configuration of VRFB, chemical composition of electrolyte, and electrochemical model, from \$200 kWh^{-1} to \$100 kWh^{-1} for a 5 kW 4 kWh VRFB system with 10 h storage (Skyllas-Kazacos *et al.* 2013). Viswanathan *et al.* calculate the cost of VRFB systems and reported that the capital cost of VRFB would be \$489 kWh^{-1} for a 1 MW, 4 MWh VRFB system in the present scenario and could reduce to \$209 kWh^{-1} in an optimistic scenario (using 1.5 M vanadium content in 5 M H_2SO_4) (Viswanathan *et al.* 2014). With this system, the levelized cost of one kWh over a system that has the operating lifetime of 20 years would be ~\$0.14-0.23 kWh^{-1}. The data from studies of Skyllas-Kazacos *et al.* and Viswanathan *et al.* were accepted and used in recent studies, such as the study for calculating the levelized cost of VRFB with addition of capacity fading and electrolyte balancing by Rodby *et al.* (Rodby *et al.* 2020). Therefore, the data from Skyllas-Kazacos *et al.* and Viswanathan *et al.* should be considered validated although they were publised 6-7 years ago.

2.2.2 Carbon components in VRFB

Figure 2-1 presents a schematic diagram of VRFB. In VRFB, electrolytes on positive side (VO^{2+}/VO_2^+) and negative side (V^{2+}/V^{3+}) are stored separately in two different tanks, and they are pumped into electrodes during the charge/ discharge. The electrolytes flow through permeable carbon/graphite felts where redox reactions occur, so carbon/graphite felts also exchange charges between electrolytes and bipolar plates during charge/discharge process. The positive and negative electrodes are separated by ion exchange membrane. Vanadium redox reactions are as follows:

<u>Positive half-cell:</u>

$$\mathrm{VO^{2+} + H_2O \underset{discharge}{\overset{charge}{\rightleftarrows}} VO_2^{+} + e + 2H^{+}} \quad E° = 1.0\ \mathrm{V\ vs.\ SHE} \tag{2-1}$$

<u>Negative half-cell:</u>

$$\mathrm{V^{3+} + e \underset{discharge}{\overset{charge}{\rightleftarrows}} V^{2+}} \qquad E° = -0.25\ \mathrm{V\ vs.\ SHE} \tag{2-2}$$

<u>Net equation:</u>

$$\mathrm{VO^{2+} + V^{3+} + H_2O \rightleftarrows VO_2^{+} + V^{2+} + 2H^{+}} \qquad E° = 1.25\ \mathrm{V\ vs.\ SHE} \tag{2-3}$$

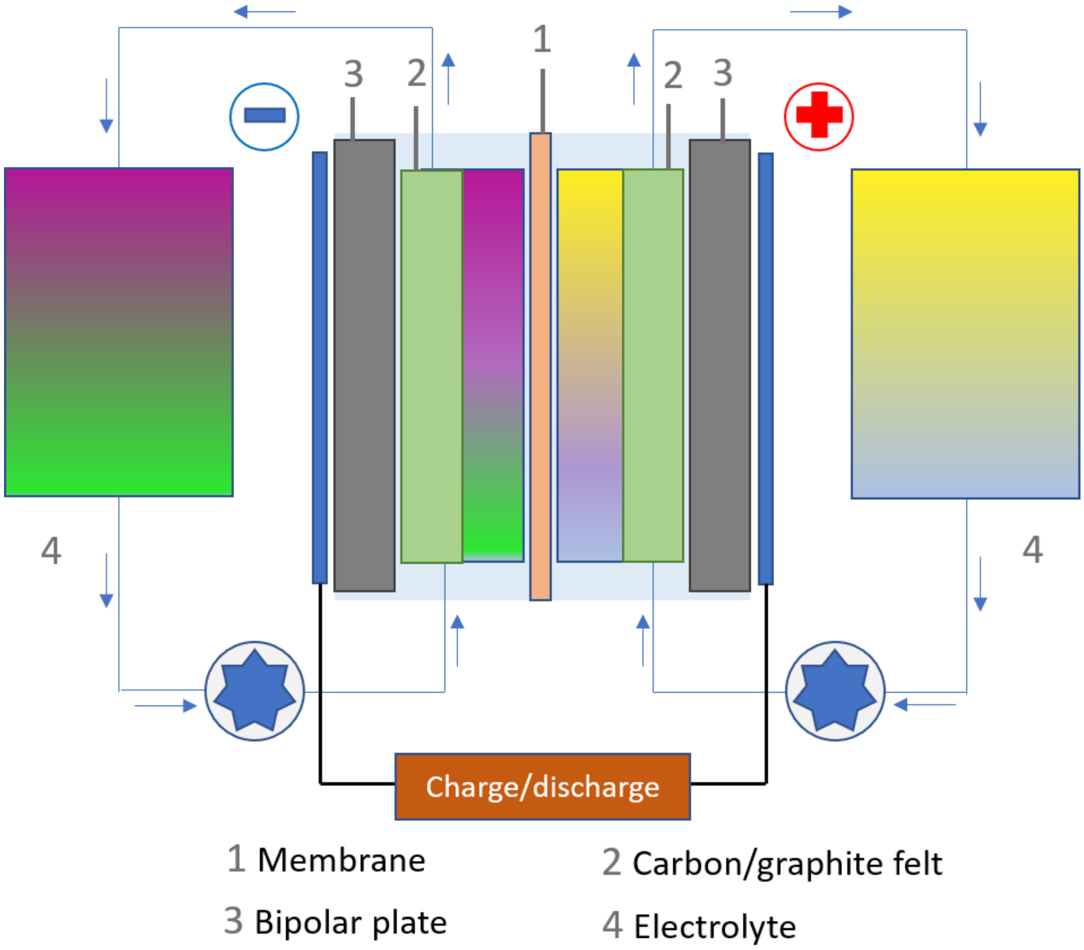

Figure 2-1 Schematic diagram of vanadium redox flow battery

Carbon/graphite felts and bipolar plates are fundamental carbon components in VRFB. Carbon/graphite felt provides reaction sites for vanadium redox reactions and geometry of felt controls mass transport of electrolyte flows throughout VRFB electrodes. Bipolar plate is also a critical component in VRFB. It provides electrical conductivity and connects adjacent cells in VRFB. The contribution of bipolar plate into vanadium redox reactions is only considered secondary to carbon/graphite felt, but the electrical conductivity of bipolar plate is important to the ohmic resistance of VRFB (Noack *et al.* 2016). Figure 2-2 illustrates the production of commercial carbon/graphite felt from SGL Carbon. Carbon/graphite felts are made from poly acrylonitrile or rayon fibres, and they undergo different carbonisation and/or graphitisation stages to achieve electrical conductivity and chemical resistance. High macro-porosity of carbon/graphite felt also permits the permeable of vanadium electrolyte solutions into felts. On the other hand, composite bipolar plates *i.e.* graphite composites are made from natural graphite mixing with polymer such as high-grade fluoropolymers through compression moulding or injection moulding. Composite bipolar plate can contain up to 80-86 wt% graphite and 14-20 wt% isolating polymer such as polypropylene (PP), phenolic resin (PF), and polyvinylidene fluoride (PVDF), allowing high electrical conductivity and chemical resistance towards corrosive electrolytes (Minke *et al.* 2016), especially in concentrated H_2SO_4 solution like vanadium solutions. High quantity of graphite ensures electrical conductivity, and polymer that acts as binder increases the processability of graphite during moulding to compromise the brittle nature of graphite, including flexural strength and deflection (Kakati *et al.* 2010). Both carbon/graphite felt and bipolar plate function together to facilitate redox reactions in VRFB.

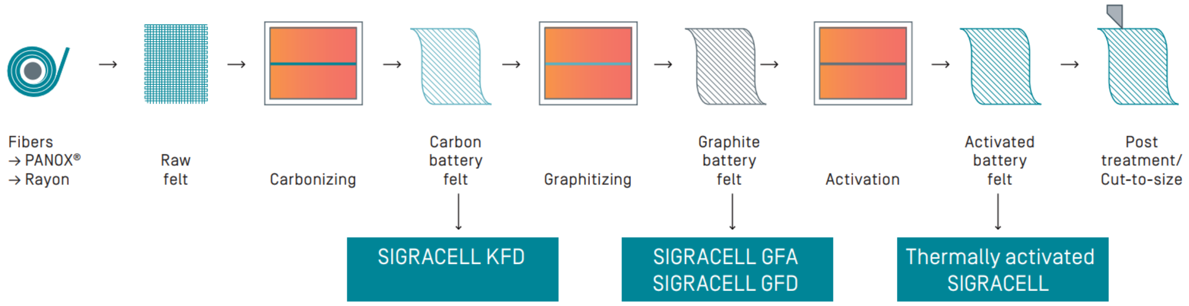

Figure 2-2 Schematic of manufacturing carbon/graphite felt from SGL Carbon

The cost of bipolar plate in a VRFB is similar to that of carbon felt, varying from 4% to 15% of total battery cost (Viswanathan *et al.* 2014) depending upon material quality, manufacturing methods and size (Minke *et al.* 2016). Regarding manufacturing bipolar plate, the total cost for a reference composite bipolar plate (25×25 cm *i.e.* 625 cm^2) obtained from compression moulding or injection moulding varies from €5 for a 1 mm-thick bipolar plate to €14 for a 9 mm-thick bipolar plate, in which the raw material cost for graphite and polymer is the main expense at 50-70%. Minke and Turek (Minke and Turek 2018) reported that bipolar plate cost varied greatly in €37-418 m^{-2} (€100 m^{-2} in average) whereas carbon felt valued between €14-63 m^{-2} (€53 m^{-2} in average), each of them sharing less than 5% of the total VRFB cost (the GBP/Euro exchange rate was ~1.1-1.15 in 2018). However, VRFB is still considered as a younger battery technology compared to others such as lithium-ion battery, so there are many uncertain factors such as electrolyte solution, membrane and input data influencing the cost of VRFB, and any models that estimate costs for VRFB system are only rough estimation. Furthermore, although been studied since 1970s, standard protocols for testing conditions, material sets and benchmarks for performance metrics of VRFB have not been established yet (Forner-Cuenca and Brushett 2019). This makes comparing and validating the accuracy of data presented in publications difficult. No standard protocols in VRFB testing coupling with insufficient studies dedicating in detailed system description and modelling framework (Minke and Turek 2018), lead to challenges in understanding the impact of bipolar plate and carbon/graphite felt on VRFB performance.

The research trend of bipolar plate includes improving electrolyte flow in VRFB electrode and developing electrically conductive materials compatible with corrosive vanadium electrolytes (Lourenssen *et al.* 2019). First, bipolar plate in contact with carbon/graphite felt creates different flow channels in VRFB electrode to reduce pressure drop and increase contact between electrolytes and electrodes. Figure 2-3 and Table 2-2 describe the geometry of some flow fields in VRFB electrodes. Studies regarding flow paths have focused on reducing pressure drops inside electrodes and overpotential to increase efficiency of VRFB (Xu *et al.* 2013, Darling and Perry 2014). The second focus of bipolar plate development is improving material for bipolar plate. Metallic bipolar plate could not be used in VRFB due to corrosiveness of electrolytes, and graphite, the main component in composite bipolar plate, is considerable expensive (Lee *et al.* 2012). Therefore, it is important to find a suitable carbon material replacing graphite in composite bipolar plate. Carbon material needs excellent electrical conductivity that is similar with or even better than graphite, but low-cost.

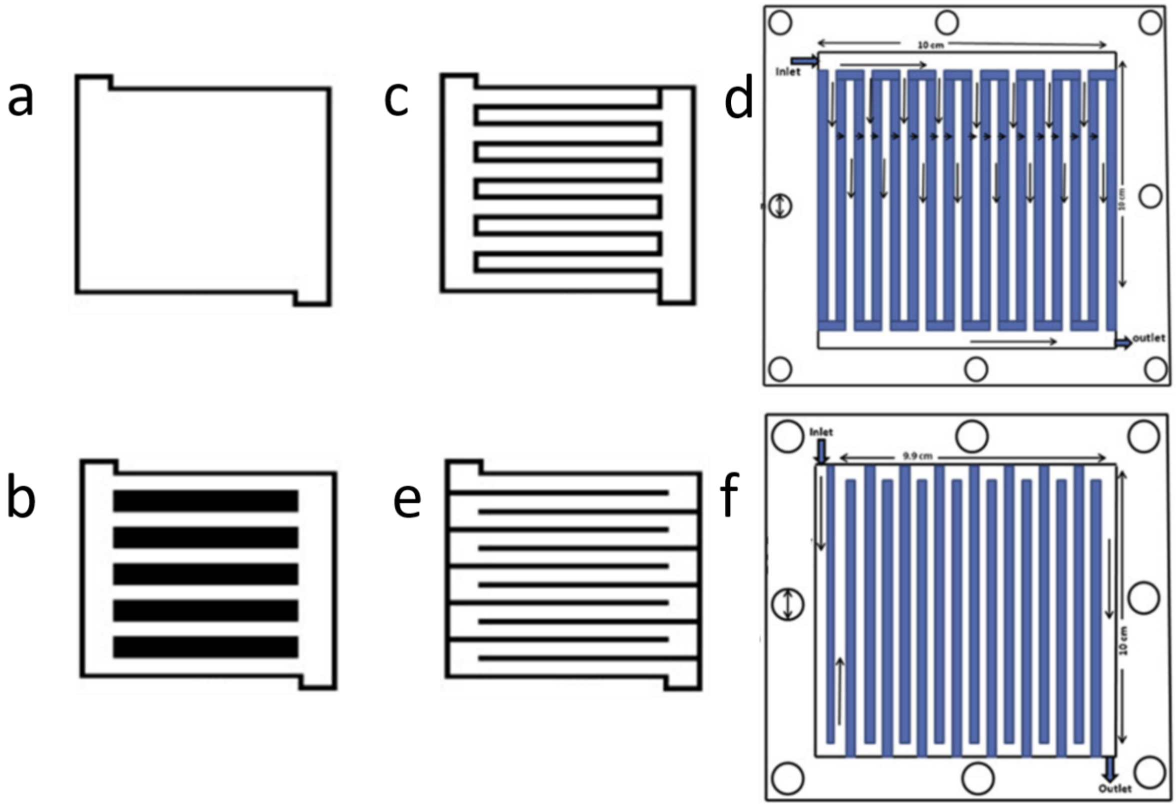

Figure 2-3 Schematic of (a) conventional, (b) parallel, (c-d) interdigitated and (e-f) serpentine flow fields in VRFB (adapted from (Lourenssen *et al.* 2019) and (Kumar and Jayanti 2016)). In practice, bipolar plates could be designed to accommodate these flow fields to reduce pressure drop and distribute electrolyte more thoroughly.

Table 2-2 Common flow channels used in VRFB (Lourenssen *et al.* 2019)

Flow path	**Description**
Conventional	A configuration allows electrolyte to flow through one electrode. The pressure drop can increase due to hydraulic resistance (Figure 2-3 a).
Parallel	This configuration creates multiple channels inside one electrode via an inlet and outlet (Figure 2-3 b).
Interdigitated	This configuration also forces electrolyte from an inlet to flow across barrier that separates adjacent channels before going to an outlet, so it initiates hydraulic convection inside one electrode (Figure 2-3 c-d).
Serpentine	This configuration creates only one electrolyte flow in an electrode but the electrolyte flow back and forth inside the electrode before reaching an outlet (Figure 2-3 e-f).

Biomass (forest residues, waste wood, agricultural products, *etc.*) contains up to 50% carbon, is the renewable and abundant carbon source (Windeatt *et al.* 2014, Prakash and Sheeba 2016). Biomass can be exploited to produce high value chemical production (mono- and oligo-saccharides, biofuels, phenolic acids, terpenoids) (Bayu *et al.* 2019, Cho *et al.* 2020), and the biomass-derived carbon product *i.e.* biochar, activated carbon (AC) – the solid product obtained from thermochemical processes can be used for many environmental applications (waste treatment, organic and inorganic substance removal) (Ahmad *et al.* 2014, Thomas *et al.* 2019) and agriculture (*i.e.* soil amendment, compost) (Das *et al.* 2020). Biochar/AC as a replacement/ substitute for carbon element in energy storage systems also attracts attention of many researchers (Ouyang and Wang 2020). The main advantages of biochar/AC are abundant in sources, various functional groups and low-cost, which is a potential replacement for graphite.

Up until now, biochar/AC is mainly incorporated on the surface of carbon/graphite felt in VRFB electrodes. Although the macro-porous structure of the felt allows electrolyte to flow through, it has low surface area (< 10 m^2 g^{-1}) and poor hydrophilicity. Therefore, various heteroatom functional groups (O, N, P, *etc.*) together with high surface area with micro-meso porous structure could increase wettability of carbon/graphite felt and enhance kinetics of vanadium redox reactions (Kim *et al.* 2015). Other studies focused on improving porosity, surface morphology and surface functional groups of electrodes in VRFB using different carbon materials, including single-walled or multi-walled CNTs (Wang *et al.* 2012, Friedl *et al.* 2013, Yang *et al.* 2018), graphene oxide (González *et al.* 2013, Shi *et al.* 2014), graphene oxide nanosheet (Han *et al.* 2011, Rui *et al.* 2012), carbon nanoparticles (Wei *et al.* 2016, Wu *et al.* 2016). These carbon materials were tested on carbon/graphite felt, and the enhancement in VRFB performance was attributed to the enhancement in surface area, surface morphology and functional groups.

However, the application of biochar/AC in VRFB has not been receiving enough attention. Using the searching tools on Web of Science, using key word “Vanadium redox flow batter*” and combining with “*mass*” and “*bio*” only presented 216 and 33 results respectively. After screening through the listed studies, there were only a handful of studies that truly used biochar/AC for bipolar plate in VRFB. The first report using biomass-derived carbon in bipolar plate is Ulaganathan *et al.* that used mesoporous coconut shell-derived AC in 2015 (Ulaganathan *et al.* 2015). Even though the role of bipolar plate as the reaction site is often considered secondary compared to carbon/graphite felt, incorporating the coconut shell-derived AC on bipolar plate resulted in higher peak currents in VO^{2+}/VO_2^+ and V^{2+}/V^{3+} couples during cyclic voltammetry (CV) test (Figure 2-4) compared to pristine bipolar plate, and reduced the charge transfer resistance from 0.30 to 0.25 Ω for the VO^{2+}/VO_2^+ couple and from 3.60 to 1.83 Ω for the V^{2+}/V^{3+} couple. Ulaganathan *et al.* reported that the improved electrochemical behaviours of bipolar plate coated with coconut shell-derived AC was assigned to high surface area (1652 $m^2\ g^{-1}$) and various oxygen functional groups such as hydroxyl, carbonyl and carboxylic groups.

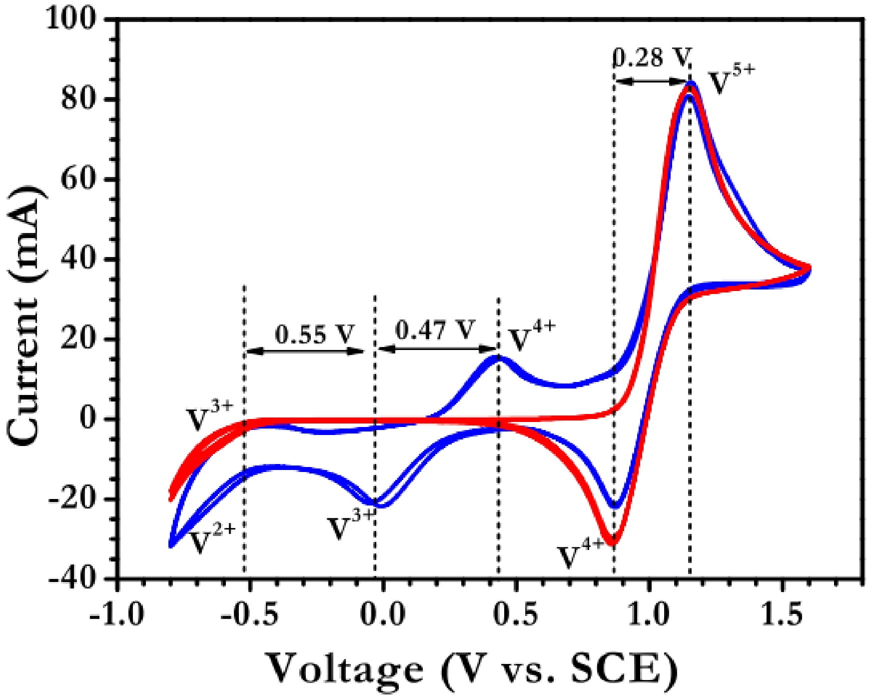

Figure 2-4 Cyclic voltammetry of pristine bipolar plated (red) and coconut-shell-derived carbon coated bipolar plate (blue) (SCE is saturated calomel electrode) (adapted from (Ulaganathan *et al.* 2015))

Further investigation on impact of biomass-derived AC on bipolar plate has been conducted. Studies of AC derived from orange peel (Maharjan *et al.* 2017) and Sal wood sawdust (Maharjan *et al.* 2019) showed that all of them had high mesopore and micropore contents and BET N_2 surface areas up to ~1900 m^2 g^{-1}. The high contents of mesopores in both orange peel-derived AC (Maharjan *et al.* 2017) and coconut shell-derived AC (Ulaganathan *et al.* 2015) were shown to enhance significantly the kinetics of vanadium redox reactions (lower charge transfer resistance and higher peak current in CV test) and increase energy efficiency of VRFB compared to pristine bipolar plate. However, coffee bean-derived AC showed that the carbon with highest micropore and mesopore volume (0.60 and 0.15 cm^3 g^{-1} respectively) had the lowest irreversibility level for the VO^{2+}/VO_2^+ couple and lowest voltage and energy efficiency for VRFB (Krikstolaityte *et al.* 2018). Sal wood-derived AC with micropore volume of ~0.42 cm^3 g^{-1} and mesopore volume of ~0.93 cm^3 g^{-1} improved kinetics of vanadium redox reactions, but the energy efficiency of this AC was the same as pristine bipolar plate (Maharjan *et al.* 2019). The enhancement reported in studies in biomass-derived materials (Ulaganathan *et al.* 2015, Maharjan *et al.* 2017, Maharjan *et al.* 2019) was explained due to the presence of oxygen functional groups as catalytic sites for vanadium redox reactions. However, these AC samples were synthesized at high temperatures (≥ 800°C), which is sufficient to eliminate most of oxygen functional groups, and the removal of oxygen functional groups at high temperatures has been ascertained through temperature-programmed desorption analysis (Hall and Calo 1989, Zielke *et al.* 1996, Zhou *et al.* 2007). Although oxygen functional groups in these AC samples were shown through the X-ray photoelectron spectroscopy (XPS) analysis (Ulaganathan *et al.* 2015, Maharjan *et al.* 2017, Maharjan *et al.* 2019), XPS provides the surface composition of material rather than bulk oxygen content (may be up to 3 nm for organic materials (Claesson *et al.* 2007)). Furthermore, the distribution of oxygen functional groups in micropores and mesopores of biochar may have different influences on kinetics of vanadium redox reactions due to the accessibility of vanadium ions to these oxygen sites. Structures of biochar/AC are also complex with a wide range of pore size distributions and surface areas depending on preparation methods and operating conditions.

From these scattering studies using biomass-derived AC on bipolar plate, generous surface area with different pore structure and heteroatom functional group contents on VRFB positively influence the performance of VRFB. Few studies using biochar on bipolar plate hinders the use of this carbon in bipolar plate and subsequently the complete replacement graphite in bipolar plate. Therefore, a systematic study to understand how characteristics of biomass-derived carbon influence behaviours of bipolar plate in VRFB is required.

2.3 Biomass-derived carbon from thermochemical processes

2.3.1 Biomass

Biomass comprises mainly three lignocellulosic elements namely cellulose, hemicellulose, and lignin (up to 95 wt%). The contents of carbon, oxygen, and hydrogen are in the range of 45.2-50.8 wt%, 43.8-48.3 wt%, and 3.2-6.5 wt% respectively (Sun *et al.* 2012, Mašek *et al.* 2013, Ding *et al.* 2017), while nitrogen content only accounts for ~1-2 wt% (Demirbas 2004, Windeatt *et al.* 2014, Intani *et al.* 2016). The remaining weight of biomass contains ash with metal elements such as Si, Ca, K, P, Al, Mg, Fe, S, Na, Ti, *etc.* (Demirbas 2004, Windeatt *et al.* 2014, Intani *et al.* 2016, Işıtan *et al.* 2016, Prakash and Sheeba 2016, Vassilev *et al.* 2017).

In three lignocellulosic elements, cellulose, a polysaccharide formula $(C_6H_{10}O_5)_n$ with n value ~6,000-8,000 for woody fibre and 14,000 for cotton fibre, is the main structural component in cell walls of green plants. Cellulose content can vary in the range of 24-47 wt%. A fundamental unit of cellulose is glucose, and they are linked by β-1,4-glycosidic bonds. These bonds can be easily broken under acid or high temperature conditions. Hemicellulose (18-45 wt%) plays a role of binder between cellulose and lignin in the cell of plant. Hemicellulose has a complex structure with several fundamental sugar units such as mannose, galactose and arabinose (Wang and Luo). The number of units in hemicellulose chain is less than 200 on average, lower than cellulose. Lignin (5-36 wt%), on the other hand, consists of many phenylpropanoid units in a nonlinear and random form, so lignin presents in a three-dimensional structure with a very complex structure. The fundamental units of lignin can be catergorised into three main groups: guaiacyl lignin (G-lignin) polymerized by guaiacyl phenylpropanoid units, hydroxyl-phenyl lignin (H-lignin) polymerised by p-hydroxy phenyl propanoid units and syringyl lignin (S-lignin) polymerised by syringyl phenylpropanoid units. Due to different functional groups on these units and the linking order between these groups, lignin structure becomes complicated. The number of units in lignin can vary between 200,000 to 300,000.

2.3.2 Pyrolysis

Pyrolysis is a thermochemical process at temperature range of 250-900°C (Demirbas 2004, Uchimiya *et al.* 2011, Mašek *et al.* 2013, Windeatt *et al.* 2014, Cheng *et al.* 2015, Yu *et al.* 2017) at low heating rates (< 100°C min^{-1}) in inert atmosphere *e.g.* N_2 (Demirbas 2004, Uchimiya *et al.* 2011, Mašek *et al.* 2013, Windeatt *et al.* 2014, Cheng *et al.* 2015, Yu *et al.* 2017) (known as slow pyrolysis) to produce biochar as the main product. The yield of biochar and its properties are mainly influenced by temperature, gas flow rate, holding time, and little affected by nature of feedstock at temperatures above 500°C. The yield of biochar is normally below 30 wt% if the temperature is higher than 700°C. Hemicellulose and cellulose decompose primarily in the range of 250-350°C and 325-400°C (Williams and Besler 1996, Yang *et al.* 2007, Rueda-Ordóñez and Tannous 2016). In the first stage of pyrolysis (200-400°C), β-1,4-glicosidic bonds inside cellulose and hemicellulose are broken to create many oligo and monosaccharides, and they decompose into anhydrosugars (*e.g.* levoglucosan) and furfurals through intramolecular dehydration and rearrangement reactions. Hemicellulose decomposes into relatively similar products of cellulose. Therefore, at temperature above 500°C, cellulose and hemicellulose decompose into volatiles (condense and non-condense gases) as the main products and repolymerise to form biochar *e.g.* 20 wt% and 8 wt% respectively (Williams and Besler 1996).

Lignin decomposes continuously to produce the char yield of 55 wt% (final temperature 720°C, 20°C min^{-1}) (Williams and Besler 1996). At temperature below 400°C, most α- and β-ether bonds in lignin are split homolytically or heterolytically due to lowest bond dissociation energy of ether bonds inside lignin, and most products from this stage consist of 4-substituted guaiacols (2-methoxyphenols), 4-substituted syringols (2,6-dimethoxyphenols), and other volatiles compounds such as coniferyl alcohol (Kawamoto 2017). When moving to a higher temperature range (> 400°C), these elements re-polymerise to form polycyclic aromatic hydrocarbons or char, or evaporate into atmosphere (Kawamoto 2017). The intermediates from lignin also react with those from cellulose and hemicellulose to create biochar. Biomass with high lignin content, therefore, tends to form more biochar.

Therefore, high heating rates *i.e.* >100°C min^{-1} promote the release of most intermediate products out of a biomass sample, leading to the formation of more gases under a short holding time (Montoya *et al.* 2017). Low heating rate stimulates biochar formation because a considerable percentage of gas and liquid products may undergo secondary coking and re-polymerization to increase biochar (Williams and Besler 1996, Montoya *et al.* 2017). Low gas flow rate allows intermediates to react with solid matrix and form biochar. A summarise of char yield of different feedstock obtained from pyrolysis at different operating conditions is presented in Table 2-3. Despite the difference in biomass feedstocks, biochar yields remain relatively similar at 20-30 wt% when temperature is above 500°C. Carbon contents of biochar can also increase to 90 wt% at 700-800°C which is desirable for bipolar plate in VRFB.

Table 2-3 Yield and properties of biochar obtained from various lignocellulosic materials over different operating conditions

Sample	**Operating conditions**			**Char yield (wt%)**	**Elemental composition (wt%)**				**Ref**
	Heat treatment temperature (°C)	**Heating rate (°C min^{-1})**	**Holding time (min)**		**C**	**H**	**N**	**O**	
Maize cob	300	15	30	33.42	73.09	3.76	0.36	19.76	(Intani *et al.* 2016)
Maize leaves	300	15	30	37.91	57.15	3.29	1.82	17.29	
	600	10	30	22.70	-	-	-	-	
Cottonseed hull	200	-	240	83.4	51.9	6.0	0.60	40.5	(Uchimiya *et al.* 2011)
	350			36.8	77	4.53	1.9	15.70	
	500			28.9	87.5	2.82	1.5	7.6	
	650			25.4	91.0	1.26	1.6	5.9	
	800			24.2	90	0.6	1.9	7	
Conocarpus waste	200	-	240	51.33	64.19	3.96	0.69	26.61	(Al-Wabel *et al.* 2013)
	400			31.86	76.83	2.83	0.87	14.16	
	600			27.22	82.93	1.28	0.71	6.55	
	800			23.19	84.97	0.62	0.90	4.87	
Jatropha-curcas shells	300	5	240	-	54.70	4.62	1.11	42.57	(Das *et al.* 2015)
	400				51.71	2.83	0.90	44.56	
	500				50.31	2.42	0.61	46.66	
	600				50.30	2.04	0.34	47.32	
Leucaena	250	10	480	70.4	55.7	5.7	0.8	37.7	(Wannapeera and Wora
	280		40	69.4	55.5	5.8	0.8	37.9	
	300		5	70.1	55.4	5.7	0.8	38.1	
	320		1	69.7	56.8	5.8	0.8	36.7	

									suwannarak 2015)
Apple wood	600	0.1	60	-	75.1	1.4	0.4	23.1	(Sun *et al.* 2012)
			0		76.9	1.3	0.4	21.4	
		1	60		72.4	1.1	0.4	26.1	
			0		75.4	1.3	0.4	22.9	
	450	0.1	60	-	70.6	1.7	0.5	27.2	
					80.8	1.9	0.5	16.8	
		1	60		72.0	1.9	0.5	25.6	
					81.7	2.2	0.6	15.5	
Wheat straw	400	5	120	40	71.34	2.96	0.63	11.43	(Bian *et al.* 2016)
Maize straw				33	60.29	3.18	0.86	0.86	
Rice straw				45	51.7	2.62	0.60	0.60	
Rice husk				43	54.98	2.35	0.33	0.33	
Pine wood	300	17	10	89.8	54.1	5.9	-	-	(Ronsse *et al.* 2013)
			60	43.7	71.3	4.7			
	450		10	29.2	82.5	3.8			
			60	27.0	86.3	3.5			
	600		10	24.4	90.0	2.6			
			60	23.3	92.3	2.3			
	750		10	23.0	92.5	1.4			
			60	22.7	92.5	1.1			
Wheat straw	300	17	10	98.4	53.2	6.2			
			60	48.6	69.3	5.4			
	450		10	31.3	78.8	4.2			
			60	27.8	82.9	3.5			
	600		10	24.9	87.7	2.3			
			60	24.4	88.4	2.0			
	750		10	26.4	87.5	1.5			
			60	23.7	93.2	1.3			
	500			36					
Malaysian wood pellets	500	10.04	20	25.55	87.32	1.43	0.33	10.92	(Halim and Swithenbank 2016)
	800	11.11	20	22.54	88.94	0.68	0.29	10.09	
Rubber wood	500	10.04	20	24.25	87.17	1.23	0.40	11.20	
	800	11.11	20	22.20	88.43	0.68	0.28	10.61	
Pine nut shell	300	-	10	-	67.23	4.12	0.91	26.18	(Chen *et al.* 2016)
	400				78.71	3.76	0.89	14.97	
	500				85.32	3.94	0.85	8.05	
	600				86.34	3.26	0.95	7.54	
	700				89.29	2.34	0.91	5.36	
Durian wood sawdust	350	10	360	66.56	40.88	8.35	5.12	45.65	(Chowdhury *et al.* 2016)
	450			41.22	52.99	6.01	2.01	38.99	
	550			24.46	75.99	1.02	0.55	22.44	
Ponderosa pine	300	-	60	62.2	54.8	6.50	0.05	38.7	(Keiluweit *et al.* 2010)
	400			35.3	74.1	4.95	0.06	20.9	
	500			28.4	81.9	3.54	0.08	14.5	
	600			23.9	89.0	2.99	0.06	8.0	
	700			22.0	92.3	1.62	0.08	6.0	

2.3.2.1 Carbonaceous structure

Carbonaceous structure can be measured through X-ray diffraction (XRD) and Raman spectroscopy. The positions and band widths of D and G peaks in Raman spectroscopy and the crystal height L_c, crystal diameter L_a and interlayer spacing between two carbon layers d_{002} in XRD indicate change of carbonaceous structure. The discussion in carbonaceous structure of other types of carbons, such as coal char, cokes, and petroleum pitch should shed light on the evolution of carbonaceous structure of biochar.

The impact of temperature on carbonaceous structure is significant. Johnson *et al.* studied the change in carbon structure of six different groups of coal chars between 300-2800°C (Johnson *et al.* 1986). The D-band width in Raman spectroscopy decreased with increasing temperature, indicating a higher ordered structure. Together with the decrease of D-band, higher temperature also increased the crystal diameter L_a of coal chars in this temperature range. However, the change in L_a and D band width can be only observed clearly over a large range of temperature, so care must be taken when interpreting the D-band width and L_a values when the temperature range is narrower. Intensity ratio between D and G peak (I_D/I_G) of coal chars increased from 1.1 to 1.7 when increasing temperature from 900 to 2400°C, and D band widths also reduced (Dong *et al.* 2009). However, the temperature did not influence the structure of metallurgic cokes with I_D/I_G stable at 1.3-1.4 in a temperature range 1300-2000°C (Dong *et al.* 2009). For coal chars and various types of petroleum pitch cokes between 400-1000°C, it was revealed (Johnson and Thomas 1987) that the other factors such as heating rate, pressure and holding time has little effect on D band width and L_a of carbon. D band widths of polymer-based carbon that was activated in CO_2 (900°C, holding time between 20-60 min) fluctuated in the range 264-289 cm^{-1}, at position 1363 ± 2 cm^{-1} and G band at 1593 ± 4 cm^{-1} (Baek *et al.* 2017), indicating the holding time did not significantly change Raman spectroscopy profiles of these carbon samples.

Studies on carbonaceous structure of biochar also yield similar results. The crystal diameter L_a of pyrolysed spruce wood char only increased up to 2.5 nm in a temperature range of 500-1000°C to 7.5 nm at 2400°C (Zickler *et al.* 2006). D band widths also decreased from 200 cm^{-1} at 500°C to ~55 cm^{-1} at 2200-2400°C, while G band width did not show a clear change. D band width of cedar wood-derived biochar decrease from 200 ± 12 cm^{-1} to 150 ± 10 cm^{-1} within a temperature range of 500-1000°C (Ishimaru *et al.* 2007). d_{002} of Acacia and Eucalyptus-wood biochar slightly reduced from 0.39 to 0.37 nm, and L_a increased from 2.2 to 4.0 nm after being pyrolyzed at 600-1200°C. However, increasing the holding time from 1 h to 5 h did not induce any obvious change to d_{002} and L_a at both 800 and 1000°C (Kumar *et al.* 1993). Analysis of cellulose-derived biochar slightly increased L_a and L_c from 3 to 5 nm, but decreased d_{002} from 0.350 to 0.341 nm and D band width with increasing temperatures from

600 to 2600°C (Lee 2004). The temperature range between 500-1000°C is the temperature in which most char achieves L_a value up to 2 nm.

Because biochar belongs to non-graphitisable carbon, carbonaceous structure of biochar evolves insignificantly with increasing temperature. Carbon materials can be divided into graphitic carbon and non-graphitic carbon (Marsh and Rodríguez-Reinoso 2006). The non-graphitic carbon can be classified into two categories: graphitisable (anisotropic) and non-graphitisable (isotropic) carbon in which the graphitisable carbon composes of graphene layers with high planarity and stacking and can transform into graphite under heat treatment beyond 2000°C (Marsh 1991). The high planarity and stacking order of graphitisable carbon allows it to go through a nematic discotic liquid crystal phase and create graphitic carbon (Figure 2-5). The carbon obtained from heat treatment of polyvinylchloride (PVC) is one example of graphitisable carbon. Biochar, on the other hand, belongs to the class of non-graphitisable carbon which cannot be turned into graphite under high temperature treatment. Various cross linkages between C, H and O in biochar originating from the cross-structure of cellulose and lignin in biomass yield extremely high activation energies (even temperature > 2000°C) to break all these bonds and remove all heteroatoms out of carbon, so it cannot go through a nematic discotic liquid crystal phase to form graphitic carbon. Therefore, unless biochar is treated in special conditions to remove all cross linkages in its structure, it is impossible to directly produce graphitic carbon from biomass using heat treatment via pyrolysis.

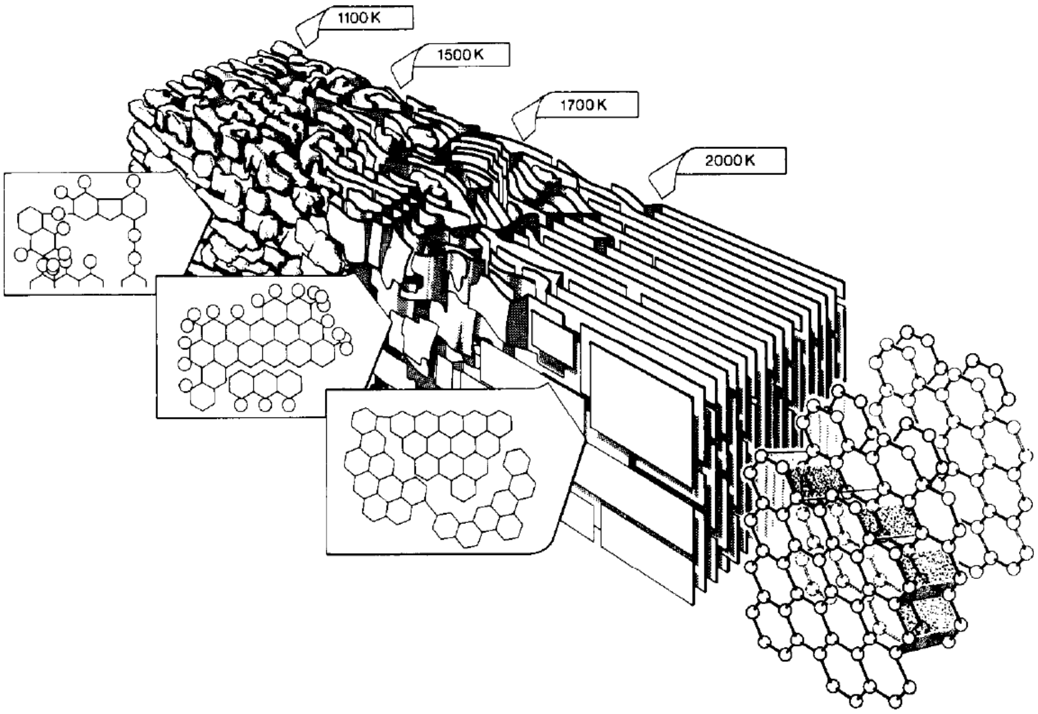

Figure 2-5 Schematic of phase changing in graphitisable carbon going when going through different temperatures (Marsh 1991)

In conclusion, temperature is the main factor governing carbonaceous structure during pyrolysis of biomass. The temperature range of 500-1000°C is sufficient to vary carbonaceous structure of biomass-derived carbon since the change in carbonaceous structure is negligible at temperatures above 1000°C.

2.3.2.2 Surface area and porosity

Surface area and porosity are important factors of biochar. Various pore sizes and high surface area are important for the diffusion and mass transfer of electrolyte ions in energy storage device application. The requirement for pore size structure and distribution and surface area in each application vary significantly. For example, in energy storage device, electrolyte ions need to contact electrode surface for electron exchange, so it is important to ensure that a sufficient surface are is present to reduce mass transfer resistance. International Union of Pure and Applied Chemistry (IUPAC), pore sizes can be classified into micropores (< 2 nm), mesopores (> 2 nm and < 50 nm) and macropores (> 50 nm). Micropores (< 2 nm) ensure high capacitance (Qiao *et al.* 2014), while mesopores (> 2 nm and < 50 nm) facilitate electrolyte ion diffusion onto electrode surface. These mesopores create reasonably short paths for ions to diffuse into reaction sites more easily, which improves kinetics (Rauda *et al.* 2013). Additionally, macropores (> 50 nm) act as ion reservoirs to adequate penetration of electrolyte ions into electrode structure. It could be seen that increasing the pore sizes will decrease the surface area, such as in carbon felt with large macroporous network only having low surface area (Zhou *et al.* 2017) and vice versa.

Pyrolysis contributes little to the development of surface area of biomass-derived biochar. The BET N_2 surface area (S_{BET}) was only ~5 m^2 g^{-1} for lignin-derived biochar pyrolysed at 350-400°C (Sharma *et al.* 2004), 2-8 m^2 g^{-1} tea waste-derived biochar treated at 400-700°C (Uzun *et al.* 2010) and 5-12 m^2 g^{-1} for duckweed-derived biochar pyrolysed at 400-700°C (Muradov *et al.* 2012). Increasing temperature from 400 to 800°C only increased S_{BET} of fir-wood derived biochar from 4 to 47 m^2 g^{-1} (Chen *et al.* 2019). S_{BET} increased from 1 to 45 m^2 g^{-1} for rapeseed-derived biochar when increasing temperature from 200 to 450 and 700°C (Zhao *et al.* 2018). A negative impact of temperature on S_{BET} for rice-straw-derived biochar was reported, surface area reducing from 141 to 46 m^2 g^{-1} with increasing temperature from 600 to 1000°C (Paethanom and Yoshikawa 2012). Very rarely, the surface area of biochar increased after pyrolysis, for example the sawdust-derived biochar obtained from pyrolysis increased the surface area from 102 to 419 m^2 g^{-1} at 450-850°C (Del Bubba *et al.* 2020), and this may be due to the impact of the original feedstock. Micropore volumes of this sawdust-derived biochar accounted for 78-90% of total pore volume. With S_{BET} of most biochar derived from biomass as aforementioned being below 50 m^2 g^{-1}, pore volumes are usually below 0.02 cm^3 g^{-1} (Muradov *et al.* 2012), indicating that pore volume is also not developed during pyrolysis.

Most studies do not provide comprehensive explanation why pyrolysis hinders the development of surface area and pore volume. Pyrolysis reaction mechanisms mainly focus on the decomposition of cellulose, hemicellulose, and lignin to create intermediates and then the formation of biochar from those intermediates, rather than on how this process could influence surface area and pore volume of biochar. Therefore, the impact of pyrolysis on surface area and pore volume is mainly speculated from characterisation of biochar surface area and pyrolysis reaction mechanisms. From the decomposition of lignocellulosic contents to secondary coking and polymerisation, there is no direct reaction that supports pore formation or enlarges pores in biochar. Even if micropores and mesopores are formed during pyrolysis, pores can also collapse and lead to the reduction of surface area. Variations in BET N_2 surface area of biochar shows that N_2 could not diffuse into small pores of biochar, resulting in the activated diffusion effect of N_2 at low temperatures (-196°C). Therefore, activating methods to enhance surface area and pore size of biochar is necessary to expand the applications of biochar, giving each application required different extent of surface area and pore volumes.

2.3.2.3 Functional groups

Pyrolysis is conducted in an inert atmosphere such as N_2 or He. Therefore, it is likely to eliminate the influence of gas phase atmospheres or liquid phase treatments on the functional groups (Figueiredo *et al.* 1999). In pyrolysis, high temperature removes the oxygenation functional groups. Total surface oxygen functional groups (C-OH and O-C=O) on fir wood-derived biochar decreased from 23.41 to 9.44 wt% when pyrolysis temperature increased from 300 to 600°C, but remained almost constant in the range 8.73-9.44 wt% when temperature continued to rise up to 900°C (Chen *et al.* 2019). The C-O/OH content decreased from 16.69 to 10.68 wt% with increasing temperature from 300 to 600°C, but the content of O-C=O reduced slightly from 8.05 to 5.09 wt% with increasing temperature from 300 to 900°C. Sawdust-derived biochar also observed a major change in surface functional groups content with temperature increasing from 450 to 650°C, but no variations were recorded when temperature increased to 850°C (Del Bubba *et al.* 2020). Most oxygen functional groups of tea waste-derived biochar were removed after being treated at 700°C, left alone the aromatic carbons in biochar (Uzun *et al.* 2010). The C and O contents in biochar were significantly influenced by temperature but little affected by heating rates when comparing the walnut shell-derived biochar obtained from pyrolysis in the temperature range of 400-800°C at heating rate 10°C min^{-1} and isothermal pyrolysis (Yuan *et al.* 2020). XPS C 1s of biochar obtained at 600-800°C were relatively similar regardless of temperatures and heating methods, while XPS C 1s of 400°C sample showed a higher phenolic content at 286-286.3 eV. Further assessment on XPS O 1s presented the stability of C-OOH groups regardless of temperature (~15 %) with increasing of C=O content in quinone and decreasing of C-OH content with increasing temperatures. The contents of C-OH, carboxyl and quinone groups in cottonseed hull-derived biochar decreased with increasing temperatures from 500 to 800°C while more aliphatic C-H were converted into aromatic C-H (Uchimiya *et al.* 2011). Another study of Mireles *et al.* on corn stover, orange peel and pistachio shell-derived biochar showed the decline in aliphatic carbon and C=O contents when increasing temperature from 350 to 600°C due to the dehydration and rearrangement of cellulose and hemicellulose in the precursor materials (Mireles *et al.* 2019). Increasing temperature to 600°C also transformed the aliphatic C-H into aromatic C-H.

2.3.3 Hydrothermal carbonisation

Hydrothermal carbonisation (HTC) is a thermochemical process conducted at low temperature range (180-300°C) to resemble the coalification process of natural biomass into coal like materials. This method is suitable for high moisture content biomass as it is treated in aqueous environment at subcritical conditions (Ciuta *et al.* 2018). When temperature increases, the water pressure also increases. Hydrogen bonds of water are weakened and more ions (H_3O^+ and OH^-) are created, and these ions can also react with biomass without the need of using acidic environment. The biomass is converted into a solid material referred to as hydrochar, liquid, and gases. The removal of hydrogen and oxygen contents from biomass in subcritical water conditions is one distinctive characteristic of HTC, which makes HTC suitable for treatment of high moisture content biomass into fuel. However, a considerably high content of oxygen functional group is still preserved in hydrochar with oxygen/carbon ratio varying from 0.25-0.6 depending on operating conditions. Since high temperatures decompose cellulose, higher lignin content normally results in higher oxygen functional groups (Donar *et al.* 2016).

Similar to pyrolysis, in HTC, temperature is the dominating factor controlling the characteristics of hydrochar (Yan *et al.* 2014, Álvarez-Murillo *et al.* 2015, Basso *et al.* 2015, Basso *et al.* 2016, Donar *et al.* 2016, Guo *et al.* 2016). Temperature has different effects on the decomposition of cellulose, hemicellulose and lignin (Wang *et al.* 2018). For cellulose, it starts to decompose after 200°C into oligomer units (containing 2-10 glucose units) due to the breakage of β-1,4-glycosidic bonds, and then into monomer units (glucose). These oligomer and monomer units undergo different reactions including dehydration, fragmentation due to the cleavage of C-C bond breaking and ring open, and isomerisation to form various components such as furfural. From these intermediates, polymerisation and condensation reactions occur to form spherical structures in hydrochar. A schematic of the formation of spherical structures in hydrochar from cellulose is illustrated in Figure 2-6. The cellulose in olive residue completely decompose by 260°C (Donar *et al.* 2016). The other study on HTC treatment of cellulose and hemicellulose mixtures also showed that temperature < 200°C has no effect on the crystallinity of cellulose (Liu *et al.* 2016). Cellulose starts to degrade after 200°C, and this process completes at 230°C (Liu *et al.* 2016). The higher temperatures required to degrade all cellulose in olive residue (260 compared 230°C) is attributed to the lignin covered outside cellulose structure. On the other hand, hemicellulose requires lower temperatures (at 180°C) compared to cellulose in order to decompose (Bobleter 1994). Hemicellulose is more amorphous compared to cellulose, and decomposes into several monomers such as glucose, mannose, and galactose. Study on poplar and wheat straw showed that hemicellulose rapidly decomposed at 200°C even with low holding time (< 10 min) (Reza *et al.* 2014).

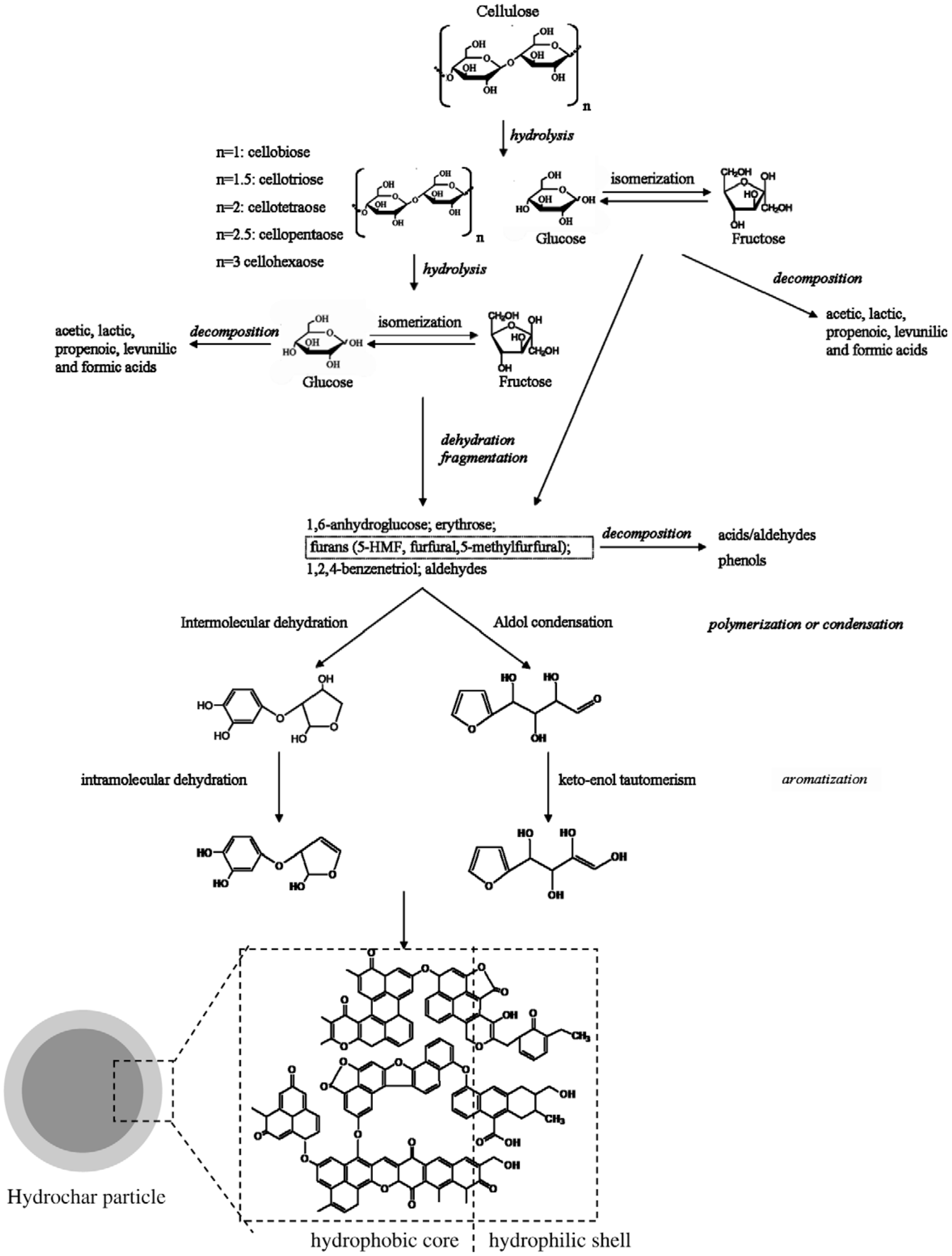

Figure 2-6 Scheme of the formation of spherical structures in hydrochar from cellulose (adapted from (Sevilla and Fuertes 2009))

Unlike cellulose, lignin is difficult to dissolve in water at below 250°C (Kang *et al.* 2012), and lignin may only decompose slowly with temperatures above 250°C and holding time over 8 h (Kang *et al.* 2012, Reza *et al.* 2014, Guo *et al.* 2015). The decomposition of lignin in HTC results in different phenol derivatives such as guaiacol, catechol, and eugenols through hydrolysis and de-alkylation reactions. The intermediates from these reactions then go through polymerisation/ cross linking reactions to form phenolic spherical structures. A part of lignin which is non-dissolved in subcritical water conditions go through intramolecular reaction such as condensation, also to form spherical structures in hydrochar (Fang *et al.* 2008). A summarised mechanism for spherical structure formation from lignin in HTC is presented in Figure 2-7.

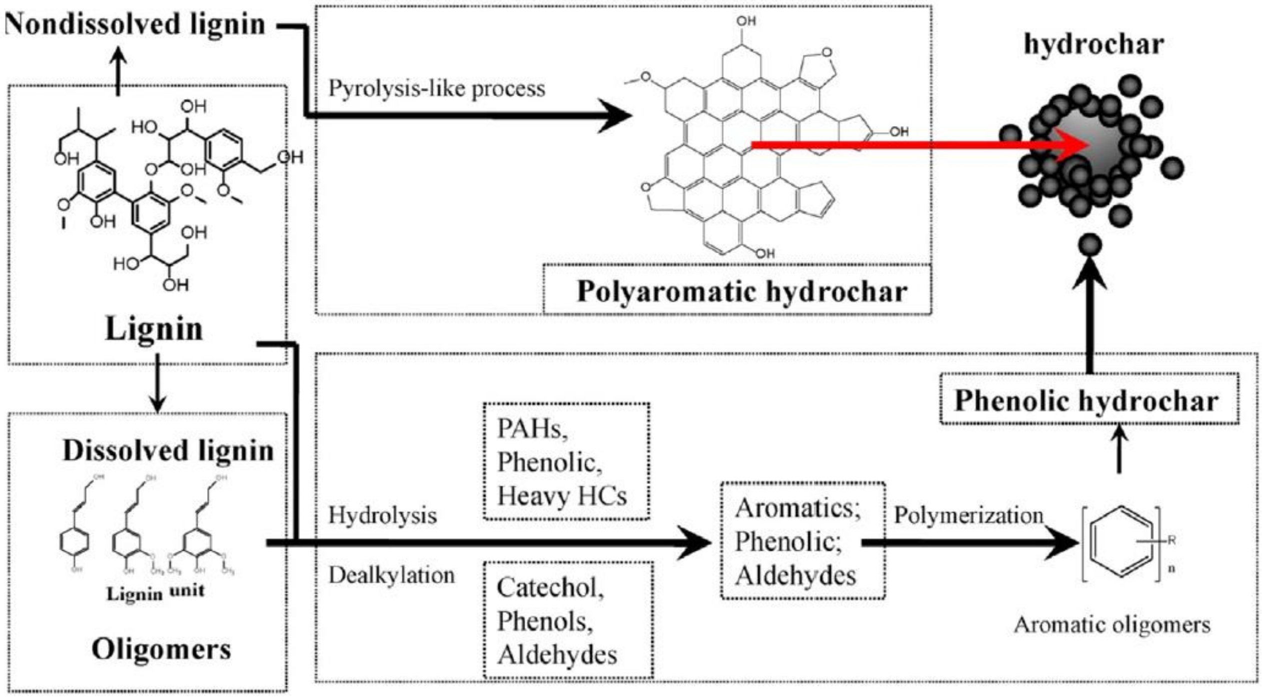

Figure 2-7 Spherical structures formation in hydrochar from lignin (adapted from Kang *et al.* (Kang *et al.* 2012) and Fang *et al.* (Fang *et al.* 2008)) presenting the reaction pathways of dissolving lignin and non-dissolving lignin in subcritical water

The yield of hydrochar is highly influenced by operating conditions of HTC, and it decreases remarkably when increasing the temperature from 180°C to 260°C. Most cellulose and hemicellulose in longan shell decomposed at 250°C and 4 h holding time (Guo *et al.* 2016), and hydrochar yields reached 45 wt%. However, the yield of longan shell-derived hydrochar only slightly reduced to 40 wt% with increasing temperature and holding time to 290°C and 8 h holding time. This indicated a stable solid yield after complete degradation of both cellulose and hemicellulose components in biomass (Guo *et al.* 2016). In operating conditions, the domination of temperature over reaction time was concluded by several studies Sevilla *et al.* (Sevilla and Fuertes 2009) and Donar *et al.* (Donar *et al.* 2016). Increasing temperature from only 230°C to 240°C could reduce the hydrochar yield from 37 wt% to 31 wt%, although the holding time at 240°C was 0.5 h compared to 1 h at 230°C. The hydrochar yields from olive residue and hazelnut shell at 260°C and 2, 4 and 6 h holding time were relatively the same (Donar *et al.* 2016), and they also remained unchanged after 4 h holding time and 220°C, at ~39 and 50 wt% respectively. This is in agreement with several other studies (Mäkelä *et al.* 2015, Zhu *et al.* 2015). In general, hydrochar yield after 250°C is higher than biochar yield after 500°C due to the retention of more oxygen functional groups in hydrochar.

2.3.3.1 Functional groups

During HTC, oxygen and hydrogen contents of biomass are reduced due to dehydration, decarboxylation and dealkylation reactions, leading to higher carbon content in hydrochar. The H/C and O/C ratios of hydrochar decrease with increasing temperature and holding time of HTC (Wang *et al.* 2018). The H/C and O/C ratios in hydrochar can fluctuate between 1.48 and 0.69 for miscanthus obtained at 190°C (5 min) to 0.74 and 0.21 for coconut fibre obtained at 350°C (30 min) respectively. Comparing the H/C and O/C ratios of hydrochar to other coals, hydrochar belongs to sub-bituminous coal rank, which is lower than anthracite and bituminous coals.

2.3.3.2 Hydrochar structure and surface porosity

Spherical structures in hydrochar are formed during HTC (Figure 2-8) (Sevilla and Fuertes 2009, Sevilla *et al.* 2011, Gong *et al.* 2014, Romero-Anaya *et al.* 2014, Donar *et al.* 2016, Guo *et al.* 2016, Liu *et al.* 2016). The size of these spherical particles vary depending on precursors, such as 0.7-2.4 μm for olive derived hydrochar (Donar *et al.* 2016), 0.4-6 μm for hydrochar derived from α-D-Glucose, D-(+)-sucrose, and potato starch (Sevilla and Fuertes 2009), and 1-10 μm for hydrochar from sawdust and straw after being treated at 250°C and 2 h (Sevilla *et al.* 2011). Although there are variety in sizes of spherical structures in hydrochar, the formation of spherical structures results in low surface area, for example, S_{BET} of wood fibre-derived hydrochar was 5-32 $m^2\ g^{-1}$ with HTC temperature of 200-240°C respectively (Liu *et al.* 2016). S_{BET} of eucalyptus sawdust and barley straw-derived hydrochar were 4 and 8 $m^2\ g^{-1}$ (Sevilla *et al.* 2011). Varying temperature (180-290°C) and holding time in HTC does not lead to significant change in surface area of hydrochar. The low S_{BET} of hydrochar derived from other feedstocks are also observed *e.g.* 3 $m^2\ g^{-1}$ (digestate at 260°C) (Garlapalli *et al.* 2016), 139 $m^2\ g^{-1}$ (Brewer's yeast powder at 190°C) (Wang *et al.* 2016), 4 $m^2\ g^{-1}$ (dewatered sewage sludge at 340°C) (He *et al.* 2016), 13 $m^2\ g^{-1}$ (oil palm shell at 260°C) (Nizamuddin *et al.* 2015). From scanning electron microscopy (SEM) and transmission electron microscopy (TEM) images, no porous network was formed during

HTC, also the subcritical water in HTC does not favour the release of volatiles out of biomass to form pores.

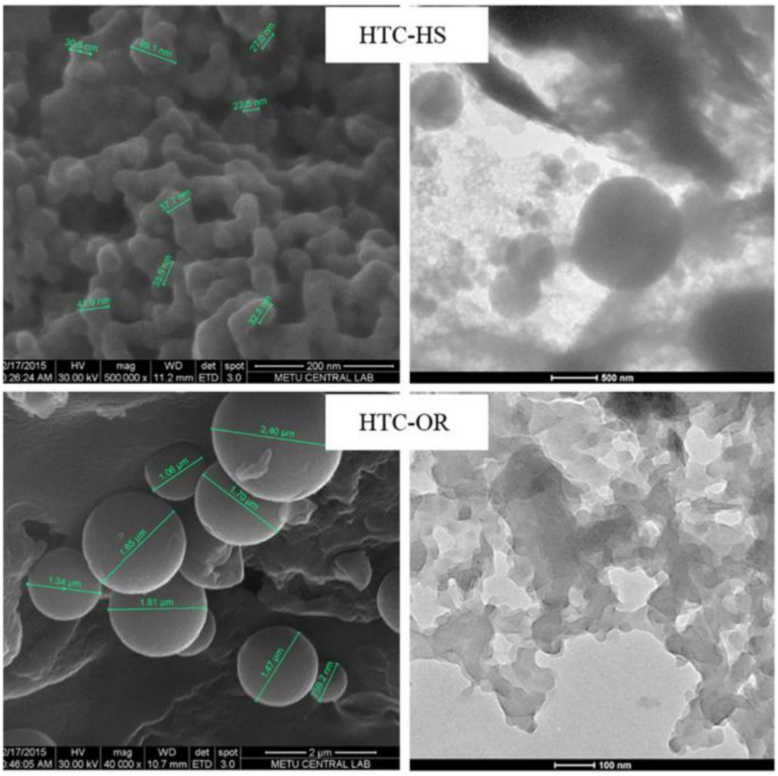

Figure 2-8 SEM (on the right) and TEM (on the left) images of carbon sphere structure obtained from hazelnut shell hydrochar (HTC-HS) and olive residue hydrochar (HTC-OR) (260°C, 4 h, and 10:1 biomass-to-water ratio) (adapted from Donar *et al.* (Donar *et al.* 2016))

Along with the inhibition of surface area development in HTC, HTC also leads to highly amorphous structure of hydrochar. The high oxygen content in hydrochar also explains the amorphous structure of hydrochar. The I_D/I_G ratio for hazelnut shell hydrochar reduced from 0.62 to 0.57 with increasing temperature from 180°C to 260°C, 4 h holding time (Donar *et al.* 2016). The same trend was observed for olive residue hydrochar (Donar *et al.* 2016).

2.4 Functionalisation/activation of biomass-derived carbon

2.4.1 Physical functionalisation/activation

Pyrolysis did not favour the formation of functional groups and pore structures in biochar. Hydrochar retained a considerable amount of oxygen, but HTC also restricted the formation of pore structures. Therefore, functionalisation/activation is important to achieve these characteristics.

2.4.1.1 CO_2 activation

CO_2 is used to modify the surface porosity of biomass-derived carbon via Boudouard reaction ($C + CO_2 \rightarrow 2CO$) at temperatures ≥ 700°C, forming micropores and mesopores in AC, and being unlikely to influence biochar functional groups (due to high temperatures). Operating conditions (including temperature, holding time and flow rate of CO_2) influences properties of AC in CO_2. The BET N_2 surface area increased from 642-644 $m^2 g^{-1}$ to 845-985 $m^2 g^{-1}$ for oak and 432-660 $m^2 g^{-1}$ to 616-712 $m^2 g^{-1}$ for corn stover with increasing temperatures from 700 to 800°C (Zhang *et al.* 2004). The highest S_{BET} of 654 $m^2 g^{-1}$ for corn cob at 850°C whereas only 140 $m^2 g^{-1}$ at 700°C (Zhang *et al.* 2020). Micropore volume (V_{micro}) and micropore surface area (S_{CO2}) of spruce wood AC also increased 633 to 832 $m^2 g^{-1}$ (Burhenne and Aicher 2014). Hickory and peanut hull were first treated in HTC at 200°C for 6 h and then activated with CO_2 in the temperature range of 600-900°C. S_{BET} and pore volumes of hickory-derived AC increased from 453 $m^2 g^{-1}$ and 0.050 $cm^3 g^{-1}$ at 600°C to 928 $m^2 g^{-1}$ and 0.054 $cm^3 g^{-1}$ at 900°C, and S_{BET} and pore volumes of peanut hull AC increased from 353 $m^2 g^{-1}$ and 0.075 $cm^3 g^{-1}$ to 1308 $m^2 g^{-1}$ and 0.114 $cm^3 g^{-1}$ (Fang *et al.* 2016).

Prolonging holding time for CO_2 activation only affects surface area and pore volume at high temperatures (> 700°C). S_{BET} of corn stalk-derived AC treated at 850°C also increased with holding time from 1 to 2 h, 559 $m^2 g^{-1}$ and 0.472 $cm^3 g^{-1}$ to 882 $m^2 g^{-1}$ and 0.599 $cm^3 g^{-1}$ (Wang *et al.* 2014). S_{BET} and pore volume of peanut hull AC remained unchanged at 349-365 $m^2 g^{-1}$ and 0.067-0.114 $cm^3 g^{-1}$ at 700°C after 1 or 2 h holding time, but S_{BET} increased significantly from 988 to 1308 $m^2 g^{-1}$ at 900°C after increasing holding time from 1 to 2 h (Fang *et al.* 2016). Because Boudouard reaction is an endothermic reaction, increasing temperatures enhances the reactivity between CO_2 and biochar, resulting in higher surface areas and pore sizes.

CO_2 treatment mainly influences V_{micro} rather than mesopore and macropore volumes at 700-950°C. CO_2 activation on buckwheat husk at 850°C did not significantly improve the total mesopore and macropore volumes of this AC compared to biochar obtained from pyrolysis in N_2 at the same temperature (0.555 ± 0.092 compared to 0.540 ± 0.084 $cm^3 g^{-1}$), measured by mercury porosimetry (Pena *et al.* 2020). V_{micro} of this buckwheat husk biochar was 0.261 $cm^3 g^{-1}$, accounting for 89% of total pore volume (0.291 $cm^3 g^{-1}$). Most AC treated under CO_2 at high temperatures (> 700°C) developed mainly micropores with gas adsorption-desorption isotherms falling into type I and sometime type IV isotherms (featuring high gas sorption uptakes at low $p/p°$ region, reaching plateau at high $p/p°$), indicating the formation of microporous AC. Some of adsorption-desorption isotherms of carbon materials activated in CO_2 are illustrated in Figure 2-9. However, at temperature > 1000°C, more carbon reacts with CO_2, reducing V_{micro} and increasing mesopore and macropore volume. Total pore volume of glucose-derived AC also increased from 0.235 $cm^3\ g^{-1}$ to 0.595 $cm^3\ g^{-1}$ at 900°C with V_{micro} being 0.482 $cm^3\ g^{-1}$ (81% of total pore), but then increased to 1.384 $cm^3\ g^{-1}$ at 1000°C with V_{micro} being 0.284 $cm^3\ g^{-1}$ (only ~20% of total pore) (Gu *et al.* 2017).

CO_2 activation is an effective method to modify surface area and porosity, but the variation in properties of precursor can make it difficult to control the change of surface and porosity under operating conditions.

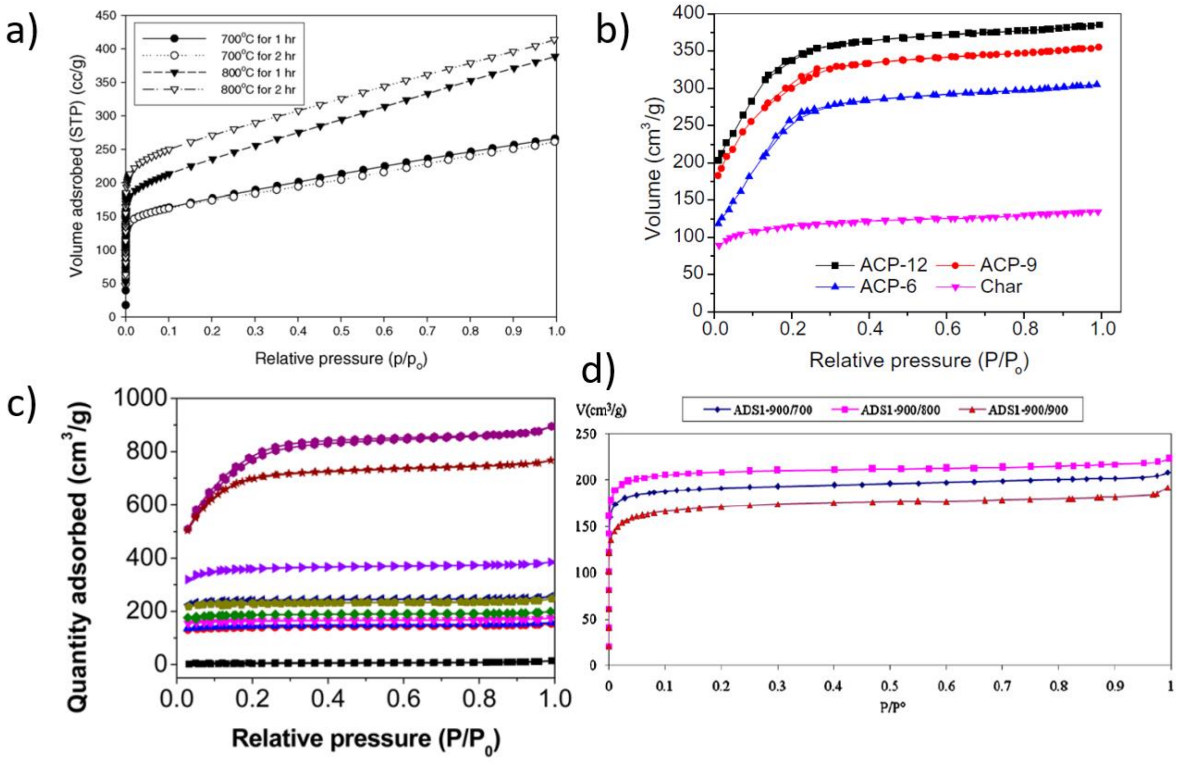

Figure 2-9 N_2 adsorption-desorption of some biomass-derived carbon materials activated in CO_2, indicating the type I isotherm according to IUPAC classification (a) oak-derived AC at 700 and 800°C, (b) corn stalk-derived AC at 850°C at 60, 90 and 120 min (c) glucose-derived AC activated with CO_2 between 800-1000°C (d) date stone from date tree carbon activated with CO_2 at 900°C (adapted from references (Zhang *et al.* 2004), (Wang *et al.* 2014), (Gu *et al.* 2017), and (Sekirifa *et al.* 2013))

2.4.1.2 NH_3 activation

Heat treatment in NH_3 environment is a common method to introduce nitrogen into carbon structure. Carbonisation of carbon materials at high temperatures with N-contained gas phase such as NH_3 has been studied for a long time. Under high temperature, NH_3 decomposes into free radicals such as NH_2, NH, atomic hydrogen and nitrogen, and these radicals then react with carbon to create nitrogen functional groups (Stöhr *et al.* 1991). This method allows a quick preparation step for carbon materials with various nitrogen contents. The reaction with NH_3 at elevated temperatures (> 600°C) also leads to improved surface area and porosity due to the gasification effect of NH_3 over carbon (Stöhr *et al.* 1991).

NH_3 activation at high temperatures significantly influences total nitrogen contents in carbon materials, with nitrogen contents increasing from 0.3-0.5 wt% in most biomass precursors to 8.56 wt% in corn straw AC (activated in NH_3 at 800°C) (Lian *et al.* 2016), 14.4-15.5 wt% in coconut AC (ammoxiated in NH_3:air (1:10) at 350°C) (Guo *et al.* 2016), 3.7-4.6 wt% in palm shell AC (activated in NH_3 400 and 800°C) (Shafeeyan *et al.* 2011), 6.5-7.3 wt% in bituminous coals (activated in NH_3 at 700°C) (Pietrzak *et al.* 2010), and 0.82-2.12 wt% in anthralur AC (activated in the temperature range of 600-1000°C) (Stöhr *et al.* 1991).

Temperature is the main factor controlling the components of nitrogen functional groups. NH_3 activation at temperature below 600°C generated amide, imide and lactam-N functional groups on biochar at the expense of C=O groups (Jansen and van Bekkum 1994). NH_3 activation at 230°C on biochar in another study also resulted in lactam and imide groups (Jansen and van Bekkum 1995). At temperatures below 400°C, carboxylic and hydroxyl oxygen groups on the surface of biochar reacted with NH_3 to form amide, amine and even nitrile groups (2-4, 2-5, and 2-6) (Shafeeyan *et al.* 2011).

$$\text{-COO}^{-}\text{NH}_4^{+} \rightarrow \text{-CO-NH}_2 + \text{H}_2\text{O} \qquad (2\text{-}4)$$

$$\text{-CO-NH}_2 \rightarrow \text{C}{\equiv}\text{N} + \text{H}_2\text{O} \qquad (2\text{-}5)$$

$$\text{-OH} + \text{NH}_3 \rightarrow \text{-NH}_2 + \text{H}_2\text{O} \qquad (2\text{-}6)$$

According to equations 2-4, 2-5, and 2-6, oxygen functional groups increase reactivity of biochar and lead to more nitrogen functional groups in biochar during NH_3 activation (Dastgheib *et al.* 2004, Shafeeyan *et al.* 2011). Amide, amine and even nitrile groups decomposed or transformed into N-5 and N-6 groups with increasing temperatures above 400°C (Jansen and van Bekkum 1995). The thermal stability of nitrogen functional groups is as follow pyrrolic-N < pyridinic-N < quaternary-N (Pels *et al.* 1995). The temperature range of 600-1000°C favours the formation of pyridinic-N (N-6) and pyrrolic-N (N-5) functional groups, and N-6 and N-5 gradually transformed into quaternary-N (N-Q) when temperature increases to 800°C (Stöhr *et al.* 1991, Jansen and van Bekkum 1995).

NH_3 treatment is also an effective method to improve surface area and porosity of biochar due to the reaction between NH_3 and carbon in biochar. Temperature and holding time influence surface area and pore volume of biochar. S_{BET} of corn straw biochar increased from 73 to 418 m^2 g^{-1} in the temperature range of 600-800°C, and S_{BET} also increased from 139 to 418 m^2 g^{-1} when increased holding time from 1 h to 3 h at 800°C (Lian *et al.* 2016). S_{BET} of pine needle-derived biochar increased to 574-1841 m^2 g^{-1} with micropores being the main pores in biochar (N_2 adsorption-desorption isotherm following a clear type I adsorption) (Wang *et al.* 2017). Corncob AC also showed high S_{BET} of 494-1154 m^2 g^{-1} when varying temperatures in the range of 700-800°C (Geng *et al.* 2016). S_{BET} of anthralur AC after NH_3 treatment at 900°C increased from 695 to 930 m^2 g^{-1}, and micropores accounted for 79% of total pore volume (0.43 out of 0.54 cm^3 g^{-1}) (Stöhr *et al.* 1991). S_{BET} of cellulose-derived AC also increased 351 to 635 m^2 g^{-1} in temperature range of 500-800°C with micropores accounting for 56-77% of total pore volume (Wutscher *et al.* 2019).

2.4.1.3 NH_3 activation in dielectric barrier discharge cold plasma

Introduction of plasma

Plasma is an ionised gas, commonly referred as the fourth state of matter (Fridman 2008, Lu *et al.* 2016, Whitehead 2016). Free electric particles (*i.e.* electrons and ions) in plasma makes it electrically conductive and responsive to electromagnetic fields. Plasma occurs during natural events such as lightning or can be created artificially by applying a strong electric field to ionise neutral particles (*i.e.* molecules) or heating up a neutral gas. Ionised gas is normally considered plasma due to its electrically neutral (balance between the number of ions and electrons). Nowadays, plasma created in atmospheric pressure is becoming more attractive due to the convenience in experiment setups. Atmospheric pressure plasma can be categorised into thermal equilibrium, local thermal equilibrium, and non-thermal equilibrium. In non-thermal equilibrium plasma (*i.e.* non-equilibrium plasma, cold plasma), temperature of electron is considerably to be much higher than those of ions and neutral molecules. The excitation energy from electrons can be transferred into vibrational and rotational states of molecular gas plasma (primary plasma processes), resulting in extremely reactive gas molecules and radicals. These processes include ionization, dissociative ionisation, electron attachment, dissociative electron attachment, and excitation:

- Ionisation: $e + M \rightarrow M^+ + 2e$
- Dissociative ionisation: $e + AB \rightarrow A^+ + B + 2e$
- Electron attachment: $e + M \rightarrow M^-$

- Dissociative electron attachment: $e + AB \rightarrow A^{-} + B$
- Excitation: $e + M \rightarrow M^{*} + e$ (This can be electronic excitation in the case of atoms and molecules and also vibrational and rotational excitation for molecules)

The secondary plasma processes involve collisions between heavy particles such as molecules and ions.

In atmospheric cold plasma, high electric field is required to initiate breakdown for gas molecules. There are two breakdown mechanisms: Townsend breakdown and streamer breakdown. In Townsend breakdown, the gas ionisation process starts with a single free electron being accelerated in the electric field, resulting in collisions with other gas molecules to release free electrons. These newly free electrons continue to be accelerated and then free more additional electrons. When electrons move towards anode, they leave behind positive ions (moving more slowly to the cathode due to difference in molecule and electron weight). Electrons and ions formed according to Townsend breakdown are assumed to not distort the external electric field.

However, the space charge created by electrons and positive ions from Townsend breakdown also creates electric field, and secondary breakdown can appear if this electric field becomes relatively strong compared to applied electric field. In this circumstance, electrons will be drifted toward the positive charge region created by positive ions rather than anode. This secondary breakdown is called streamer breakdown. Streamer breakdown is a type of transient electrical discharge which forms at the surface of a conductive electrode carrying a high voltage in an insulating medium, and it becomes more profound in atmospheric pressure plasma. It can develop into a spark discharge (*i.e.* high current density). Methods to prevent the transition from streamer discharge into spark discharge include manipulating the streamer development time or limiting the current density on the conductive electrode. These methods can include increasing the local electric field strength by using sharp objects (*i.e.* corona discharge), limit discharge current by using dielectric barriers, and improve the heat transfer by forced convection via high gas flowrate by using highly thermal conductive gas (*e.g.* hydrogen, helium).

Dielectric barrier discharge cold plasma

Dielectric barrier discharge (DBD) cold plasma is a type of cold plasma in which one or both electrodes are covered by dielectric layers. Due to higher dielectric constants of dielectric barriers compared to gases, the dielectric barrier layer may increase breakdown strength for streamer breakdown. Although streamer breakdown is initiated at random points between electrodes in DBD, it does not lead to arc discharge due to self-extinguishing effect of gas flow between electrodes. Gas flow removes any accumulation of charge on surface of dielectric barrier layers, so it reduces the local electric field. Under gas flow, random streamer breakdowns are then distributed homogeneously. This creates a uniform non-equilibrium plasma. Furthermore, dielectric barrier layers provide sufficient insulation to limit conduction current and charge transfer, and subsequently prevent spark discharge. Therefore, cold plasma in an atmospheric pressure gas with large volume can be created by DBD, which is easy to control and can be applied in many applications. The advantage of DBD cold plasma also include the operation under wide range of gas pressures (could be up to 10^6 Pa) with the gap distance between dielectric barrier layers varying in the range of 0.1 mm to several centimetres. Dielectric barriers, made from glass, quartz, polymer, ceramic, *etc.*, protect electrodes under any corrosive gas atmospheres and reduce electrode erosion. Therefore, DBD cold plasma is simple, stable, and economical.

DBD cold plasma has been traditionally used to create ozone from air, but it can also be used to polymerise small molecules containing heteroatoms into carbon precursor or alter surface porosity. However, only some studies have explored the application of DBD cold plasma in introducing heteroatoms such as nitrogen from gas or liquid sources into a carbon material until now. For example, some studies in incorporating nitrogen in carbon materials using cold plasma showed that nitrogen contents could reach 2.2-4.4 at% for treated CNTs (Chetty *et al.* 2009, Fang *et al.* 2019) to 1.9-8.5 at% for treated graphene (Shao *et al.* 2010, Wang *et al.* 2010). With the advantages from DBD cold plasma, using DBD cold plasma in NH_3 medium may be a potential pathway to incorporate nitrogen into biochar as a replacement for conventional NH_3 heat treatment. Although NH_3 heat treatment is effective to incorporate nitrogen into biochar, this method requires high temperatures and heat resistant materials for reactors. Until now, the influence of DBD cold plasma in incorporating nitrogen into carbon materials, especially biochar has not been studied thoroughly. Furthermore, it is difficult to directly compare the data from different studies because of the disparate operating conditions and different DBD system setups. Figure 2-10 and Table 2-4 describe details of some DBD systems used in some studies. The plasma active area and the gap between two dielectric barriers could vary significantly.

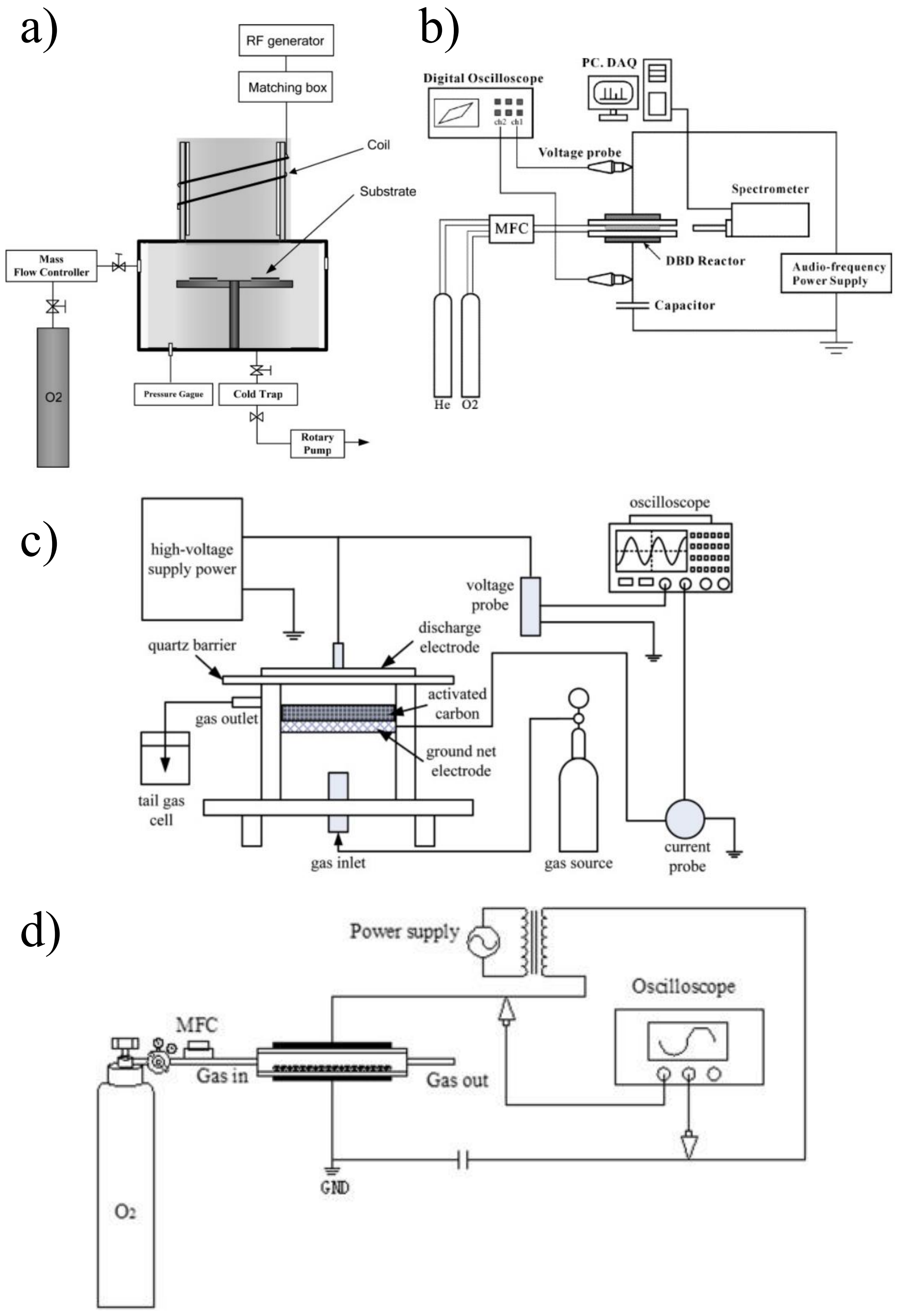

Figure 2-10 Different dielectric barrier discharge experimental system setups (adapted from Tang *et al.* (Tang *et al.* 2007), Lee *et al.* (Lee *et al.* 2005), Qu *et al.* (Qu *et al.* 2013) and Zhang *et al.* (Zhang *et al.* 2016))

Table 2-4 Description of some DBD experimental setups

Reference	**Experimental setup**
Lee *et al.* (Lee *et al.* 2005)	Two parallel-plate type size of 217×200 mm, barrier thickness of 3 mm, and barrier-to-barrier gap of 5 mm
Qu *et al.* (Qu *et al.* 2013)	Ground electrode was round metal net, (diameter 60 mm). The discharge electrode (round thin metallic slice, thickness 2 mm, diameter 100 mm) was placed onto quartz barrier (foursquare thin quartz slice, thickness 2 mm, side length 150 mm). The gap space between the quartz barrier and ground net electrode was maintained at 6 mm.
Zhang *et al.* (Zhang *et al.* 2016)	Two quartz parallel-plates and two stainless plates. The size of quartz and stainless plates were, respectively, 100 × 40 mm (barrier thickness 2 mm) and 80 × 40 mm (barrier-to-barrier gap 8 mm)

In the study of Ning *et al.*, walnut shell was first pyrolysed in in N_2 at 700°C for 1 h and activated in KOH at 700°C to obtained AC. This AC was then functionalised using cold plasma at voltages of 5.6-8.0 kV, and it was shown that cold plasma had little effect on S_{BET} and total pore volume of the AC (Ning *et al.* 2018). Nitrogen and oxygen contents increased from 0.4 and 13.8 at% from pristine AC to 0.7 and 16.1 at% in DBD cold plasma-treated AC, respectively, and nitrogen groups in this DBD cold plasma-treated walnut shell AC were assigned to amide and amine groups without any further explanation from the authors.

Other studies using different forms of cold plasma reported nitrogen groups to pyridinic-N, pyrrolic-N and quaternary-N rather than amide and amine groups. Nitrogen content in carbon nanotubes (CNTs) activated in microwave plasma increased from 0.05 wt% to 1.9 wt%, and nitrogen groups were assigned pyridinic-N and pyrrolic-N (based on merely XPS N1s peaks at 397 and 400 eV) (Chen *et al.* 2010). Nitrogen contents on synthesised graphene activated in N_2 plasma chamber also increased from 0.1 at% to 1.4 at%, and these nitrogen groups were ascribed to pyridinic-N, pyrrolic-N and quaternary-N (Wang *et al.* 2010). Figure 2-11 shows the XPS N1s peaks of some plasma treated carbon materials, in which all of them assigned pyridinic-N, pyrrolic-N, quaternary-N and N-oxides to nitrogen groups formed during plasma treatment.

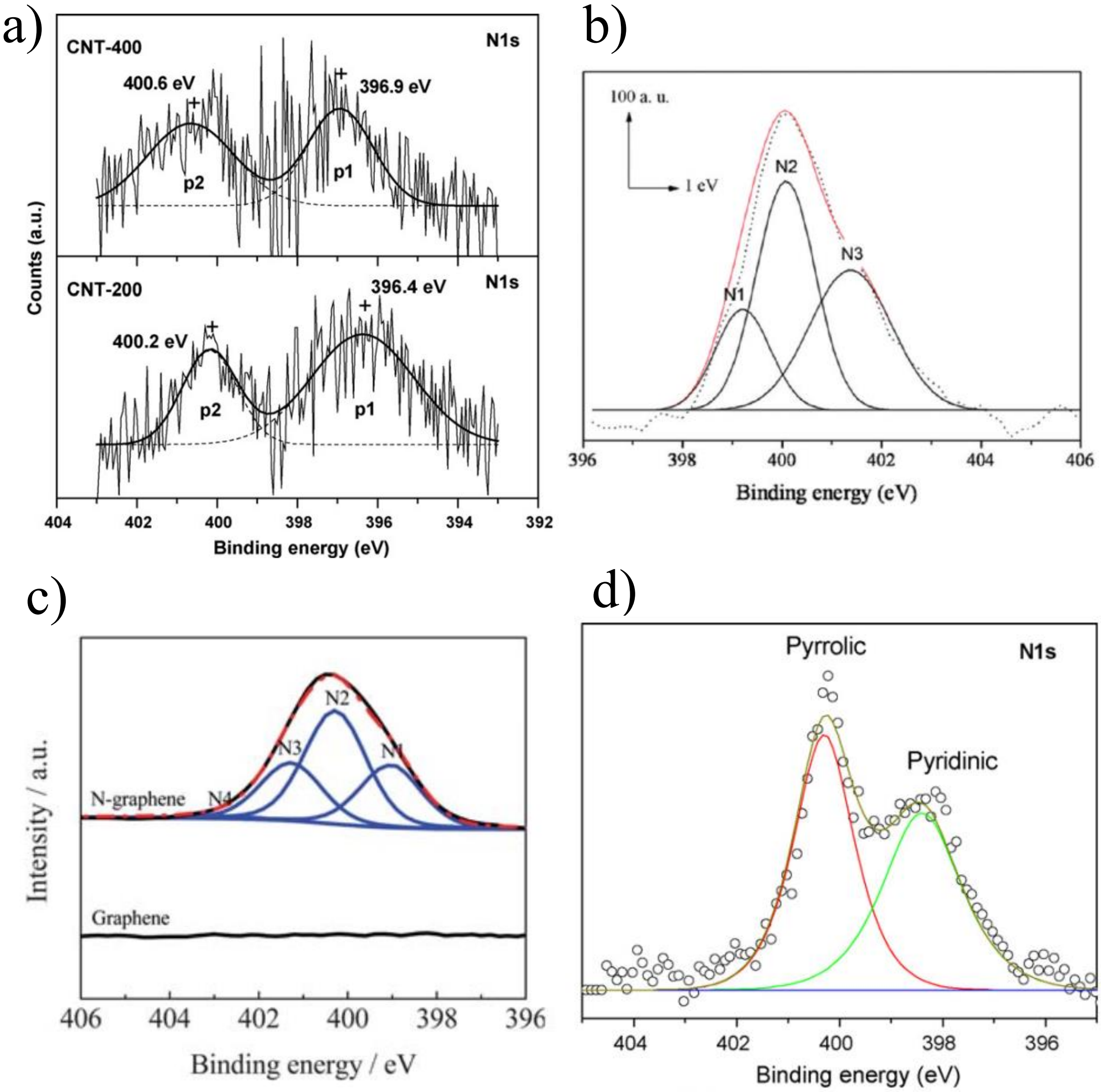

Figure 2-11 XPS N1s of some functionalised carbons with nitrogen through plasma treatment: (a) CNTs functionalised in N_2 microwave plasma at 200 and 400 W (Chen *et al.* 2010), (b) graphene treated in N_2 plasma (Wang *et al.* 2010), (c) graphene treated using N_2 plasma chamber at 200 mTorr, plasma power 140 W for 20 min (Shao *et al.* 2010), and (d) multiwalled CNTs treated in N_2 plasma at 120 W for 20 min (Chetty *et al.* 2009)

The lack of understanding about nitrogen components formed during cold plasma treatment and the variation in nitrogen contents the make it difficult to apply DBD cold plasma treatment in functionalising carbon materials. Therefore, it is necessary to explore how operating conditions of plasma influence both nitrogen contents and the specific types of nitrogen groups.

2.4.2 Chemical functionalisation/ activation

2.4.2.1 Functionalisation/ activation by metallic bases

Chemical activation has been deployed to improve the characteristics of biochar such as KOH (Wu *et al.* 2005, Tay *et al.* 2009, Cha *et al.* 2010, Liu *et al.* 2016), NaOH (Park *et al.* 2013, Volperts *et al.* 2019) and K_2CO_3 (Hayashi *et al.* 2002, Tay *et al.* 2009). KOH and NaOH, under elevated temperatures (600-1000°C), react with carbon in biomass to form metallic K and Na and their basic salt Na_2CO_3 and K_2CO_3. These salts continue to react with C to form K and Na (Lillo-Ródenas *et al.* 2003, Lillo-Ródenas *et al.* 2004). The consumption of char, coupling with the release of gases (H_2 and CO), creates more pores and widens pore sizes, increasing porosity in biomass structure (Tay *et al.* 2009).

$$6KOH + 2C \rightarrow 2K + 3H_2 + 2K_2CO_3 \quad (1)$$

$$K_2CO_3 + 2C \rightarrow 2K + 3CO \quad (2)$$

$$6NaOH + 2C \rightarrow 2Na + 3H_2 + 2Na_2CO_3 \quad (3)$$

$$Na_2CO_3 + 2C \rightarrow 2Na + 3CO \quad (4)$$

KOH, NaOH, K_2CO_3 and Na_2CO_3 are frequently used to modify surface area and pore volume. Table 2-5 summaries S_{BET} and pore volume of AC that was activated in KOH, K_2CO_3 and NaOH. Temperature is one of the main operating conditions governing surface area and porous structure in AC when using KOH, K_2CO_3 and NaOH activation. With KOH, S_{BET} and pore volume of lotus seedpod AC increased from 870 $m^2\ g^{-1}$ and 0.53 $cm^3\ g^{-1}$ at 700°C to 2864 $m^2\ g^{-1}$ and 1.60 $cm^3\ g^{-1}$ at 900°C respectively after KOH activation (Liu *et al.* 2016). S_{BET} of rice straw AC also increased from 140 to 772 $m^2\ g^{-1}$ after KOH activation at 700°C (KOH:rice straw char ratio = 1:1), and the pore volume increased from 0.092 to 0.442 $cm^3\ g^{-1}$ (Cha *et al.* 2010). S_{BET} of coconut and pistachio shell AC reached the highest value ~1750 $m^2\ g^{-1}$ after K_2CO_3 activation at 800°C, while the maximum S_{BET} of almond, oil palm and walnut shell AC was only ~1150 $m^2\ g^{-1}$ at the same conditions (Hayashi *et al.* 2002). Increasing the temperature from 500 to 800°C increased S_{BET} significantly by promoting the formation of micropores in all biochar, but S_{BET} reduced when temperature increased to 900°C due to the development of mesopores (Figure 2-12). S_{BET} of orange peel AC that was activated by K_2CO_3 also increased 6 to 1177 $m^2\ g^{-1}$ when the temperature increased from 500 to 900°C, and S_{BET} reached a plateau at around 1000°C (1228 $m^2\ g^{-1}$) (Köseoğlu and Akmil-Başar 2015). Micropores also dominated pore size distribution in this AC at all temperatures used, but mesopore formation was promoted at 1000°C.

From Table 2-5, the ratio of activating agent/biochar or activating agent/biomass also influences pore volume and subsequently surface area. Increasing this ratio results in higher V_{micro} due to reaction between carbon in biochar with KOH/K_2CO_3. V_{micro} of fir wood AC could account to more than 80% of V_{total}, being 0.50 out of 0.61 $cm^3 g^{-1}$ of total pore volume at 780°C with KOH/biochar ratio = 0.5 (Wu *et al.* 2005). V_{micro} and V_{total} of fir wood AC increased to 1.17 and 1.53 $cm^3 g^{-1}$ respectively when KOH/biochar ratio increased to 6. Micropores continue to develop until reaching a plateau, and then mesopores start to form as the expense of micropores. V_{micro} and V_{total} of alder wood AC were 0.883 and 1.184 $cm^3 g^{-1}$ respectively at 700°C with NaOH/wood char ratio = 2 (micropore accounts for 75% of V_{total}), but they increased to 0.902 and 1.417 $cm^3 g^{-1}$ respectively with NaOH/wood char ratio = 3 with micropore being ~64% of V_{total} (Volperts *et al.* 2019). However, the point where micropores stop developing and shifting to mesopores is still unclear in literature due to scattering data in literature.

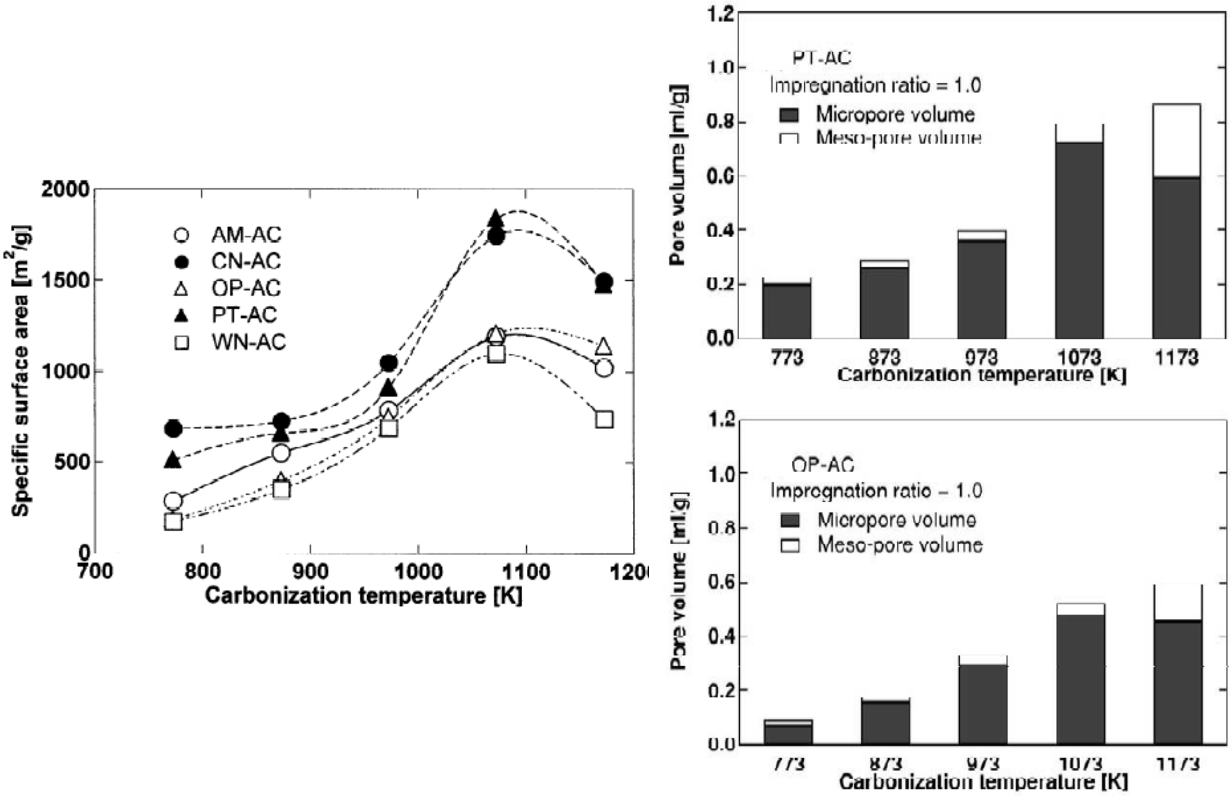

Figure 2-12 Left: Influence of temperatures on porosity of nut shell-derived AC (AM-AC: almond shell, CN: coconut shell, OP: oil palm shell, PT: pistachio shell, WN: walnut shell), Right: Micropore and mesopore volumes of pistachio shell and oil palm shell biochar at different temperatures (adapted from (Hayashi *et al.* 2002))

Table 2-5 Characteristics of activated carbon treated with KOH, K_2CO_3 and NaOH

Raw material	**Activation method**	**S_{BET} (m^2 g^{-1})**	**V_{total} (cm^3 g^{-1})**	**V_{micro} (cm^3 g^{-1})**	**Ref**
Soybean waste	KOH/soybean waste = 1, heat treatment at 600°C for 1 h (10°C min^{-1})	600	0.299	0.213	(Tay *et al.* 2009)
	KOH/soybean waste = 1, heat treatment at 800°C for 1 h (10°C min^{-1})	619	0.291	0.143	
	K_2CO_3/soybean waste = 1, heat treatment at 600°C for 1 h (10°C min^{-1})	644	0.336	0.272	
	K_2CO_3/soybean waste = 1, heat treatment at 800°C for 1 h (10°C min^{-1})	1352	0.680	0.400	
Rice straw	Pyrolysed at 500°C for 1 h. KOH/biochar = 1, heat treatment at 700°C for 2 h (5°C min^{-1})	772	0.422	-	(Cha *et al.* 2010)
Fir wood	Pyrolysed at 450°C for 1.5 h. KOH/biochar = 0.5, heat treatment at 780°C for 1 h (10°C min^{-1})	891	0.61	0.50	(Wu *et al.* 2005)
	Pyrolysed at 450°C for 1.5 h. KOH/biochar = 1, heat treatment at 780°C for 1 h (10°C min^{-1})	1371	0.81	0.65	
	Pyrolysed at 450°C for 1.5 h. KOH/biochar = 4, heat treatment at 780°C for 1 h (10°C min^{-1})	2179	1.24	0.97	
	Pyrolysed at 450°C for 1.5 h. KOH/biochar = 6, heat treatment at 780°C for 1 h (10°C min^{-1})	2794	1.54	1.17	
Lotus seedpod	KOH/lotus seedpod = 1.68, hydrothermal carbonised at 120°C for 2 h. Heat treatment at 700°C for 2 h (4°C min^{-1})	870	0.53	0.38	(Liu *et al.* 2016)
	KOH/lotus seedpod = 1.68, hydrothermal carbonised at 120°C for 2 h. Heat treatment at 800°C for 2 h (4°C min^{-1})	1813	1.05	0.22	
	KOH/lotus seedpod = 1.68, hydrothermal carbonised at 120°C for 2 h. Heat treatment at 900°C for 2 h (4°C min^{-1})	2864	1.60	0.84	
Orange peel	K_2CO_3/ orange peel = 1:1. Heat treatment at 500°C for 1 h in N_2 (10°C min^{-1})	9	0.01	0.01	
	K_2CO_3/ orange peel = 1:1. Heat treatment at 700°C for 1 h in N_2 (10°C min^{-1})	477	0.23	0.21	

Raw material	Activation method	S_{BET} ($m^2\ g^{-1}$)	V_{total} ($cm^3\ g^{-1}$)	V_{micro} ($cm^3\ g^{-1}$)	Ref
	K_2CO_3/ orange peel = 1:1. Heat treatment at 800°C for 1 h in N_2 (10°C min^{-1})	621	0.30	0.22	(Köseoğlu and Akmil-Başar 2015)
	K_2CO_3/ orange peel = 1:1. Heat treatment at 900°C for 1 h in N_2 (10°C min^{-1})	1177	0.59	0.40	
	K_2CO_3/ orange peel = 1:1. Heat treatment at 1000°C for 1 h in N_2 (10°C min^{-1})	1228	0.78	0.16	
Loblolly pine	Pyrolysed at 300°C for 15 min. NaOH/biochar = 2.13. Heat treatment at 800°C for 2 h (3°C min^{-1})	1250	1.072	0.289	(Park *et al.* 2013)
	Pyrolysed at 350°C for 15 min. NaOH/biochar = 2.13. Heat treatment at 800°C for 2 h (3°C min^{-1})	702	0.487	0.241	
	Pyrolysed at 500°C for 15 min. NaOH/biochar = 2.13. Heat treatment at 800°C for 2 h (3°C min^{-1})	346	0.290	0.128	
	Pyrolysed at 700°C for 15 min. NaOH/biochar = 2.13. Heat treatment at 800°C for 2 h (3°C min^{-1})	57	0.054	0.013	
Alder wood char	NaOH/wood char = 2. Heat treatment at 600°C in Ar.	1787	0.887	0.789	(Volperts *et al.* 2019)
	NaOH/wood char = 3. Heat treatment at 600°C in Ar.	2333	1.200	0.939	
	NaOH/wood char = 2. Heat treatment at 650°C in Ar.	2038	1.002	0.860	
	NaOH/wood char = 3. Heat treatment at 650°C in Ar.	2699	1.337	0.917	
	NaOH/wood char = 2. Heat treatment at 700°C in Ar.	2295	1.184	0.883	
	NaOH/wood char = 3. Heat treatment at 700°C in Ar.	2845	1.417	0.902	
Cellulose	Pyrolysed at 450°C for 4 h. NaOH/char = 3. Heat treatment at 700°C in Ar.	2728	1.354	0.932	(Volperts *et al.* 2019)

Table footnote: S_{BET}: surface area obtained from N_2 adsorption-desorption at -196°C, V_{total}: total pore volume, V_{micro}: micropore volume

2.4.2.2 Activation by acids

Some acids such as H_3PO_4 and HNO_3 can be used as activating agents for carbon materials.

H_3PO_4 activation

The impact of phosphorus functional groups on performance of VRFB have been discussed in Chapter 1, with phosphorus functional groups being able to act as catalytic sites for vanadium redox couples. H_3PO_4 is used to incorporate phosphorus into carbon structure, and the phosphorus content is highly influenced by the operating conditions of activating methods. H_3PO_4 activation directly on biomass rather than biochar (obtained at high temperatures) tends to incorporate more phosphorus due to more flexible structure of biomass compared to biochar. Phosphorus content also increases with increasing temperature from 0.2-3.6 at% at 300-400°C to 5.4-8.52 at% at 500-800°C for wood, apricot stone, and olive stone derived AC (Lee and Reucroft 1999, Benaddi *et al.* 2000, Puziy *et al.* 2005, Bedia *et al.* 2011). Sucrose biochar had the highest phosphorus content at 15.24 wt% (Lysenko *et al.* 2012).

Pre-heating treatment biomass also influences the incorporation of phosphorus into biomass-derived carbon. Hay derived AC which underwent a pre-pyrolysis treatment at 500°C for 1 h could incorporate 6.3-6.4 wt% of phosphorus after being activated in H_3PO_4 at 600°C for 0.5 h (Kazmierczak-Razna *et al.* 2017). Sucrose that was first pyrolysed at 900°C for 2.5 h and then activated in H_3PO_4 at 800°C only incorporated 2.03 wt% of phosphorus into biochar, but the phosphorus content went up to 15.24 wt% after one step activation with H_3PO_4 at 800°C (Lysenko *et al.* 2012). At 500°C, only cellulose and hemicellulose decompose, a proportion of functional groups in lignin may retain, so these functional groups could react with H_3PO_4 to form new phosphorus groups after activation. Biomass undergoes pre-heating treatment at high temperatures *i.e.* above 700°C is difficult for H_3PO_4 to react with a rigid carbon structure to incorporate new functional groups into biochar. Anthracite, a hard and compact coal with little impurities, could only incorporated a small range of phosphorus content of 0.3-1.1 wt% in a temperature range of 600-800°C (Ma *et al.* 2018). Therefore, biomass that is pre-treated at low temperatures is likely to incorporate more phosphorus that at high temperatures.

Besides phosphorus contents, phosphorus components are also influenced by operating conditions. Most phosphorus groups on polyimide-based carbon remained at phosphate-like structure at temperatures of 500°C (132.2 eV of XPS binding energy), but completely transformed into pyrophosphate (133.1 eV) and metaphosphate (134.2 eV) at 800°C with pyrophosphates and metaphosphates contents being ~45.6-57.6% and ~36.1-46.8% of total phosphorus content (1.64-11.17 at%) (Huang *et al.* 2018). Pyrophosphate groups also dominated in waste coffee derived AC with 50.3-64.8% of total phosphorus content (5.0-13.3 at%) compared to 29.8-34.1% of metaphosphate regardless of impregnation ratio (H_3PO_4/ biomass = 0.5-3) (Huang *et al.* 2013). However, the assignment of only pyrophosphate and metaphosphate groups to phosphorus functional groups is not accurate because it only assumes C-O-P bonds and neglects C-P bonds, although C-P bonds can be formed simultaneously. Therefore, some studies assigned phosphorus groups into C-PO_3/C_2-PO_2 groups (resembling C-P-O bonds) (132.9 eV), C-O-PO_3/$(C-O)_3PO$ groups (resembling C-O-P bonds) (134.0 eV) and phosphorus pentoxide (P_4O_{10}) (136.0 eV).

The content of C-PO_3/C_2-PO_2 on anthracite coal reduced from 56.7% of total phosphorus to 40.5% when temperature increased from 600 to 800°C, while C-O-PO_3/$(C-O)_3PO$ content increased from 42.3% to 54.9% (Ma *et al.* 2018). P_4O_{10} content increased slightly from 1.0 to 4.6% with increasing temperature due to thermal decomposition of phosphorus groups (Ma *et al.* 2018). Phosphorus content of olive stone biochar were 3.6-4.8 at% in temperature range of 400-800°C, and the distribution of phosphorus functional groups shifted from C-O-PO_3/$(C-O)_3PO$ (higher binding energy) to C-PO_3/C_2PO_2 (lower binding energy) when temperature increased from 400°C to 800°C (Bedia *et al.* 2011). AC derived from lignin, olive stone, ply wood, and hemp canes at 450-500°C also showed the majority of phosphorus groups was C-O-PO_3/$(C-O)_3PO$ groups rather than C-PO_3/C_2PO_2, and C-O-PO_3/$(C-O)_3PO$ tended to decompose at 800°C into C-PO_3/C_2PO_2 (Bedia *et al.* 2009). The same shift from C-O-PO_3/$(C-O)_3PO$ to reduced state C-PO_3/C_2PO_2 was observed for lignin derived AC (García-Mateos *et al.* 2018).

H_3PO_4 has been used as an activating agent to increase the porosity of AC. A heating range of 400-600°C is effective to promote development of surface porosity, while increasing temperature up to 800-1000°C tends to diminish this effect. For example, white oak AC treated by H_3PO_4 in the temperature range of 150-650°C reached the highest micropore volume at 350°C (0.7 $cm^3\ g^{-1}$) and mesopore volume at 500°C (0.55 $cm^3\ g^{-1}$), and the pore volume decreased with increasing temperatures from 500 to 650°C (Solum *et al.* 1995). Coconut shell AC that was treated with H_3PO_4 achieved the highest S_{BET} of 1275 $m^2\ g^{-1}$ at 450°C. S_{BET} of olive stone-derived carbon decreased from 1173 to 875 $m^2\ g^{-1}$ when temperature increased from 400 to 800°C (H_3PO_4/biomass = 0.5) and also decreased from 1648 to 1294 $m^2\ g^{-1}$ (H_3PO_4/biomass = 1) and 1342 to 1073 $m^2\ g^{-1}$ (H_3PO_4/biomass = 2) in the same temperature range.

Despite these results, it is still unclear about how operating conditions could cooperate to determine phosphorus content and different phosphorus components. Phosphorus components is governed by temperature, but it is unclear how concentration of H_3PO_4 and holding time can impact phosphorus contents. Therefore, it is important to understand about its mechanism.

HNO_3 activation

The use of HNO_3 in treating biomass often aims to increase oxygen surface functional groups rather than increase surface area and porosity. The influence of HNO_3 solution at various concentrations on surface chemistry of AC has been studied by Noh and Schwarz (Noh and Schwarz 1990). The HNO_3 treatment did not significantly change the S_{BET} (fluctuating in the range of 1015-1150 $m^2\ g^{-1}$) at all treating conditions, but it increased the oxygen contents and surface acidity significantly (Table 2-6). According to the acid/base titration results, carboxylic acid was the most abundant oxygen functional groups, then lactone/ lactone and finally phenol.

Table 2-6 The acid base titration result of activated carbon treated in HNO_3 at different concentrations (Noh and Schwarz 1990)

HNO_3 concentration (M)	**0**	**0.2**	**0.4**	**1.0**	**2.0**
HCl (mequiv g^{-1})	0.738	0.599	0.314	0.163	0.143
NaOH (mequiv g^{-1})	0.04	0.276	0.478	0.887	1.709
Na_2CO_3 (mequiv g^{-1})	-	-	0.127	0.351	0.503
$NaHCO_3$ (mequiv g^{-1})	-	-	-	0.334	0.117
NH_3 acidity (mmol g^{-1})	2.35	3	4.24	5.18	6.41

The impact of HNO_3 on coconut shell-derived AC was studied by Jia and Thomas (Jia and Thomas 2000). Coconut shell-derived AC treated with HNO_3 7.5 M increased the oxygen content significantly from 3.2 wt% to 15.3 wt% (after 4 h treatment) and 21.9 wt% (after 48 h treatment). Incorporated oxygen functional groups ranged from carboxylic, lactone/ lactol and phenolic, and these functional groups were removed with increasing temperatures in the range of 300-800°C. These coconut shell carbons after being heated to 800°C reduced the oxygen content sharply to 2.6 and 3.8 wt%. Polyacrylonitrile-derived carbon after being treated with HNO_3 7.5 M for 48 h also increased oxygen content from 2.18 to 19.75 wt% with various contents of carboxylic, lactone/ lactol and phenolic (Xiao and Thomas 2005). Pecan shell AC after being treated with HNO_3 4 M also increased significantly in carboxylic content (Cao *et al.* 2019). Other studies on almond shell (Moreno-Castilla *et al.* 1995), wood and coconut shell (Kim *et al.* 2019), also showed the similar effect of HNO_3 on modifying the oxygen surface functional groups.

2.5 Conclusions

Renewable energy has the potential to replace deteriorating fossil fuels such as petroleum and coal, as well as ensure more sustainable supply for energy requirement in the future. However, the intermittent nature and geographical constraint of renewable energy restricts the application of renewable energy into all end-user demands, especially with renewable energy sources including sunlight, wind and ocean currents (which can be converted directly into grid). Therefore, a suitable energy storage allows the integration of these energy sources into grid system. Among energy storages, VRFB is a potential candidate due to its safety, long life cycles and no cross-contamination between cathode and anode. However, it is important to reduce the capital, operational and maintenance cost of VRFB to enhance its usage. One of the main components in VRFB is composite bipolar plate with main content being graphite. Studies on carbon/graphite felt positively suggested that oxygen functional groups and surface area/ porosity are important for VRFB performance. The bipolar plate, however, is usually considered as a secondary contribution to the electrode performance compared to carbon/graphite felt in VRFB, so studies on alternative materials for the bipolar plate has not received enough attention. Using biochar, a redundant and inexpensive carbon source, to replace graphite in the bipolar plate, not only reduces the price, but also enables better performance compared to the traditional composite bipolar plate. Some early studies on the application of biochar into bipolar plate have been conducted, and they suggest that high surface area, functional groups, and carbonaceous structure are desirable characteristics for biochar in bipolar plate. However, it lacks systematic studies on how these characteristics of biochar could influence the performance of bipolar plate in VRFB.

The main method to convert biomass into biochar is pyrolysis, but pyrolysis/carbonisation of biomass even up to 2000°C cannot completely convert biomass into graphite due to heteroatoms creating many cross-linkages between C, H and O in carbon structure. Pyrolysis results in ultra-micropores in biochar, and majority of ultra-micropores are inaccessible by N_2 molecules during the N_2 adsorption-desorption at -196°C, which results in low BET N_2 surface area ($< 50\ m^2\ g^{-1}$). Therefore, other activation methods is required to widen ultramicropores and increase mesopore volume. Temperatures above 500-600°C decompose completely cellulose and hemicellulose and significantly lignin, so it removes most functional groups in biomass. HTC is normally used as pre-treatment method for biomass precursors in coal production, resulting in highly amorphous solid materials (hydrochar) which contains considerable amounts of oxygen and hydrogen. Spherical structures are formed during HTC with low surface areas and no porous network. Therefore, the properties of biochar and hydrochar are not well-suited for direct use in bipolar plates. Activation to increase surface area and porosity, functional groups and carbonaceous structure is important to make it more feasible to apply biochar and hydrochar into bipolar plate. Furthermore, it lacks understanding on how each of these properties could influence bipolar plate performance in VRFB.

Activation methods using CO_2 and NH_3 at high temperatures allow the development of porosity of carbon and the incorporation nitrogen into carbon structure (in the case of NH_3). Using KOH, NaOH, K_2CO_3 and Na_2CO_3 can also increase the porosity of carbon structure to different extent. Regarding incorporating heteroatom into biomass-derived carbon, using dielectric barrier discharge cold plasma in NH_3 atmosphere is a promising method to introduce nitrogen into carbon structure without undergoing high heat treatment, but not many studies have been conducted to understand impact of this procedure on biochar. Phosphorus can be incorporated through H_3PO_4 activation. This functionalisation not only increase phosphorus content in the forms of different phosphorus functional groups type, but also modify the surface porosity of material. These activation methods allow to create a wide range of biochar which facilitates the application into composite bipolar plate.

In summary, the following chapters will explore these areas:

- Convert walnut shell into walnut shell-derived carbon using pyrolysis under N_2 atmosphere, activation under CO_2 and NH_3 atmospheres, treatment with HNO_3 and heat treatment with K_2CO_3 to systematically vary surface area, porosity, functional groups and carbonaceous structure of walnut shell-derived carbon materials.
- Incorporate nitrogen into walnut shell-derived carbon using dielectric barrier discharge cold plasma under NH_3 and incorporate phosphorus using heat treatment, and relate physicochemical characteristics of carbon materials with operating conditions.
- Conduct electrochemical experiments (cyclic voltammetry and electrochemical impedance spectroscopy) on some walnut shell-derived carbon samples to understand the influence of surface area, porosity, functional groups and carbonaceous structure on the kinetics of vanadium redox reactions.

Chapter 3

Experimental methodologies

This chapter comprises three main sections of experimental methodologies. The first one describes material preparation including the thermochemical (pyrolysis, hydrothermal carbonisation) and functionalisation procedures (activating with K_2CO_3, HNO_3, heat treatment and cold plasma dielectric barrier discharge in NH_3 atmosphere, and heat treatment with H_3PO_4 solutions). The second section explains the techniques used for characterising biomass-derived carbon, including surface area and porosity (CO_2 adsorption-desorption at 0°C, N_2 adsorption-desorption at -196°C and scanning electron microscopy), heteroatom functional groups (X-ray photoelectron spectroscopy, temperature-programmed desorption, acid/base titration and Fourier-transform infrared spectroscopy), chemical composition (total elemental analysis and inductively coupled plasma-mass spectrometry) and carbonaceous structure (Raman spectroscopy and X-ray diffraction). The third section explains the electrochemical measurement using cyclic voltammetry and electrochemical impedance spectroscopy.

3.1 Materials preparation

According to International Nut and Dried Fruit Council report in 2017/2018, walnut was second to almond as the most consumed tree nuts in high-income economies (18 wt%) and the first consumed tree nut in middle-income economies (29 wt%) (International Nut and Dried Fruit Council 2018). This results in abundant walnut shells being disposed in landfills although some of them is used as an abrasive medium. The contents (dry ash free) of carbon, hydro and oxygen in walnut shells were 47.93 wt%, 6.52 wt% and 45.55 wt% respectively. Walnut shells with particle size of ~1 mm, which was purchased directly from UKGE Ltd., was used for further treatment Figure 3-1. This walnut shell was used as a soft medium for metal cleaning. Biomass-derived carbon from walnut shells were prepared using various methods to vary surface area and porosity, functional group and carbonaceous structure.

Figure 3-1 Walnut shells used for pyrolysis and hydrothermal carbonisation experiment

3.1.1 Conversion from walnut shells into biomass-derived carbon

3.1.1.1 Pyrolysis of walnut shells

In this study, biochar was prepared from walnut shells (particle size ~ 1mm) by pyrolysis at 600 – 1000°C under N_2 atmosphere with a heating rate of 8.5 ± 0.1°C min^{-1}. Activated carbon (AC) was also prepared from walnut shells (particle size ~ 1mm) in CO_2 atmosphere instead of N_2. The biochar/AC samples were labelled as X/T-h in which X = N_2 indicating N_2 atmosphere and CO_2 for CO_2 atmosphere, T is the final pyrolysis temperature in °C and h is the holding time in hours after the system reached the desired temperature. For example, AC CO_2/800-1 indicates the sample obtained from pyrolysis at 800°C and 1 h holding time in CO_2 atmosphere. Figure 3-2 presented biochar CO_2/800-1 obtained after pyrolysis with particle size ~0.5-0.7 nm. It is unnecessary to increase temperature over 1000°C which negatively influences porosity of biochar as discussed in section 2.3.2.1, and temperature above 600°C is sufficient to transform cellulose and hemicellulose into biochar/AC as discussed in section 2.3.2. This range of temperature and low heating rate allows to obtain most biochar from biomass.

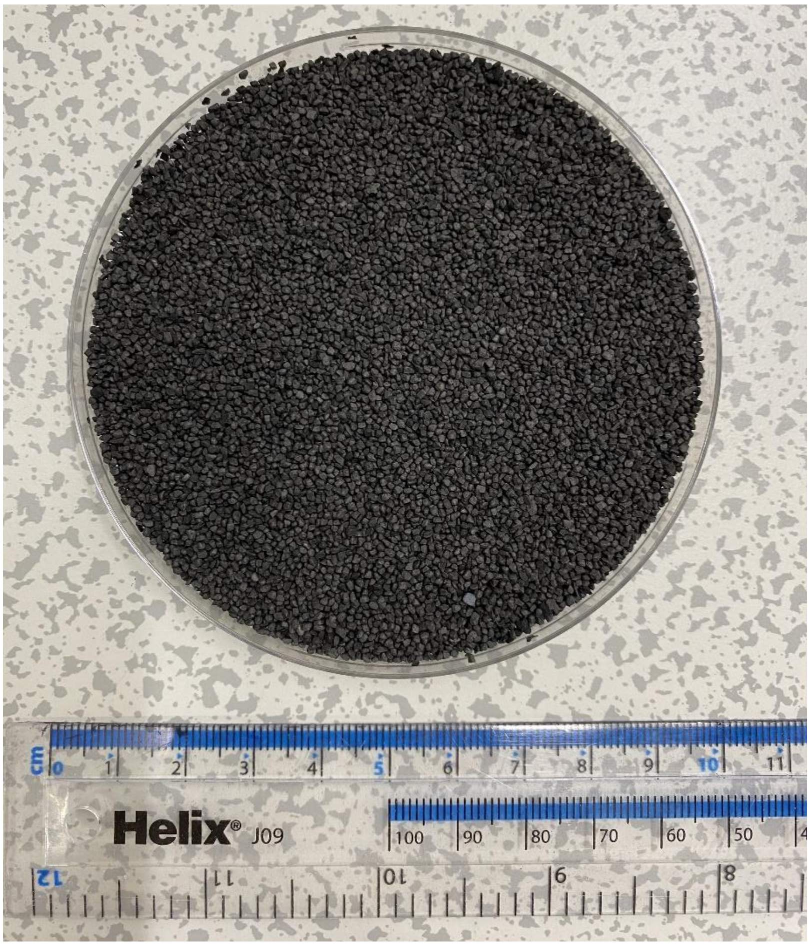

Figure 3-2 A biochar sample obtained after pyrolysis experiment (CO_2/800-1)

A schematic of pyrolysis system is illustrated in Figure 3-3. The vertical cylinder furnace used for pyrolysis experiment had the length of 270 mm and diameter of 70 mm. Temperatures inside the furnace were monitored through three thermocouples being placed from 35, 45 and 55 mm away from axis of the furnace, with the resolution of ± 5°C. A temperature profile of heating up to 700°C is illustrated in Figure 3-4. The temperatures reported in this study were the lowest temperatures among all three thermocouples. Walnut shells were placed in the centre of the bottom of the furnace. In each run, ~80 ± 2 g of walnut shells was used. N_2 or CO_2 (flow rate 100 mL min^{-1}) was used and flowed from the top to the bottom of the furnace. The bio-oil was collected in a series of two condensers, with cool packs being used to condense all bio-oil. The yield of biochar was determined based on the difference between the weight of sample before and after the pyrolysis reaction.

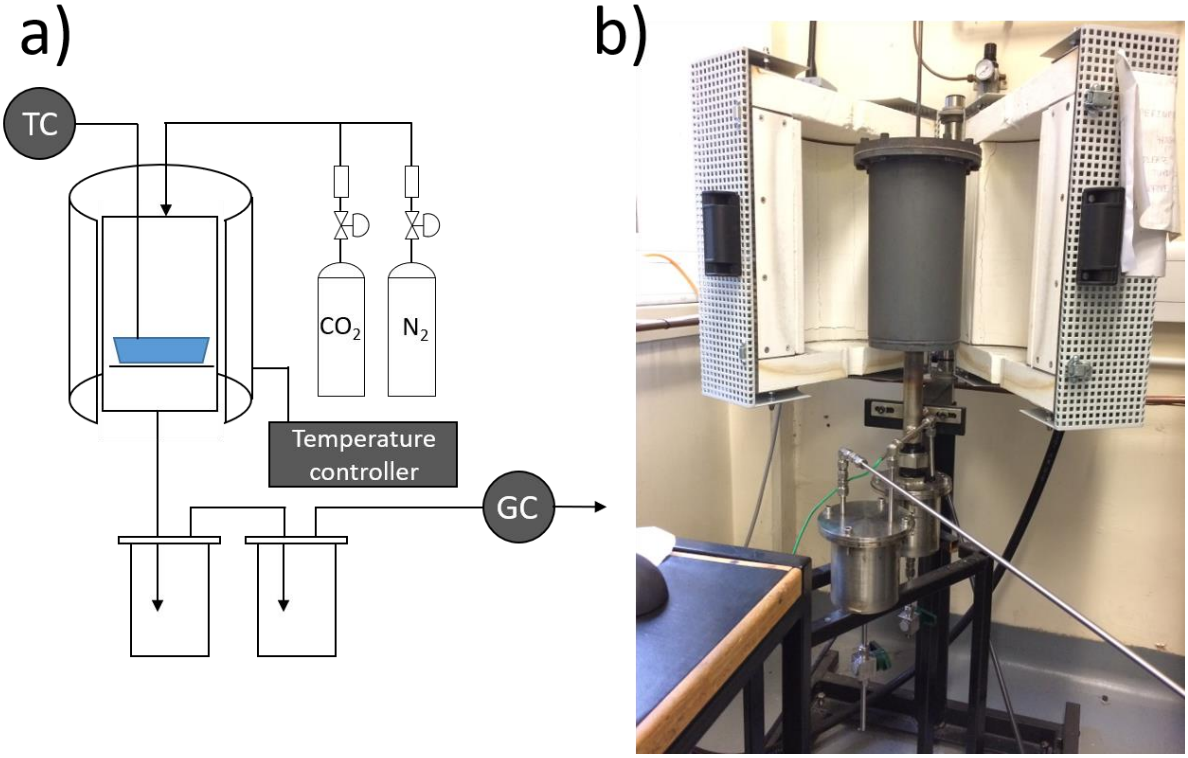

Figure 3-3 (a) Schematic and (b) image of pyrolysis system (GC: gas chromatography, TC: thermocouple)

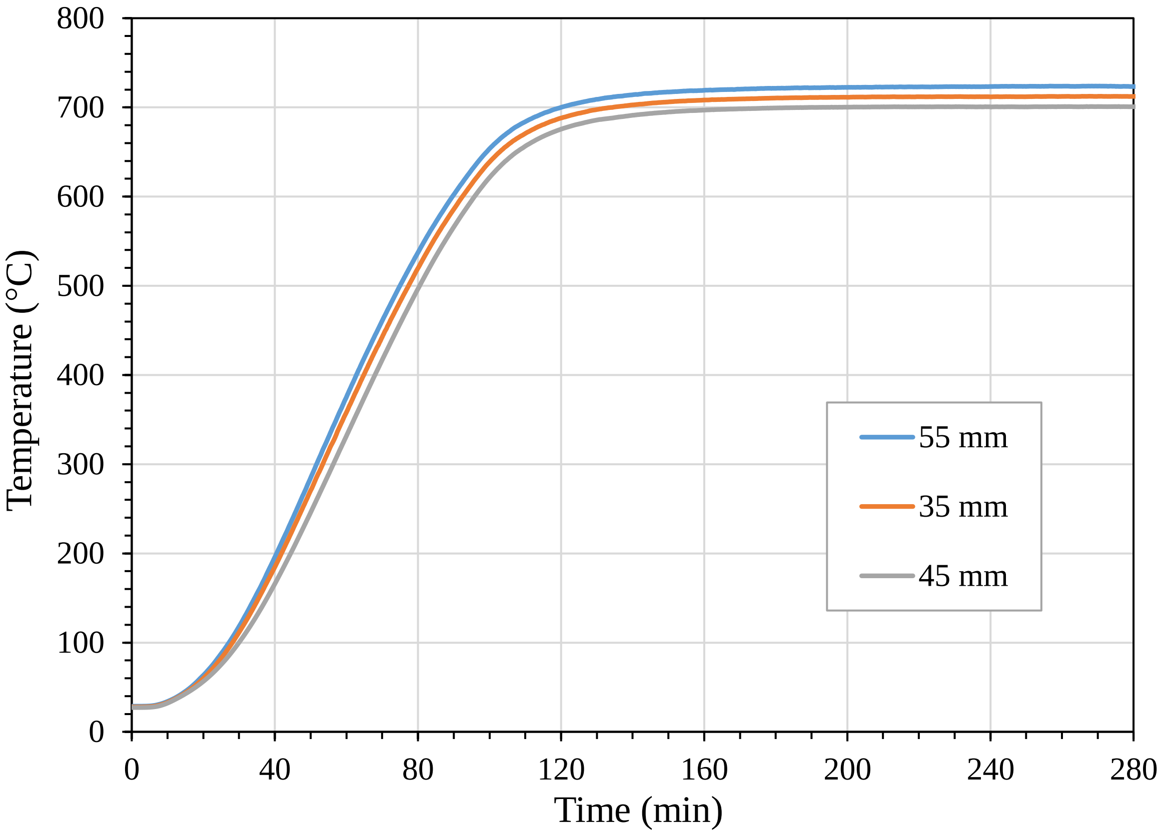

Figure 3-4 A temperature profile at 700°C of the furnace for pyrolysis experiment from three thermocouples placed at 35, 45 and 55 mm away from the axis of the cylinder furnace

3.1.1.2 Hydrothermal carbonization of walnut shells

200 ± 1 g of walnut shells were treated in a 2-liter Parr reactor (series 4600) with 700 ± 1 g of deionised (DI) water at 200, 250, and 290°C under auto-generated pressure in 2 h to create hydrochar. The hydrochar obtained from this process were named HY200, HY250 and HY290, respectively in which prefix "HY" indicating hydrochar, and 200, 250 and 290 indicating the final temperature of HTC in °C. The temperature was achieved using nozzle heating bands and was kept within ± 5°C. The mixture of walnut shells and DI water was purged with N_2 for at least 20 min to remove all oxygen inside the reactor and eliminate all side reactions between oxygen and biomass at high temperatures. The N_2 gas valve was closed after the purging completed and heat was then applied to the reactor.

As discussed in section 2.3.3 on HTC using water as medium, temperatures below 200°C is unlikely impose any effect on cellulose but decompose most of hemicellulose (Bobleter 1994), and temperature at 250°C decomposes most of cellulose in walnut shells but leaves lignin almost intact (Donar *et al.* 2016). The temperature at 290°C is able to dissolve a part of lignin inside walnut shells and form hydrochar (Fang *et al.* 2008). The domination of temperature over holding time in determining the decomposition and formation of spherical structures in hydrochar was also proved by Overend *et al.* through severity factor R_0 (Overend *et al.* 1987):

$$R_0 = log_{10}\left[te^{\left(\frac{T-100}{14.75}\right)}\right] \tag{3-1}$$

(in which t is holding time in min, and T is the temperature in °C)

The severity factor showed that when increasing temperature from 200 to 250 and 290°C at 2 h holding time, R_0 factor increases from 5.02 to 6.50 and 7.67. However, R_0 only increases slightly from 6.19 to 6.79 when increasing holding time from 1 h to 4 h at 250°C. Therefore, it is unnecessary to prolonging holding time further than 2 h. The 700 g of DI water was used in this Parr reactor to ensure that a third of the vessel was filled according to the safety guideline by the manufacturer. The heating rate applied for HTC was ~3-3.5 °C min^{-1} and kept constant for all final temperatures, so it took approximately 56 ± 1 min to reach 200°C, 72 ± 1 min to reach 250°C and 85 ± 1 min to reach 290°C. A slow heating rate ensures the biomass and water being heating homogenously inside Parr reactor.

After reaction, the vessel was cooled down naturally overnight to reach ambient temperatures. The formed gas in the reactor was released into the fume cupboard by slowly opening the gas valve. Hydrochar was easily separated from liquid through vacuum filtration, and then was several times with DI water until pH reached 6 was ~6-7. A schematic of the whole experiment apparatus is showed in Figure 3-5. A rupture disc is installed on the head of Parr reactor. In the event of overpressure, this rupture disc will open to release the inside pressure.

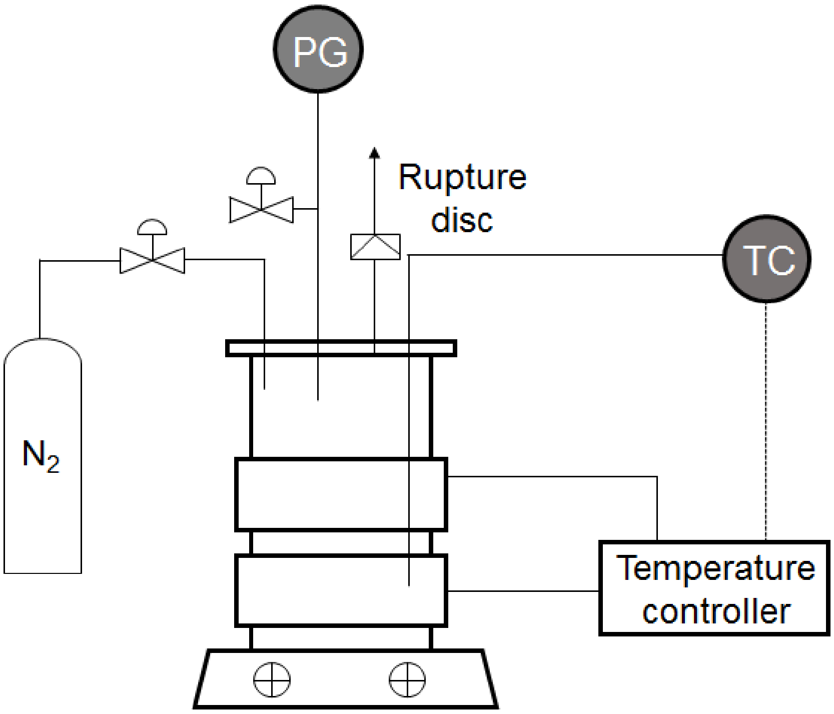

Figure 3-5 Schematic of hydrothermal carbonization system (PG: pressure gauge, TC: thermocouple)

3.1.2 Functionalisation of biomass-derived carbon

3.1.2.1 Potassium carbonate-treated biochar

K_2CO_3 is a common activating agent that increases the surface area (Hayashi *et al.* 2002) (Köseoğlu and Akmil-Başar 2015) due to its reaction with biochar $K_2CO_3 + 2C \rightarrow 2K + 3CO$ as discussed in section 2.4.2.1. Therefore, treatment with K_2CO_3 is employed to increase the surface area of biochar for electrochemical applications. The influence of K_2CO_3 on surface area and porosity of different biochar samples is not studied in this PhD thesis, so only one sample was chosen for K_2CO_3 treatment. AC CO_2/800-1 were chemically activated by K_2CO_3 to adjust the porosity structure in order to investigate the effect of porosity on electrochemical performance of biochar. Around 15.0 ± 0.1 g of CO_2/800-1 was soaked in 50 ± 1 mL of DI water mixed with 15.0 ± 0.1 g K_2CO_3 for 24 h to achieve K_2CO_3/AC ratio = 1:1. DI water was used to homogenously disperse K_2CO_3 and increase the adsorption of K_2CO_3 into the carbon material. This K_2CO_3/AC ratio was adapted from other studies because this ratio is optimal for increasing surface area and porosity of AC (Hayashi *et al.* 2002, Köseoğlu and Akmil-

Başar 2015). The soaked AC was dried in the oven at 60°C overnight until all water content evaporated. The oven temperature at 60°C was used to avoid any unnecessary reactions that might occur during drying. After that, the carbon was treated at 800°C for 2 h under CO_2 atmosphere (100 ± 5 mL min^{-1}). This biochar was then washed with HCl 0.2 M and DI water until pH was ~6-7 and then extracted using a Soxhlet apparatus with 400 mL DI water as the solvent to remove residual water soluble compounds. This carbon is denoted as CO_2/800-1-K_2CO_3.

3.1.2.2 Functionalisation biochar with oxygen

Functionalising biochar using HNO_3 increase oxygen content by incorporating various oxygen groups including carboxylic, lactone/lactol and phenolic (Jia and Thomas 2000). A simple heat treatment at different temperatures following HNO_3 treatment subsequently reduces oxygen content in biochar to create a series of biochar with relative similar surface area, porosity and carbonaceous structure but different oxygen contents.

AC CO_2/800-1 were chemically treated by nitric acid to introduce new oxygen functional groups into the carbon structure. 10.0 ± 0.1 g of CO_2/800-1 was refluxed in 200 ± 1 mL HNO_3 7.5 M at 95°C for 6 h as discussed in section 2.4.2.2. This AC was then washed with DI water until pH was ~6-7, and then extracted using a Soxhlet apparatus with 400 ± 1 mL of DI water to remove all residual acid and water-soluble compounds in AC for at least 72 h. This AC was denoted as CO_2/800-1-HNO_3. AC CO_2/800-1-HNO_3 was then treated at 400 and 800°C in H_2 atmosphere (40 mL min^{-1}) for 2 h, and the products were denoted as CO_2/800-1-HNO_3/400 and CO_2/800-1-HNO_3/800 respectively. Further heat treatment at 400 and 800°C gradually reduces the oxygen content of CO_2/800-1-HNO_3 and creates a series of AC with different oxygen contents without modifying surface area, porosity and carbonaceous structure. A sketch of functionalisation with HNO_3 is shown in Figure 3-6.

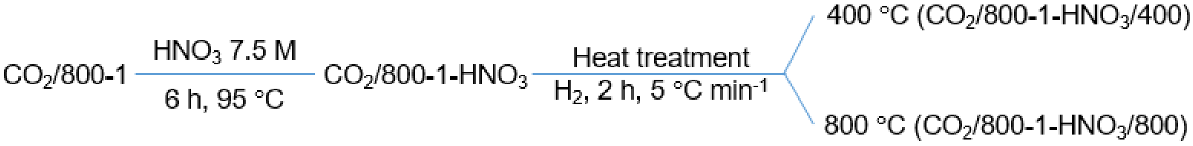

Figure 3-6 Schematic of biochar functionalised with HNO_3 and further heat treatment at 400 and 800°C

3.1.2.3 Functionalisation biochar with nitrogen

Nitrogen incorporation by heat treatment

The impact of nitrogen on kinetics of vanadium redox reactions has not been studied extensively compared to oxygen. However, some first results in literature showed that incorporating nitrogen into electrodes might benefit vanadium reactions. For example, incorporating nitrogen into carbon felt poly acrylonitrile using pyrrole-2-carboxaldehyde (C_5H_5NO) at 1000°C for 1 h under N_2 atmosphere slightly increased surface area (31 m^2 g^{-1} compared to 7 m^2 g^{-1} of pristine felt) but reduced the nitrogen content (from 19.2 at% to 4.2 at%) due to the removal of C≡N groups in poly acrylonitrile (Schnucklake *et al.* 2019). It also created many defects on surface of carbon felt (Figure 3-7). This heat treatment reduced the charge transfer resistance from 104 Ω to 78 Ω, thereby improving the reversibility of VO^{2+}/VO_2^+ (Schnucklake *et al.* 2019).

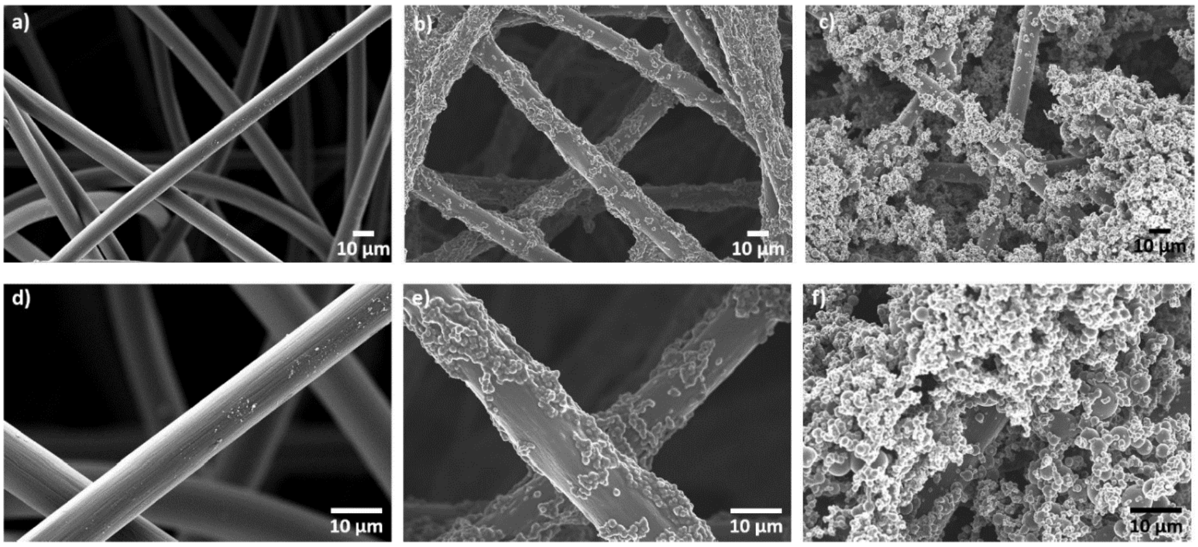

Figure 3-7 SEM image of carbon felt (a,d), nitrogen incorporated carbon felt (b,e) and nitrogen-sulphur incorporated carbon felt (c,f) (Schnucklake *et al.* 2019)

Therefore, the impact of nitrogen in vanadium redox reactions should be explored. Heat treatment has been used to incorporating various nitrogen groups, including pyridinic-N, pyrrolic-N, and quaternary-N into biochar/AC. A schematic of nitrogen incorporation is illustrated in Figure 3-8. 1.00 ± 0.01 g of N_2/800-1 was packed inside a quartz tube using quartz wool and was further treated at 600°C and 800°C in NH_3 atmosphere (40 mL min^{-1}) for 2 h, denoted as N_2/800-1-NH_3/600 and N_2/800-1-NH_3/800 respectively. Biochar N_2/600-1 and N_2/1000-1 were thermally treated in NH_3 atmosphere (40 mL min^{-1}) at 800°C for 2 h to give N_2/600-1-NH_3/800 and N_2/1000-1-NH_3/800 respectively. The difference in temperature between 600 and 800°C allows different nitrogen contents to be incorporated into biochar (Stöhr *et al.* 1991). Furthermore, gasification under NH_3 atmosphere also modifies porous structure of biochar at high temperatures (Lian *et al.* 2016, Wang *et al.* 2017).

Hydrochar HY200, HY250 and HY290 were also thermally treated in NH_3 atmosphere (40 ± 2 mL min^{-1}) at 800°C for 2h to give HY200-NH_3/800, HY250-NH_3/800 and HY290-NH_3/800.

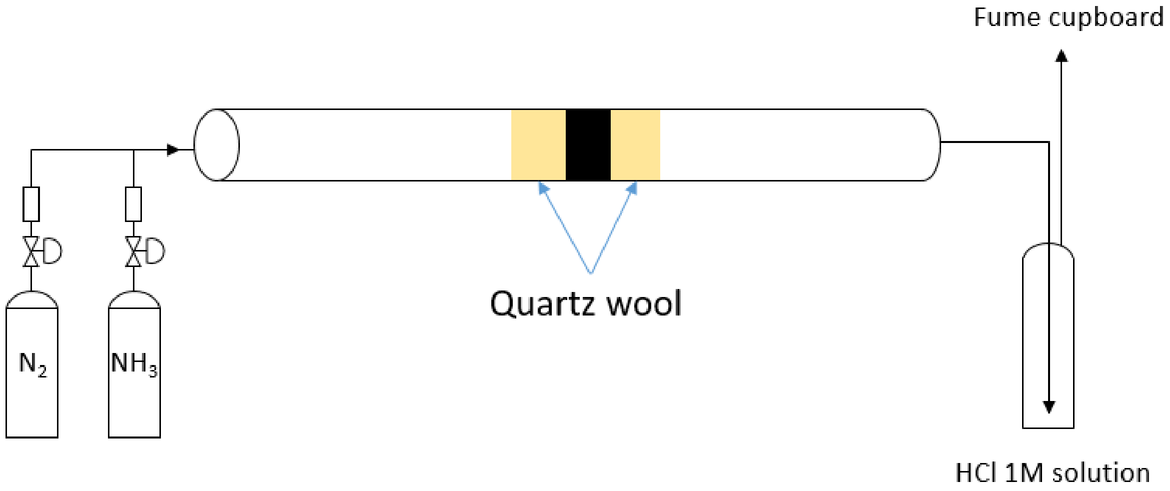

Figure 3-8 Schematic of experiment system used for nitrogen incorporation using heat treatment under NH_3 and phosphorus incorporation using heat treatment under N_2

Nitrogen incorporation by cold plasma dielectric barrier discharge cold plasma

DBD cold plasma, on the other hand, is a promising method to functionalise carbon materials at ambient temperatures and atmospheric pressure (as discussed in section 2.4.1.3), and the use of dielectric barrier layers in cold plasma also creates non-thermal equilibrium plasma safely. However, the use of DBD cold plasma in incorporating nitrogen into carbon materials, especially biochar has not been studied thoroughly.

The aims of this PhD study was not to examine the influence of different DBD setups on properties of biochar, so the experiment setup for DBD cold plasma in this PhD thesis was based on the two-quartz-tube system that has been used in other studies within the same research group (Diaz-Silvarrey *et al.* 2018, Harris *et al.* 2018). In this experiment, biochar N_2/800-1 was systematically treated in NH_3 atmosphere using the DBD system (Figure 3-9), and the choice of biochar for this experiment was consistent with biochar thermally treated in NH_3. The DBD active space was created in the gap between two quartz tubes, with the outer tube having inner diameter of 15 mm (Figure 3-10a) and the inner tube having outer diameter of 8 mm (Figure 3-10b). The outer electrode was a 316 stainless steel mesh with the length of 8 cm (Figure 3-10c), and the inner electrode was a tin foil (Figure 3-10b). Biochar N_2/800-1 was loaded inside the gap between two quartz tubes (Figure 3-10d).

The NH_3 flow rate was changed from 20 ± 2 mL min^{-1} to give L carbon (low gas flow rate) to 40 ± 2 mL min^{-1} to give H carbon (high gas flow rate). The plasma power applied varied from

20 ± 2, 40 ± 2 and 80 ± 2 W and held at the desired power level for 1 or 2 h. With DBD cold plasma-treated biochar, the designated code, for example, N_2/800-1-L40W1 indicated the carbon treated at 40 W for 1 h at low NH_3 flow rate – 20 mL min^{-1}, and this rule was applied for other DBD cold plasma-treated biochar. Hydrochar HY200, HY250 and HY290 also underwent DBD treatment at 80 ± 2 W in NH_3 (40 ± 2 mL) to give HY200-H80W2, HY250-H80W2 and HY290-H80W2, respectively. The systematic variation in cold plasma power, holding time and NH_3 flow rate creates a series of DBD cold plasma-treated biochar and hydrochar with different nitrogen content and nitrogen functional groups, which is discussed in Chapter 5.

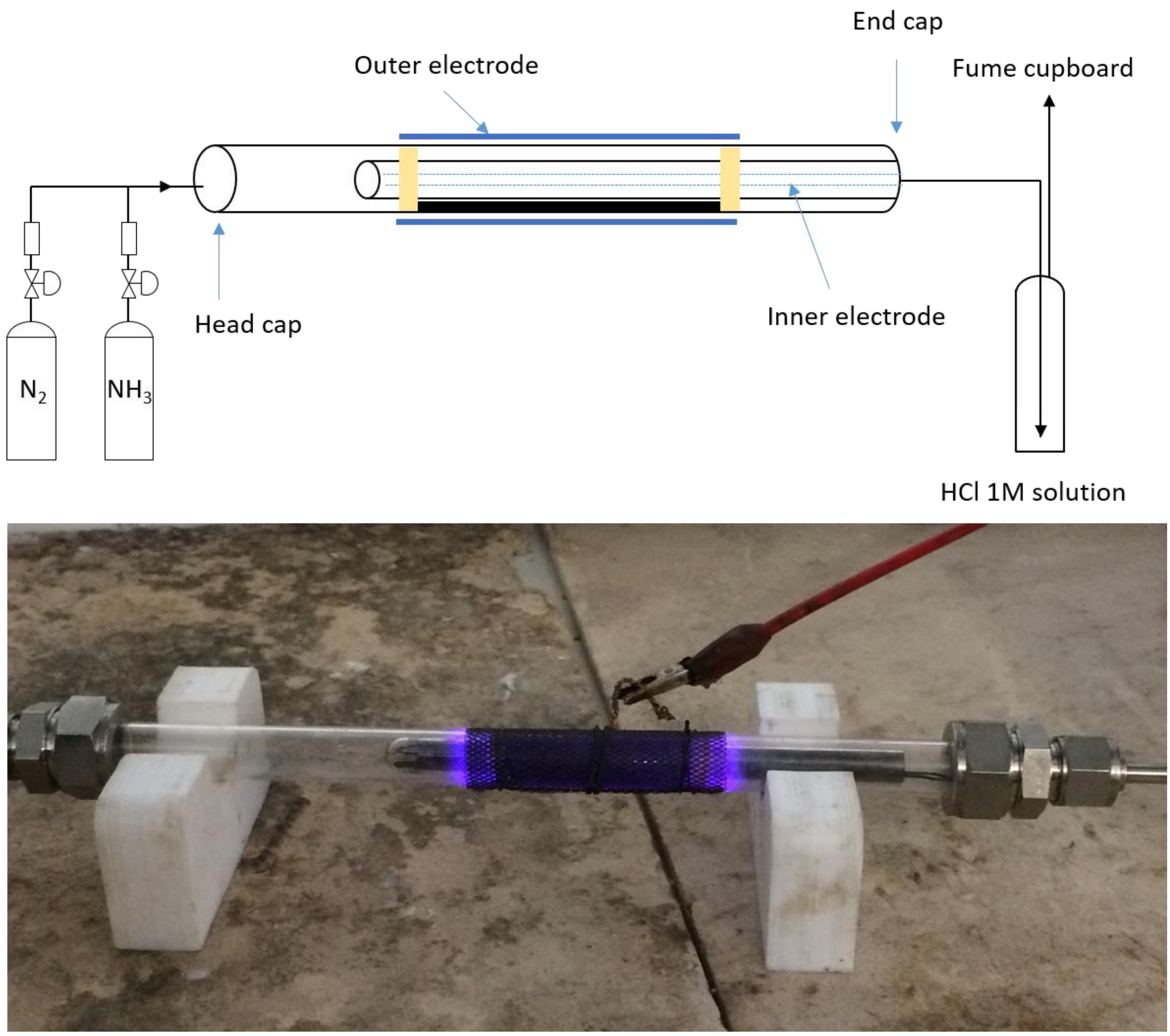

Figure 3-9 Schematic and image of dielectric barrier discharge cold plasma setup used for nitrogen functionalisation

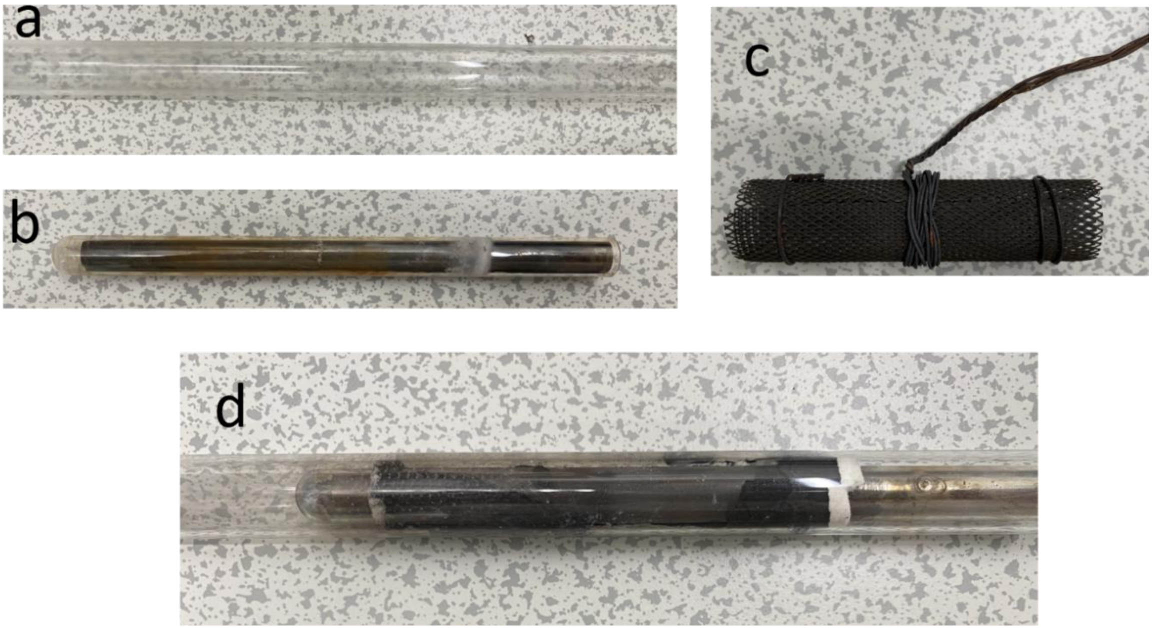

Figure 3-10 Components of dielectric barrier discharge cold plasma system: (a) The quartz tube as outer dielectric barrier (inner diameter = 15 mm), (b) The quartz tube as inner dielectric barrier (outer diameter = 8 mm) with a tin foil inside as inner electrode, (c) 316 stainless steel mesh as outer electrode and (d) two quartz tube were put together with biochar loaded between the gap of those two barriers

3.1.2.4 Phosphorus incorporation

AC CO_2/800-1 were chemically activated by phosphoric acid to introduce phosphorus functional groups into carbon structure. Approximately 2.00 ± 0.01 g of CO_2/800-1 was soaked in 30.5 mL H_3PO_4 at various concentrations (0.5 M, 2 M, and 5 M) to examine the influence of phosphorus concentrations. This wide range of H_3PO_4 concentration was to assess of influence of H_3PO_4 concentration on phosphorus functional groups, which is discussed later in Chapter 6. AC CO_2/800-1 was immersed in H_3PO_4 solution at 2, 3, 4, 6, 10, 16 and 24 h, and it showed that the mass of AC CO_2/800-1 reached saturation after 24 h, so all AC was immersed in H_3PO_4 solutions for 24 h prior heat treatment (Figure 3-11). AC after being immersed in H_3PO_4 solutions was then dried at 60°C for 24 h to remove most of moisture without inducing any reactions between H_3PO_4 and AC.

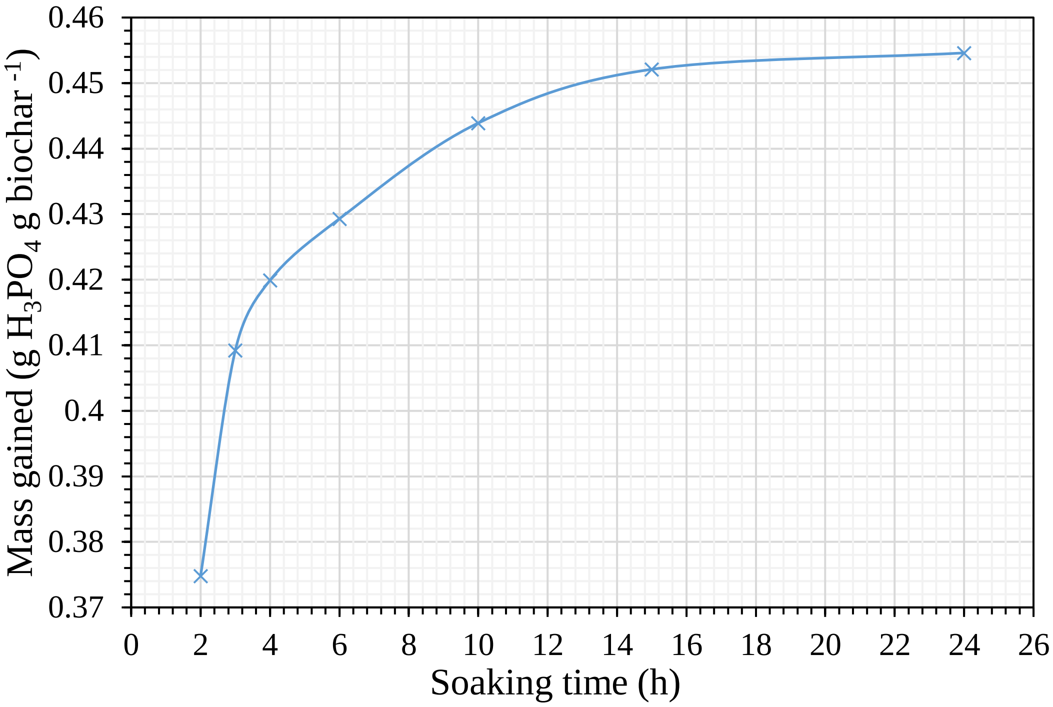

Figure 3-11 Adsorption test on AC CO_2/800-1 in H_3PO_4 2 M at 2, 3, 4, 6, 10, 16 and 24 h

The impregnated carbon was further treated at 600, 700, 800 or 1000°C under N_2 atmosphere (40 ± 1 mL min^{-1}) for 2 h, denoted as CO_2/800-1/H_3PO_4/T-C, in which T is the final temperature in °C and C is the concentration of phosphoric acid used in M. For example, CO_2/800-1-H_3PO_4/800-2 indicates the AC CO_2/800-1 treated at 800°C using H_3PO_4 2 M. As discussed in section 2.4.2.2 about the influence of H_3PO_4 on biomass-derived carbon, this wide range of temperature of 600-1000°C, coupled with the change in H_3PO_4 concentration from 0.5 to 5 M, could greatly influence phosphorus contents, phosphorus functional groups and porous structure of AC.

To investigate the impact of holding time, AC CO_2/800-1 soaked in 2 M H_3PO_4 was then treated at 800°C at 1 and 3 h holding time, giving CO_2/800-1-H_3PO_4/800-2-1h and CO_2/800-1-H_3PO_4/800-2-3h respectively. One sample of CO_2/800-1 was treated at 800°C without H_3PO_4 impregnation to give CO_2/800-1-H_3PO_4/800-0 for comparison. AC CO_2/800-1 after being soaked at 0.5 M, 2 M and 5 M were then treated at 800°C in NH_3 atmosphere (40 mL min^{-1}) for 2 h to give CO_2/800-1-H_3PO_4/NH_3-0.5, CO_2/800-1-H_3PO_4/NH_3-2, and CO_2/800-1-H_3PO_4/NH_3-5 respectively.

All AC activated with phosphoric acid were washed with DI water until pH was ~6-7, and then extracted using a Soxhlet apparatus with 400 ± 1 mL of DI water to remove all residual acid (using a simple check with $BaCl_2$ solution to test $Ba_3(PO_4)_2$ precipitate) and water-soluble compounds in AC for at least 72 h.

3.2 Material characterisation

3.2.1 Gas physisorption techniques

Gas physisorption including CO_2 adsorption-desorption at 0°C and N_2 adsorption-desorption at -196°C has been used to determine the surface area of carbon samples.

3.2.1.1 Isotherm classification

According to International Union of Pure and Applied Chemistry (IUPAC) on physisorption data for gas/solid systems, most physisorption isotherms of gases on solids can be classified into six different types as presented in Figure 3-12 (Thommes *et al.* 2015).

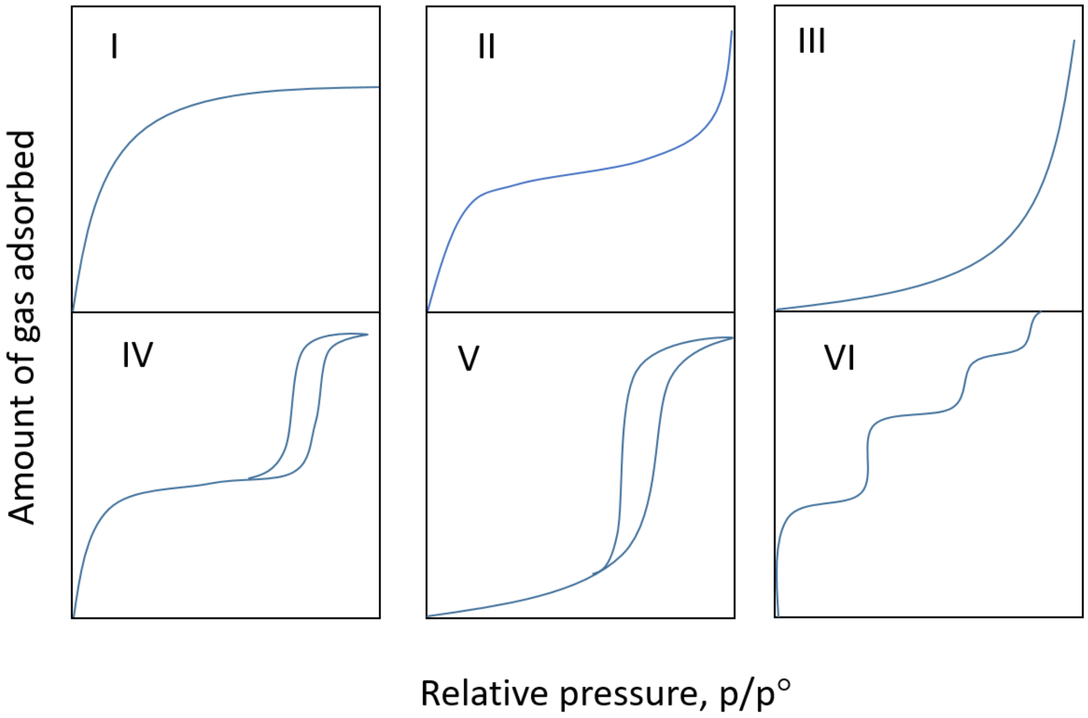

Figure 3-12 IUPAC classifications of isotherms

Type I isotherm is normally referred to a microporous material in which adsorbate molecules quickly fill up these micropore until $p/p° = 0.1$ rather than form a monolayer coverage on the surface of the material. The fill up process al process almost completes at $p/p° \approx 0.5$.

Type II isotherm presents an unrestricted monolayer-multilayer adsorption on a non-microporous or macroporous material. At low $p/p°$ (< 0.3), adsorbate molecules form a monolayer coverage on the surface of carbon material, and multilayer coverage occurs at high $p/p°$ and fill up all pores. Both type I and II are frequently observed for carbon materials (Nishi and Inagaki 2016).

Type III isotherm indicates weak gas-solid adsorption, resulting in low gas adsorption at low *p/p*°. The adsorption process, however, is fostered at high *p/p*° thanks to the adsorbate-adsorbate interaction.

Type IV isotherm is similar to type II isotherm but having a hysteresis loop as the distinctive feature. The hysteresis loop observed at high *p/p*° in type IV isotherm can be attributed to the capillary condensation of adsorbate in mesopores of the material.

Type V isotherm is similar to type III isotherm, but it has a hysteresis loop observed at high *p/p*°, which could be referred to a certain amount of mesopore inside adsorbent.

Type VI isotherm demonstrates stepwise multilayer adsorption, usually observed in uniform non-porous adsorbent.

3.2.1.2 Dubinin-Radushkevich micropore volume determination by CO_2 adsorption-desorption

Microporous structure was analysed with CO_2 as adsorbate at 0°C using Intelligent Gravimetric Analyser (IGA), Hiden Isochema Ltd (Figure 3-13). The system is an ultrahigh vacuum system fully controlled by the computer, which automatically recorded isotherms and monitored admitted/emitted gas at each pressure point in the pressure set between 0 and 100 kPa (Figure 3-13). Analytical CO_2 vapour (99.99%) was supplied from BOC.

The pressure accuracy was controlled at ± 0.02% of the pressure set point, and pressures were controlled by three pressure transducers at three different ranges 0-0.2 kPa, 0-10 kPa, and 0-100 kPa. Sample temperatures were monitored throughout experiment with errors ± 0.1°C with temperature being maintained by a cooling bath. At each adsorption step, the equilibrium value was determined as being 99.9% of the predicted value, calculated in real time using mass uptake profile. The microbalance had a long-term stability of ± 1 μg with a weighing resolution of 0.2 μg. After achieving mass equilibrium, IGA increased pressure to next set point in 60-100 s to eliminate the risk of disruption of the microbalance and maintained constantly during adsorption steps. Prior to each run, ~50 mg of carbon sample was degassed at 150°C overnight under vacuum ($<10^{-6}$ Pa) for all moisture to be removed until achieving a constant weight before a static gas sorption/desorption isotherm was recorded. CO_2 adsorption-desorption isotherm is analysed based on Dubinin-Radushkevich (DR) model. Detailed explanation of DR model and example of common types of DR plot deviations can be referred to Appendix A.1. DR micropore volume was obtained from CO_2 adsorption isotherm at 0°C within pressure range 0-100 kPa, equivalent to relative pressure range *p/p*° =

2.7×10^{-7}-3×10^{-2}. A CO_2 adsorption-desorption isotherm at 0°C and DR plot sample are illustrated in Figure 3-14.

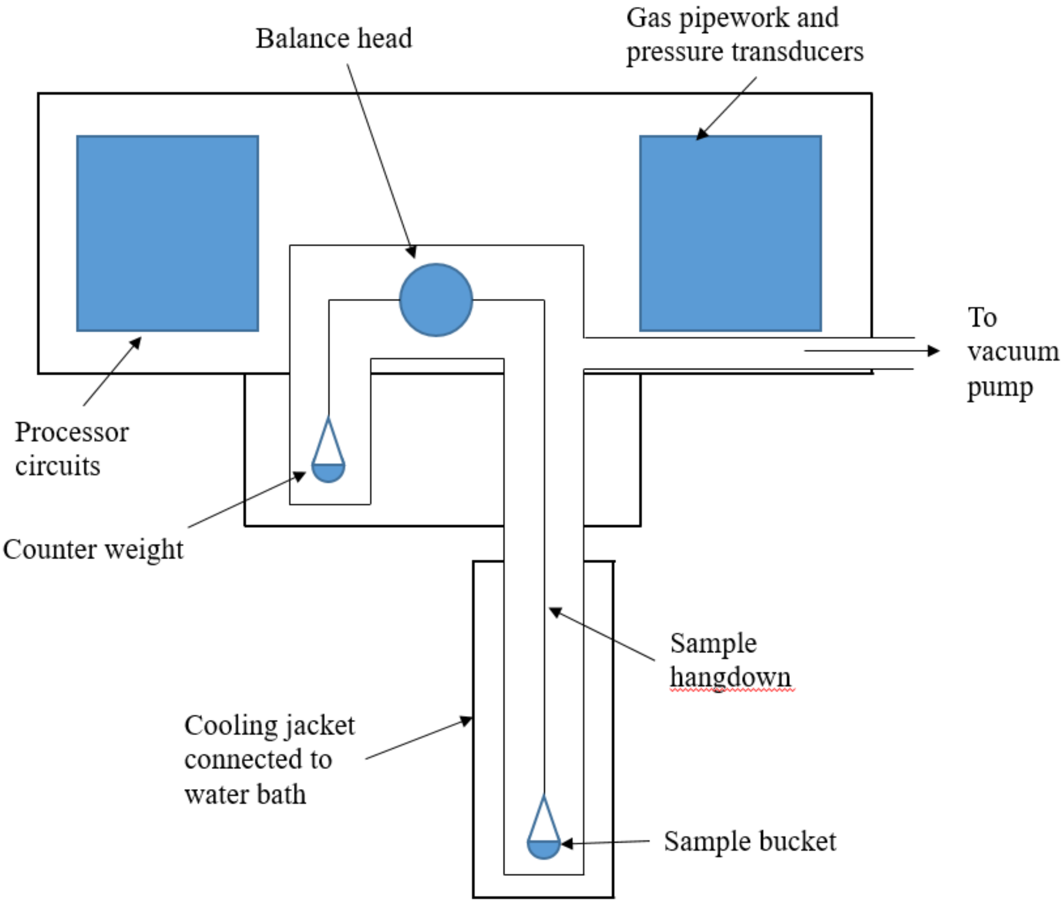

Figure 3-13 Schematic of intelligent gravimetric analyser (IGA)

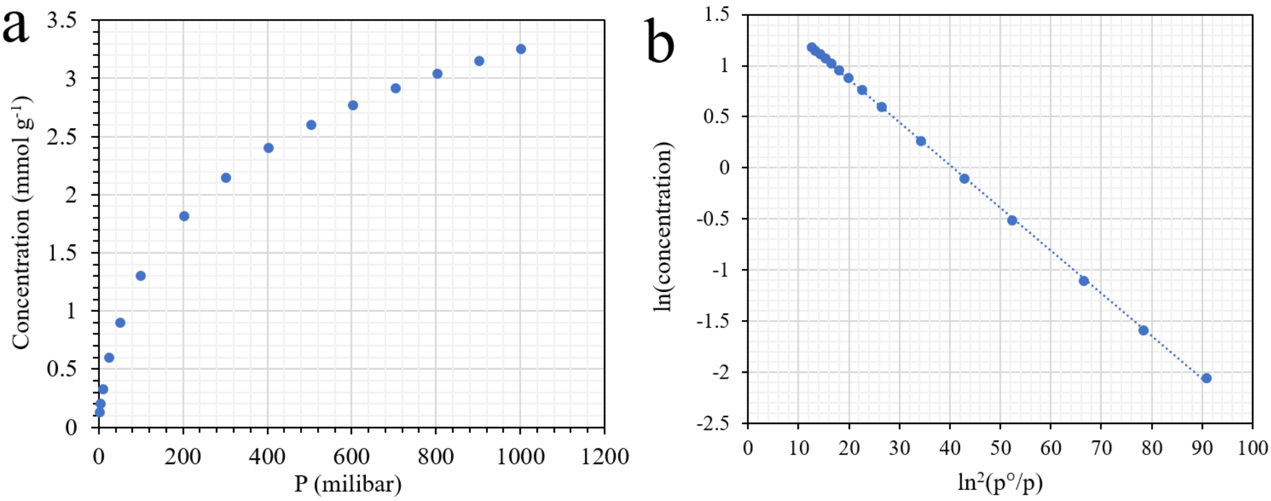

Figure 3-14 (a) CO_2 adsorption-desorption isotherm at 0°C and (b) DR plot of AC CO_2/800-1

3.2.1.3 Brunauer–Emmett–Teller (BET) surface area and total pore size determined by N_2 adsorption-desorption

N_2 adsorption-desorption isotherms at -196°C were performed using a Thermo Fisher Scientific Surfer analyser. The system functions in volumetric method and is fully controlled by computer. At each adsorption step, the analyser delivered accurately known aliquot of gas into a known mass of a sample, and the absolute pressure inside the system was recorded continuously. The amount of gas adsorbing into the sample is calculated based on the difference in the amount gas delivered into system and the amount of gas not adsorbing by the sample (which was monitored through the absolute pressure of the system). Prior to each run, ~100 mg of sample was loaded into a burette and degassed overnight at 150°C in a separate degassing unit to remove all moisture at pressure < 10^{-3} kPa. The fully degassed burette was then mounted into the analyser and the temperature was achieved by submerging the burette in liquid nitrogen.

Detailed explanation of the BET model can be referred to Appendix A.2. The isotherm of AC CO_2/800-1 is shown in Figure 3-15. N_2 adsorption-desorption isotherms were used to determine BET surface area in the range $p/p° = 1\times10^{-3}$-0.06 instead of $p/p°$ = 0.05-0.3 (Figure 3-16a). Majority of biochar/AC shows type I/IV adsorption at -196°C with N_2 quickly filling up these micropores until $p/p°$ = 0.1 rather than forming a monolayer of coverage. Therefore, the range $p/p° = 1\times10^{-3}$-0.06 was chosen to represent the period where a monolayer of N_2 is forming on the surface of biochar/AC, and also to ensure that the c value (a dimensionless constant in BET equation) has a positive value. The total pore volume was defined from the amount of N_2 adsorbed at $p/p°$ = 0.995 (Figure 3-16b). DR micropore volume obtained from N_2 adsorption at -196°C was also obtained.

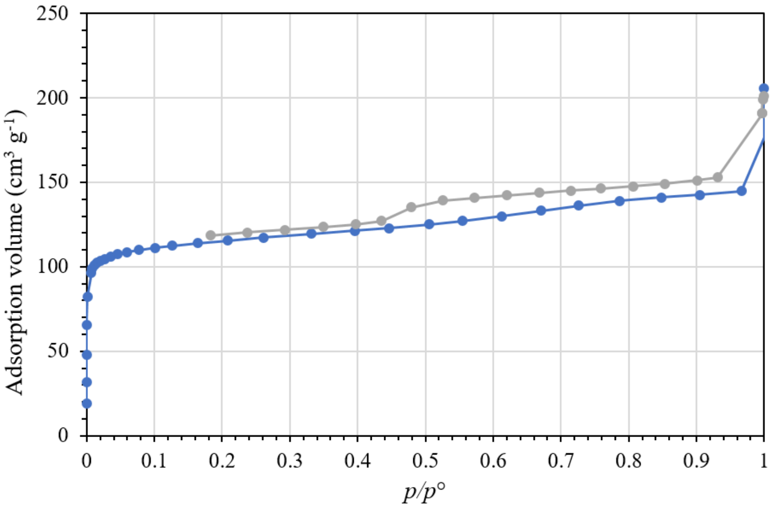

Figure 3-15 N_2 adsorption-desorption isotherm at -196°C of AC CO_2/800-1

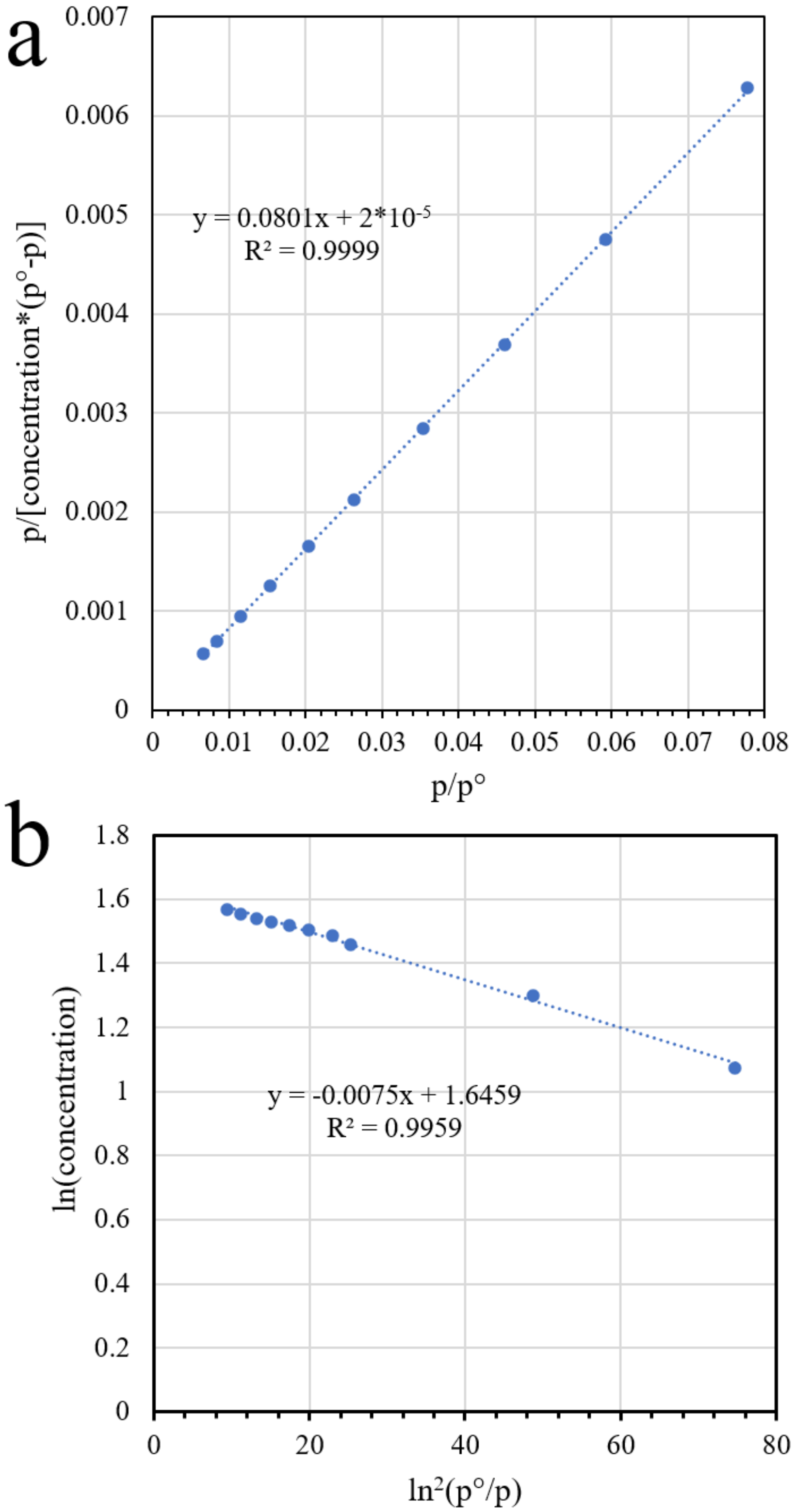

Figure 3-16 (a) BET plot and (b) DR plot from N_2 adsorption-desorption isotherm at -196°C of AC CO_2/800-1

3.2.2 Functional groups characterisation

3.2.2.1 Total elemental analysis

CHN analysis was carried out on a CE Instrument elemental analyser model EA1110. The technique used is high temperature combustion at temperature 1000°C with exothermic tin combustion to 1600°C. Helium was used as carrier gas (120 mL min^{-1}). Outlet gas was separated by GC (2m packed column (Porapak QS 50/80 mesh)) and detected by thermal conductivity with oven temperature isothermal at 65°C.

Oxygen analysis was carried out on a Fisons instrument elemental analyser model EA1108, configured for oxygen analysis. The technique used is the Unterzaucher pyrolysis method – high temperature thermal decomposition and conversion of sample oxygen into carbon monoxide followed by GC separation and detection by thermal conductivity (Kirk and Wilkinson 1970). Pyrolysis temperature was 1060°C, using helium as carrier gas (100 mL min^{-1}). Outlet gas was separated by GC (1m packed column (molecular sieve 5A)) with oven temperature at 65°C. Both instrument for CHN and oxygen analysis were calibrated and verified using certified reference chemicals traceable to NIST primary standards.

3.2.2.2 X-ray photoelectron spectroscopy

X-ray photoelectron spectroscopy (XPS) is an analytical method to investigate the chemistry composition of materials by bombarding the material surface by an X-ray having a constant energy, $h\nu$, in vacuum (Konno 2016). The working mechanism of XPS instrument and the process of data interpretation can be referred to Appendix B.1.

XPS was performed using a Thermo Fisher Scientific K-alpha$^+$ spectrometer. Samples were analysed using a micro-focused monochromatic Al X-ray source (72 W) over an area of approximately 400 μm. Data was recorded at pass energies of 150 eV for survey scans and 40 eV for high resolution scan with 1 eV and 0.1 eV step sizes respectively. Charge neutralisation of the sample was achieved using a combination of both low energy electrons and argon ions. Data analysis was performed in CasaXPS software using a Shirley type background and Scofield cross sections, with an energy dependence of -0.6.

It is recommended that using a reasonable number of peaks for each element coupling with constrained FWHM and peak shape, and binding energy values fluctuating in a few tenths of electron volts deliver a consistent quality of data interpretation (Konno 2016). Therefore, all components in one specific peak were constrained to share the same FWHMs with a Gaussian/ Lorentzian peak shape (ratio 70/30). The number of chemical states in each peak were kept to minimum to avoid over interpreting the data. The XPS C 1s peaks were deconvoluted into C=C sp^2 (284.5 ± 0.2 eV), C-C sp^3 (285.2 ± 0.2 eV), C-O (286.4 ± 0.2 eV), C=O (287.9 ± 0.3 eV), O-C=O (289.1 ± 0.3 eV) (Yang *et al.* 2009, Maharjan *et al.* 2017). The XPS O 1s peaks were separated into C=O (531.4 ± 0.2 eV), C-O/OH (532.4 ± 0.3 eV), O-C=O (533.4 ± 0.3 eV) and some chemisorbed oxygen and H_2O (535.5 ± 0.5 eV) (Wang *et al.* 2001, Yang *et al.* 2009, Huang *et al.* 2018). The XPS N 1s peak were deconvoluted into pyridinic (N-6, 398.7 ± 0.3 eV), pyrrolic (N-5, 400.3 ± 0.3 eV), quaternary (N-Q, 401.4 ± 0.3 eV), and pyridinic N-oxides and unknown nitrogen (N-X, 405.5 ± 2.5 eV) (Pels *et al.* 1995, Chen *et al.* 2018), and XPS P 2p peak were separated into C-PO_3/ C_2-PO_2 (133 ± 0.3 eV), C-O-P (134.6 ± 0.3 eV) and pentoxide P_4O_{10} (136 ± 0.4 eV) (Wu and Radovic 2006, Rosas *et al.* 2012, Ma *et al.* 2018). An example of a XPS profile is shown in Figure 3-17.

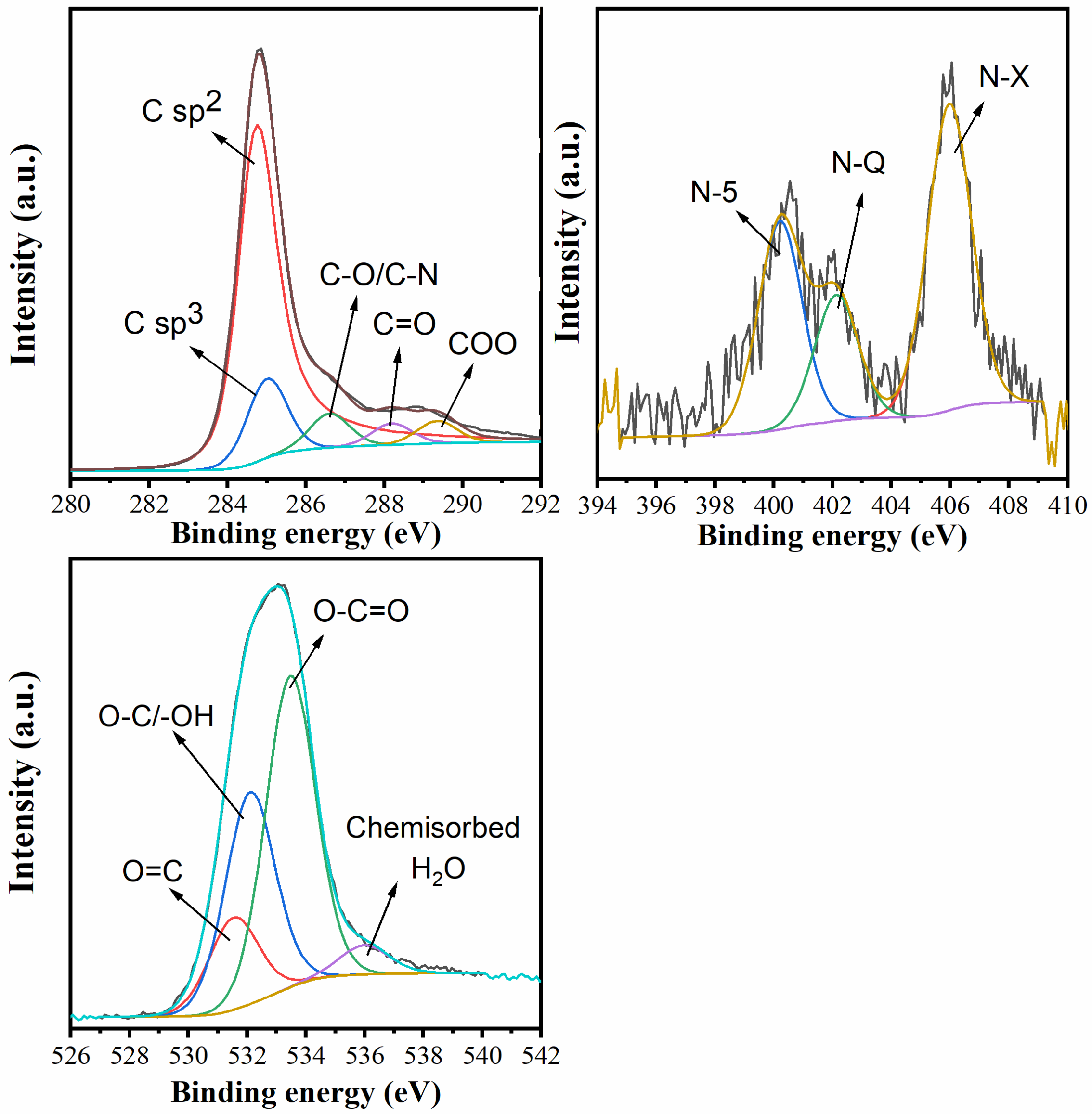

Figure 3-17 XPS spectra of (a) C 1s, (b) N 1s and (c) O 1s of AC CO_2/800-1-HNO_3

3.2.2.3 Temperature-programmed desorption

Temperature-programmed desorption (TPD) has been used to characterise surface and total functional groups in carbon materials for years. In a TPD run, the amount of sample can vary from 5-10 mg (Jones *et al.* 1995, Zhu *et al.* 1997, Boudou *et al.* 2003), 50 mg (Turner and Thomas 1999) to 100-200 mg (Zhou *et al.* 2007) with higher amount being required for low concentration of functional groups. However, high amount of sample may result in non-uniformity of temperatures, increase thermal stags, and prevent the release of desorbed gases to the surrounding atmosphere. The sample is placed in an inert crucible (Al_2O_3, graphite, etc.) under an inert gas atmosphere (He, Ne, Ar, etc.) and a constant heating rate is applied to the sample. When temperatures increase, different functional groups are decomposed at different temperatures (due to different thermal stability) into small gas compounds such as CO_2, CO, H_2O (oxygen functional groups), N_2, NH_3, HCN, and NO (nitrogen functional groups), and the amount of these compounds are then analysed through a quadrupole mass spectrometer. The functional groups of one carbon materials can be determined based on temperature profiles and the types and amounts of desorbed gases and vapours emerging. TPD peaks are a function of temperature, and desorption gases and decomposition temperatures of different functional groups are presented in Table 3-1 (Ishii and Kyotani 2016).

Thermogravimetric analysis (TGA) is frequently combined with TPD to reveal more information about thermal behaviours of carbon samples. Mass losses in TGA at higher temperatures are frequently associated with the decomposition of functional groups at different temperatures (Table 3-1), and help estimate the amount of functional groups. As carbon is not good as heat conducting, a sufficient low heating rate is recommended to avoid thermal stags, so typically a heating rate not higher than 10°C min^{-1} is frequently used (Chen 2016).

Table 3-1 Desorption gases and decomposition temperatures of oxygen, nitrogen and phosphorus functional groups

Main functional groups	Component	Desorption gases and decomposition temperatures (°C)
Oxygen functional groups	Carboxylic	CO_2 at 200-350 (Jia and Thomas 2000), 200-400 (Zielke *et al.* 1996), 280-302 (Yue *et al.* 1999), and 327 (Calo *et al.* 1997)

Main functional groups	Component	Desorption gases and decomposition temperatures (°C)
	Lactone/ lactol	CO_2 at 300-500 (Jia and Thomas 2000), 550-600 (Zielke *et al.* 1996), 190-650 (Marchon *et al.* 1988)
	Anhydrides	CO at 400-450 (Zielke *et al.* 1996) CO and CO_2 at 400 (Yue *et al.* 1999) CO and CO_2 at 627 (Calo *et al.* 1997)
	Phenol/ hydroquinone	CO at 600-700 (Zielke *et al.* 1996)
	Carbonyl/ quinone	CO at 800-900 (Zielke *et al.* 1996), 780 (Yue *et al.* 1999) CO + H_2O at 792 and 827 (Turner and Thomas 1999)
	Semiquinone	CO at 700-980 (Marchon *et al.* 1988)
	Pyrone	CO at 1200-1300 (Fritz and Hüttinger 1993)
Nitrogen functional groups	Pyridinic	HCN and NH_3 at 827, N_2 at 1127 (Yue *et al.* 1999)
	Pyrrolic	Converse to pyridinic under mild pyrolysis temperatures between 460-800°C ((Stańczyk *et al.* 1995), (Lahaye *et al.* 1999)) and quaternary-nitrogen at higher temperatures ((Stańczyk *et al.* 1995),(Schmiers *et al.* 1999))
	Quaternary	N_2 at 1227 (Yue *et al.* 1999). Some quaternary-nitrogen was stable at > 1400°C.
	Pyridinic N-oxides	NO at 247 and 287 (Yue *et al.* 1999)

Experimental procedure

TPD, coupling with TGA, was carried out using a Netzsch Jupiter STA 449C interfaced to an Aeolos QMS 403 quadrupole mass spectrometer, with He as the carrier gas (35 mL min^{-1}). Around 16.0 ± 0.5 mg of sample was placed into an Al_2O_3 crucible, and heated at 10°C min^{-1} until 1300°C. The sample was covered with an aluminium perforated mesh to ensure no sample was blown out of the crucible during heating up procedure. The sample was subjected to a series of depressurization/pressurization cycles with He, to purge air from the system prior to the analysis. The gas evolution profiles were monitored for the following mass/charge (m/z) values, 12, 14, 17, 18, 28, 30, and 44 which correspond to C, N, $^{14}N^{1}H_3$ and $^{16}O^{1}H$, H_2O, $^{12}C^{16}O$ and $^{14}N_2$, $^{14}N^{16}O$ and $^{12}C^{16}O_2$ (Jones *et al.* 1995, Xiao *et al.* 2005). All ion currents from mass spectrometer were multiplied with 10^{12}, and then the backgrounds were subtracted from ion currents. The TPD signals were preserved the same for all

3.2.2.4 Acid/base titration

The oxygen functional groups contents were further investigated using acid/ base titration method developed by Boehm (Boehm 2002). 1.00 ± 0.01 g aliquots of biochar/AC were reacted with 25.0 ± 0.1 mL of NaOH 0.1 N, Na_2CO_3 0.1 N, $NaHCO_3$ 0.1 N and HCl 0.1 N for 72 h, which was deemed to be adequate for carbon materials with high BET N_2 surface area (1000-3000 m^2 g^{-1}) to reach equilibrium (Puri and Bansal 1964). After that, the solutions were filtered to remove the aliquots. Determination of excess base were carried out using HCl 0.1 N with methyl orange (pH for colour change between 3.1 and 4.4), and determination of excess acid were carried out using NaOH 0.1 N with phenolphthalein (pH for colour change between 8.2 and 10). The concentration of acidic sites were calculated based on the assumption that NaOH reacts with carboxylic, lactonic and phenolic groups ($pK_b = -1.7$), Na_2CO_3 reacts with carboxylic and lactonic groups ($pK_b = 3.8$) and $NaHCO_3$ reacts with carboxylic groups ($pK_b = 7.6$) (Boehm 2002). The total content of basic sites was determined from the titration with HCl. Each filtration and titration step was conducted in less than 30 min to minimise the effect of CO_2 in air atmosphere (Seung Kim and Rae Park 2016).

3.2.2.5 Fourier-transform infrared spectroscopy

Fourier-transform infrared spectroscopy (FT-IR) is a non-destructive analysis used to characterise chemistry compositions of carbon materials. In FT-IR, an entire wavelength range of infrared (IR) light is beamed into carbon sample, and the IR is absorbed if a frequency of the IR is as the same as a frequency of one vibration of the molecule. FT-IR instrument uses the Fourier transform (a mathematical process) to produce absorption spectra based on this absorption and calculate how the absorption is at each wavelength. With the development of attenuated total reflectance (ATR) technique, the IR can be used for bulk sample with the incident IR from samples being totally reflected at the ATR prism surface and it can increase the adsorption depth of IR to 1 μm (De Haseth *et al.* 2007), providing more in-depth analysis information. The stretching and deformation vibrations in chemical groups have specific adsorption spectra in FT-IR, and these can be used to identify the chemical functional groups in molecules (Hasegawa 2017). Some of general vibration modes of chemical groups are shown in Table 3-2.

Table 3-2 FTIR spectra of oxygen and nitrogen functional groups

Functional groups	**Wavenumber (cm^{-1})**	**Vibration/ Assignment**	**Ref**
Oxygen functional groups			
C-OH	~3430 ~1200 1182 1030-1155 1087	O-H stretching in phenolic and aliphatic C-O stretching and O-H bending C-O stretching in phenolic C-O in ether group C-O in esters, ethers, and phenol group	(Xiao and Thomas 2005, Niu *et al.* 2017) (Jia and Thomas 2000, Zhang *et al.* 2018, Kahoush *et al.* 2019)
Lactone (C-OO-C)	1734		(Jia and Thomas 2000, Xiao and Thomas 2005)
COOH and COO- (carboxylate)	1717 1550-1610 1360-1450	C=O in carboxylic acid Asymmetric COO vibration Weak asymmetric COO stretching band	(Jia and Thomas 2000, Xiao and Thomas 2005)
C=O	1733 1740 1635 1648	C=O in aldehyde C=O from carbohydrates Carbonyl groups C=O in quinone and pyridone structures C=O vibration conjugated with an aromatic ring	(Kahoush *et al.* 2019) (Nagel *et al.* 2019) (Jia and Thomas 2000) (Niu *et al.* 2017)
Aliphatic (CH, CH$_2$, CH$_3$)	2852 and 2921 2880 and 2935	C-H symmetric and asymmetric C-H stretching	(Jia and Thomas 2000) (Nagel *et al.* 2019)
Aromatic ring	1576	Stretching of aromatic rings conjugated with C=O	(Jia and Thomas 2000, Xiao and Thomas 2005)
Nitrogen functional groups			
-NH- (secondary amine)	3345, 3426	N-H stretching vibration	(Zhang *et al.* 2018, Kahoush *et al.* 2019)
Amide I	1672	C=N stretching	(Khare *et al.* 2005)

Functional groups	**Wavenumber (cm^{-1})**	**Vibration/ Assignment**	**Ref**
	1564	H-N-H bending C=N or C=C	
Pyridinic-N Pyrrolic-N	1512 1541	Pyridinic (N-6) Pyridonic	(Jia *et al.* 2002, Xiao and Thomas 2005)
Indolic/ pyrrolic	1570 1550-1640 1582	N-H stretching vibration for amide group NH_2 scissoring	(Jia *et al.* 2002, Xiao and Thomas 2005, Kahoush *et al.* 2019, Picard *et al.* 2019)

Experimental procedure

Functional groups were further examined by Fourier-transform infrared spectroscopy (FTIR) on a Cary 630 spectrometer with a Diamond-ATR optic from 650 to 4000 cm^{-1}. The spectral resolution was 4 cm^{-1}. A FTIR profile of hydrochar HY250 is shown in Figure 3-18. CO_2 presents a doublet peak between 2300-2380 cm^{-1} for antisymmetric stretching mode and a single peak at ~670 cm^{-1} for bending mode. H_2O, being a nonlinear molecule, has more complex vibration-rotation modes compared to CO_2, and H_2O spectra can be observed between 1400-2000 cm^{-1} (De Haseth *et al.* 2007).

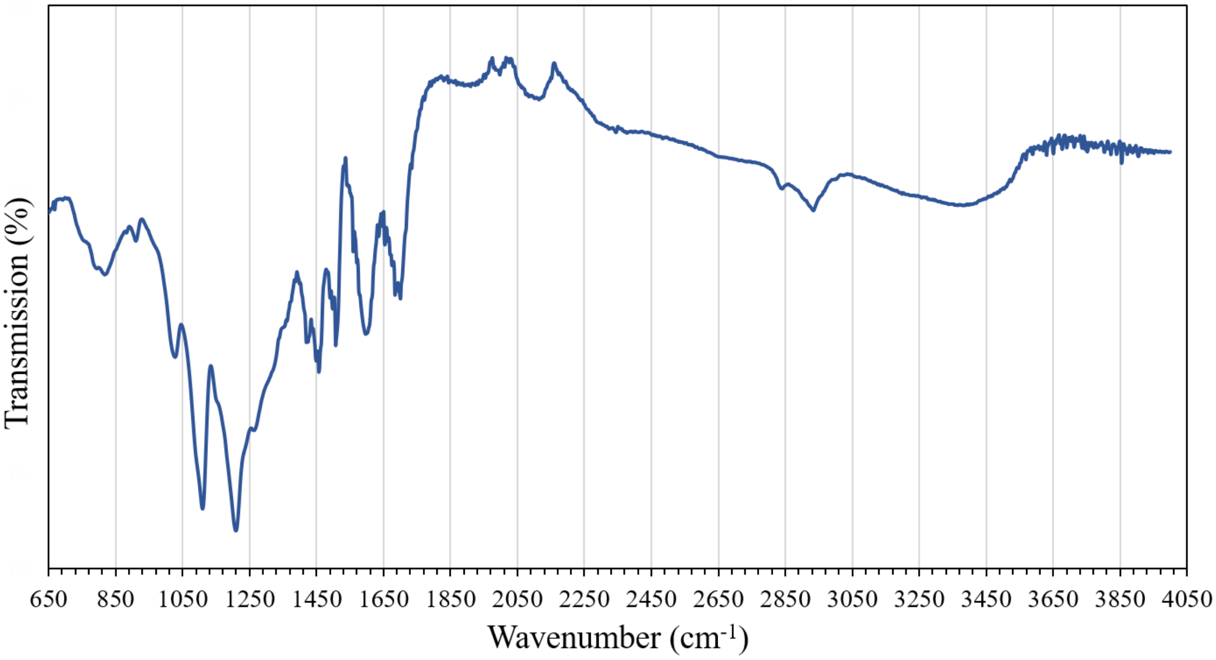

Figure 3-18 FTIR profile of hydrochar HY250

3.2.2.6 Inductively coupled plasma mass spectrometry

Inductively coupled plasma-mass spectrometry (ICP-MS) is a destructive elemental analysis technique. Chemical compounds in an analyte are atomised and then ionised in plasma under inert atmosphere, so the amount of these ions is measured in a quadrupole mass spectrometry. The concentration of elements inside the analyte is proportional to the amount of ions being measured, so the concentration in original samples can be determined (Taylor 2001). ICP-MS allows the quantification of many different elements in one run and has been used to characterise a wide range of elements, mainly metallic elements in carbon samples. As carbon samples are usually in solid form, it is necessary to degrade samples into liquid form through dry ashing or wet ashing techniques with the use of strong acids such as HNO_3 or $HClO_4$ (Kalra 1997).

Phosphorus content was investigated using a Thermo X series11 ICP-MS. 100 ± 1 mg of carbon material were agitated with 2.0 ± 0.1 mL of HNO_3 and refluxed for 72 h in a perfluoroalkoxy alkanes vial. After that, the mixture was diluted with deionised water into 50.0 ± 0.1 mL solution, and 1.0 ± 0.1 mL of this new solution was further diluted to 10 mL of solution prior to measurement. The phosphorus content was determined using m/z 31 (2001). To the best of my knowledge, there was no standard procedure for extracting inorganic elements from carbon materials to acid solutions, so this experimental procedure was based on general knowledge from literature review.

3.2.3 Carbonaceous structure

3.2.3.1 Raman spectroscopy

In Raman spectroscopy, carbon sample is irradiated under a laser beam, and it reflects the elastically scattered light (Rayleigh scattering) as the same frequency and weak non-elastically scattered beams (Stoke and anti-Stoke scattering) with slightly different frequencies from the original radiation. Raman spectroscopy collects the non-elastically Stoke Raman scattered light to identify chemical fingerprint of carbon, and it has been used to detect structural defects in carbon materials such as lattice and edge defects, and finite size of carbon crystals. The limit of depth in Raman spectroscopy is up to 30-60 nm from the surface of carbon sample (Kaburagi *et al.* 2016).

In the first-order Raman spectrum, G band at around ~1582 cm^{-1} (Nemanich and Solin 1979), is the high-frequency E_{2g} symmetry first-order mode with relatively high intensity due to “in-plane” atomic displacements of finite graphite from opposite directions. Meanwhile, D band at ~1360 cm^{-1} is related to disorder structure of carbon in graphite or A_{1g} symmetry breathing modes of sp^2 atom in aromatic rings, so D band is not observed in perfect graphite crystal (Figure 3-19) (Reich and Thomsen 2004). D band requires the presence of six-fold aromatic rings (Ferrari and Robertson 2000), and has been shown to be dependent on the excitation laser energies and shifted to higher frequencies with higher laser energies (Figure 3-20) (Ferrari and Robertson 2001). In higher Raman frequencies region or the second-order Raman spectrum, overtones and combination of D and G bands are also observed in which the 2D band at ~2720 cm^{-1} is the first overtone of D band, and the G+D band at ~2950 cm^{-1} is the combination of D and G bands (Wang *et al.* 1990). The change in shape of 2D band can be used to distinguish graphene and graphene-layers (Ferrari *et al.* 2006).

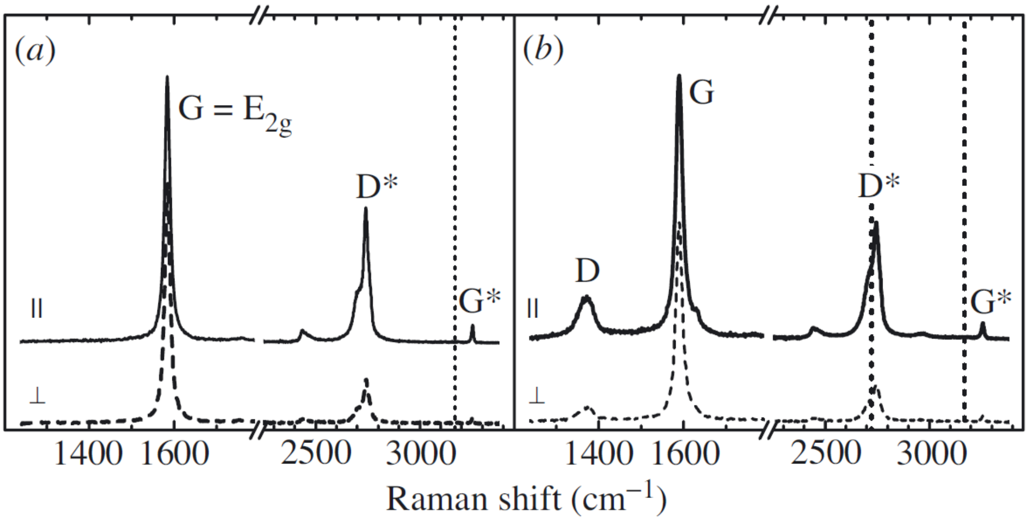

Figure 3-19 Raman spectrum of (a) a perfect crystallite with G band at 1583 cm^{-1} and (b) graphite in the presence of disorder in the focal spot of the laser with an additional D band at 1370 cm^{-1} (Reich and Thomsen 2004)

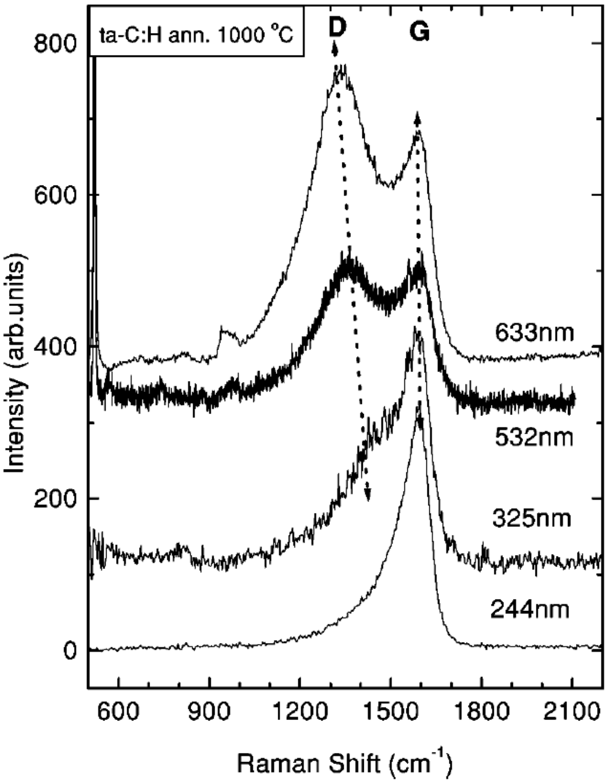

Figure 3-20 Raman spectra of a hydrogenated amorphous carbon with a significant sp^3 carbon annealed in vacuum at 1000°C (ta-C:H) with different excitation energies (Ferrari and Robertson 2001). After being annealed, all hydrogen was removed.

The I_D/I_G ratio (intensity ratio between D and G peaks) is widely accepted to present the degree of ordered carbon in carbon materials (Arkhipova *et al.* 2017, Kierkowicz *et al.* 2018), while the area ratios between D and G peaks (A_D/A_G) are less commonly reported. Due to the dispersion of D band under different excitation energies, including both band positions and bandwidths, care should be taken when interpreting Raman spectroscopy data even when most laser wavelengths used are in the visible region (Ferrari and Robertson 2004).

Experimental procedure

Raman spectroscopy was carried out on a Horiba LabRAM HR Evolution Raman spectrometer to analyse carbonaceous structure (Ar laser, λ = 532 nm, source power 455 mW, 95% laser power). A non-dispersive filter was used to reduce the power applied to walnut shell-derived carbon to ~1% of the power coming from the laser. The samples were observed using an Olympus LMPLFLN20× magnification objective. Each Raman spectrum was obtained as the sum of 10 accumulations of 10 s acquisitions. OriginPro 2017 was used for peak fitting in the range of 800–1800 cm^{-1} (first-order region). Background was subtracted by forming a baseline using the regions of 800–950 cm^{-1} and 1750–1800 cm^{-1}. Raman spectra of walnut shell-derived carbon were not smoothed before curve fitting to reduce errors of data processing. An example of Raman spectra after being fitted with OriginPro software is illustrated in Figure 3-21.

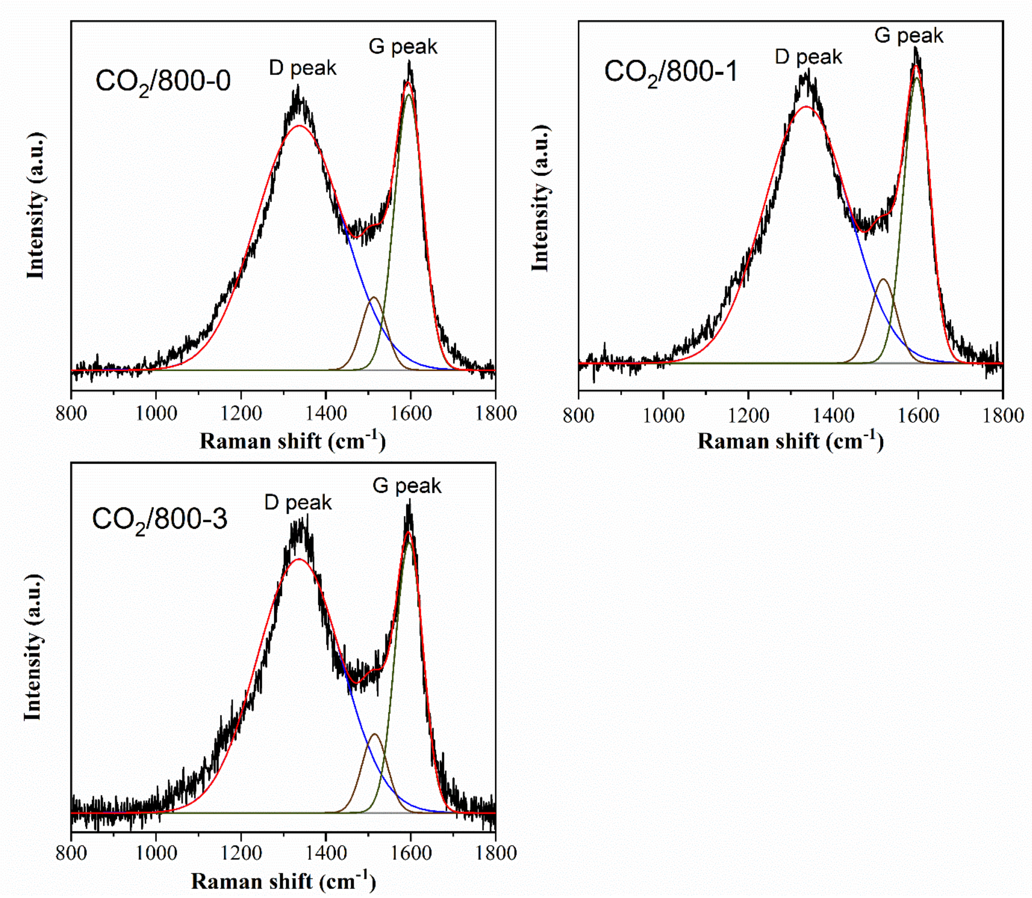

Figure 3-21 Raman spectroscopy profiles of AC treated in CO_2 atmosphere at 800°C at 0 h (CO_2/800-0), 1 h (CO_2/800-1) and 3 h (CO_2/800-3)

2.3.2 X-ray diffraction

X-ray diffraction (XRD) is a popular method for carbon structure characterisation. The Cu Kα radiation is typically used for collecting diffraction patterns of carbon samples. A monochromatic radiation is diverged from a divergence slit and beamed into the sample. Scattered radiation from the diffracted beam is removed by a scattering slit. If the geometry of X-ray, the diffraction angle θ, is in match with Bragg's equation, an increase of reflective radiation intensity will be observed and collected.

$$d = \lambda/2\,sin\,\theta \tag{3-2}$$

in which d is the interlayer space (nm), λ is the wavelength of the X-ray radiation, and θ is the diffraction angle (Iwashita 2016). The interlayer space (d_{002}) was determined through Bragg's law equation: $n\lambda_{XRD} = 2d_{002}sin(\theta_{002})$. The interlayer space between 2 graphite layers d_{002} is 0.3354 nm, and it is much higher in amorphous carbon due to heteroatoms such as hydrogen, oxygen and nitrogen and weak van der Waals interaction between carbon layers (Iwashita 2016). In carbon samples, the peak between 20-30° for turbostractic carbon and at 26.6° for graphite indicates the stack width of graphite crystallite (002) structure, denoted as the L_a (along a-axis). The peak at 43° represents the stack height of graphite crystal, or the honeycomb structure (100) formed by multiple graphene layers, denoted as L_c (along c-axis).

XRD was analysed on a PANalytical X'Pert Pro MPD, powered by a Philips PW3040/60 X-ray generator and fitted with an X'Celerator* detector, scanning between 5–80° with a scan step of 0.0334225, using Cu Kα radiation ($\lambda = 1.540598$ nm) at 40 kV and a current of 40 mA. The Scherrer's equation was used to determine the relative carbon nano-crystal thickness L_c, and crystallite diameter L_a (Iwashita *et al.* 2004, Stein *et al.* 2017):

$$L_c = \frac{0.89\lambda_{XRD}}{\beta_{002}\, cos(\theta_{002})} \tag{3-3}$$

$$L_a = \frac{1.84\lambda_{XRD}}{\beta_{100}\, cos(\theta_{100})} \tag{3-4}$$

in which λ_{XRD} is the wavelength of the incident X-ray radiation, β_{002} and β_{100} are the full width at half maximum of the (002) and (100) peaks, and θ_{002} and θ_{100} are the positions of the (002) and (100) peaks. An example of XRD pattern of AC CO_2/800-1 and how to define β_{002} and β_{100}, θ_{002} and θ_{100} from XRD profile is illustrated in Figure 3-22:

- The peak (002) is defined from the degree with the lowest X-ray intensity in the 10-20° region to the degree with the lowest X-ray intensity in the 30-40° region. β_{002} is defined as half of the value of this region.
- The peak (100) is defined from the degree with the lowest X-ray intensity in the 30-40° region to the degree with the lowest X-ray intensity in the 50-70° region. β_{100} is defined as half of the value of this region.
- θ_{002} is defined as the degree with the highest intensity in the 20-30° region, and θ_{100} is defined as the degree with the highest intensity in the 40-50° region.

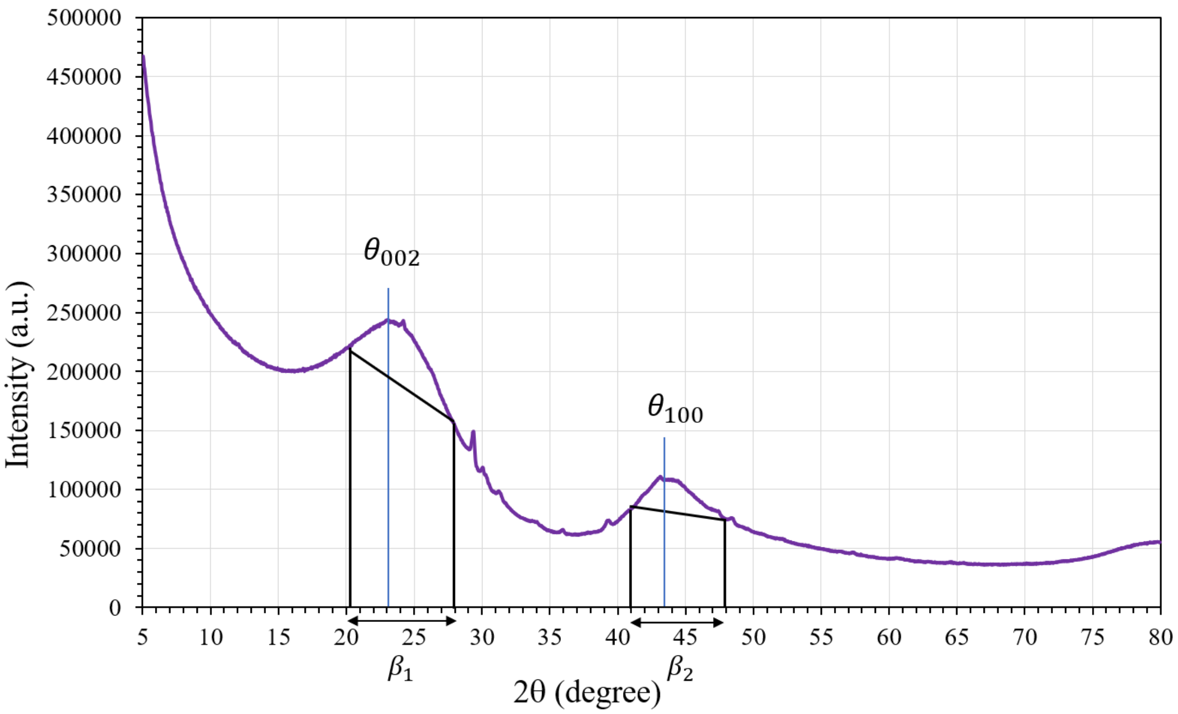

Figure 3-22 Full width at half maximum of the (002) and (100) peaks (β_{002} and β_{100}) and positions of the (002) and (100) peaks (θ_{002} and θ_{100}) from XRD spectrum of AC CO_2/800-1

To explore crystal structure of walnut shell-derived carbon, some samples were further examined with selected area electron diffraction (SAED), transmission electron microscopy bright-field (TEM-BF), transmission electron microscopy dark-field (TEM-DF) and high-resolution TEM (HR-TEM). These techniques were performed on a FEI Tecnai T20 AEM microscope operated at 200 kV.

3.3 Electrochemical measurement

3.3.1 Sample preparation

Walnut shell-derived carbon obtained after preparations was ground into fine powder (< 250 µm). 90 ± 1 mg of walnut shell-derived carbon and 10 ± 1 mg of polyvinylidene fluoride (PVDF) as binder (10 wt%) were thoroughly mixed, and a homogeneous slurry was produced by dispersing the mixture in 1.0 ± 0.1 mL of N-methyl-2-pyrrolidone solution. PVDF is a non-reactive thermoplastic fluoropolymer which is resistant to corrosive chemicals and non-toxic, and the mixture of walnut shell-derived carbon and PVDF at weight ratio 90:10 formulated the ratio between graphite and polymer in other composite bipolar plate (Minke *et al.* 2016). The use of PVDF and the mixture ratio between walnut shell-derived carbon and PVDF has been used in other studies (Maharjan *et al.* 2017, Maharjan *et al.* 2019). Although there are several available types of polymer that can be used in composite bipolar plate (Minke *et al.* 2016), this PhD thesis did not aim to investigate the influence of polymer on bipolar plate performance. Therefore, PVDF was chosen as the polymer. The electrodes were prepared by coating the slurry (30 ± 1 μL cm^{-2}) onto one surface of 0.6 mm thick expanded bipolar plates (TF6, SGL Carbon) to create a coated area of 1 cm^2 (1 cm × 1 cm). A coated electrode with the mixture of walnut shell-derived carbon and PVDF is illustrated in Figure 3-23.

To further understand the surface morphology of the mixture of walnut shell-derived carbon and PVDF on bipolar plate, scanning electron microscope (SEM) was performed by the JEOL JSM-5600LV on some samples. Walnut shell-derived carbons are non-conductive materials in general, so gold coating on these samples were conducted to increase the conductivity of samples. SEM images with different magnifications from 250 to 50,000 was obtained.

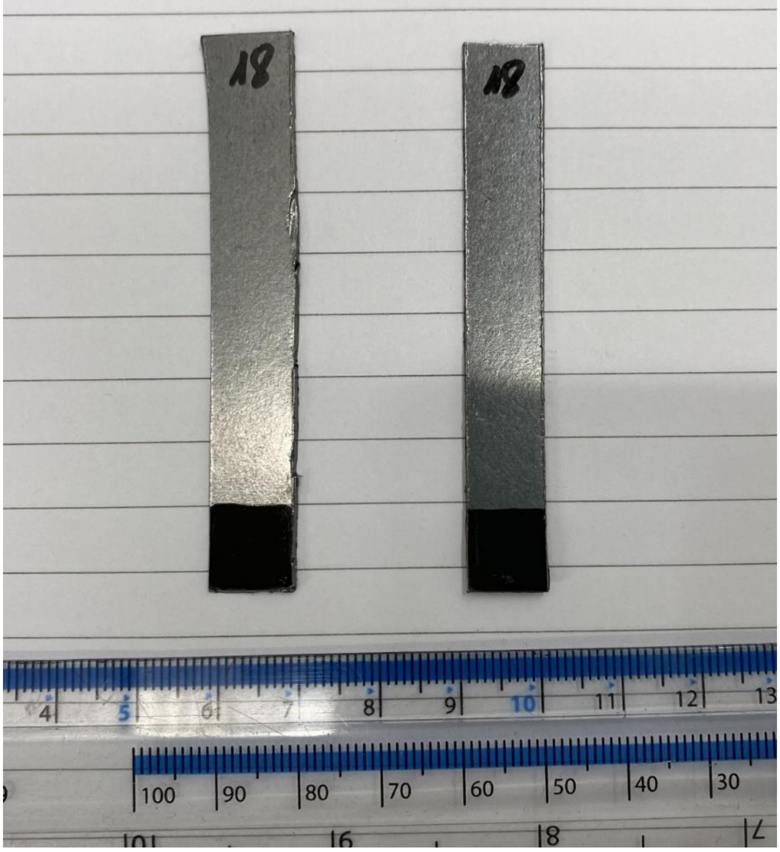

Figure 3-23 A sample of commercial bipolar plates (TF6, SGL Carbon) coated with walnut shell-derived carbon and PVDF (area 1×1 cm^2)

3.3.2 Cyclic voltammetry

Electrodes after being coated were used for cyclic voltammetry (CV), and CV was recorded in a three-electrode cell using a PARSTAT potentiostat (PMC-1000) with the commercial vanadium solution 1.6 M $V^{3.5+}$ in 4.5 M total sulphate electrolyte solution (GFE, Nuremberg, Germany). The counter electrode (CE) was a platinum wire to avoid any unnecessary side reactions during CV and the reference electrode (RE) was mercury saturated electrode in 1 M H_2SO_4 (MSE). The applied voltage window is between -1.3 and 1 V vs RE. The CVs reported in this article were steady-state CVs, which obtained after a full cycle scan with the voltage window mentioned above, at scan rate 20 mV s^{-1}. A three-electrode electrochemical cell set up is showed in Figure 3-24. Nitrogen is used as inert atmosphere to protect electrolyte from being oxidised by air oxygen. Before entering the electrochemical cell, nitrogen flowed through a pre-bubbler containing DI water to create saturated nitrogen, which minimised concentration changes due to loss of water in the cell during the sparging process. This created a nitrogen blanket over the vanadium solution and eliminated side reactions between air oxygen and vanadium species.

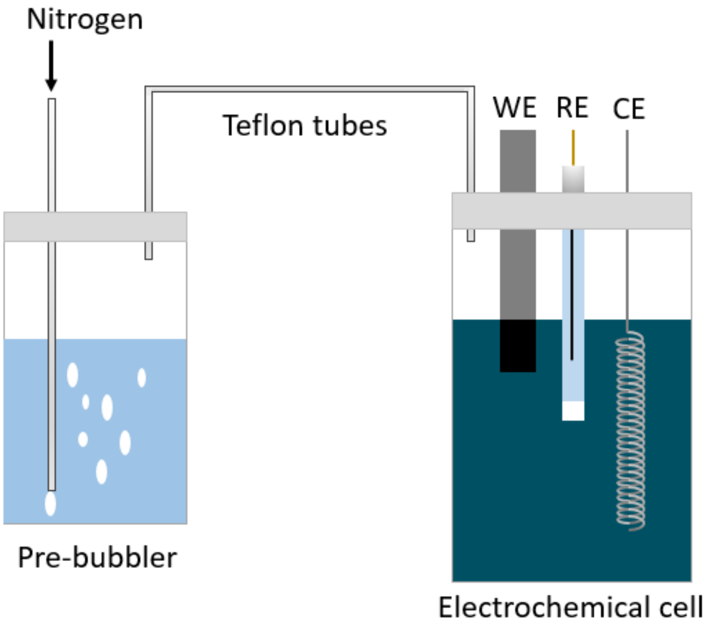

Figure 3-24 Schematic of the three-electrode electrochemical cell (WE: working electrode, RE: reference electrode, CE: counter electrode)

3.3.3 Electrochemical impedance spectroscopy

3.3.3.1 Electrolyte synthesis

In order to obtain $V^{4.5+}$ solution (mixture of 50% V^{4+} and 50% V^{5+}), the commercial 1.6 M $V^{3.5+}$ in 4.5 M total sulphate electrolyte solution (GFE, Nuremberg, Germany) was electrolysed in a two-compartment flow cell separated by a cation exchange membrane (Fumatech, GmbH, Bietigheim, Germany) with electrodes comprising of PAN based carbon felt (SIGRACELL GFD 4.6 EA, SGL Carbon) of thickness 4.6 mm and bipolar plate (TF6, SGL Carbon). The electrolysis was conducted under N_2 atmosphere to prevent the oxidation of electrolyte ions with oxygen in atmosphere. The necessary time for electrolysis to achieve the state of charge was calculated using Faraday equation:

$$m = \frac{QM}{Fz} = \frac{ItM}{Fz} \tag{3-5}$$

$$n = \frac{Q}{Fz} = \frac{It}{Fz} \tag{3-6}$$

In which m is the mass of the substance liberated at an electrode (g), Q is the total electric charge passed through electrolyte (C), F = 96485 C mol^{-1} is the Faraday constant, M is the molecular weight of the substance (g mol^{-1}), and z is the number of electron transferred per ion of the substance. For example, in order to synthesize 80 mL of $V^{2.5+}$ on negative half-cell and 80 mL of $V^{4.5+}$ on positive half-cell from 1.6 M $V^{3.5+}$ solution, the required time for charging is (given current applied I = 0.25 A):

$$1.6 \times 0.08 = \frac{0.25t}{96485 \times 1} \Rightarrow t = 49400\,(\text{s}) \approx 13\text{ h } 43\text{ min } 20\text{ s}$$

3.3.3.2 Experimental procedure and EIS model

$V^{4.5+}$ solution after being synthesized was used for electrochemical impedance spectroscopy (EIS). The electrode prepared for CV experiment was also used for EIS. This experiment was also recorded in a three-electrode cell with the same setup as CV (Figure 3-24, section 3.3.2), using a MGP-2 battery test station potentiostat, using the frequency range from 20 kHz to 100 mHz at alternating current signal of 10 mV.

The equivalent circuit model (Figure 3-25) was used to explain EIS data, and it was applicable to all the samples investigated. However, in various cases, some components were not necessary.

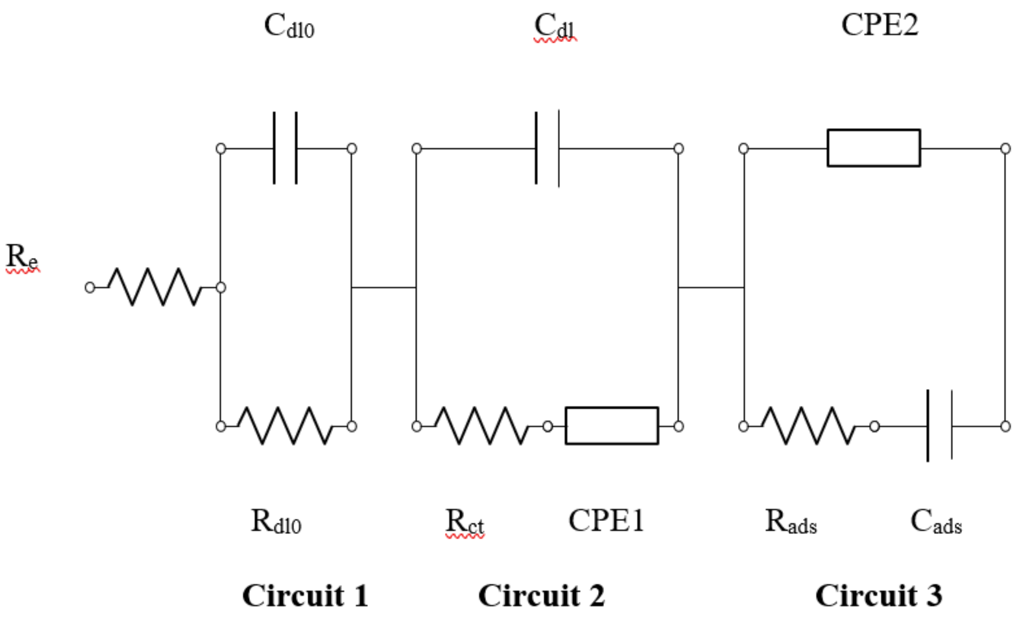

Figure 3-25 EIS equivalent circuit model

In which:

- C_{dl0}, R_{dl0} and R_{dl} are the capacitance and resistances the double layer.
- R_{ct} is the charge transfer resistance.
- R_{ads} and C_{ads} are the adsorption resistance and capacitance.
- Components CPE1 and CPE2 are constant phase elements, which have Warburg impedances of the form

$$Z = \frac{Yinv}{(i\omega)^{\varphi}}$$

The angular frequency is ω. As φ approaches 1, the impedance Z becomes a capacitor with *Yinv* equal to the inverse of the capacitance, whereas when φ approaches 0, it becomes a resistor with *Yinv* equal to the resistance. Further analysis of the model in Figure 3-25 is described in 7.3Appendix B.3.

Chapter 4

Synthesis and characterisation of walnut shell-derived carbon

This chapter looks at the systematic change in characteristics of walnut shell-derived carbon (biochar and activated carbon (AC)), including surface area and porosity, functional groups and carbonaceous structure with changes in operating conditions. Furthermore, the walnut shell-derived carbon was functionalised with various activating agents including HNO_3, K_2CO_3, and NH_3. Although they are conventional functionalising techniques, they provided a wide range of walnut shell carbons with different properties. The obtained walnut shell-derived carbon was then used with polyvinylidene fluoride (PVDF) to formulate composite bipolar plate using in VRFB. Therefore, for the first time, it allows the assessment of correlations between physicochemical properties of walnut shell-derived carbon and kinetics of vanadium redox reactions in a systematic viewpoint. The results not only help establish the understanding of using biomass-derived carbon as a bipolar plate precursor in VRFB but also help evaluate the suitability of methodology.

The VO_2^+/ VO^{2+} and V^{2+}/V^{3+} couples gave well defined peaks with the former being the most intense in cyclic voltammetry (CV), but the $V^{3+/}VO^{2+}$ couple was very weak. The results show that the for V^{2+}/V^{3+} and VO^{2+}/VO_2^+ couples in the CVs were enhanced for carbonization temperatures up to 800°C and oxygen and nitrogen functionalization. These changes are accompanied by changes in the electrical impedance spectroscopy. The V^{3+}/VO^{2+} couple was enhanced with change with functionalization. The electrochemistry results are discussed in relation to changes in carbon structure and functional groups.

4.1 Gas adsorption-desorption behaviours

BET surface area measurements cannot provide accurate information for ultramicroprous (< 0.7 nm) carbons due to activated diffusion effects at -196°C. CO_2 adsorption at 0°C is routinely used to measure ultra-micropore volume and surface area (S_{CO2}) of porous carbons using the Dubinin-Radushkevich (DR) equation (Garrido *et al.* 1987, Rexer *et al.* 2014). This is due to better diffusion of CO_2 into this size range of micropores in carbons at the higher temperature (0°C). The DR model fitted the isotherms obtained (CO_2 adsorption isotherm and DR plot of AC CO_2/800-1 is shown in Figure 4-1 and DR plots for other walnut shell-derived carbon are illustrated in Figure C-1 and Figure C-2), indicating that the pore size distributions in walnut shell-derived carbons were of Gaussian type. S_{CO2} increased with increasing pyrolysis temperature in both N_2 and CO_2 atmosphere, from 600°C to 800°C (Table 4-1) due to higher temperatures increasing the amount of volatiles removed (Johnson *et al.* 1986, Xia *et al.* 2019). However, increasing the temperature up to 1000°C in inert atmosphere *i.e.* N_2 annealed the carbon structure and reduced S_{CO2} (320 ± 2 m^2 g^{-1} for biochar N_2/1000-1 compared to 758 ± 5 m^2 g^{-1} for CO_2/1000-1).

On the other hand, the pyrolysis atmosphere had a major influence on the S_{BET} of AC unlike S_{CO2}. CO_2 reacted with walnut shells *via* the Boudouard reaction at heat treatment temperatures (HTTs) > 700°C ($C + CO_2 \rightarrow 2CO$) (Lahijani *et al.* 2015) and widened the pores of CO_2/800-1, resulting in a higher S_{BET} of AC CO_2/800-1 compared to biochar N_2/800-1 (482 m^2 g^{-1} compared to 29 m^2 g^{-1}) (pyrolysis at 800°C in N_2 is likely to anneal biochar). An increase in pyrolysis holding time at high temperatures intensifies the reaction between walnut shell/biochar and CO_2 through the Boudouard reaction and higher S_{BET} subsequently (Table 4-1). Gases emerged during thermal treatment of walnut shells were collected and analysed, and the profiles of gas evolution during pyrolysis under N_2 and activation treatment under CO_2 of walnut shell from ambient temperature to 800°C is shown in Figure 4-2. Figure 4-2 also shows that CO emerged significantly compared to H_2 and CH_4 at 700°C and 800°C when using CO_2 atmosphere, but when pyrolysing walnut shells in N_2 atmosphere, only a small amount of H_2, CH_4 and CO emerged. This supports the reaction between CO_2 and walnut shell carbons at > 700°C.

Overall, the S_{CO2} of walnut shell-derived carbon did not appear to be significantly affected by the choice of carrier gas employed during thermal treatments, whereas a significant increase for the S_{BET} was observed when CO_2 was used. This is mainly due to activated diffusion effect, normally observed for carbonised materials, molecular sieve carbons, and ACs with very low percentages of carbon (< 5%) reacting with oxidising agents like O_2, CO_2 during gasification (Garrido *et al.* 1987). One important evidence to support the activated diffusion in N_2-biochar series in this study is adsorption kinetic of CO_2 at 0°C (Figure C-3). Biochar N_2/600-1, N_2/700-1 and N_2/800-1 took more than 500 s to achieve the equilibrium pressure step 50-100 mbar, and biochar N_2/1000-1 did not reach equilibrium even after 21,600 s (~ 6 h).

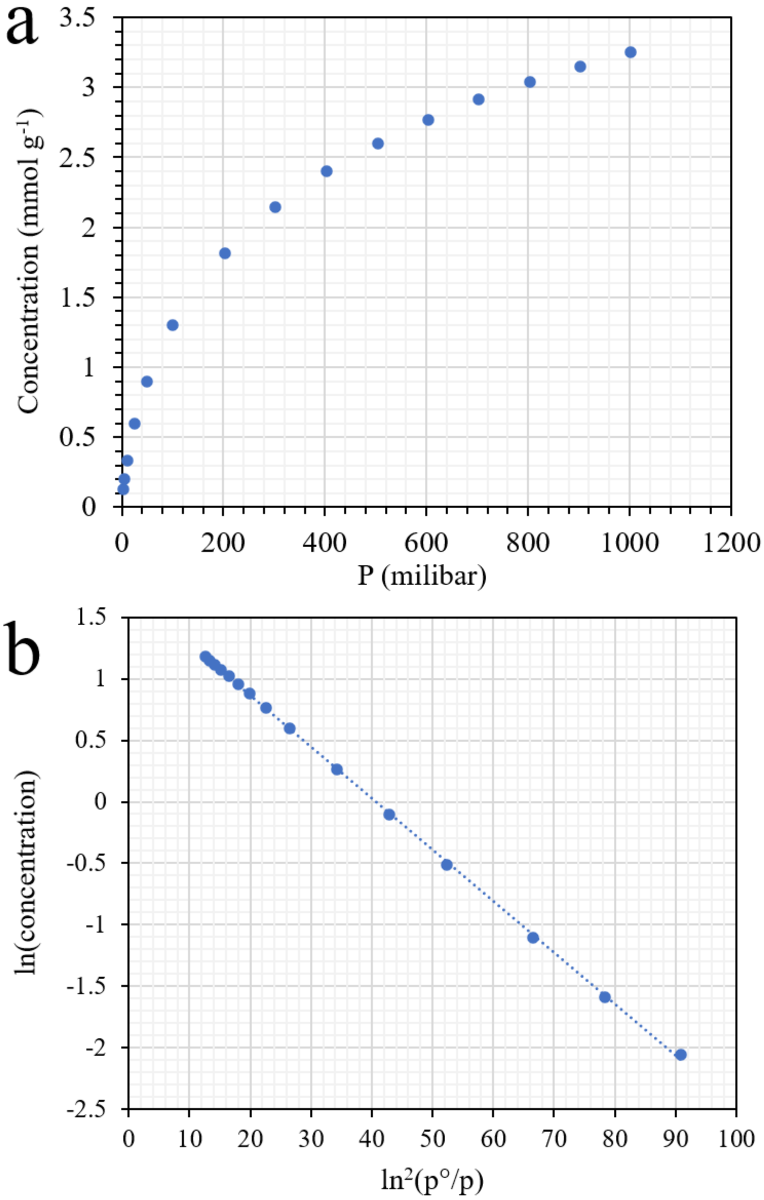

Figure 4-1 (a) CO_2 adsorption isotherm at 0°C and (b) DR plot of AC CO_2/800-1

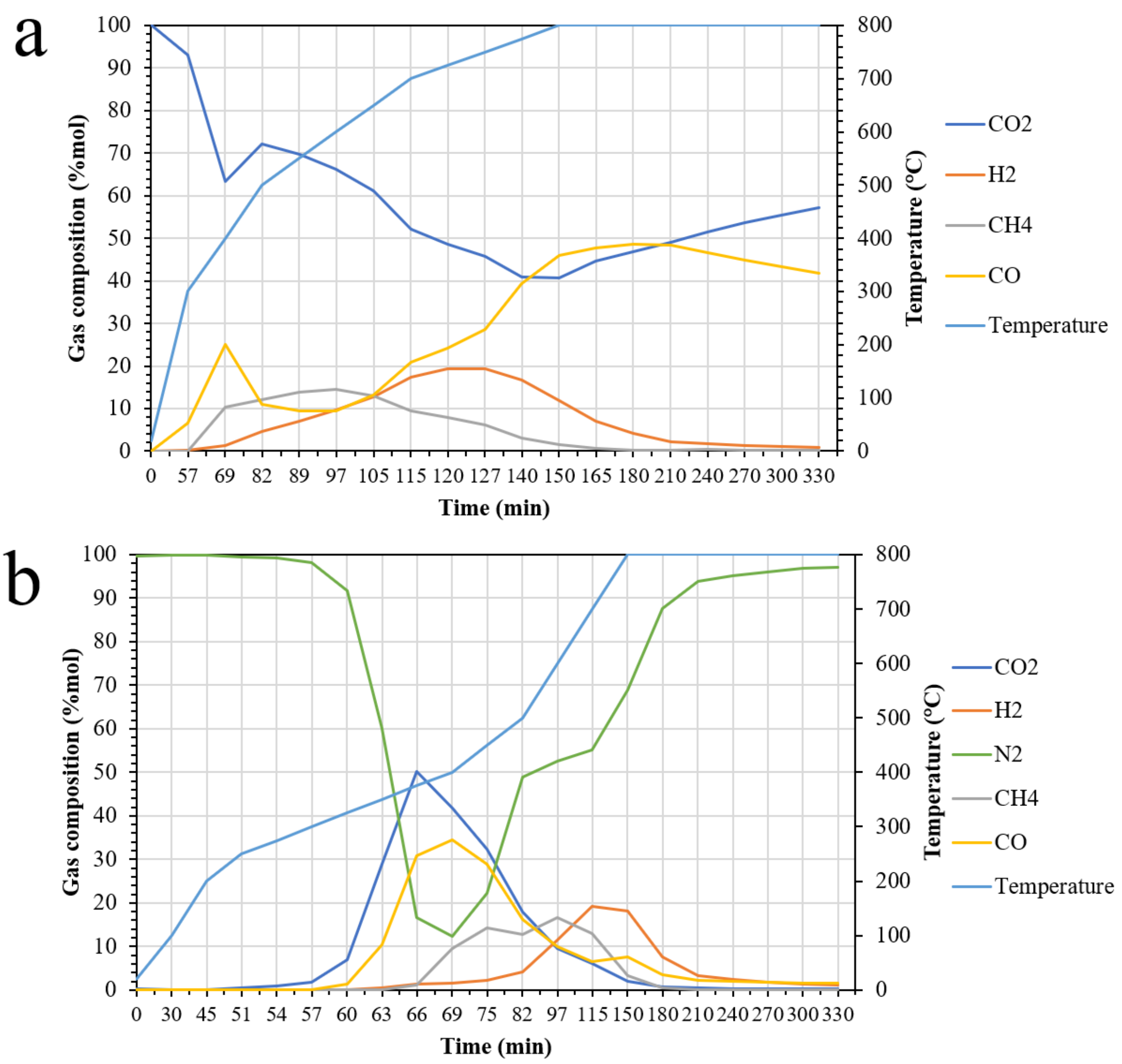

Figure 4-2 Gas profiles of walnut shell-derived carbon treated at 800°C (a) under CO_2 atmosphere and (b) under N_2 atmosphere

Table 4-1 Pore structure characterization by CO_2 and N_2 adsorption-desorption

Carbon sample	**S_{CO2} (m^2 g^{-1})**	**V_{CO2} (cm^3 g^{-1})**	**S_{BET} (m^2 g^{-1})**	**V_{N2} (cm^3 g^{-1})**	**V_{micro} (cm^3 g^{-1})**	**V_{meso} (cm^3 g^{-1})**
N_2/600-1	501 ± 3	0.187 ± 0.001				
N_2/700-1	543 ± 3	0.203 ± 0.001				
N_2/800-1	591 ± 4	0.220 ± 0.001	29 ± 1	0.050 ± 0.001	0.009	0.041
N_2/1000-1	320 ± 2	0.121 ± 0.001				
CO_2/700-1	607 ± 4	0.226 ± 0.001	503 ± 11	0.342 ± 0.003	0.196	0.146
CO_2/800-0	611 ± 4	0.228 ± 0.001	448 ± 10	0.254 ± 0.003	0.189	0.065
CO_2/800-1	632 ± 4	0.235 ± 0.001	482 ± 10	0.265 ± 0.003	0.181	0.084
CO_2/800-3	641 ± 4	0.239 ± 0.001	564 ± 12	0.318 ± 0.003	0.226	0.092
CO_2/1000-1	758 ± 5	0.282 ± 0.001	704 ± 15	0.380 ± 0.004	0.271	0.109
CO_2/800-1-K_2CO_3	795 ± 5	0.296 ± 0.001	681 ± 14	0.337 ± 0.003	0.266	0.071
CO_2/800-1-HNO_3	519 ± 3	0.193 ± 0.001	590 ± 13	0.307 ± 0.003	0.223	0.084
CO_2/800-1-HNO_3/400	632 ± 4	0.236 ± 0.001	559 ± 12	0.345 ± 0.003	0.217	0.128
CO_2/800-1-HNO_3/800	626 ± 4	0.233 ± 0.001	726 ± 15	0.355 ± 0.003	0.299	0.056
N_2/800-1-NH_3/600	542 ± 3	0.202 ± 0.001	3 ± 1	0.013 ± 0.001	0	0.013
N_2/800-1-NH_3/800	686 ± 4	0.256 ± 0.001	720 ± 15	0.337 ± 0.003	0.273	0.064

Note: S_{CO2}: ultramicropore surface area, determined by using DR plot and CO_2 adsorption at 0°C; V_{CO2}: ultramicropore volume determined using DR plot on CO_2 adsorption at 0°C; S_{BET}: total surface area determined by BET plot ($p/p° = 1\times10^{-3}$-0.06) and N_2 adsorption at -196°C; V_{N2}: total pore volume determined by N_2 adsorption at -196°C at $p/p° = 0.995$; V_{micro}: micropore volume (0.3-2 nm) determined by using DR plot on N_2 adsorption at -196°C; V_{meso}: subtraction of V_{micro} from V_{N2}.

K_2CO_3 was reported as an activating agent for increasing the porosity of carbons thanks to reaction between K_2CO_3 and carbon materials ($K_2CO_3 + 2C \rightarrow 2K + 3CO$) (Köseoğlu and Akmil-Başar 2015), so K_2CO_3 was used as an activating agent to modify the porosity of AC CO_2/800-1 in this work. It can be seen from Table 4-1 that the pore volume associated with mesoporosity (V_{meso} = 0.071 cm^3 g^{-1}) was reduced following K_2CO_3 treatment, whereas the pore volume associated with microporosity (V_{micro}) increased (0.266 cm^3 g^{-1} and Figure 4-3). Köseoğlu *et al.* examined the N_2 adsorption capacity of orange peel-derived AC treated with K_2CO_3 at 500-1000°C; the S_{BET} of AC increased with increasing temperature and reached 621 m^2 g^{-1} at 800°C which was similar to S_{BET} of CO_2/800-1-K_2CO_3 (681 m^2 g^{-1}) (Köseoğlu and Akmil-Başar 2015). Mestre *et al.* reported higher S_{BET} of AC obtained from K_2CO_3 treatment (781-1419 m^2 g^{-1}), but their experimental procedure allowed lignin inside biomass (lignin was obtained through digestion and polycondensation with H_2SO_4 solution to remove cellulose and hemicellulose) to react directly with K_2CO_3 at 800°C, while in this work K_2CO_3 only reacted with solid walnut shell-derived carbon after heat treatment, resulting in a lower surface area (Mestre *et al.* 2019). Table 4-1 shows K_2CO_3 reacted with carbon and increased significantly S_{BET} of AC CO_2/800-1-K_2CO_3 (681 ± 14 m^2 g^{-1}) compared to AC CO_2/800-1 (482 ± 10 m^2 g^{-1}), but the total V_{N2} only changed slightly (only ~13%). This was likely due to an increase in microporosity at the expense of mesoporosity. The reaction between K_2CO_3 and C consumed the carbon content and created pores in the material. Furthermore, at 800°C, CO_2 evolving from the decomposition of K_2CO_3 can also react with carbon in gasification reactions to form pores in carbon structure.

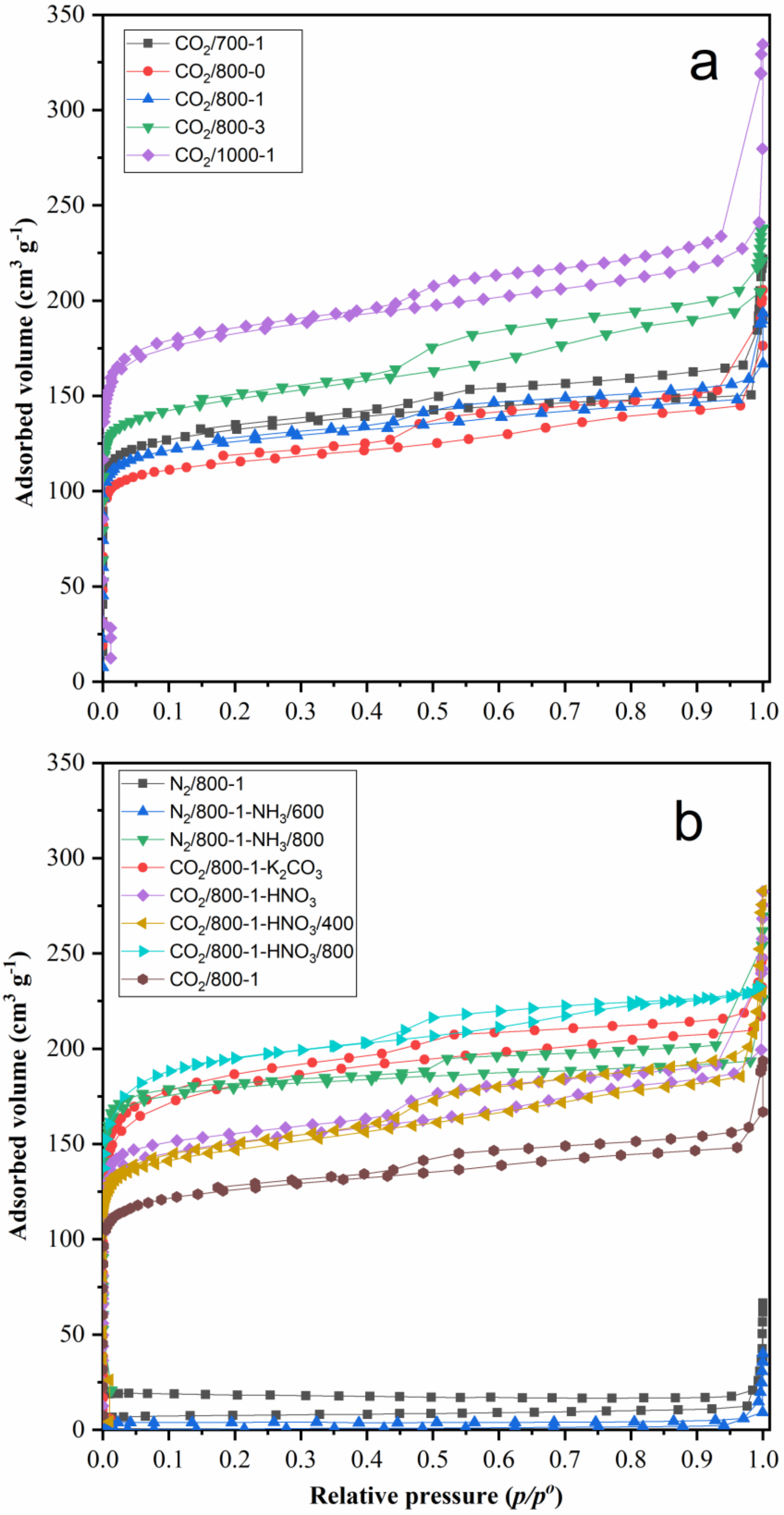

Figure 4-3 N_2 adsorption-desorption isotherms at -196°C for (a) AC treated in CO_2 at 700°C (CO_2/700-1), 800°C (CO_2/800-0, CO_2/800-1, CO_2/800-3), and 1000°C (CO_2/1000-1) b) biochar pyrolysed in N_2 at 800°C (N_2/800-1), AC treated with K_2CO_3 (CO_2/800-1-K_2CO_3), HNO_3 (CO_2/800-1-HNO_3, CO_2/800-1-HNO_3/400, CO_2/800-1-HNO_3/800) and heat treated with NH_3 at 600 and 800°C (N_2/800-1-NH_3/600 and N_2/800-1-NH_3/800, respectively)

NH_3 treatment not only modifies the nitrogen content in biochar N_2/800-1 (Zhu *et al.* 1997), but also changes the morphology (Zhu *et al.* 1995). As explained in literature review section 2.4.1.2 and experimental methodologies section 3.1.2.3 on nitrogen incorporation by heat treatment, difference in temperature results in different nitrogen contents and also different proportions of nitrogen species, so two different temperatures of 600 and 800°C was used in this work. NH_3 treatment at 600°C reduced both S_{CO2} and S_{BET} to 542 and 3 m^2 g^{-1}, respectively and this could be attributed to sintering effect at high temperature (Table 4-1). In N_2/800-1-NH_3/600 activated diffusion effects limited the N_2 adsorption at -196°C as shown by the much higher CO_2 adsorption at 0°C (Marsh 1987). However, higher treatment temperature at 800°C led to gasification reactions between NH_3 and carbon, increasing both S_{CO2} and S_{BET} to 686 and 720 m^2 g^{-1}, respectively, compared to N_2/800-1 (Mian *et al.* 2018, Wang *et al.* 2019).

On the other hand, HNO_3 treatment slightly increased the S_{BET} from 482 m^2 g^{-1} of CO_2/800-1 to 590 m^2 g^{-1} of CO_2/800-1-HNO_3, but it also reduced the S_{CO2} of AC CO_2/800-1-HNO_3 (519 m^2 g^{-1}) compared to its precursor CO_2/800-1 (632 m^2 g^{-1}) which might be due to the change in some ultramicropores (Table 4-1). Therefore, it can be concluded that HNO_3 treatment only significantly altered surface oxygen functional groups without markedly influencing the surface area and total porosity. Further heat treatment in H_2 removed the oxygen functional groups from micropores and increased S_{CO2} back to similar to AC CO_2/800-1 (632 m^2 g^{-1} for CO_2/800-1-HNO_3/400 and 626 m^2 g^{-1} for CO_2/800-1-HNO_3/800). This was also observed in the study of Noh and Schwarz (Noh and Schwarz 1990).

4.2 Functional group characterisation

4.2.1 X-ray photoelectron spectroscopy (XPS)

XPS allows the surface composition of walnut shell-derived carbon to be analysed down to a depth of 5 nm (Konno 2016). The XPS analysis of 11 heat-treated biochar and AC samples (N_2/600-1 to CO_2/1000-1) were similar regardless of temperature, holding time, and gas environment (N_2 or CO_2) (Table 4-2). The carbon contents varied between 88.5 and 91.6 at% (average 89.94 ± 0.75 at%), while oxygen accounted for 6.9-9.2 at% (average 8.34 ± 0.66 at%) (Table 4-2). No trends with temperature or holding time were observed. The remaining elements consisted of K, Ca, and Si (up to 2 at%), which originally are in biomass feedstock, and these elements were also determined through XPS profiles of walnut shell-derived carbons. Significant amounts of nitrogen were not detected in the spectra of this series of carbons (Table 4-2). XPS C 1s peaks were deconvoluted into several peaks, including C=C sp^2 (284.5 ± 0.2 eV), C-C sp^3 (285.2 ± 0.2 eV), C-O (286.4 ± 0.2 eV), C=O (287.9 ± 0.3 eV), O-C=O (289.1 ± 0.3 eV) (Yang *et al.* 2009, Maharjan *et al.* 2017). The surface composition of the C sp^2, C sp^3 and various oxygen-containing surface functional groups obtained from curve resolution of the C 1s peaks are shown in Table 4-2. The oxygen species are only minor (<10%) components in the C 1s peaks thereby limiting the accuracy to which they can be determined by curve resolution of this peak. The C sp^2 and C sp^3 surface contents were 52.8 ± 7.7 and 29.3 ± 7.3 at%, respectively.

The surface oxygen functional groups were determined directly from the O 1s peaks, and they were deconvoluted into four peaks, including C=O (531.4 ± 0.2 eV), C-O/OH (532.4 ± 0.3 eV), O-C=O (533.4 ± 0.3 eV) and some chemisorbed H_2O (535.5 ± 0.5 eV) (Kozlowski and Sherwood 1986, Wang *et al.* 2001, Yang *et al.* 2009, Huang *et al.* 2018) (Table 4-3). These direct measurements of oxygen surface species from the O 1s peaks are considered more accurate than determining oxygen species from the high energy tail of the asymmetric C 1s peaks (see Figure 4-4a and c for comparison). The C-O/C-OH, C=O, O-C=O and chemisorbed H_2O expressed as percentage of total oxygen contents obtained from O 1s peaks of the 11 biochar and AC samples treated in N_2 and CO_2 were 33.3 ± 3.3%, 37.4 ± 4.9%, 25.9 ± 6.0% and 3.5 ± 0.7%, respectively (Table 4-3). This analysis showed that the 11 samples prepared under N_2 and CO_2 atmospheres (N_2/600-1 to CO_2/1000-1 in Table 4-2) had similar surface oxygen compositions.

Table 4-2 Elemental analysis and oxygen functional analysis of carbons obtained from X-ray photoelectron spectroscopy (XPS)

Carbon sample	**Atomic content (at%)**				**Components from C 1s profile (at%)**				
	C	**N**	**O**	**K, Ca and Si**	**C sp^2**	**C sp^3**	**C-O/OH**	**C=O**	**O-C=O**
N_2/600-1	89.6 ± 0.3	0.0	9.1 ± 0.2	1.3	42.0 ± 4.1	40.7 ± 11.0	4.0 ± 0.2	1.7 ± 0.3	1.2 ± 0.1
N_2/600-3	89.5 ± 0.3	0.0	9.2 ± 0.2	1.3	43.0 ± 4.2	38.9 ± 11.2	4.3 ± 0.2	1.9 ± 0.3	1.4 ± 0.1
N_2/700-1	89.9 ± 0.3	0.0	8.2 ± 0.2	1.9	54.6 ± 5.3	27.2 ± 7.3	4.9 ± 0.3	2.0 ± 0.3	1.2 ± 0.1
N_2/800-1	90.0 ± 0.3	0.3 ± 0.1	8.1 ± 0.2	1.6	77.8 ± 7.5	8.8 ± 2.2	1.8 ± 0.2	0.9 ± 0.2	0.7 ± 0.2
N_2/800-3	89.8 ± 0.3	0.0	8.4 ± 0.2	1.8	65.2 ± 6.4	17.7 ± 4.8	4.1 ± 0.2	1.7 ± 0.3	1.1 ± 0.1
N_2/1000-1	89.9 ± 0.3	0.0	8.4 ± 0.2	1.7	50.2 ± 4.9	30.0 ± 8.1	6.2 ± 0.3	2.3 ± 0.4	1.2 ± 0.1
CO_2/700-1	89.9 ± 0.3	0.0	8.4 ± 0.2	1.7	52.4 ± 5.1	29.6 ± 8.0	4.5 ± 0.2	2.0 ± 0.3	1.4 ± 0.1
CO_2/700-3	91.6 ± 0.3	0.0	6.9 ± 0.2	1.5	66.8 ± 6.5	19.4 ± 5.2	3.2 ± 0.2	1.4 ± 0.2	0.8 ± 0.1
CO_2/800-1	90.0 ± 0.3	0.0	8.3 ± 0.2	1.7	50.5 ± 4.9	30.3 ± 8.6	5.4 ± 0.3	2.2 ± 0.4	1.6 ± 0.2
CO_2/800-3	90.6 ± 0.3	0.0	7.7 ± 0.2	1.7	51.3 ± 5.0	29.7 ± 8.0	5.8 ± 0.3	2.2 ± 0.4	1.6 ± 0.2
CO_2/1000-1	88.5 ± 0.3	0.0	9.0 ± 0.2	2.5	54.2 ± 5.3	25.8 ± 7.0	5.8 ± 0.3	1.9 ± 0.3	0.8 ± 0.1
CO_2/800-1-K_2CO_3	92.9 ± 0.2	0.0	7.1 ± 0.2	0.0	62.4 ± 6.1	19.3 ± 5.2	5.7 ± 0.3	2.3 ± 0.4	3.2 ± 0.3
CO_2/800-1-HNO_3	85.7 ± 0.3	0.8 ± 0.1	13.5 ± 0.2	0.0	58.0 ± 4.1	15.6 ± 3.6	5.3 ± 0.5	3.3 ± 0.2	3.5 ± 0.3
CO_2/800-1-HNO_3/400	90.3 ± 0.3	1.3 ± 0.2	8.4 ± 0.1	0.0	66.0 ± 4.7	14.6 ± 3.4	4.9 ± 0.5	2.3 ± 0.1	2.5 ± 0.2
CO_2/800-1-HNO_3/800	96.8 ± 0.3	0.3 ± 0.1	2.9 ± 0.1	0.0	90.9 ± 6.4	2.1 ± 0.5	1.4 ± 0.1	0.0	2.3 ± 0.2
N_2/800-1-NH_3/600	94.7 ± 0.3	2.6 ± 0.3	2.7 ± 0.1	0.0	86.4 ± 1.5	7.0 ± 0.3	1.3 ± 0.2	0.0	0.0
N_2/800-1-NH_3/800	93.1 ± 0.3	4.9 ± 0.2	1.8 ± 0.1	0.2	78.4 ± 1.4	11.1 ± 0.4	3.2 ± 0.6	0.4 ± 0.4	0.0

Note: The percentage of C-O/OH, C=O and O-C=O in Table 2 were obtained from C 1s peak rather than O 1s peak. Therefore, the sum of the various O peak species obtained from C 1s peaks do not correspond with the total oxygen contents obtained from survey spectra whereas they do for oxygen components in O 1s peaks.

HNO_3 treatment successfully incorporated oxygen functional groups into AC as the total oxygen content increased from 8.1 at% in CO_2/800-1 to 13.5 at% in CO_2/800-1-HNO_3 (Figure 4-4). Furthermore, both C-O/OH, and O-C=O contents in CO_2/800-1-HNO_3 from O 1s peak increased significantly compared to CO_2/800-1, while C=O decreased (Table 4-3). This was consistent with titration results, which confirmed an acidic surface, and TPD results, discussed in the later sections. Heat treatment of CO_2/800-1-HNO_3 in H_2 gradually decreased the surface oxygen content from 13.5 at% for CO_2/800-1-HNO_3 to 8.4 for CO_2/800-1-HNO_3/400 and 2.9 at% for CO_2/800-1-HNO_3/800 (Table 4-2). The proportion of C-O/C-OH in total surface oxygen increased during the heat treatment whereas the proportion of O-C=O in surface oxygen decreased, but the major change was the decrease in total oxygen content. This is also consistent with the TPD results discussed later which show that CO_2 desorption is negligible from CO_2/800-1-HNO_3/800.

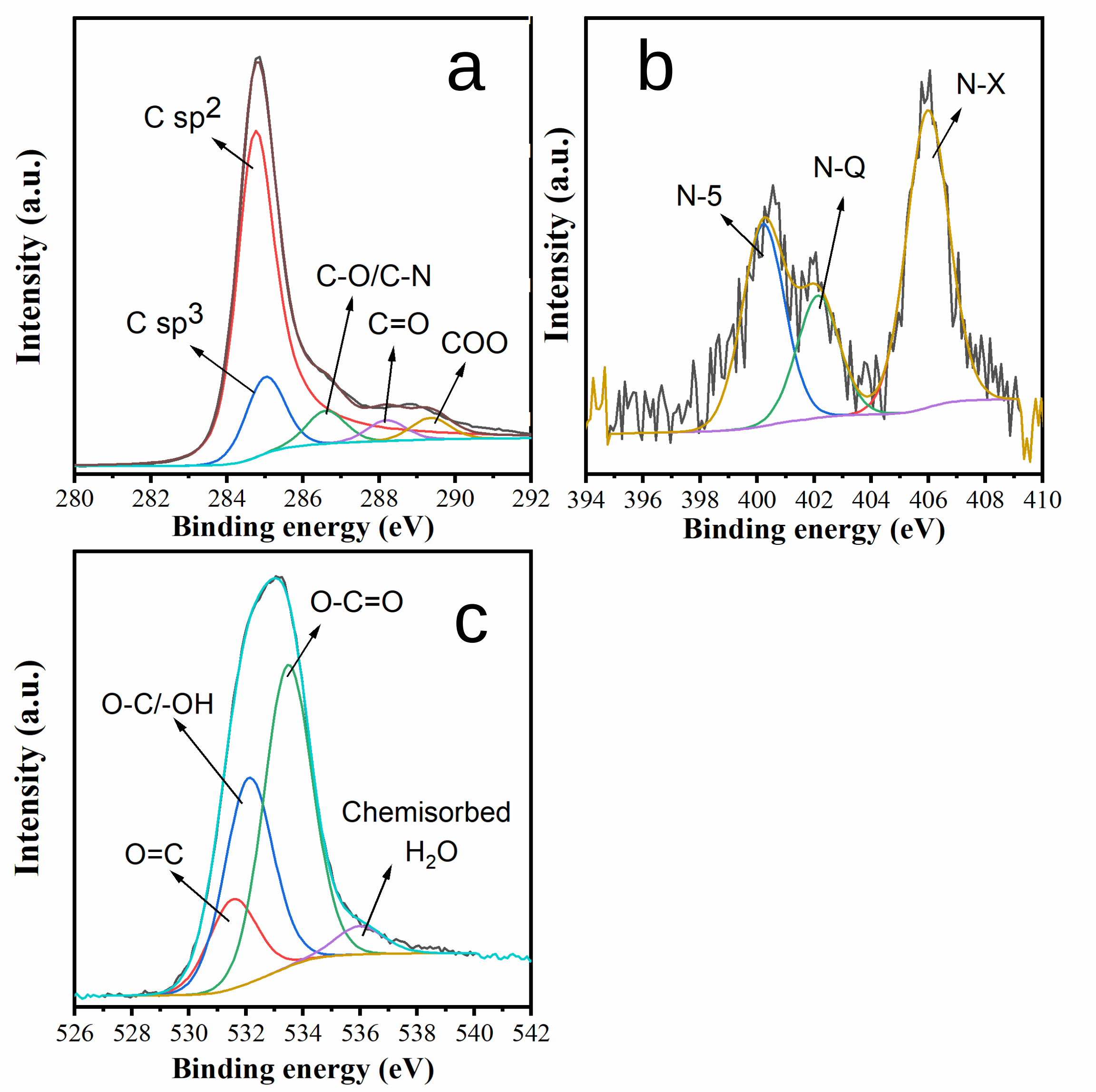

Figure 4-4 XPS spectra of (a) C 1s, (b) N 1s and (c) O 1s of AC CO_2/800-1-HNO_3

Treatment of CO_2/800-1 with K_2CO_3 resulted in a small decrease in the surface oxygen from 8.3 to 7.1 at% with increased proportions C-O/C-OH and O-C=O but decreased proportion of C=O. The titration results discussed later show that the surface has an increased acidic character consistent with the increased O-C=O. The TPD results also showed CO_2 evolution starting at 550°C, which was not present in the precursor starting material CO_2/800-1 and this is consistent with the incorporation of lactone groups in the carbon structure.

Table 4-3 Oxygen functional analysis from X-ray photoelectron spectroscopy

Carbon sample	**Components from O 1s profile (at%)**			
	C-O/OH	**C=O**	**COOH**	**Chemisorbed H_2O**
N_2/600-1	3.0 ± 0.2	2.6 ± 0.2	3.3 ± 0.1	0.3 ± 0.1
N_2/600-3	3.2 ± 0.3	2.8 ± 0.2	3.0 ± 0.1	0.3 ± 0.1
N_2/700-1	3.0 ± 0.2	3.2 ± 0.2	1.7 ± 0.1	0.3 ± 0.1
N_2/800-1	2.5 ± 0.2	3.2 ± 0.2	2.0 ± 0.1	0.4 ± 0.1
N_2/800-3	3.1 ± 0.3	3.3 ± 0.2	1.7 ± 0.1	0.3 ± 0.1
N_2/1000-1	3.0 ± 0.2	3.2 ± 0.2	1.9 ± 0.1	0.3 ± 0.1
CO_2/700-1	2.9 ± 0.2	3.0 ± 0.2	2.2 ± 0.1	0.3 ± 0.1
CO_2/700-3	2.2 ± 0.2	2.9 ± 0.2	1.5 ± 0.1	0.3 ± 0.1
CO_2/800-1	2.5 ± 0.2	2.9 ± 0.2	2.7 ± 0.1	0.3 ± 0.1
CO_2/800-3	2.1 ± 0.2	3.1 ± 0.2	2.3 ± 0.1	0.3 ± 0.1
CO_2/1000-1	3.2 ± 0.3	4.0 ± 0.2	1.5 ± 0.1	0.3 ± 0.1
CO_2/800-1-K_2CO_3	3.1 ± 0.1	0.8 ± 0.1	2.7 ± 0.1	0.5 ± 0.1
CO_2/800-1-HNO_3	4.3 ± 0.3	2.0 ± 0.2	6.6 ± 0.1	0.6 ± 0.1
CO_2/800-1-HNO_3/400	2.9 ± 0.2	1.2 ± 0.1	3.8 ± 0.1	0.5 ± 0.1
CO_2/800-1-HNO_3/800	1.5 ± 0.1	0.4 ± 0.1	0.8 ± 0.1	0.2 ± 0.1
N_2/800-1-NH_3/600	1.6 ± 0.1	0.3 ± 0.1	0.7 ± 0.1	0.1 ± 0.1
N_2/800-1-NH_3/800	0.5 ± 0.1	0.8 ± 0.1	0.4 ± 0.1	0.1 ± 0.1

NH_3 treatment increased nitrogen content, and simultaneously reduced the surface oxygen content sharply from 8.1 at% for the precursor (biochar N_2/800-1) to 2.7 and 1.8 at% for N_2/800-1-NH_3/600 and N_2/800-1-NH_3/800, respectively (Table 4-2). The O 1s spectra showed that a temperature of 600°C markedly reduced C=O while temperature of 800°C was required to remove most of the C-O/O-H (Table 4-3).

XPS N 1s spectra was deconvoluted into four components: pyridinic (N-6, 398.7 ± 0.3 eV), pyrrolic (N-5, 400.3 eV ± 0.3 eV), quaternary (N-Q, 401.4 ± 0.3 eV), and pyridinic N-oxides and unknown nitrogen (N-X, 405.5 ± 2.5 eV) (Pels *et al.* 1995, Chen *et al.* 2018). The nitrogen content of AC N_2/800-1-NH_3/800 was higher than N_2/800-1-NH_3/600, with 4.9 at% compared to 2.6 at%, and pyridinic and pyrrolic groups were two dominant forms of nitrogen with similar N-6/N-5 ratios (~2:1) (Table 4-4). Although XPS did not reveal much difference in the oxygen surface chemistry of N_2 biochar series in the temperature range 600-1000°C, NH_3 treatment at high temperatures incorporated a mixture of pyridinic, pyrrolic, quaternary and N-oxide groups, which changed the surface properties. The XPS N 1s spectrum of CO_2/800-1-HNO_3 (total N content 0.8%) in Figure 4-4 shows that the main nitrogen species present was N-X (N-oxide species) with smaller amounts of N-5 and N-Q functional groups. This contrasts with N_2/800-1-NH_3/800 and N_2/800-1-NH_3/600 where pyridinic (N-6) was the main nitrogen functional group (Table 4-4 and Figure 4-5).

Table 4-4 XPS N 1s profiles of nitrogen functional groups of N_2/800-1-NH_3/600 and N_2/800-1-NH_3/800

Carbon sample	**Content of each N component (at%)**				
	N-6	**N-5**	**N-Q**	**N-X**	**Total N content**
N_2/800-1-NH_3/600	1.4	0.7	0.3	0.2	2.6 ± 0.3
N_2/800-1-NH_3/800	2.6	1.4	0.6	0.3	4.9 ± 0.2

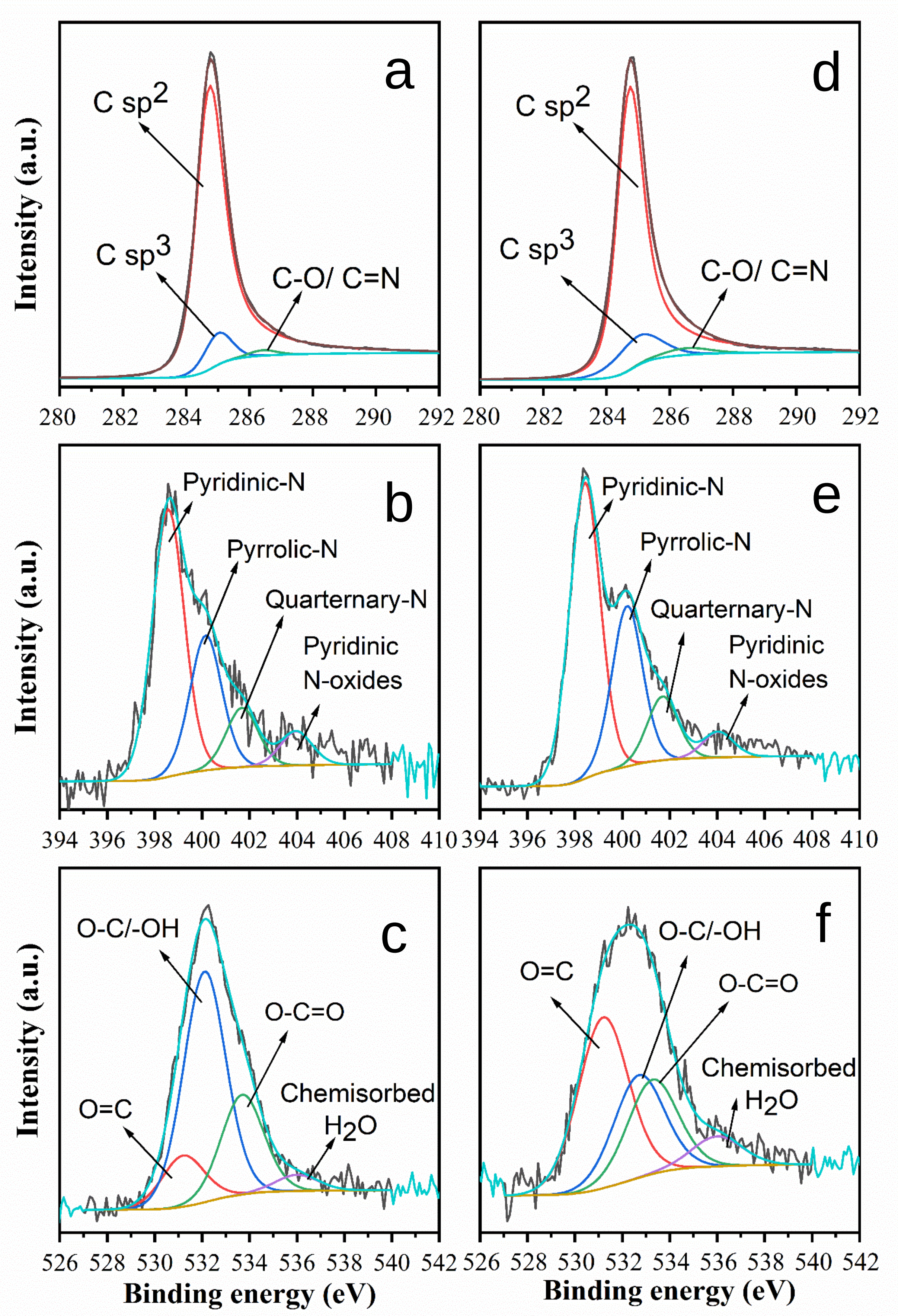

Figure 4-5 X-ray photoelectron spectroscopy of (a) C 1s, (b) N 1s and (c) O 1s of biochar N_2/800-1-NH_3/600, and (d) C 1s, (e) N 1s and (f) O 1s of N_2/800-1-NH_3/800

4.2.2 Total elemental CHNO analysis

Total elemental CHNO analysis reveals the total composition of each walnut shell-derived carbon sample, which is different from XPS result. From Table 4-5, oxygen contents of walnut shell-derived carbon activated in CO_2 were generally higher than biochar pyrolysed under N_2 atmosphere. Oxygen contents in N_2-biochar series increased slightly from 6.69 wt% (N_2/600-1) to 9.19 wt% (N_2/800-1) but reduced significantly to 3.64 wt% (N_2/1000-1). On the other hand, oxygen contents in CO_2-activated carbon series reduced from 10.28 wt% to 7.54 wt% with increasing temperature from 700 to 800°C, but increasing significantly to 14.14 wt% at 1000°C. This could be due to the incorporation of CO_2 into AC at high temperature and changed oxygen contents subsequently (Park *et al.* 2015, Lee *et al.* 2017). However, the difference of oxygen contents in total CHNO analysis was not reflected in XPS data (Table 4-2 and Table 4-3), indicating that pyrolysis/gasification mainly influenced total oxygen contents rather the surface content of walnut shell-derived carbons. In all biochar/AC, hydrogen only accounted for only 0.36-2.22 wt% and nitrogen only accounted for 0.29-0.47 wt%. Low total nitrogen contents in biochar/AC (0.29-0.44 wt%) showed that nitrogen did not present in the surface of biochar/AC which coincides with XPS result (Table 4-2).

Table 4-5 Total elemental CHNO analysis

Carbon sample	**Elemental content (wt%, dry ash free)**			
	C	**H**	**N**	**O**
N_2/600-1	90.80 ± 0.77	2.22 ± 0.06	0.29 ± 0.02	6.69 ± 0.41
N_2/800-1	88.86 ± 0.32	1.63 ± 0.05	0.32 ± 0.02	9.19 ± 0.24
N_2/1000-1	95.53 ± 0.14	0.36 ± 0.03	0.47 ± 0.01	3.64 ± 0.06
CO_2/700-1	87.48 ± 0.44	1.90 ± 0.04	0.34 ± 0.01	10.28 ± 0.39
CO_2/800-1	90.52 ± 0.21	1.63 ± 0.09	0.31 ± 0.01	7.54 ± 0.12
CO_2/1000-1	83.57 ± 0.27	1.85 ± 0.11	0.44 ± 0.01	14.14 ± 0.15
CO_2/800-1-K_2CO_3	86.82 ± 0.32	1.49 ± 0.10	0.53 ± 0.02	11.16 ± 0.20
CO_2/800-1-HNO_3	72.97 ± 0.25	1.88 ± 0.04	1.31 ± 0.01	23.84 ± 0.21
CO_2/800-1-HNO_3/400	85.14 ± 0.56	1.23 ± 0.15	1.20 ± 0.01	12.43 ± 0.23
CO_2/800-1-HNO_3/800	88.11 ± 0.12	1.89 ± 0.12	0.43 ± 0.01	9.57 ± 0.01
N_2/800-1-NH_3/800	83.02 ± 0.28	1.83 ± 0.01	4.76 ± 0.01	10.39 ± 0.30

Regarding AC treated in HNO_3, total oxygen content increased from 7.54 wt% in CO_2/800-1 to 23.84 wt% in CO_2/800-1-HNO_3. Further heat treatment to 400°C and 800°C continues to decrease oxygen content to 12.43 wt% and 9.57 wt% respectively. This coincides with the change in surface oxygen contents detected from XPS (Table 4-3).

NH_3 treatment increased total nitrogen content from 0.32 wt% in N_2/800-1 to 4.76 wt% in N_2/800-1-NH_3/800, and this is similar to the 4.9 at% of surface nitrogen detected in XPS. This indicates NH_3 treatment at 800°C incorporated nitrogen onto surface of AC rather than in bulk. Moreover, total oxygen content of N_2/800-1-NH_3/800 was 10.39 wt% which is similar to the total oxygen content of N_2/800-1 (9.19 wt%). XPS O 1s data showed that surface oxygen content of N_2/800-1-NH_3/800 reduced significantly to 1.8 at% (see Table 4-2). Therefore, it concluded that NH_3 heat treatment removed surface oxygen from biochar and incorporated nitrogen mainly on the surface.

4.2.3 Acid and base titrations

Walnut shell-derived carbon samples have amphoteric characteristics in aqueous solution due to the presence of various functional groups. Basic nitrogen and oxygen functional groups in the carbon structure and the π-electron system of carbon basal planes can bind protons from aqueous solution giving basic characteristics. Oxygen functional groups present in walnut shell-derived carbons have Bronsted acid characteristics. Boehm proposed that carboxylic acid groups are neutralised by $NaHCO_3$, lactone and lactol groups and carboxyl groups are neutralized by Na_2CO_3 while phenolic groups are only neutralised by NaOH (Boehm 2002). Therefore, the differences between $NaHCO_3$ and Na_2CO_3 titrations is a measure of the lactone/lactol groups while the difference between Na_2CO_3 and NaOH titrations represents phenolic groups on carbon surface. HCl neutralizes surface basic groups and the carbon basal plane π electron systems. The titration results are shown in Table 4-6. This simple acid/ base titration analysis is used to cross examine functional group data obtained from XPS, while CHNO elemental analysis cannot reveal any information regarding the composition of oxygen functional groups.

Table 4-6 Acid and base titration values for walnut shell-derived carbons (mequiv g^{-1})

Carbon sample	NaOH	Na_2CO_3	$NaHCO_3$	HCl
CO_2/700-1	0.311	0.101	0.036	0.427
CO_2/800-1	0.029	0	0	0.618
CO_2/1000-1	0	0	0	0.453
N_2/600-1	0.024	0	0	0.317
N_2/800-1	0	0	0	0.506

Carbon sample	**NaOH**	**Na_2CO_3**	**$NaHCO_3$**	**HCl**
N_2/1000-1	0	0	0	0.228
CO_2/800-1-HNO_3	1.883	1.260	0.912	0.037
CO_2/800-1-HNO_3/400	1.138	0.223	0.206	0
CO_2/800-1-HNO_3/800	0.494	0	0	0
CO_2/800-1-K_2CO_3	0.510	0.214	0.166	0.253
N_2/800-1-NH_3/800	0.287	0	0	0.541

The results obtained from acid and base titration for CO_2/800-1, CO_2/800-1-HNO_3, CO_2/800-1-HNO_3/400, and CO_2/800-1-HNO_3/800 showed that HNO_3 oxidation led to the incorporation of carboxylic, lactone/lactol and phenolic groups, which were consistent with both the XPS O 1s and C 1s data and increase in total oxygen content in CHNO analysis, and consistent with the results of coconut shell-derived AC in the studies of Jia and Thomas and Jia *et al.* (Jia and Thomas 2000, Jia *et al.* 2002). HNO_3 treatment incorporated carboxylic, lactone/lactol and phenolic groups to the coconut shell-derived AC, resulting in an increase of these oxygen functional groups contents to 2.45, 1.13 and 1.86 mequiv g^{-1}. Further heat treatment to 800°C gradually decreased the contents of these groups in coconut shell-derived AC to 0.0, 0.05 and 0.46 mequiv g^{-1}, respectively. A small amount of nitrogen (0.8 at%) was also incorporated in the carbon structure through the form of nitric-oxide groups in AC CO_2/800-1-HNO_3.

The HCl titration results showed that CO_2/800-1, N_2/800-1 and N_2/1000-1 were basic carbons. CO_2/700-1 contained mainly phenolic and lactone/lactol groups with a small amount of carboxylic groups as well as some basic groups. Moreover, the titration results of CO_2/800-1-K_2CO_3 showed K_2CO_3 treatment also introduced a range of oxygen functional groups and increased the acidity of sample compared to CO_2/800-1. This was supported by the TPD results in section 4.2.4, where CO_2 desorbed from CO_2/800-1-K_2CO_3 at 600-1000°C, confirming the incorporation of carboxylic, lactone, lactol, quinone functional groups into CO_2/800-1 through K_2CO_3 treatment as discussed later in the next section 4.2.4. The existence of these oxygen functional groups was consistent with hazelnut husk-derived AC treated with K_2CO_3 with carboxylic, lactonic and phenolic contents being 1.10, 0.65 and 0.85 mequiv g^{-1} (Imamoglu *et al.* 2016). However, analysis of the XPS O 1s and C 1s peaks of CO_2/800-1-K_2CO_3 and CO_2/800-1 did not confirm this difference (Table 4-2 and Table 4-3), XPS reveals information about surface layer rather than in bulk composition (up to 5 nm (Konno 2016)).

4.2.4 Temperature programmed desorption

Temperature programmed desorption (TPD) provides information on the thermal stability and desorption products of decomposition of surface species. This allows an insight into the surface functional groups present in carbon samples.

In general, the temperatures in which CO_2 (m/z 44), CO (m/z 28), and H_2O (m/z 18) evolved during TPD analysis increased with the increasing of HTTs of walnut shell-derived carbons. The TPD thermogravimetric profile of AC CO_2/700-1 had a higher mass loss than those of CO_2/800-1, CO_2/1000-1 and N_2/800-1 (Figure 4-6), indicating a greater extent of decomposition consistent with the lower temperature. The titration results show that CO_2/700-1 has a small amount of oxygen functional groups. From Figure 4-7, the CO_2 TPD (m/z 44) peak was observed at ~665°C with a wider temperature range (250-800°C). The corresponding TPD CO (m/z 28) profiles was observed in temperature range 600-1100°C, corresponding to decomposition of acid anhydrides, carbonyls, lactones and lactols (carboxylic group derivatives) between 600-700°C, hydroquinones/ semiquinones up to 1000°C (Zielke *et al.* 1996, Figueiredo *et al.* 1999, Turner and Thomas 1999). Ethers also decomposed into CO in the same desorption temperature of carbonyl groups (Zhuang *et al.* 1994). The initial temperature of m/z 28 CO desorption in AC CO_2/700-1 at ~690°C (peak at 795°C) compared to 770 and 820°C of N_2/800-1 and CO_2/800-1 (peak at 885 and 850°C, respectively) follows the trend expected for increasing temperature. Samples pyrolysed or activated at 800°C or above (CO_2/800-1, N_2/800-1 and CO_2/1000-1) had only a very small m/z 44 peak at 350°C due to a small amount of carboxylic groups (as seen in XPS O 1s Table 4-3) with the intensity of this peak being only one third of CO_2 desorption at 800-1000°C (Figure 4-7). The TPD profiles of H_2O (m/z 18) generally started at similar temperatures to the desorption profiles for the other species and originated from reactions of mobile surface species. Previous heat treatment studies of HNO_3 oxidised carbons showed (Jia and Thomas 2000, Jia *et al.* 2002, Xiao and Thomas 2005) that the order of thermal stability was in the order: carboxylic acid < lactone/lactol < phenolic, semiquinone, carbonyl < chromene/pyrone although temperature ranges may overlap. The desorption of CO and CO_2 from these walnut shell-derived carbon samples in similar temperatures range confirmed the presence of various oxygen functional groups as discussed in XPS and acid/base titration experiment.

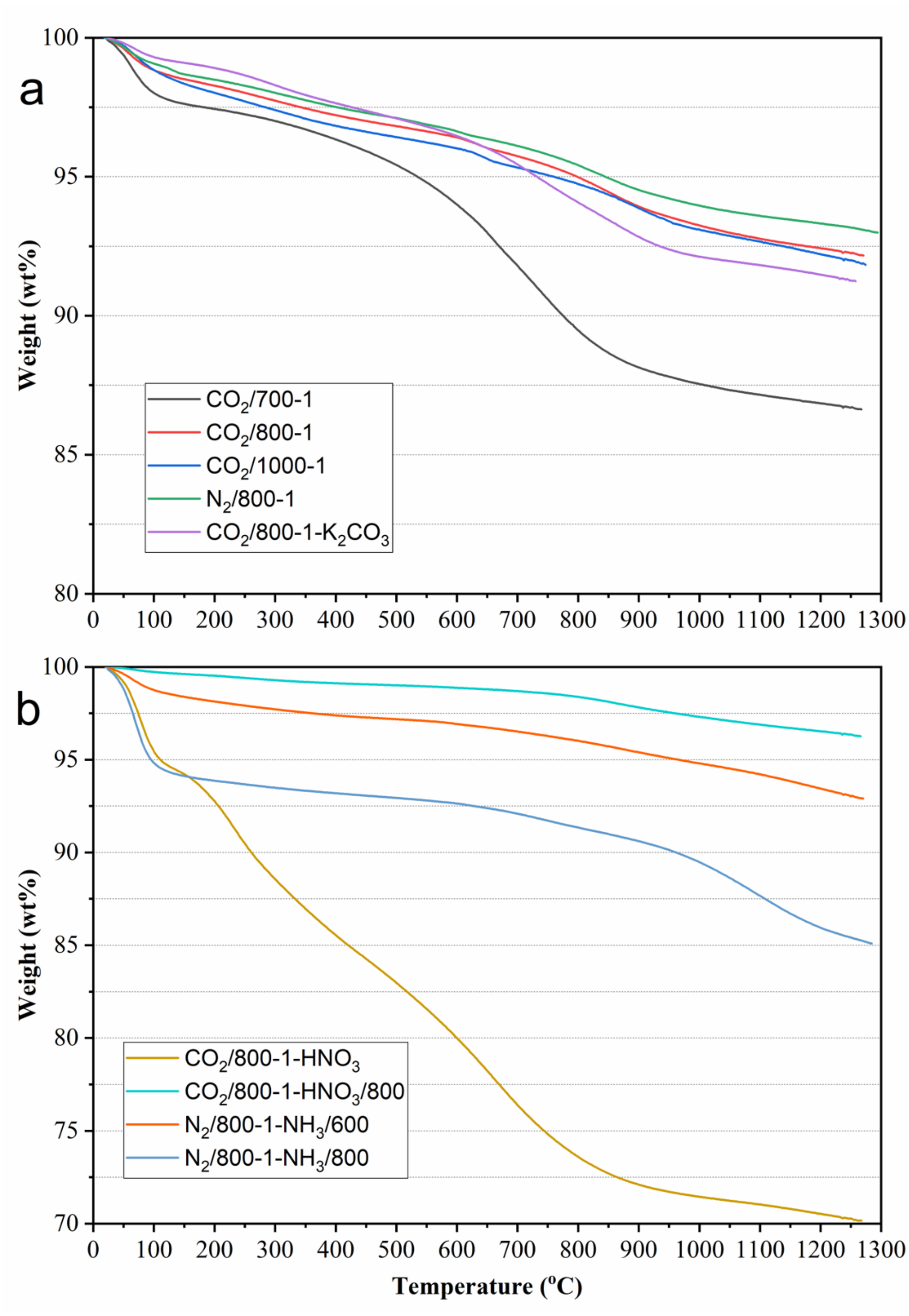

Figure 4-6 TGA profiles of (a) AC CO$_2$/700-1, CO$_2$/800-1, CO$_2$/1000-1, CO$_2$/800-1-K$_2$CO$_3$, biochar N$_2$/800-1 and (b) AC CO$_2$/800-1-HNO$_3$, CO$_2$/800-1-HNO$_3$/800, N$_2$/800-1-NH$_3$/600, N$_2$/800-1-NH$_3$/800

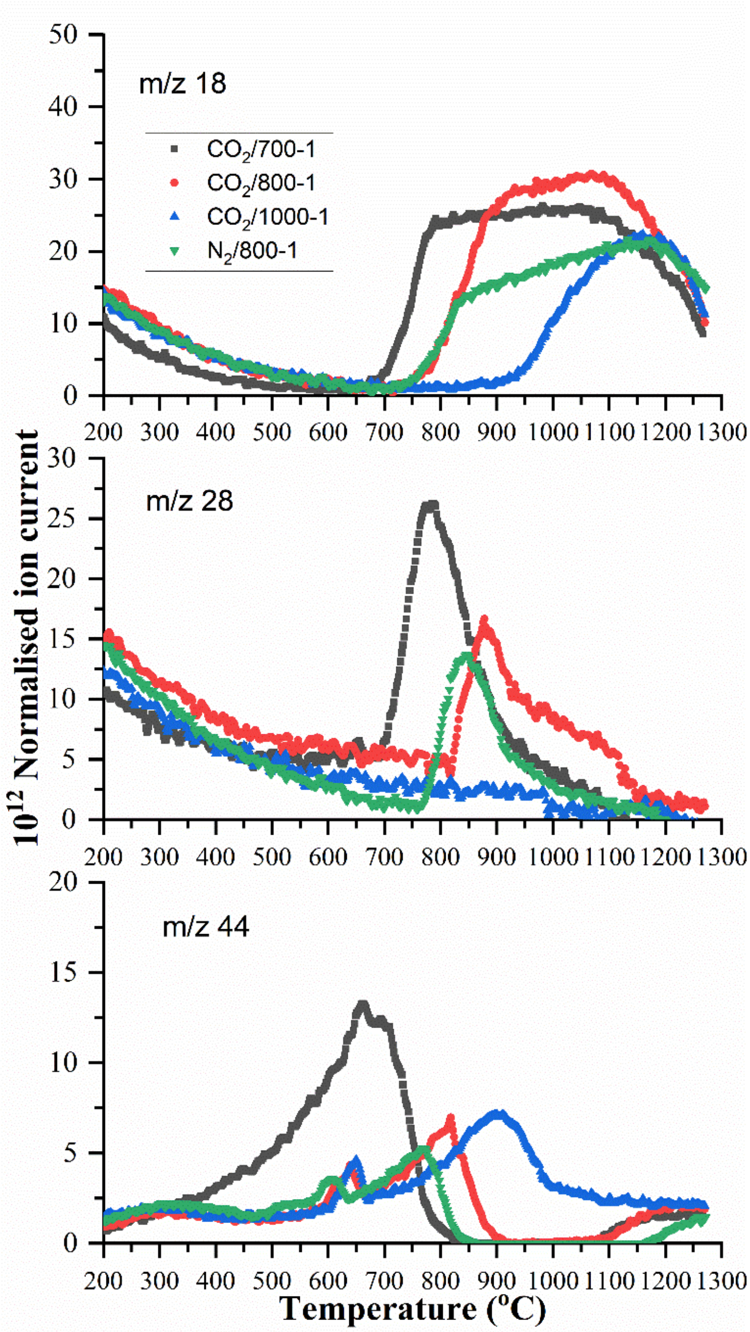

Figure 4-7 TPD profiles of AC CO_2/700-1, CO_2/800-1, CO_2/1000-1 and biochar N_2/800-1 in He at 10°C min^{-1}

The main difference in the TPD profiles of AC CO_2/800-1-K_2CO_3 from CO_2/800-1 was the bimodal CO_2 desorption peaks at 725 and 875°C (Figure 4-7 and Figure 4-8). The low temperature peak at 725°C was attributed to lactone/carbonyl while the high temperature peak at 875°C, which coincided with the start of H_2O evolution, may originate from semiquinones and reaction of surface species. Moreover, less H_2O and CO was desorbed from CO_2/800-1-K_2CO_3 during TPD compared to CO_2/800-1. Therefore, this TPD results were in good agreement with the titration results (Table 4-6).

HNO_3 treatment introduced new oxygen functional groups to AC CO_2/800-1-HNO_3 with a wide CO_2 desorption temperature range of 250-900°C (Figure 4-8). This was consistent with previous TPD studies of HNO_3 oxidized carbons (Jia and Thomas 2000, Jia *et al.* 2002, Xiao *et al.* 2005, Xiao and Thomas 2005). The low temperature CO_2 TPD peak at ~250°C coincided with the temperature where H_2O was also desorbed and consistent with the decomposition of carboxylic acid groups. The other TPD peaks represented desorption of carboxylic anhydride, lactone, carbonyls from different surface sites with increasing temperatures. Further H_2O desorption started at ~780°C. The TPD profile of NO (m/z 30) from CO_2/800-1-HNO_3 had a peak at 200°C (range 150-400°C) and this coincides with a TPD peak for m/z 28, which was attributed to N_2 desorption (Figure 4-8). The low temperature decomposition of pyridinic N-oxides was reported by Xiao *et al.* (Xiao *et al.* 2005). The emergence of pyridinic N-oxides from CO_2/800-1-HNO_3 is in agreement with the XPS as shown in Figure 4-4. Heat treatment of CO_2/800-1-HNO_3 to 800°C removed the majority of these oxygen functional groups forming AC CO_2/800-1-HNO_3/800 (see XPS data in Table 4-2 and Table 4-3). TPD profile of AC CO_2/800-1-HNO_3/800 was similar to that of CO_2/800-1, showing the effect of temperatures (Figure 4-7 and Figure 4-8).

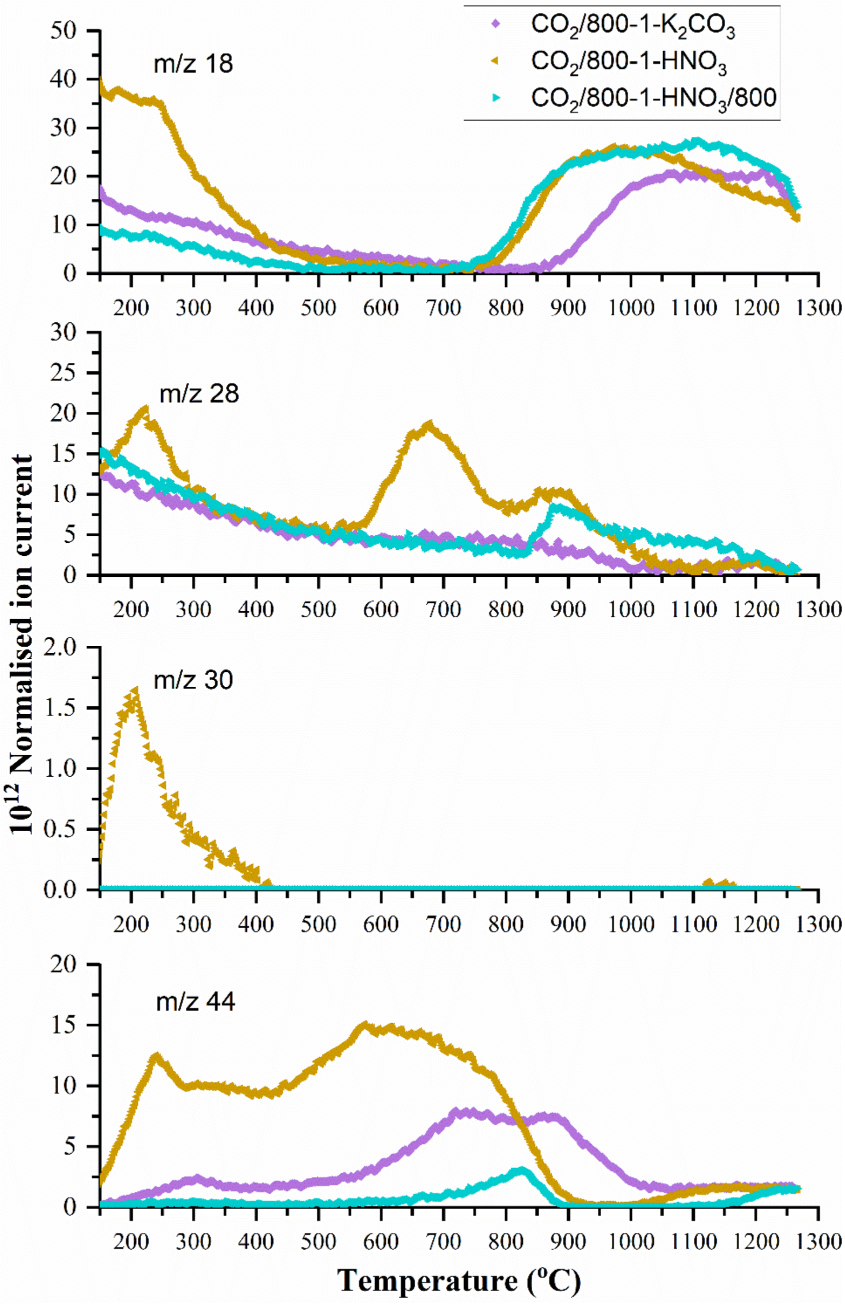

Figure 4-8 TPD profiles of K_2CO_3 treated carbon (CO_2/800-1-K_2CO_3) and HNO_3 treated carbons (CO_2/800-1-HNO_3 and CO_2/800-1-HNO_3/800) in He at 10°C min^{-1}

Comparing m/z 14 and m/z 28 TPD profiles of carbon samples N_2/800-1-NH_3/600 and N_2/800-1-NH_3/800, these two samples showed small CO desorption peaks at ~850-900°C and then released N_2 up to 1200°C as shown by the similarity in m/z 14 and 28 peaks (Figure 4-9). Nitrogen surface functional groups in carbon react on the surface to form N_2 (Xiao *et al.* 2005). There is no difference between the TPD profiles of m/z 17 and m/z 18 of these samples indicating negligible NH_3 desorption, so N_2 is the major nitrogen-contained desorption product. The thermal stability of nitrogen functional groups in carbon has been shown previously shown as pyridine N-oxide < pyrrolic-N < pyrridinic-N < quaternary-N with pyrrolic-N gradually transforming into pyrridinic-N, and subsequently into quaternary-N with increasing temperatures (Pels *et al.* 1995, Xiao *et al.* 2005). At high temperatures, mobile nitrogen surface species reacted to form N_2 through reaction: $-C(N)_m + -C(N)_{f \text{ or } m} \rightarrow N_2 + 2C_f$, in which $-C(N)_m$ is the mobile surface nitrogen functional group and $–C(N)_f$ is the fixed nitrogen functional group. Both AC N_2/800-1-NH_3/600 and N_2/800-1-NH_3/800 showed TPD peaks for m/z 30 (NO) at 550-820°C which coincided with CO_2 release (Figure 4-9). Pyridine N-oxides decomposed at lower temperatures into NO. There was no m/z 30 NO evolution from TPD profiles of biochar pyrolysed in N_2 and AC treated in CO_2 recorded, indicating that there was no pyridine N-oxides on the surface of those samples. These nitrogen-contained desorption products coincided with the nitrogen species detected in XPS (Figure 4-5 and Table 4-4) discussed previously. The agreement of results from XPS, acid/base titration and TPD confirmed the presence of various oxygen and nitrogen functional groups in walnut shell-derived carbons, which will be useful for the analysis of electrochemical behaviours of walnut shell-derived carbon samples later.

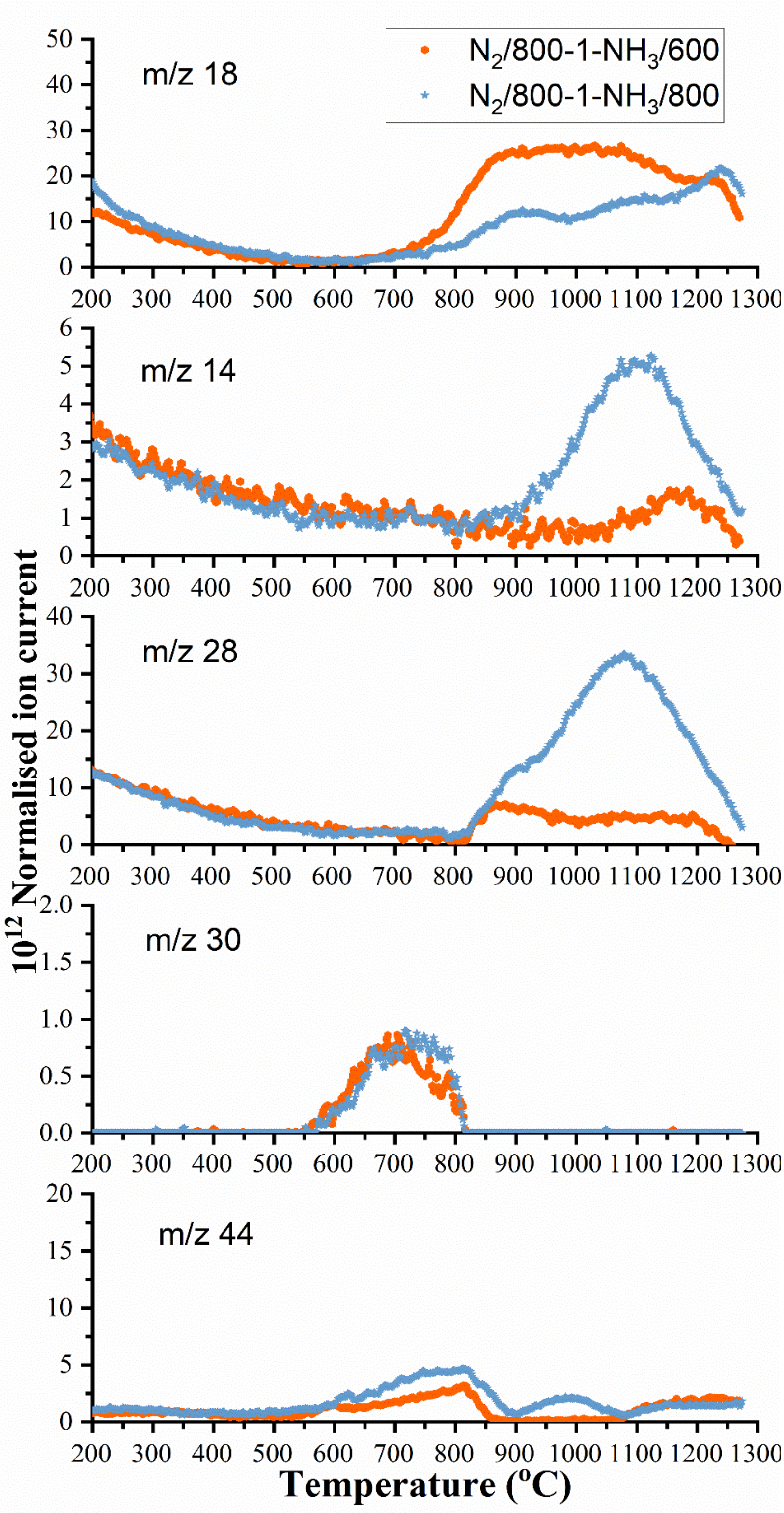

Figure 4-9 TPD profiles of NH_3 heat-treated AC N_2/800-1-NH_3/600 and N_2/800-1-NH_3/800 in He at 10°C min^{-1}

4.3 Carbonaceous structure

In Raman spectroscopy, the D peak is attributed to the breathing mode of A_{1g} in disordered carbon-ring clusters (near K-zone boundary) with more than five aromatic rings, and G peak indicates the breathing mode of E_{2g} in all C sp^2 sites (Ferrari and Robertson 2000). The small peak at ~1510 cm^{-1} (A peak) presents amorphous carbon with linking to oxygen functional groups (Tsaneva *et al.* 2014, Smith *et al.* 2016, Stein *et al.* 2017). The I_D/I_G ratio (intensity ratio between D and G peaks) is widely accepted to present the degree of ordered carbon in carbon materials (Arkhipova *et al.* 2017, Kierkowicz *et al.* 2018), while the area ratios between D and G peaks (A_D/A_G) are less commonly reported. The Raman spectra were fitted using D, G and A peaks without the need for additional peaks. In this study, no Raman spectrum of walnut shells could be recorded due to decomposition leading to structural change under laser irradiation, even at the lowest power.

Walnut shell-derived carbons show markedly increased I_D/I_G ratio with increasing temperature, either in N_2 or CO_2 atmosphere (from 0.69 in N_2/600-1 to 1.02 in N_2/1000-1 and from 0.84 in N_2/600-1 to 1.00 in CO_2/1000-1) (Table 4-7). This is because increasing temperature led to carbon structure rearrangement resulting in a higher ordered structure. Full width at half maximum of D peak (W_D) also reduced gradually with increasing temperature from 259.6 cm^{-1} in AC CO_2/700-1 to 218.3 in CO_2/1000-1, indicating the enhanced ordered structure of walnut shell-derived carbons (Table 4-7) (Johnson *et al.* 1986). Meanwhile, effects of holding time and carrier gas were negligible with I_D/I_G ratio remaining almost constant regardless of pyrolysis temperatures. Full width at half maximum of G peak (W_G), D and G peak positions are included in Table 4-7, but none of these parameters show marked changes with holding time or carrier gas. Moreover, the change in D and G peak positions fell into the resolution of instrument, so no significant conclusions regarding carbon structure could be obtained from the D and G peak positions (Cuesta *et al.* 1994).

HNO_3 oxidation of AC did not change the Raman spectra of the precursor significantly (0.92 of CO_2/800-1-HNO_3 compared to 0.91 of CO_2/800-1). Further heat treatment of AC CO_2/800-1-HNO_3, and chemical treatment with K_2CO_3 and NH_3 increased the I_D/I_G ratio slightly compared to the corresponding CO_2/800-1 and N_2/800-1 precursors.

Table 4-7 Raman spectroscopy parameters I_D/I_G (Intensity ratio between D and G peaks), A_D/A_G (Area ratio between D and G peaks), full-width at half maximum of D peak (W_D) and G peak (W_G), and D and G peak positions of walnut shell-derived carbons

Carbon sample	**I_D/I_G**	**A_D/A_G**	**W_D (cm^{-1})**	**W_G (cm^{-1})**	**D-peak position (cm^{-1})**	**G-peak position (cm^{-1})**
N_2/600-0	0.69 ± 0.01	2.67 ± 0.02	292.8 ± 1.8	75.2 ± 0.2	1354.0 ± 0.2	1594.7 ± 0.3
N_2/600-1	0.69 ± 0.02	2.71 ± 0.03	291.1 ± 1.8	74.6 ± 0.2	1352.1 ± 0.2	1595.2 ± 0.3
N_2/600-3	0.72 ± 0.01	2.73 ± 0.03	292.8 ± 1.8	75.1 ± 0.2	1349.8 ± 0.2	1596.5 ± 0.9
N_2/700-0	0.78 ± 0.01	2.73 ± 0.04	263.7 ± 1.4	75.3 ± 1.9	1339.9 ± 0.2	1596.5 ± 0.3
N_2/700-1	0.81 ± 0.01	2.79 ± 0.04	262.1 ± 1.6	74.7 ± 0.2	1339.4 ± 0.2	1597.3 ± 0.2
N_2/700-3	0.84 ± 0.03	2.82 ± 0.01	259.1 ± 1.4	79.0 ± 1.6	1338.9 ± 0.4	1595.2 ± 0.9
N_2/800-0	0.91 ± 0.04	2.93 ± 0.06	241.0 ± 3.2	77.7 ± 0.6	1337.3 ± 1.5	1597.5 ± 2.0
N_2/800-1	0.90 ± 0.02	2.83 ± 0.09	250.6 ± 5.8	79.9 ± 0.6	1341.1 ± 0.2	1596.2 ± 1.3
N_2/800-3	0.94 ± 0.02	2.88 ± 0.01	245.9 ± 5.8	79.9 ± 3.7	1343.2 ± 2.0	1598.3 ± 0.3
N_2/1000-0	0.95 ± 0.04	2.91 ± 0.06	239.2 ± 5.5	77.9 ± 0.6	1337.3 ± 3.0	1593.3 ± 0.2
N_2/1000-1	1.01 ± 0.01	2.61 ± 0.04	213.7 ± 4.9	82.6 ± 3.9	1343.5 ± 3.1	1593.3 ± 0.2
N_2/1000-3	1.02 ± 0.01	2.53 ± 0.04	207.2 ± 4.8	83.7 ± 4.0	1342.1 ± 3.1	1592.9 ± 0.2
CO_2/700-0	0.80 ± 0.01	2.78 ± 0.00	264.5 ± 1.6	77.0 ± 1.1	1337.9 ± 1.1	1594.6 ± 1.3

Carbon sample	**I_D/I_G**	**A_D/A_G**	**W_D (cm^{-1})**	**W_G (cm^{-1})**	**D-peak position (cm^{-1})**	**G-peak position (cm^{-1})**
CO_2/700-1	0.84 ± 0.01	2.91 ± 0.00	259.6 ± 6.1	79.7 ± 2.3	1340.8 ± 2.4	1595.9 ± 1.9
CO_2/700-3	0.87 ± 0.01	2.90 ± 0.01	258.1 ± 1.7	78.1 ± 1.1	1337.5 ± 0.9	1594.5 ± 0.9
CO_2/800-0	0.90 ± 0.01	2.89 ± 0.05	246.7 ± 2.8	78.9 ± 1.0	1338.4 ± 0.6	1596.3 ± 1.0
CO_2/800-1	0.91 ± 0.01	2.86 ± 0.02	239.9 ± 3.8	76.7 ± 1.9	1337.3 ± 0.8	1596.2 ± 0.8
CO_2/800-3	0.93 ± 0.01	2.90 ± 0.05	231.1 ± 3.5	74.1 ± 3.2	1336.7 ± 0.4	1597.7 ± 1.8
CO_2/1000-0	0.95 ± 0.01	2.88 ± 0.02	230.1 ± 3.6	75.9 ± 1.9	1335.4 ± 0.8	1595.7 ± 0.8
CO_2/1000-1	1.00 ± 0.01	2.70 ± 0.02	218.3 ± 3.5	80.6 ± 2.0	1339.6 ± 2.8	1594.0 ± 0.8
CO_2/800-1-HNO_3	0.92 ± 0.01	2.26 ± 0.02	220.5 ± 3.5	89.5 ± 2.2	1344.8 ± 0.8	1599.1 ± 0.8
CO_2/800-1-HNO_3/400	0.89 ± 0.02	2.49 ± 0.02	234.9 ± 3.7	84.1 ± 2.1	1345.7 ± 0.8	1598.8 ± 0.8
CO_2/800-1-HNO_3/800	0.96 ± 0.01	3.01 ± 0.02	209.8 ± 3.3	66.9 ± 1.6	1338.4 ± 0.8	1605.1 ± 0.8
CO_2/800-1-K_2CO_3	0.98 ± 0.01	2.57 ± 0.02	213.0 ± 3.4	81.2 ± 2.0	1341.4 ± 0.8	1600.0 ± 0.8
N_2/800-1-NH_3/600	0.90 ± 0.02	3.09 ± 0.04	241.7 ± 5.6	70.6 ± 0.5	1333.6 ± 0.2	1597.1 ± 1.3
N_2/800-1-NH_3/800	0.99 ± 0.02	3.19 ± 0.05	220.6 ± 5.1	68.2 ± 0.5	1337.7 ± 0.3	1602.6 ± 1.3

Powder X-ray diffraction (PXRD) profiles of these samples were typical for amorphous carbon with two broad peaks at ~22-23° and ~43° presenting for (002) and (100) carbon crystallite (Figure 4-10). Some PXRD profiles had some small peaks related to ash content ($CaCO_3$ and SiO_2) (Mori *et al.* 2009). Crystallite thickness (L_C), crystal diameter (L_a), and interlayer distance (d_{002}) are given in Table 4-8. Increasing HTTs reduced d_{002}, and L_C, and increased L_a significantly, indicating a more ordered structure, and this is in line with Raman spectroscopy results. L_a also increased with holding time (at 800°C), indicating the rearrangement of amorphous carbon at edges of carbon-nanocrystals into the basal plane (Johnson *et al.* 1986). Moreover, CO_2 gasified carbon and removed more aliphatic carbon groups. This led to the development of carbon crystallites with dewrinkling of carbon graphene sheets and higher L_a (Zhang *et al.* 2008). Chemical activation with K_2CO_3, HNO_3 and NH_3 combined with heat treatment (800°C in this study) allowed structural modification followed by the removal of volatiles and carbon structure rearrangement. This can be observed through the increase L_a of these samples. Changes in carbon structure, as shown by PXRD (decreasing d_{002}, L_c and increasing L_a with temperatures (see Table 4-8)) and Raman results (increasing I_D/I_G and decreasing W_D with increasing temperatures), may influence electrochemical performance through an increase the electrical conductivity of carbons and electron transfer.

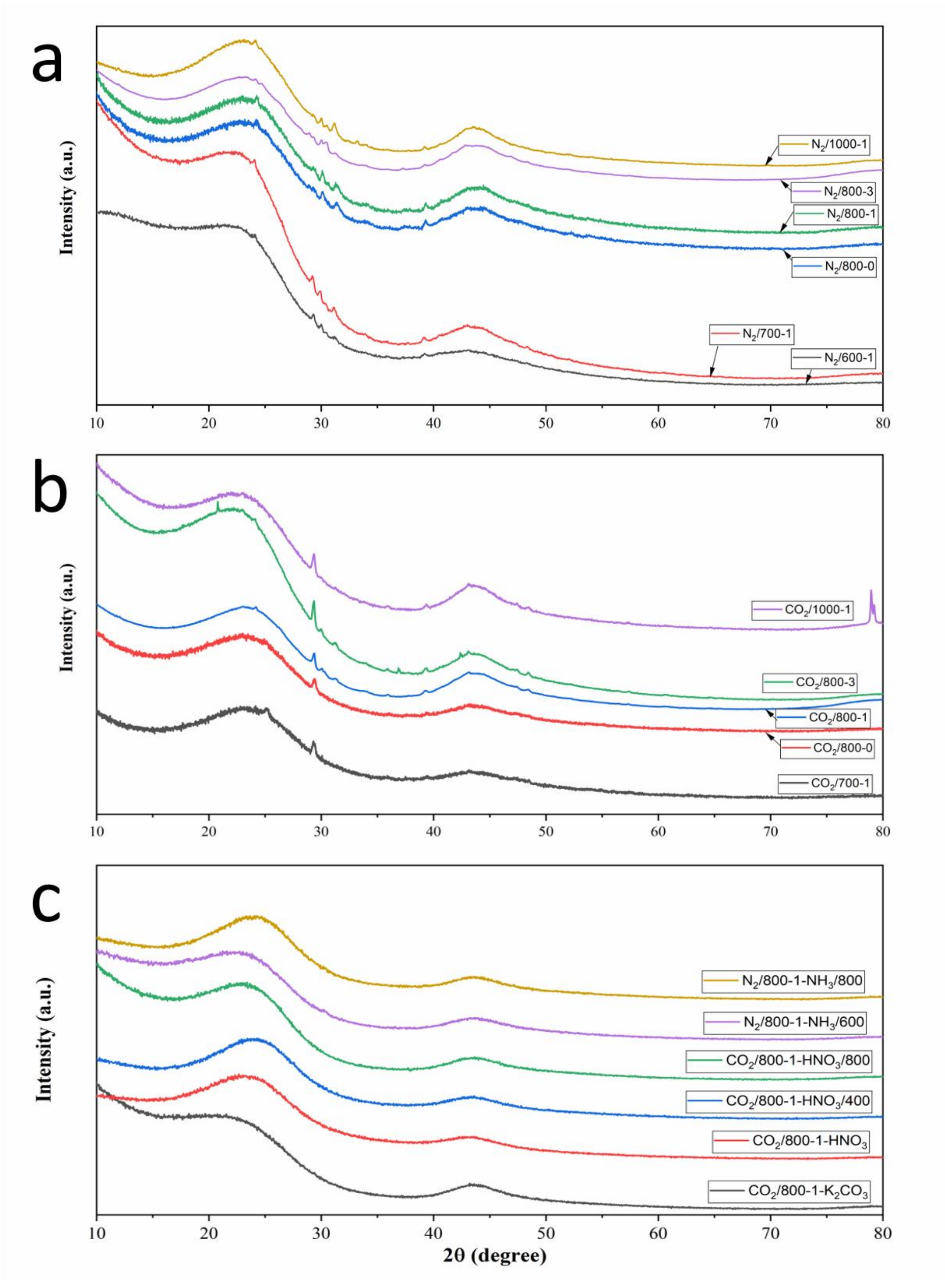

Figure 4-10 PXRD patterns of walnut shell-derived carbon (a) N_2/600-1, N_2/700-1, N_2/800-0, N_2/800-1, N_2/800-3 and N_2/1000-1, (b) CO_2/700-1, CO_2/800-0, CO_2/800-1, CO_2/800-3, CO_2/1000-1 and (c) CO_2/800-1-K_2CO_3, N_2/800-1-NH_3/600, N_2/800-1-NH_3/800, CO_2/800-1-HNO_3, CO_2/800-1-HNO_3/400, CO_2/800-1-HNO_3/800

Table 4-8 Crystallite thickness L_c, interlayer distance d_{002}, and crystal diameter L_a from XRD

Carbon sample	Crystal thickness, L_c (Å)	Interlayer distance, d_{002}, (Å)	Crystal diameter, L_a (Å)
N_2/600-1	10.75 ± 0.05	4.14 ± 0.02	18.33 ± 0.25
N_2/700-1	10.19 ± 0.05	4.008 ± 0.02	21.10 ± 0.30
N_2/800-0	10.02 ± 0.05	3.83 ± 0.02	20.09 ± 0.28
N_2/800-1	10.29 ± 0.05	3.86 ± 0.02	22.47 ± 0.31
N_2/800-3	9.98 ± 0.05	3.83 ± 0.01	23.57 ± 0.33
N_2/1000-1	9.99 ± 0.05	3.86 ± 0.02	26.85 ± 0.37
CO_2/700-1	9.54 ± 0.05	3.90 ± 0.02	19.98 ± 0.28
CO_2/800-0	9.79 ± 0.05	3.86 ± 0.02	23.52 ± 0.33
CO_2/800-1	9.91 ± 0.05	3.86 ± 0.02	23.15 ± 0.32
CO_2/800-3	9.32 ± 0.05	3.86 ± 0.02	24.31 ± 0.34
CO_2/1000-1	10.23 ± 0.05	4.04 ± 0.02	28.71 ± 0.40
CO_2/800-1-HNO_3	10.07 ± 0.05	3.92 ± 0.02	25.65 ± 0.35
CO_2/800-1-HNO_3/400	10.32 ± 0.05	3.66 ± 0.01	25.98 ± 0.36
CO_2/800-1-HNO_3/800	10.81 ± 0.05	3.80 ± 0.02	24.01 ± 0.33
CO_2/800-1-K_2CO_3	8.55 ± 0.04	4.12 ± 0.02	27.87 ± 0.39
N_2/800-1-NH_3/600	10.07 ± 0.05	4.18 ± 0.02	23.00 ± 0.32
N_2/800-1-NH_3/800	10.24 ± 0.05	3.76 ± 0.01	26.99 ± 0.37

TEM-BF and TEM-DF images of one AC sample (CO_2/800-0) are illustrated in Figure 4-11a and Figure 4-11b. TEM-DF image (Figure 4-11b) by (002) diffraction beam shows contrast from crystalline graphite appearing bright in the image. SAED pattern (Figure 4-11c) fits well with micro-graphite (hexagonal structure, a = 0.242 ± 0.005 nm, c = 0.660 ± 0.005 nm). The real distance between carbon layers is 0.33 nm as shown in Figure 4-11d. This confirms the presence of small carbon nanocrystals randomly distributed throughout the walnut shell-derived carbon.

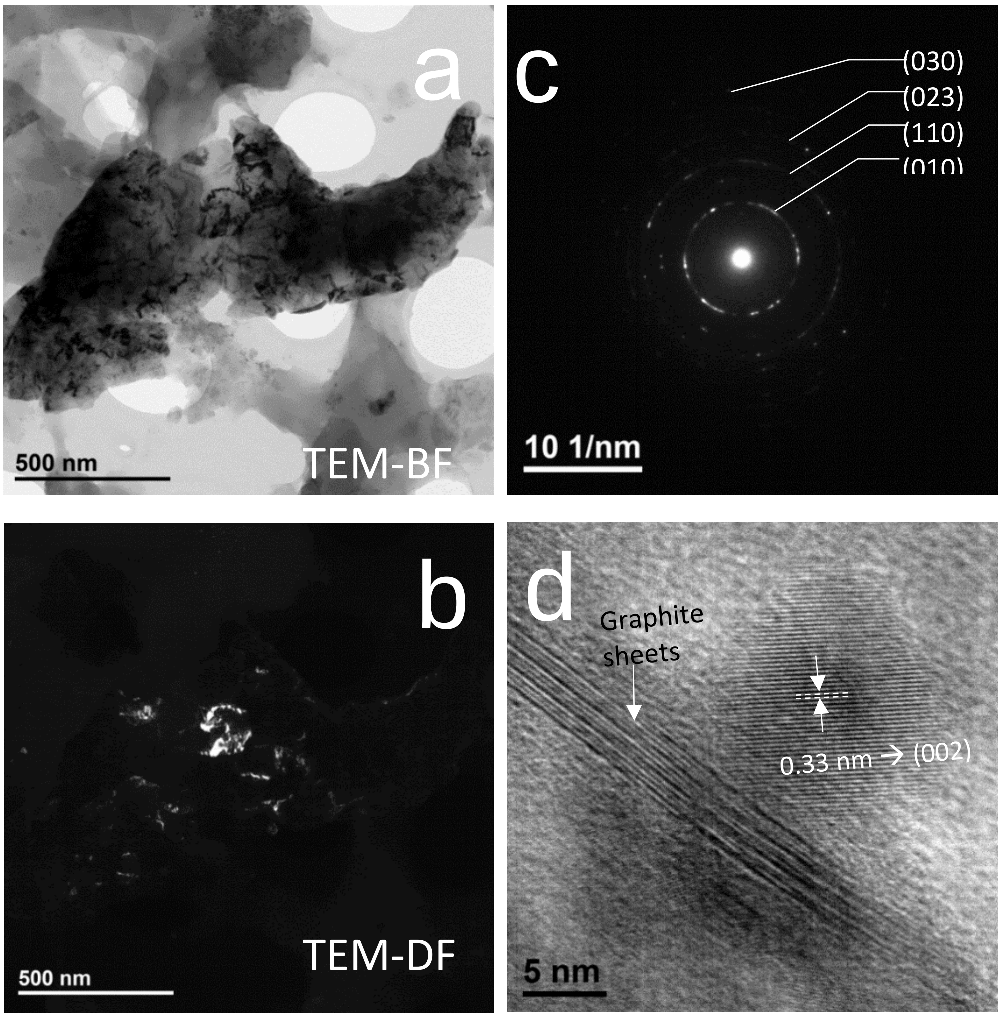

Figure 4-11 (a) TEM-BF image, (b) TEM-DF image, (c) SAED pattern and (d) HR-TEM of AC CO_2/800-0

4.4 Electrochemical behaviour

4.4.1 Cyclic voltammetry

Gas adsorption-desorption behaviour, functional groups and carbonaceous structure analysis indicate that temperature and gaseous atmosphere are the dominant factors influencing structural characteristics of walnut shell-derived carbon. Therefore, several samples at different temperatures were chosen for cyclic voltammetry (CV). In order to prepare for electrochemical experiment, walnut shell-derived carbon was mixed with polyvinylidene fluoride (PVDF) as a binder to create PVDF/walnut shell-derived carbon composites. Comparison of scanning electron microscope (SEM) images on walnut shell-derived carbon samples and PVDF/walnut shell-derived carbon composite (from Figure C-4 to Figure C-9) showed that there is no macropore structure on both the carbons and PVDF/walnut shell-derived carbon composites, and the preparation procedure did not alter the carbon structure remarkably. This also rules out any possible impact of macropores on electrochemical behaviours.

Peak currents of VO^{2+} oxidation to VO_2^+ increased with increasing pyrolysis HTT, from 0.125 A in PVDF/walnut shell-derived carbon composite CO_2/700-1 (0.72 V) to 0.155 A in CO_2/800-1 (0.75 V) and from 0.091 A (N_2/600-1 at 0.68 V) to 0.136 A (N_2/800-1 at 0.74 V). The increase in peak current of VO^{2+} oxidation may be attributed to the development of carbonaceous structure, and increasing pyrolysis temperature from 600°C to 800°C improves carbon structural order as shown by PXRD and Raman studies (Table 4-7 and Table 4-8), which supports electron transfer at electrode surfaces.

Increasing HTTs from 800°C up to 1000°C in either in a N_2 or CO_2 atmosphere, did not influence VO^{2+} oxidation, and the VO^{2+} oxidation was markedly enhanced on AC treated in CO_2 rather than biochar pyrolysed under N_2. Higher peak currents were observed for VO_2^+ reduction to VO^{2+} for electrodes used AC from activation in CO_2 rather than biochar in N_2 atmosphere (Figure 4-12), but they followed the same trend.

In terms of porosity and surface area, the CO_2 DR micropore volume range (0.226-0.235 $cm^3\ g^{-1}$) and the N_2 total pore volumes (0.254-0.380 $cm^3\ g^{-1}$) show that the porous structures of AC treated in CO_2 series do not vary greatly (Table 4-1). Comparison of BET N_2 pore volume and N_2 DR micropore volume shows that 57-81% of total pores of CO_2 series are micropore. Furthermore, as discussed in section 4.1 on adsorption kinetics of CO_2 adsorption at 0°C on N_2 biochar series, and comparison of the CO_2 and N_2 (-196°C) adsorption studies for biochar pyrolysed in N_2 series, these show that there are activated diffusion effects for N_2 adsorption at -196°C. The CO_2 DR micropore volumes for the N_2 biochar series was in the range 0.121-0.220 $cm^3\ g^{-1}$ (Table 4-1). Therefore, it appears that changes in CV with HTT > 800°C are not strongly related to porosity.

Also in this temperature range, XPS shows that surface oxygen functional groups varied over a relatively narrow range for the above samples (6.9-9.2 at%) (Table 4-2), and the oxygen surface functional groups are similar. Acid/base titration results (see Table 4-6) also did not show significant change in functional groups with both N_2 biochar series and CO_2 activated carbon series are mainly basic carbons. However, the total oxygen content of CO_2/1000-1 is significantly higher than CO_2/800-1, 4.14 wt% compared to 7.54 wt%, while oxygen content of N_2/1000-1 reduced markedly from 9.19 wt% in N_2/800-1 to 3.64 wt% (see Table 4-5). The change in TPD profiles of CO_2 activated carbon series (as discussed in section 4.2.4) also showed that there are more changes in total oxygen functional groups of walnut shell-derived carbon rather than on the surface. Therefore, it is important to look at other walnut shell-derived carbons chemically treated to explore the role of functional groups.

For V^{2+}/V^{3+} couple, the V^{2+} oxidation to V^{3+} was intensified on electrode surfaces with biochar pyrolysed in CO_2, from 0.004 A (PVDF/walnut shell-derived carbon composite CO_2/700-1) to 0.013 A (CO_2/800-1) and 0.031 A (CO_2/1000-1), but this was not observed with electrodes with biochar pyrolysed in N_2 (Figure 4-12). Furthermore, the most distinctive difference for AC treated in CO_2 compared to N_2 is the oxidation of V^{3+} to VO^{2+}. A slight peak at 0.1 V (vs MSE) indicate the conversion of V^{3+} to VO^{2+} (Figure 4-12). This phenomenon has been reported in some previous works (Ulaganathan *et al.* 2015, Maharjan *et al.* 2017, Kumar *et al.* 2018). Increasing currents at the area where no redox reaction occurs on AC treated in CO_2 also presented higher capacitance of electrodes.

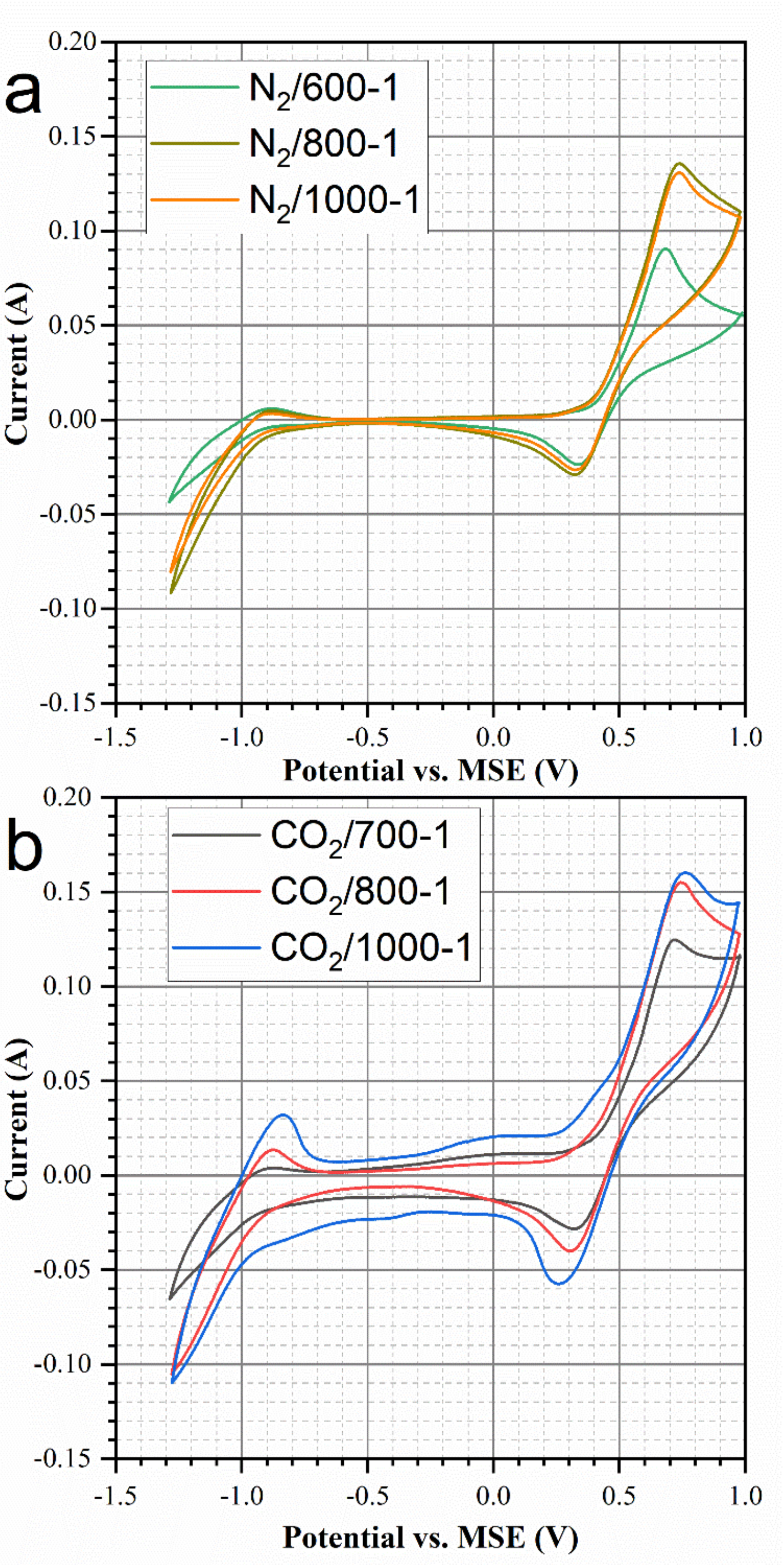

Figure 4-12 Cyclic voltammetry (CV) profiles of (a) biochar pyrolysed under N_2 (N_2/600-1, N_2/800-1, N_2/1000-1) and (b) AC treated under CO_2 (CO_2/700-1, CO_2/800-1, CO_2/1000-1)

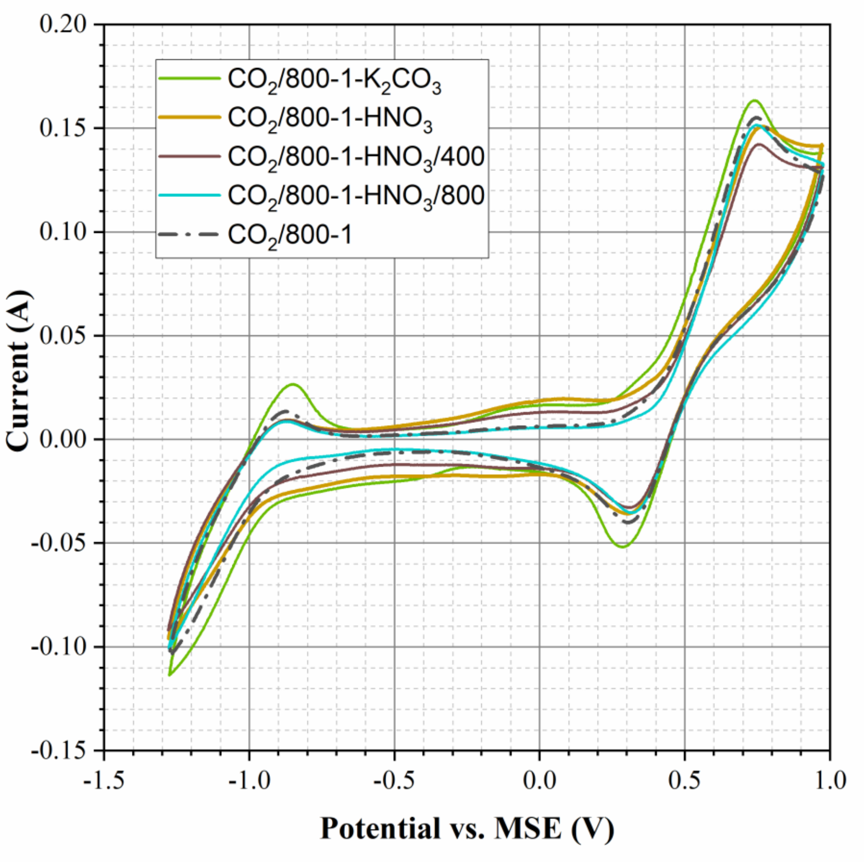

Figure 4-13 Cyclic voltammetry profiles of K_2CO_3-treated AC (CO_2/800-1-K_2CO_3) and HNO_3-treated ACs (CO_2/800-1-HNO_3, CO_2/800-1-HNO_3/400 and CO_2/800-1-HNO_3/800) in comparison to the precursor CO_2/800-1

The overall CV profiles of AC oxidised by HNO_3 (CO_2/800-1-HNO_3, CO_2/800-1-HNO_3/400 and CO_2/800-1-HNO_3/800) show some changes compared to CV of the precursor CO_2/800-1 (Figure 4-13). PVDF/walnut shell-derived carbon composite CO_2/800-1-HNO_3 showed improvement in currents in V^{2+}/V^{3+} and V^{3+}/VO^{2+} conversions. Heat treatment to 400 and subsequently 800°C reduced the currents of V^{2+}/V^{3+} and V^{3+}/VO^{2+} back to precursor CO_2/800-1. The conversion of V^{3+}/VO^{2+} couple which became pronounced in AC CO_2/800-1-HNO_3, and this effect was decreased in CO_2/800-1-HNO_3/800. Porosity of these AC samples were similar (see Table 4-1), and the HTT of 800°C of CO_2/800-1 also prevented any changes in carbonaceous amorphous structure (Table 4-7 and Table 4-8).

However, both surface and total oxygen functional groups were varied to different extents as shown in XPS O1s (Table 4-2 and Table 4-3), total oxygen contents (Table 4-5), acid/base titration (Table 4-6) and TPD results (section 4.2.4). It has been known that oxygen functional groups could enhance wettability of walnut shell-derived carbon and act as electro-catalytic sites for redox reactions to occur (Li *et al.* 2011, Taylor *et al.* 2017, Li *et al.* 2019), but the influence of oxygen functional groups was only observed for low surface area or well-defined structure carbon materials. Li *et al.* attributed the enhanced kinetics of V^{2+}/V^{3+} to C−OH groups introduced on the surface of carbon felt following thermal activation (Li *et al.* 2019). This commercial carbon felt used by Li *et al.* had a low surface area and was thermal durable, so its surface area should not change drastically even with thermal treatment, and the improved kinetics of V^{2+}/V^{3+} can be attributed to the increase of oxygen functional groups. In another study, Li *et al.* attributed the improved kinetics of vanadium redox reactions to carboxyl groups on multi-walled CNTs with its maximum surface area 362 m^2 g^{-1}, which was much lower than the surface area obtained in this study, and the structure of multi-walled nanotubes was more well-defined than biomass-derived carbons (Li *et al.* 2011). Therefore, it indicates the role of oxygen functional groups to V^{2+}/V^{3+} and V^{3+}/VO^{2+} couples.

K_2CO_3-treated AC CO_2/800-1-K_2CO_3 had better CV profile compared to CO_2/800-1 in conversion of V^{2+}/V^{3+} and V^{3+}/VO^{2+} (Figure 4-13). The K_2CO_3 treatment did not change molecular structure (Table 4-7 and Table 4-8), and increased CO_2 DR micropore volume (0.235 to 0.296 cm^3 g^{-1}) and N_2 total pore volumes (0.299 to 0.337 cm^3 g^{-1}) (Table 4-1). Treatment of CO_2/800-1 with K_2CO_3 at 800°C results in the basic functional group titration value decreasing from 0.618 mequiv g^{-1} to 0.253 mequiv g^{-1}. Titration studies show that CO_2/800-1-K_2CO_3 is amphoteric with mainly phenolic groups (Table 4-6). The NaOH titration value is ~×2 the HCl titration value. TPD shows doublet CO_2 peak at 720 and 870°C with CO_2 loss starting at ~600°C. XPS of CO_2/800-1-K_2CO_3 shows that the reaction has led to a marked decrease in the carbonyl peak and an increase in C-O/OH compared with starting material CO_2/800-1. The XPS O 1s spectrum shows that the surface groups mainly comprise of C-O/OH and O-C=O with only small contribution from C=O.

Biochar N_2/800-1 was activated in NH_3 at 600 and 800°C resulting in two AC samples with different pore structures and nitrogen contents. These changes have been discussed in sections related to gas adsorption-desorption behaviour and functional groups. Nitrogen incorporated in the carbon was shown to have a positive impact on vanadium redox reactions through simulation models (Xu *et al.* 2019). Here, the increase in nitrogen content improved the reaction kinetics of the VO_2^+ reduction to VO^{2+} and the V^{2+} oxidation to V^{3+} in N_2/800-1-NH_3/600 (Figure 4-14). S_{BET} of AC N_2/800-1-NH_3/600 decreased compared to N_2/800-1 (3 m^2 g^{-1} compared to 29 m^2 g^{-1}) with reduced V_{CO2} and no V_{micro} (Table 4-1) and no change in V^{3+}/VO^{2+} couple was detected like in CO_2-treated or HNO_3-treated AC samples. Comparison of CO_2 micropore volume and N_2 total pore volume (Table 4-1) is evident that there is activated diffusion effect in N_2/800-1-NH_3/600. This enhanced kinetics, coupling with low porous structure, is supporting evidence for the impact of nitrogen content on electro-catalytic activity of carbon electrodes. On the other hand, the kinetics of the oxidation of V^{2+} to V^{3+} and the reduction of VO_2^+ to VO^{2+} were enhanced markedly (Figure 4-14), as a result of the improved porous structure and surface nitrogen content (Table 4-1 and Table 4-4). The development of porosity also facilitates the transition of V^{3+}/VO^{2+} couple, being similar to CO_2/1000-1 sample.

These results suggested that in order to investigate the impact of heteroatom functional groups, both surface area and pore structure should be similar, otherwise the influence of pore structure could obscure the impact of functional groups. Shao *et al.* attributed the improved performance of the VO^{2+}/VO_2^+ couple (the positive side of VRFB) to the incorporation of N in the mesoporous carbon, but the BET N_2 surface areas of the NH_3-treated AC samples could have contributed significantly to their performance as it increased to 1100 $m^2\ g^{-1}$ compared to 500 $m^2\ g^{-1}$ of the untreated material (Shao *et al.* 2010).

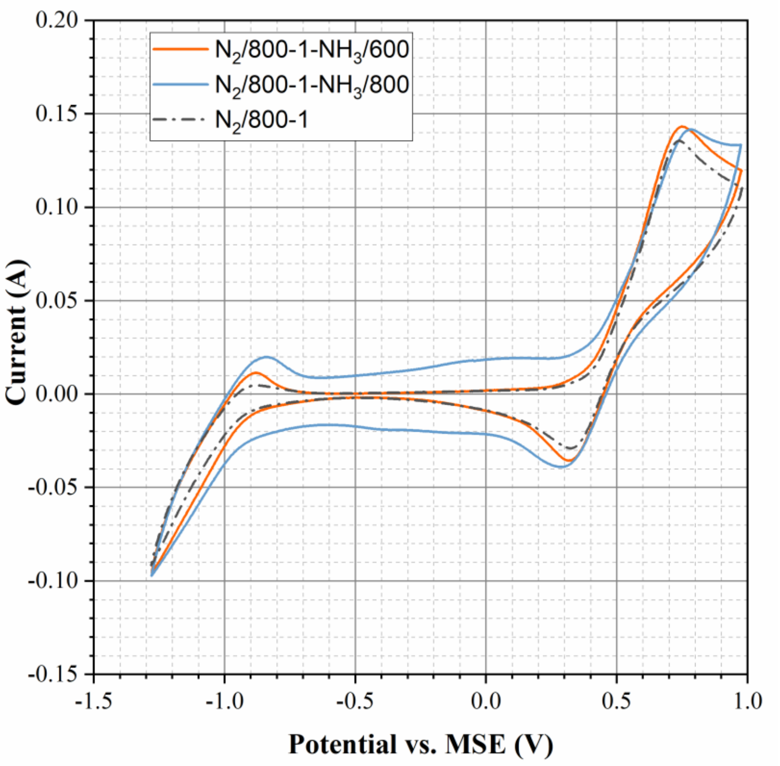

Figure 4-14 Cyclic voltammetry profiles of NH_3-treated AC samples (N_2/800-1-NH_3/600 and N_2/800-1-NH_3/800) in comparison with the precursor (N_2/800-1)

4.4.2 Electrochemical impedance spectroscopy (EIS)

EIS was conducted to further explore the impact of properties of biochar on vanadium redox couples. Figure 4-15a, b and Table C-1a, b show the variation of electrical impedance spectra for PVDF/walnut shell-derived carbon composite electrodes with biochar prepared in N_2 and AC prepared in CO_2, respectively. It is evident that both temperature and gaseous atmosphere have a marked effect on the electrical impedance spectra. The effect of temperature is similar in both N_2 and CO_2 with marked changes in the high frequency part of the spectra for 800°C. At temperatures < 800°C, walnut shell-derived carbon surface has amphoteric properties while at 800°C, walnut shell-derived carbon has virtually only basic characteristics. The basic functional groups are pyrone, chromene and ketones and the π electron systems of carbon basal planes. CO_2/800-1 (0.618 mequiv g^{-1}) has slightly more basic groups than N_2/800-1 (0.506 mequiv g^{-1}) (Table 4-6). Comparison of EIS spectra for electrodes prepared under N_2 and CO_2 atmospheres at 800 and 1000°C shows that the former is shifted to higher resistance (See Figure 4-15 a and b). Also, for both the N_2 and CO_2 series the shift in EIS profiles follows the same trend with lower resistance for walnut shell-derived carbon carbonized at 800°C. Previous studies have shown that the electrical resistance properties of high-density polyethylene/carbon black composites were modified by gasification and liquid phase chemical treatment of the carbon black (Mather and Thomas 1997).

As discussed in section 4.4.1 about the impact of carbonaceous amorphous structure, surface area and porosity of N_2 biochar series and CO_2 AC series on CV spectra, there should be limited diffusion of vanadium ions ($[VO(H_2O)_5]^{2+}$, $[VO_2(H_2O)_4]^+$ or $[VO_2(H_2O)_3]^+$) into the PVDF/walnut shell-derived carbon composite structure during EIS, and it also appears that changes in EIS with HTT are not strongly related to carbon pores and amorphous structure parameters studied.

There are possibly particle size or surface composition effects due to CO_2 gasification, which leads to different electrode properties. XPS O1s shows that there is a significant difference in the peak assigned to COOH for AC treated in CO_2 (Table 4-3). There is a peak in the EIS profile which appears as a shoulder in the low frequency, which occurs at ~15 Hz for the CO_2 carbonization series and lower (~ 2 Hz) for the corresponding N_2 series. The peak is only very weakly present in N_2/800-1. The frequency shift for the CO_2 series compared with the N_2 series is possibly due to diffusion differences in these electrodes. The electrode prepared from the low temperature biochar N_2/600-1 has a well-defined part of the semicircle in the high frequency region indicating a single time constant whereas the corresponding peaks for electrodes prepared from N_2/800-1 and N_2/1000-1 both have two weak peaks (~750 and 10,000 Hz) indicative of two time constants. The series of AC prepared in CO_2 atmosphere showed a similar trend with HTT with very weak peaks in the high frequency region for electrodes prepared from CO_2/800-1 and CO_2/1000-1. The results indicate that both HTT and gaseous atmosphere are factors which influence EIS, indicating that surface oxygen functional groups influence EIS. Carbonization results in loss of volatile species heteroatom (O, H, N) species increase in XRD parameters, L_a and L_c and Raman spectra have been shown over a large temperature range although the small temperature range 600-1000°C means that changes are close to the uncertainties in the values (Table 4-7 and Table 4-8).

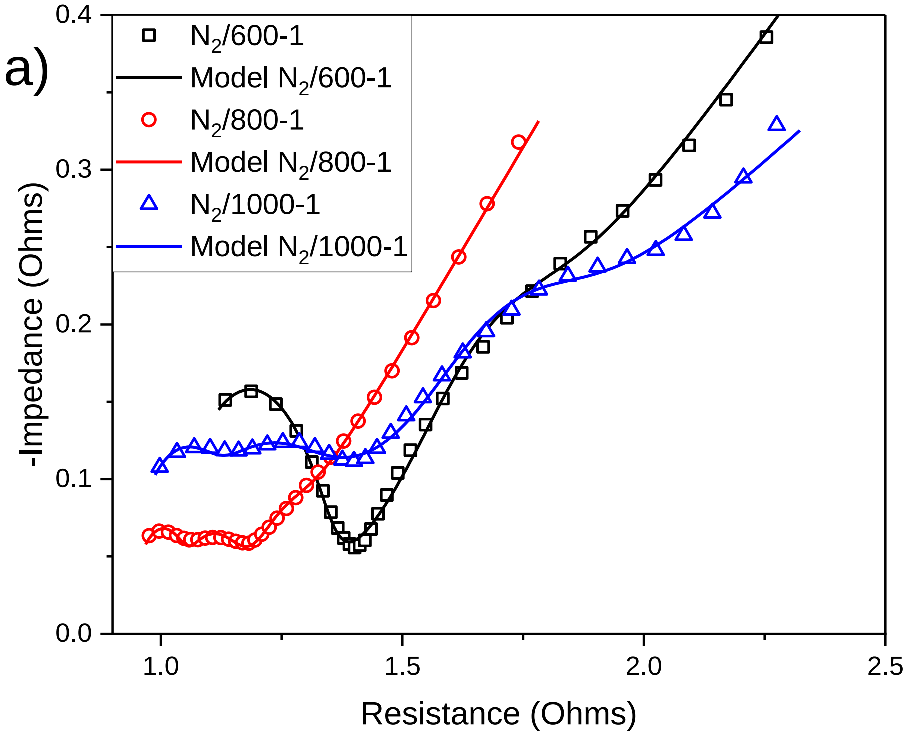

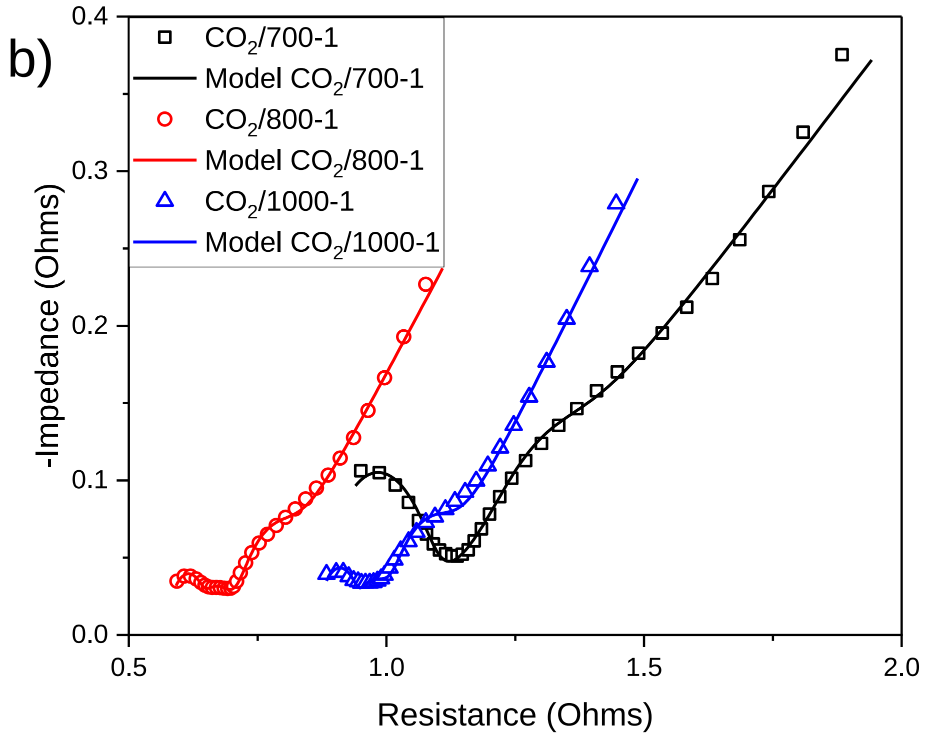
b)
CO2/700-1
Model CO2/700-1
CO2/800-1
Model CO2/800-1
CO2/1000-1
Model CO2/1000-1
-Impedance (Ohms)
Resistance (Ohms)
0.0
0.1
0.2
0.3
0.4
0.5
1.0
1.5
2.0

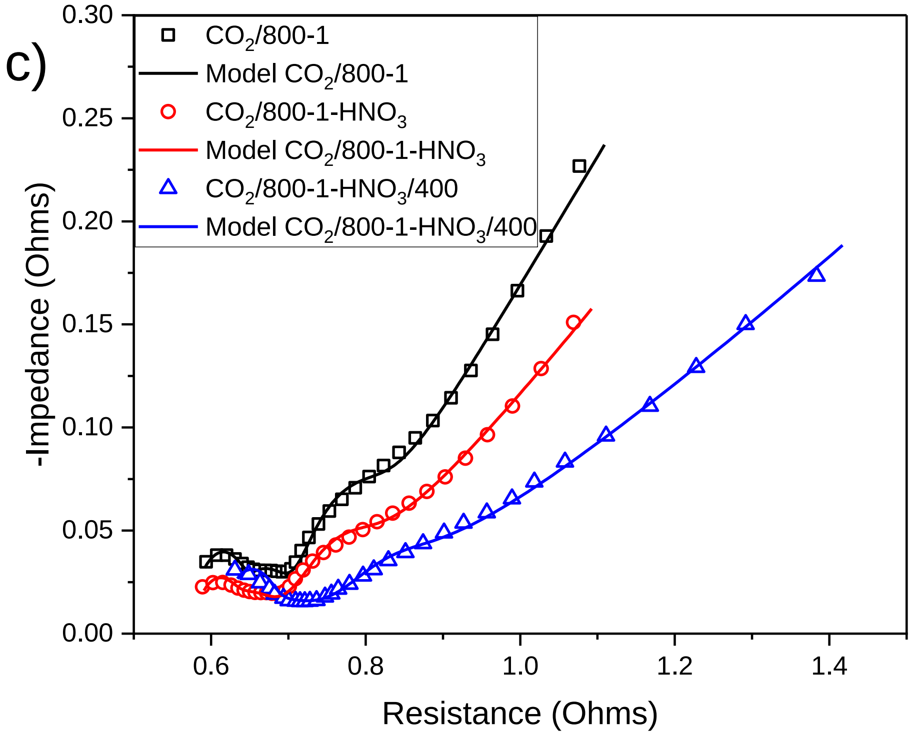
c)
CO2/800-1
Model CO2/800-1
CO2/800-1-HNO3
Model CO2/800-1-HNO3
CO2/800-1-HNO3/400
Model CO2/800-1-HNO3/400
-Impedance (Ohms)
Resistance (Ohms)
0.00
0.05
0.10
0.15
0.20
0.25
0.30
0.6
0.8
1.0
1.2
1.4

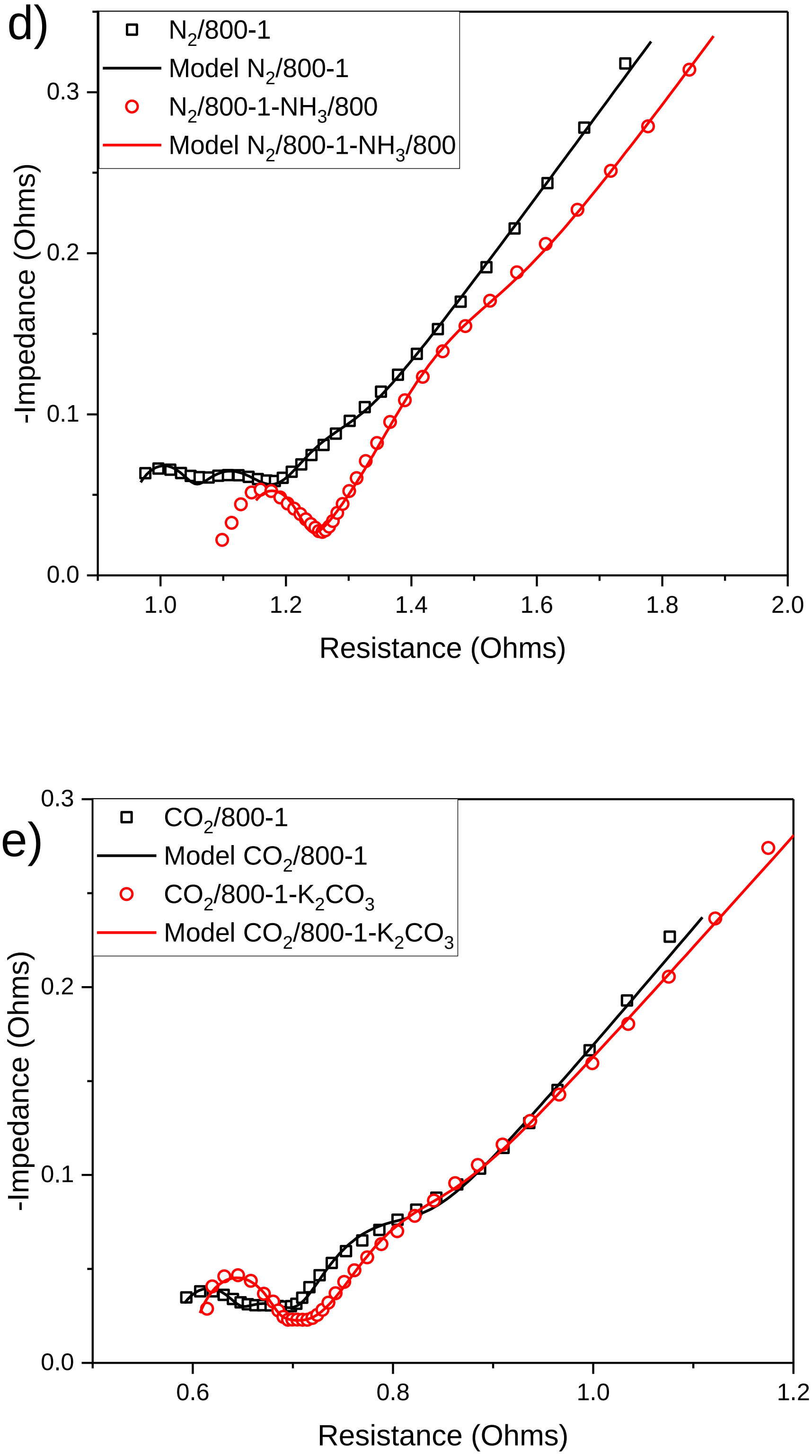

Figure 4-15 Nyquist plots for electrodes fabricated from PVDF and walnut shell-derived carbon prepared in VO^{2+}/VO_2^+ solution at various temperatures and subjected to chemical treatment procedures: a) carbonization under N_2 (600-1000°C); b) carbonization under CO_2 (700-1000°C); c) HNO_3 treatment series with further heat treatment; d) NH_3 treatment at 800°C and e) K_2CO_3 treatment at 800°C

A comparison of the electrical impedance spectra for electrodes prepared from AC CO_2/800-1, CO_2/800-1-HNO_3 and CO_2/800-1-HNO_3/400 is shown in Figure 4-15c and Table C-1c. It is apparent that chemical treatment followed by heat treatment of biochar shifts the EIS profile to higher resistance. However the low frequency (15-20 Hz) peak is present in the EIS of electrodes prepared from these carbons. The porosity (Table 4-1) and carbonaceous structures (Table 4-7 and Table 4-8) of these samples are very similar. However, there is a significant difference in surface and bulk oxygen content, the surface functional group concentrations and the amphoteric character of the surface as discussed in XPS (section 4.2.1), total elemental analysis (section 4.2.2) and acid/base titration (section 4.2.3). These differences in surface oxygen characteristics are an explanation of the differences in EIS.

Biochar N_2/800-1 was treated with NH_3 to form N_2/800-1-NH_3/800 and the EIS for the corresponding electrodes are shown in Figure 4-15d and Table C-1d. The EIS profile of the electrode prepared from N_2/800-1-NH_3/800 is shifted to higher resistance compared to the N_2/800-1 electrode. The two weak peaks present in the high frequency region of the EIS of the N_2/800-1 electrode change to a more intense single peak for the N_2/800-1-NH_3/800 electrode. This is consistent with a more homogeneous surface in NH_3 heat-treated AC. Also, the low frequency at ~2 Hz EIS peak associated with diffusion/kinetics is present as a clear shoulder. The surface composition of the NH_3 heat-treated AC is very different from the chemical analysis of the bulk sample as well as from the starting biochar N_2/800-1. The sample has a high nitrogen content, but also the surface oxygen content is very low. The nitrogen surface species are: pyridinic-N 2.4 at%, pyrrolic-N 1.4 at%, quaternary-N 0.6 at% and N-X 0.3 at% (see Table 4-4). XPS shows that the surface oxygen content is 1.8% whereas bulk oxygen from direct chemical analysis was 10.4 wt%. The porous and carbonaceous amorphous structures are very similar. Therefore, the change in EIS can be attributed to NH_3 removing most of the surface oxygen and incorporating nitrogen surface groups.

CO_2/800-1 was treated with K_2CO_3 at 800°C to form AC CO_2/800-1-K_2CO_3 and electrical impedance profiles for the electrodes prepared for these samples are shown in Figure 4-15e and Table C-1e. The changes in carbonaceous amorphous structure, porosity, and functional groups between CO_2/800-1 and CO_2/800-1-K_2CO_3 have been discussed CV section 4.4.1. It is evident that the 2 weak high frequency EIS peaks at 750 and 12,000 Hz observed for N_2/800-1 have been replaced by a single peak at 23,000 Hz in CO_2/800-1-K_2CO_3. The very weak low frequency peak mentioned earlier at 15 Hz corresponds to a shoulder ~10 Hz in CO_2/800-1-K_2CO_3. It is apparent that K_2CO_3 treatment at 800°C has a marked effect on the EIS. K_2CO_3 treatment at 800°C influences the porous structure as shown by small increases in CO_2 DR micropore volume (0.235 to 0.296 $cm^3\ g^{-1}$) and N_2 total pore volumes (0.299 to 0.337 $cm^3\ g^{-1}$) (Table 4-1). The more homogenous surface is a possible explanation of the change in the high frequency region of the EIS of CO_2/800-1-K_2CO_3 compared with CO_2/800-1.

4.5 Conclusion

The influence of the structural and chemical characteristics of sustainable walnut shell-derived carbons on vanadium redox reactions have been explored. The main aspects of carbonaceous structural characteristics considered in relation to the vanadium redox reactions were the porous and molecular structure, and surface chemistry in particular, functional groups. Two series of carbons were prepared by carbonization of walnut shell under N_2 and CO_2 atmospheres over a range of HTTs. The suites of carbons used were predominantly ultramicroporous with similar gas adsorption characteristics. The walnut shell-derived carbon samples were subjected to further treatment to incorporate functional groups. The most intense couple in the CV was VO^{2+}/VO_2^{+}, and this increased in intensity for carbonization under both N_2 and CO_2 up to 800°C, but only very small changes were observed on increase in temperature to 1000°C. The CV profiles for samples carbonized in CO_2 atmosphere gave a weak peak for the V^{2+}/V^{3+} couple which increased with increasing temperature, whereas the V^{3+}/VO^{2+} peaks were weaker but showed the same trend. The V^{3+}/VO^{2+} peaks were not observed for biochar carbonized under N_2. The oxidation of VO^{2+} to VO_2^{+} was affected by differences in molecular structure for walnut shell-derived carbon prepared under N_2 and CO_2 which was a function of heat treatment temperatures.

Carbons with a temperature of 800°C were used for functionalisation studies to avoid the effects of structural change with temperature. Oxidation of carbon (HTT 800°C) with HNO_3 resulted in the incorporation of a mixture of acidic carboxylic, lactone, lactol anhydride functional groups and in particular, the increased intensity of the V^{3+}/VO^{2+} couple was observed, but smaller intensity changes for the V^{2+}/V^{3+} and VO^{2+} /VO_2^{+} couples. This change in intensity of the V^{3+}/VO^{2+} couple is ascribed to interaction of these surface groups with $[V(H_2O)_6]^{3+}$ and $[VO(H_2O)_5]^{2+}$. When this oxidized sample was heat treated to 400°C, mainly carboxylic groups decomposed, and the intensity of the V^{3+}/VO^{2+} couple reduced. Heat treatment to 800°C removed more oxygen functional groups with both the CV and Nyquist plots being similar to the original AC indicating close to reversibility when the oxygen functional groups are decomposed. Treatment with K_2CO_3 at 800°C showed small increases in all the CV intensities of the V^{2+}/V^{3+}, V^{3+}/VO^{2+} and VO^{2+}/VO_2^{+} couples. XPS showed that this treatment procedure also incorporated carboxylic groups into the carbon structure. Gas phase NH_3 treatment resulted in the incorporation of nitrogen as pyridinic and pyrrolic groups on the surface carbon structure and increases in all three couples. The nitrogen surface groups may interact with the species in solution. Carbonization at temperatures up to 800°C give the largest increase in the VO^{2+}/VO_2^+ couple in cyclic voltammetry while functional groups increase in the V^{2+}/V^{3+} and V^{3+}/VO^{2+} couples. This is accompanied by an increase in apparent carbon crystallite size. The incorporation of acidic oxygen functional groups enhances the V^{3+}/VO^{2+} couple, and this is attributed to adsorption effects through ion exchange. Pyridinic and pyrrolic groups also enhance V^{2+}/V^{3+} and V^{3+}/VO^{2+} CV intensities.

Chapter 5

Dielectric barrier discharge cold plasma treatment of biochar and hydrochar in NH_3 environment

This chapter aims to explore the influence of operating conditions of dielectric barrier discharge cold plasma in NH_3. Through the difference in properties of biochar (the solid product obtained from pyrolysis) and hydrochar (the solid product obtained from HTC), the impact of DBD cold plasma on nitrogen and oxygen functional groups, surface area and porosity, and carbonaceous structure will be revealed. DBD cold plasma powers were varied in the range of 20-80 W, holding time in the range of 1-2 h and NH_3 flow rate in the range of 20-40 mL min^{-1}. The results show that DBD cold plasma power is a dominant factor over holding time and NH_3 gas flow rate influencing nitrogen functionalisation. Amine-N and amide-N are two main nitrogen species incorporated on surface of biochar and hydrochar during plasma treatment. Increasing DBD cold plasma power from 20 W to 80 W increase the ration of amine-N/amide-N. Compared to NH_3 heat treatment, it has been revealed that both treatments modifies surface functional groups. However, NH_3 heat treatment replaces surface oxygen with pyridinic-N, pyrrolic-N and quaternary-N whereas NH_3 DBD cold plasma retains most surface oxygen. It is recommended to use different analysis techniques such as temperature programmed desorption and FTIR to examine nitrogen functional groups besides X-ray photoelectron spectroscopy due to overlapping binding energies of amine, amide, and pyridinic-N, pyrrolic-N and quaternary-N. DBD cold plasma has negligible influence on porous structure and carbonaceous structure of both biochar and hydrochar. Amine-N and amide-N groups at amine-N/amide-N ratio of 0.91 benefits for the conversion of VO^{2+} and VO_2^+ ions, but pyridinic-N and pyrrolic-N groups are more effective than amine-N and amide-N groups in supporting the oxidation from VO^{2+} to VO_2^+. However, DBD cold plasma treated-carbon samples show higher reversibility of VO^{2+}/VO_2^+ couple due to the retainment of various oxygen functional groups.

5.1 Biomass-derived carbons as precursors for nitrogen functionalisation

Characteristics of biochar N_2/600-1, N_2/800-1 and N_2/1000-1 using for dielectric barrier discharge cold plasma and NH_3 heat treatment have been characterised in Chapter 4.

Hydrochar was prepared from hydrothermal carbonisation (HTC) at 200, 250 and 290°C for 2 h to obtain hydrochar HY200, HY250 and HY290 respectively as described in section 3.1.1.2 of Chapter 3. Powder X-ray diffraction (PXRD) pattern of walnut shells and hydrochar are illustrated in Figure 5-1. XRD of walnut shell consists of two peaks at 16° and 22° presenting for cellulose and hemicellulose in biomass respectively (Ma *et al.* 2017). The similarity between XRD patterns of HY200 and walnut shells showed that HTC treatment at 200°C did not decompose cellulose and hemicellulose in HY200. This is in line with the study of Guo *et al.* In this study, cellulose only starts to decompose after 200°C into oligomer units (containing 2-10 glucose units) due to the breakage of β-1,4-glycosidic bonds, and then monomer units (glucose), and it continues to decompose until 260°C (Donar *et al.* 2016). Therefore, cellulose remained unchanged after treated at 200°C.

On the other hand, increasing temperature of HTC to 250 and 290°C removed XRD patterns of cellulose and hemicellulose in HY250 and HY290, indicating the decomposition of cellulose and hemicellulose in walnut shell. However, XRD patterns of HY250 and HY290 only consisted of a broad peak at ~24° rather than two typical peaks at ~24° and 44° of a biomass-derived carbon (Zeng *et al.* 2015, Lim *et al.* 2017) or pyrolysed biochar in this study (Figure 5-1). This revealed that some micro graphite crystals were created under HTC process, but hydrochar remained as amorphous carbon.

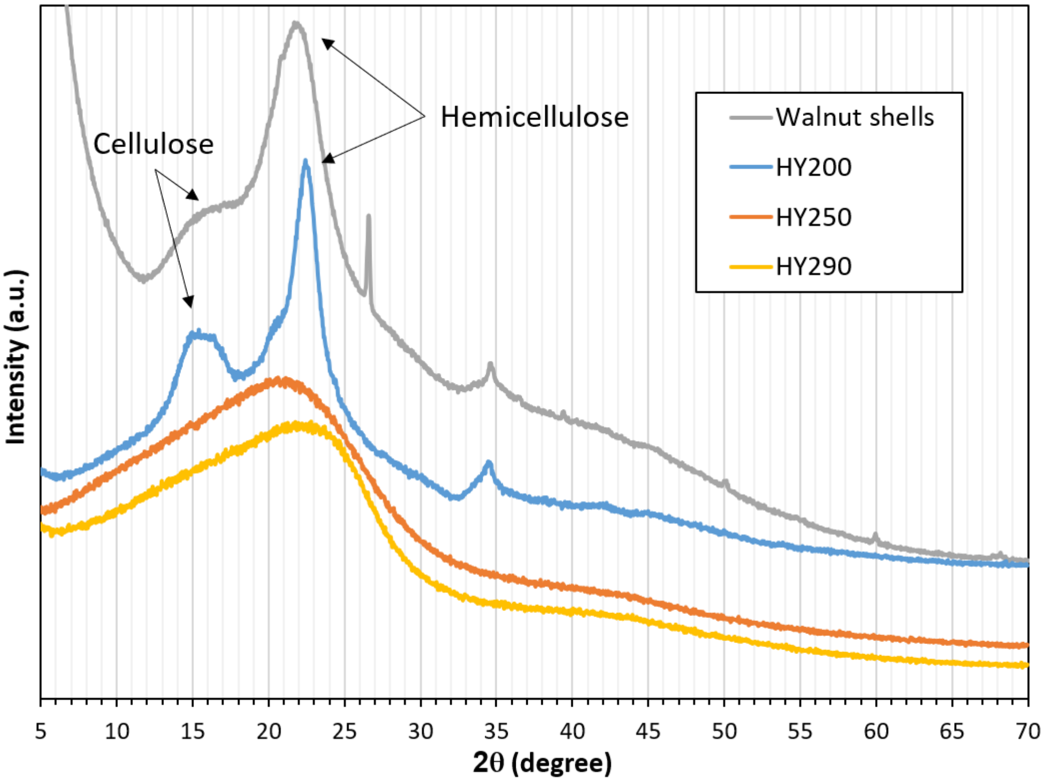

Figure 5-1 XRD patterns of hydrochar HY200, HY250 and HY290

SEM images of HY200 showed no typical spherical structures in hydrochar compared to HY250 and HY290 (Figure 5-2). During HTC, oligomer and monomer units decomposing from cellulose undergo different reactions including dehydration, fragmentation due to the cleavage of C-C bond breaking and ring open, and isomerisation to form various components such as furfural. From these intermediates, polymerisation and condensation reactions occur to form spherical structures in hydrochar. Therefore, the lack of spherical structures in HY200 also confirmed that the presence of cellulose in this hydrochar due to insufficient temperature to transform walnut shells, and higher temperatures of 250 and 290°C resulted in formation of spherical structures. Furthermore, from SEM images, HTC treatment did not permit the release of volatiles out of biomass and inhibit the formation of pore network in hydrochar compared to pyrolysis/ gasification.

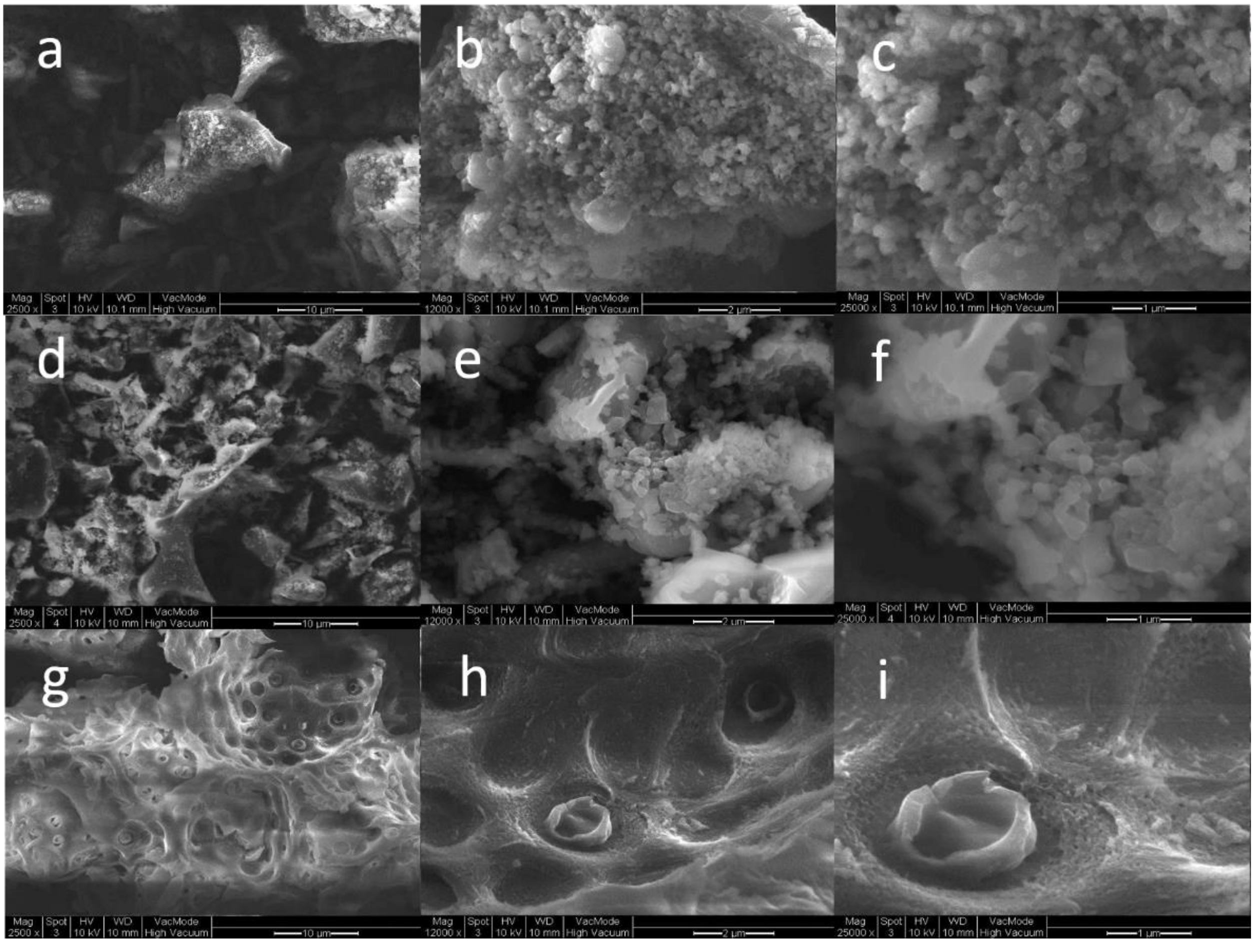

Figure 5-2 SEM images of hydrochar obtained from hydrothermal carbonisation after 2 h holding time at (a-c) 290°C (HY290), (d-f) 250°C (HY250) and (g-i) 200°C (HY200)

Functional groups of hydrochar were characterised by XPS. XPS analysis of hydrochar revealed that carbon contents of hydrochar were in the range of 82.2-84.5 at% and oxygen contents varied in the range of 15.5-17.8 at% (Table 5-1). In general, the carbon contents of hydrochar were lower than those of pyrolyzed biochar (81.6-84.3 at% compared to 88.5-90 at% - Table 5-1 and Table 4-2), but the oxygen contents were higher than those of pyrolysed biochar in this study (15.4-17.8 at% compared to 8.1-9.1 at% Table 5-1 and Table 4-2). This is because operating conditions of HTC is less severe than pyrolysis, so it reserves more oxygen functional groups in hydrochar. No other elements such as N, K, Ca and Si were found during XPS analysis of hydrochar as they were removed during HTC treatment.

Table 5-1 Elemental analysis of hydrochar from X-ray photoelectron spectroscopy

Carbon sample	**Atomic content (at%)**			
	C	**N**	**O**	**K, Ca, and Si**
HY200	82.4 ± 0.6	0.0	17.6 ± 1.1	0.0
HY250	82.2 ± 0.3	0.0	17.8 ± 0.2	0.0
HY290	84.5 ± 0.3	0.0	15.5 ± 0.1	0.0

XPS C 1s peaks of hydrochar were deconvoluted into C sp^2, C sp^3, C-O/OH, C=O and O-C=O (Table 5-2). The contents of C sp^2 and C sp^3 were only in the range of 13.3-25.0 at% and 1.9-42.4 at% respectively, and the range of C sp^2 content was much lower compared to 42.0-77.8 at% of pyrolysed biochar (Table 4-2). The remaining carbon species of hydrochar were C-O/OH, C=O and O-C=O. The high contents of oxygen functional groups confirmed by XPS is in line with the amorphous carbonaceous structure detected by XRD. XPS O 1s peaks of hydrochar revealed that most oxygen functional groups stayed in the forms of C-O/OH and COOH in all three hydrochar (Table 5-3). Most oxygen functional groups in biomass stayed in the forms of C-O/OH from cellulose and hemicellulose, so HTC might not alter these C-O linkages or convert them into COOH groups.

Table 5-2 Carbon functional groups from hydrochar from X-ray photoelectron spectroscopy

Carbon sample	**Components from C 1s profiles (at%)**				
	C sp^2	**C sp^3**	**C-O/OH**	**C=O**	**O-C=O**
HY200	19.4 ± 1.2	1.9 ± 1.3	25.0 ± 1.6	23.3 ± 1.2	12.9 ± 3.1
HY250	13.3 ± 1.5	19.5 ± 1.7	28.3 ± 2.4	16.9 ± 0.9	4.3 ± 0.1
HY290	25.0 ± 2.6	42.4 ± 2.8	13.4 ± 3.2	3.3 ± 2.0	0.7 ± 0.2

Table 5-3 Oxygen functional groups of hydrochar from X-ray photoelectron spectroscopy

Carbon sample	**Components from O 1s profile (at%)**			
	C-O/OH	**C=O**	**COOH**	**Chemisorbed H_2O**
HY200	4.5 ± 2.4	0	6.5 ± 0.8	6.6 ± 2.8
HY250	3.7 ± 0.6	0.1 ± 0.1	8.7 ± 0.1	5.3 ± 0.4
HY290	10.9 ± 0.8	3.1 ± 0.1	1.5 ± 0.8	0

FTIR profile of hydrochar showed various peaks in the region 1100-1900 cm^{-1} (Figure 5-3), indicating a wide range of oxygen functional groups and in agreement with results obtained in XPS (Table 5-2 and Table 5-3). There were C-O/OH groups in all samples. The band at 3300-3400 cm^{-1} of O-H stretching in phenolic and aliphatic (Xiao and Thomas 2005, Niu *et al.* 2017), and C-O stretching and O-H bending at ~1200 cm^{-1} (Jia and Thomas 2000, Xiao and Thomas 2005) revealed the presence of C-O/OH groups in hydrochar. Several peaks indicated the presented of C=O, O-C=O and aromatic rings in the range of 1500-1700 cm^{-1}, including C=O stretching in carboxylic acid at ~1700 cm^{-1} (Jia and Thomas 2000, Xiao and Thomas 2005), O-C=O asymmetric vibration in the range of 1550-1610 cm^{-1} (Jia and Thomas 2000), and stretching of aromatic rings conjugated with C=O (Jia and Thomas 2000, Xiao and Thomas 2005). C-H symmetric and asymmetric peaks at 2842 and 2933 cm^{-1} presented in all hydrochar samples (Jia and Thomas 2000, Nagel *et al.* 2019). The intensity of –C–O stretching and O–CH_3 vibration for lignin in hydrochar at 960-1060 cm^{-1} decreased with increasing temperature from 200 to 290°C, indicating the decomposition of lignin during HTC (Meng and Wang 2020). A small peak of aliphatic –CH_2 at 1420–1448 cm^{-1} only observed for HY200, while the peak for aromatic C-H at 748–876 cm^{-1} were shown in FTIR spectra of HY250 and HY290 (Liu *et al.* 2020). Therefore, FTIR profiles of hydrochar showed various oxygen functional groups with considerable content of aliphatic carbon and a small amount of C sp^2. This is in line with XPS analysis of these hydrochar samples (Table 5-3).

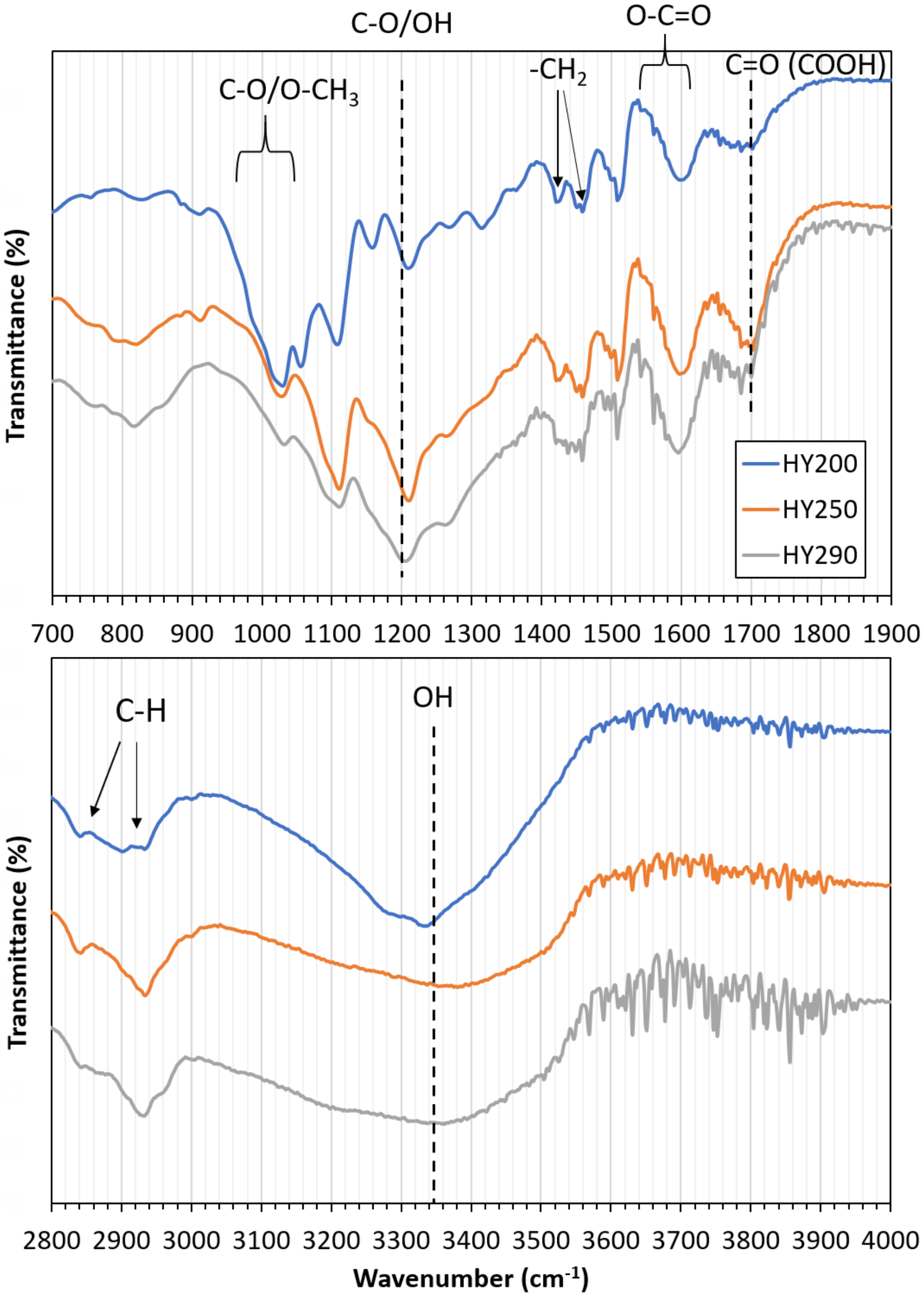

Figure 5-3 FTIR spectra of hydrochar obtained from hydrothermal carbonisation after 2 h holding time at 200°C (HY200), 250°C (HY250) and 290°C (HY290)

5.2 Functionalisation of biochar

Thermal treatment of biochar in NH_3 is commonly used to incorporate nitrogen species into carbon materials. However, it is energy-intensive due to high temperatures required (> 600°C). Dielectric barrier discharge (DBD) cold plasma, on the other hand, does not require high temperature for dissociation of NH_3 molecules. In DBD cold plasma, an external applied electric field is applied between two electrodes to ionise neutral particles. Temperatures of electrons are considerably much higher than temperatures of ions and neutral particles in gas atmosphere. The excitation and vibrational energy from electrons can be transferred into ions and electrons such as ionization, electron attachment, and excitation. Fundamental details of DBD cold plasma have been described in section 2.4.1.3. DBD cold plasma allows the operation at atmospheric pressure and ambient temperatures without requiring heat resistance materials and furnace as in thermal treatment in NH_3. Therefore, DBD cold plasma could be a potential replacement of heat treatment in NH_3. However, the mechanism of incorporating nitrogen into biochar in NH_3 atmosphere using DBD cold plasma has not been fully understood. Therefore, the next two sections 5.2 and 5.3 aim to explore the incorporating mechanism of nitrogen into biochar and hydrochar using DBD cold plasma.

5.2.1 Total elemental CHNO analysis

Total CHNO contents of functionalised biochar are presented in Table 5-4. While total nitrogen contents of DBD cold plasma-treated biochar N_2/800-1-H20W2, N_2/800-1-H40W2 and N_2/800-1-H80W2 increased slightly from 0.32 wt% (N_2/800-1) to 1.06-1.65 wt%, total oxygen contents reduced significantly from 9.19 wt% (N_2/800-1) to 3.02-4.67 wt% (Table 5-4). Moreover, total carbon contents increased slightly from 88.86 wt% (N_2/800-1) to 92.46-95.01 wt%. The increase of total nitrogen content of DBD cold plasma-treated biochar were lower than surface nitrogen content detected in XPS, which is discussed in section 5.2.2. Therefore, DBD cold plasma treatment altered the surface composition of biochar rather than total elemental composition. To the best of my knowledge, most studies on plasma-treated carbon materials only focused on surface elemental content without reporting total CHNO elemental contents. Therefore, it is difficult to compare elemental CHNO contents of DBD cold plasma-treated biochar with other studies.

The elemental compositions of DBD cold plasma-treated biochar are also different from elemental contents of NH_3 heat-treated AC N_2/800-1-NH_3/800 (Table 5-4). Total oxygen content of N_2/800-1-NH_3/800 was preserved after NH_3 heat treatment (10.39 wt% compared to 9.19 wt%), and nitrogen content increased remarkably to 4.76 wt% as an expense of carbon content. Table 5-4 also shows that nitrogen contents of NH_3 heat-treated AC decreased from 8.28 wt% to 2.70 wt% with increasing pyrolysis temperatures from 600 to 1000°C. This is due to higher ordered carbonaceous structure of N_2/1000-1 compared to N_2/800-1 and N_2/600-1 (XRD and Raman spectroscopy data from Table 4-7 and Table 4-8).

Table 5-4 Total elemental CHNO analysis

Carbon sample	**Elemental content (wt%, dry ash free)**			
	C	**H**	**N**	**O**
N_2/800-1	88.86 ± 0.32	1.63 ± 0.05	0.32 ± 0.02	9.19 ± 0.24
N_2/800-1-H20W2	94.42 ± 0.16	0.92 ± 0.01	1.39 ± 0.04	3.27 ± 0.12
N_2/800-1-H40W2	92.46 ± 0.18	1.22 ± 0.03	1.65 ± 0.06	4.67 ± 0.09
N_2/800-1-H80W2	95.01 ± 0.20	0.91 ± 0.02	1.06 ± 0.04	3.02 ± 0.14
N_2/800-1-NH_3/800	83.02 ± 0.28	1.83 ± 0.01	4.76 ± 0.01	10.39 ± 0.30
N_2/600-1	90.80 ± 0.77	2.22 ± 0.06	0.29 ± 0.02	6.69 ± 0.41
N_2/600-1-NH_3/800	84.24 ± 0.45	0.87 ± 0.12	8.28 ± 0.07	6.61 ± 0.40
N_2/1000-1	95.53 ± 0.14	0.36 ± 0.03	0.47 ± 0.01	3.64 ± 0.06
N_2/1000-1-NH_3/800	93.12 ± 0.26	0.38 ± 0.04	2.70 ± 0.01	3.79 ± 0.22

5.2.2 X-ray photoelectron spectroscopy

Surface elemental contents of DBD cold plasma-treated biochar

The XPS surface elemental analysis of biochar treated with DBD cold plasma are presented in Table 5-5 and Table 5-7. Surface elemental analysis of biochar from XPS in percentage of weight is shown in Table 5-6. DBD cold plasma treatment successfully incorporated nitrogen atoms onto the surface of biochar N_2/800-1. XPS N 1s contents increased significantly from 0.3 at% in N_2/800-1 to the range of 3.9-8.7 at% of DBD cold plasma-treated biochar regardless of operating conditions (plasma power, holding time and gas flow rate). Table 5-7 and Table 5-6 show that surface nitrogen contents of N_2/800-1-H20W2, N_2/800-1-H40W2 and N_2/800-1-H80W2 were in the range of 4.9-6.5 in at% and 5.7-7.5 in wt%, significantly higher than total nitrogen content 1.06-1.675 wt% of precursor N_2/800-1 (Table 5-4). This indicated most nitrogen incorporated into surface of biochar rather than in bulk.

Table 5-5 shows that XPS C 1s contents in biochar N_2/800-1 reduced from 90.0 at% to 80.5-86.1 at% when treated in DBD cold plasma, but the total carbon contents slightly increased from 88.86 wt% to 92.46-95.01 wt% (Table 5-4). Surface oxygen content in N_2/800-1 (8.1 at%) remained similar compared to DBD cold plasma-treated biochar (8.0-10.4 at%), but the total oxygen contents significantly decreased from 9.19 wt% (in N_2/800-1) to 3.02-4.67 wt% (Table 5-4).

These can be concluded that on the surface, carbon is replaced with nitrogen atoms from NH_3, but oxygen remains intact during cold plasma treatment. Total oxygen, on the other hand, is removed during plasma treatment. Several studies used different plasma techniques such as microwave plasma in N_2 (Chen *et al.* 2010) or plasma at vacuum pressure (Wang *et al.* 2010) to modify surface elemental contents. Therefore, it is difficult to directly compare results between these studies. However, the overall trend showed that nitrogen can be incorporated into carbon materials at vacuum pressures. For example, Wang *et al.* incorporated 0.11-0.18 at% to 1.26-1.35 at% of nitrogen into graphene after treatment in N_2 plasma chamber at 750 mTorr, plasma power 100 W at different holding time of 20, 40, 60 and 100 min (Wang *et al.* 2010). Chetty *et al.* showed that the nitrogen content in multiwalled carbon nanotubes increased to 4.4 at% after being treated in N_2 plasma chamber at 20 Pa (30 mL min^{-1}) at plasma power 120 W for 20 min (Chetty *et al.* 2009).

Elemental compositions from XPS C 1s, O 1s and N 1s of DBD cold plasma-treated biochar

Further peak fittings were applied to XPS C 1s, O 1s and N 1s peaks to understand surface chemistry of biochar. The high resolution C 1s peaks were deconvoluted into five peaks, including C=C sp^2 (284.5 ± 0.2 eV), C-C sp^3 (285.2 ± 0.2 eV), C-O (286.4 ± 0.2 eV), C=O (287.9 ± 0.3 eV), O-C=O (289.1 ± 0.3 eV) (Table 5-5, Figure 5-5) (Yang *et al.* 2009, Maharjan *et al.* 2017). DBD cold plasma treatment showed a significant reduction in C sp^2 content from 77.8 at% (biochar N_2/800-1) to 32.5-57.8 at% (after DBD cold plasma treatment). Furthermore, C sp^3 contents also increased from 8.8 at% (N_2/800-1) to 20.9-34.9 at% (after cold plasma treatment), which resulted in the reduction in C sp^2/ C sp^3 ratio from 8.8 at% (N_2/800-1) to 0.9-2.7 at% (DBD cold plasma-treated biochar). The study of Polaki *et al.* showed that C sp^2/ sp^3 ratio of diamond like carbon film decreased significantly from 1.5 to 0.67 after 30 min of H_2 plasma treatment (pulsed DC power 100 V, 50 kHz, 5×10^{-6} mbar) due to the etching effect of C=C bonds by the hydrogen ions/ radicals formed during (Polaki *et al.* 2015). Although gas atmosphere used in the study of Polaki *et al.* (H_2) was different from NH_3, the carrier gas NH_3 used in this study was also rich in hydrogen content, so it is reasonably to extrapolate from the result of Polaki *et al.* that hydrogen ions/ radicals formed during DBD cold plasma reacted with unsaturated carbon Csp^2 on the surface of biochar and reduced C sp^2/C sp^3 (Table 5-5).

XPS O 1s profiles of DBD cold plasma-treated biochar showed significant differences in C-OH, C=O and O-C=O contents obtained from XPS C 1s and O 1s peaks (Table 5-7). The total oxygen contents obtained from XPS C 1s peaks did not equal to the total oxygen content obtained due to different peak resolutions, so it is more accurate to use the oxygen contents obtained from O 1s peaks:

- From Table 5-7, C-OH contents of biochar treated at 20 W increased to 5.1-6.6 at% from 2.5 at%, whereas the C=O contents reduced from 3.0 at% to 0.5-2.1 at% (for N_2/800-1). The same trend was also observed for biochar treated at 80 W. This indicates that DBD cold plasma treated biochar in NH_3 atmosphere can convert C=O into C-OH. However, there was a considerable difference for biochar treated at 40 W.
- For DBD cold plasma-treated biochar at 40 W at NH_3 flow rate 40 mL min^{-1}, the C-O content increased after 1 h treatment to 3.5 at% but decreased to 2.2 at% (N_2/800-1-H40W1 and N_2/800-1-H40W2 respectively). However, the C=O content decreased from 3.2 at% (N_2/800-1) to 2.6 at% after 1 h treatment but then increased to 5.1 at% when holding time was prolonged to 2 h. The same trend was observed for plasma power 40 W at the low flow rate 20 mL min^{-1}: the C-OH content increased from 2.5 at% (N_2/800-1) to 7.1 at% and then dropped to 4.1 at% whereas the C=O content decreased to 0.8 at% and then increasing back to 3.5 at% (biochar N_2/800-1-L40W1 and N_2/800-1-L40W2). The cold plasma treatment had little impact on the O-C=O content (2.0 at% for N_2/800-1 and 1.4-1.6 at% for cold plasma treated N_2/800-1 biochar).

The different changes of C-OH and C=O contents for biochar treated at 40 W showed that more C-OH functional groups were formed due to the incorporation of hydrogen in NH_3 molecules into C=O, but then these C-OH groups were re-oxidised into C=O with increasing holding times.

Table 5-5 Elemental analysis and oxygen functional analysis of carbons obtained from X-ray photoelectron spectroscopy

Carbon sample	**Atomic content (at%)**				**Components from C 1s profiles (at%)**					**C sp^2/ C sp^3 ratio**
	C	**N**	**O**	**K, Ca and Si**	**C sp^2**	**C sp^3**	**C-O/OH**	**C=O**	**O-C=O**	
N_2/800-1	90.0 ± 0.3	0.3 ± 0.1	8.1 ± 0.2	1.6	77.8 ± 7.5	8.8 ± 2.2	1.8 ± 0.2	0.9 ± 0.2	0.7 ± 0.2	8.8
N_2/800-1-H20W1	84.5 ± 0.2	5.8 ± 0.2	8.5 ± 0.5	1.2	38.6 ± 2.1	32.0 ± 2.2	8.7 ± 0.7	2.7 ± 0.4	2.5 ± 0.2	1.2
N_2/800-1-H20W2	83.5 ± 0.2	6.7 ± 0.2	8.3 ± 0.4	1.5	39.8 ± 2.2	29.8 ± 2.1	8.7 ± 1.1	2.7 ± 0.2	2.5 ± 0.3	1.3
N_2/800-1-L20W1	82.1 ± 0.2	5.2 ± 0.2	10.1 ± 0.5	2.6	32.5 ± 1.8	34.9 ± 2.4	9.2 ± 0.6	3.6 ± 0.3	1.9 ± 0.2	0.9
N_2/800-1-L20W2	82.7 ± 0.2	5.8 ± 0.2	9.4 ± 0.4	2.1	41.6 ± 2.3	27.8 ± 2.1	8.2 ± 0.4	2.8 ± 0.2	2.3 ± 0.1	1.5
N_2/800-1-H40W1	86.1 ± 0.2	3.9 ± 0.1	8.0 ± 0.3	2.0	57.8 ± 2.9	20.9 ± 2.2	4.6 ± 0.6	1.6 ± 0.2	1.2 ± 0.3	2.8
N_2/800-1-H40W2	83.3 ± 0.2	4.9 ± 0.2	9.1 ± 0.4	2.7	49.5 ± 6.4	24.4 ± 4.9	5.8 ± 1.1	1.7 ± 0.3	1.9 ± 0.2	2.0
N_2/800-1-L40W1	81.7 ± 0.2	6.6 ± 0.2	9.5 ± 0.4	2.2	43.3 ± 2.3	27.4 ± 2.0	6.7 ± 0.5	2.3 ± 0.3	2.0 ± 0.4	1.6
N_2/800-1-L40W2	80.5 ± 0.2	8.7 ± 0.3	9.2 ± 0.4	1.6	34.5 ± 1.8	32.5 ± 2.4	8.5 ± 0.6	2.4 ± 0.3	2.6 ± 0.4	1.1
N_2/800-1-H80W1	82.6 ± 0.2	5.8 ± 0.2	9.0 ± 0.3	2.6	50.7 ± 4.4	23.1 ± 2.7	5.2 ± 0.8	1.6 ± 0.7	2.0 ± 0.3	2.1
N_2/800-1-H80W2	80.6 ± 0.2	6.5 ± 0.3	10.0 ± 0.5	2.9	46.7 ± 2.5	23.9 ± 2.8	5.7 ± 0.5	2.2 ± 0.1	2.1 ± 0.2	2.0
N_2/800-1-L80W1	81.0 ± 0.2	6.0 ± 0.3	10.4 ± 0.5	2.6	40.0 ± 2.1	32.0 ± 3.0	5.1 ± 0.4	1.7 ± 0.2	2.2 ± 0.2	1.3
N_2/800-1-L80W2	83.1 ± 0.2	6.1 ± 0.3	8.2 ± 0.3	2.6	37.8 ± 2.0	32.9 ± 3.1	7.0 ± 0.4	2.6 ± 0.2	2.8 ± 0.3	1.1
N_2/600-1-NH_3/800	90.4 ± 0.2	5.6 ± 0.2	4.0 ± 0.2	0.0	58.6 ± 3.1	22.7 ± 1.3	6.1 ± 0.6	1.8 ± 0.3	1.2 ± 0.1	2.6
N_2/800-1-NH_3/800	93.1 ± 0.3	4.9 ± 0.2	1.8 ± 0.1	0.2	78.4 ± 1.4	11.1 ± 0.4	3.2 ± 0.6	0.4 ± 0.4	0.0	7.1
N_2/1000-1-NH_3/800	92.6 ± 0.2	3.1 ± 0.1	4.3 ± 0.2	0.0	49.5 ± 2.6	34.9 ± 2.0	5.8 ± 0.6	1.3 ± 0.2	1.1 ± 0.1	1.4

Table 5-6 Elemental CNO analysis from XPS (converted from atomic percentage at% to wt%)

Carbon sample	**Elemental content (wt%, dry ash free)**		
	C	**N**	**O**
N_2/800-1	89.0	0.3	10.7
N_2/800-1-H20W1	82.4	6.6	11.0
N_2/800-1-H20W2	81.6	7.6	10.8
N_2/800-1-L20W1	80.7	6.0	13.3
N_2/800-1-L20W2	81.1	6.6	12.3
N_2/800-1-H40W1	85.0	4.5	10.5
N_2/800-1-H40W2	82.3	5.7	12.0
N_2/800-1-L40W1	80.0	7.5	12.5
N_2/800-1-L40W2	78.2	9.9	11.9
N_2/800-1-H80W1	81.5	6.7	11.8
N_2/800-1-H80W2	79.4	7.5	13.1
N_2/800-1-L80W1	79.5	6.9	13.6
N_2/800-1-L80W2	82.2	7.0	10.8
N_2/600-1-NH_3/800	88.4	6.4	5.2
N_2/800-1-NH_3/800	92.0	5.6	2.4
N_2/1000-1-NH_3/800	90.8	3.6	5.6

.

Table 5-7 Nitrogen and oxygen functional analysis of carbons obtained from X-ray photoelectron spectroscopy

Carbon sample	**Component from N 1s profiles (at%)**				**N-6/N-5 ratio**	**Components from O 1s profile (at%)**			
	N-6	**N-5**	**N-Q**	**N-X**		**C-O/OH**	**C=O**	**COOH**	**Chemisorbed H_2O**
N_2/800-1	0.0	0.0	0.0	0.0		2.5 ± 0.2	3.2 ± 0.2	2.0 ± 0.1	0.4 ± 0.1
N_2/800-1-H20W1	1.2 ± 0.2	4.2 ± 0.1	0.3 ± 0.1	0.1 ± 0.1	0.28	6.3 ± 0.5	0.5 ± 0.1	1.5 ± 0.1	0.2 ± 0.1
N_2/800-1-H20W2	1.7 ± 0.3	4.5 ± 0.2	0.4 ± 0.1	0.1 ±0.1	0.37	5.5 ± 0.4	1.3 ± 0.2	1.4 ± 0.1	0.1 ± 0.1
N_2/800-1-L20W1	1.4 ± 0.2	2.8 ± 0.2	0.9 ± 0.1	0.1 ±0.1	0.50	5.1 ± 0.4	2.1 ± 0.2	2.5 ± 0.2	0.4 ± 0.1
N_2/800-1-L20W2	0.3 ± 0.2	5.1 ± 0.1	0.2 ± 0.1	0.2 ± 0.1	0.06	6.6 ± 0.5	1.0 ± 0.1	1.5 ± 0.2	0.3 ± 0.1
N_2/800-1-H40W1	1.5 ± 0.2	1.7 ± 0.1	0.6 ± 0.2	0.1 ± 0.1	0.88	3.7 ± 0.3	2.6 ± 0.2	1.5 ± 0.2	0.2 ± 0.1
N_2/800-1-H40W2	1.9 ± 0.2	2.3 ± 0.1	0.6 ± 0.1	0.1 ± 0.1	0.83	2.2 ± 0.2	5.1 ± 0.3	1.5 ± 0.2	0.3 ± 0.1
N_2/800-1-L40W1	2.6 ± 0.2	3.0 ± 0.2	0.8 ± 0.1	0.2 ± 0.1	0.87	7.1 ± 0.6	0.8 ± 0.1	1.4 ± 0.1	0.2 ± 0.1
N_2/800-1-L40W2	3.7 ± 0.2	4.1 ± 0.3	0.9 ± 0.2	0.1 ± 0.1	0.90	4.1 ± 0.3	3.5 ± 0.3	1.4 ± 0.1	0.2 ± 0.1
N_2/800-1-H80W1	3.0 ± 0.1	1.9 ± 0.1	0.7 ± 0.2	0.2 ± 0.1	1.58	6.4 ± 0.5	0.9 ± 0.1	1.4 ± 0.2	0.3 ± 0.1
N_2/800-1-H80W2	3.5 ± 0.3	2.3 ± 0.2	0.5 ± 0.2	0.2 ± 0.1	1.52	5.3 ± 0.4	3.0 ± 0.2	1.5 ± 0.2	0.2 ± 0.1
N_2/800-1-L80W1	3.2 ± 0.3	2.2 ± 0.2	0.4 ± 0.1	0.2 ± 0.1	1.33	4.9 ± 0.4	3.7 ± 0.3	1.6 ± 0.2	0.2 ± 0.1
N_2/800-1-L80W2	2.8 ± 0.2	2.4 ± 0.2	0.7 ± 0.2	0.2 ± 0.1	1.17	6.2 ± 0.5	0.1 ± 0.1	1.6 ± 0.2	0.3 ± 0.1
N_2/600-1-NH_3/800	3.0 ± 0.2	1.5 ± 0.2	0.8 ± 0.2	0.3 ± 0.1	2.00	2.2 ± 0.2	0.7 ± 0.2	1.0 ± 0.1	0.1 ± 0.1
N_2/800-1-NH_3/800	2.6 ± 0.2	1.4 ± 0.1	0.6 ± 0.1	0.3 ± 0.1	1.86	0.5 ± 0.1	0.8 ± 0.1	0.4 ± 0.1	0.1 ± 0.1
N_2/1000-1-NH_3/800	1.6 ± 0.2	0.9 ± 0.1	0.4 ± 0.1	0.2 ± 0.1	1.78	2.2 ± 0.2	0.9 ± 0.2	1.0 ± 0.1	0.2 ± 0.1

Figure 5-4 presents the XPS N 1s peaks of three DBD cold plasma-treated biochar at 20 W (N_2/800-1-H20W2), 40 W (N_2/800-1-H40W2) and 80 W (N_2/800-1-80W2). One possible interpretation of XPS N 1s data is to deconvolute into four components: pyridinic (N-6, 398.7 ± 0.3 eV), pyrrolic (N-5, 400.3 eV ± 0.3 eV), quaternary (N-Q, 401.4 ± 0.3 eV), and pyridinic N-oxides and unknown nitrogen (N-X, 405.5 ± 2.5 eV) (Figure 5-4) (Pels *et al.* 1995, Chen *et al.* 2018). A shift of binding energy from N-5 to N-6 was observed with increasing DBD treating power. The N-Q contents of all DBD cold plasma-treated biochar were < 1 at%, and the N-X contents were negligible. While the total nitrogen contents for DBD cold plasma-treated biochar remained similar in the range of 3.9-8.7 at% (Table 5-7), low DBD power (20 W) favoured the formation of N-5, whereas high power plasma (40 W and 80 W) enhanced the formation of N-6. The N-6/N-5 ratio was 0.06-0.50 at 20 W, and 0.83-0.90 at 40 W and 1.17-1.58 at 80 W.

Based on analysis from XPS, the transformation of N-5 to N-6 with increasing plasma power DBD cold plasma-treated biochar was similar with the evolution of nitrogen species in carbon materials treated in NH_3 with increasing temperatures (Pels *et al.* 1995). In the study of Pels *et al.*, N-5 was the dominating nitrogen species in carbazole and acridine treated in NH_3 at 600°C but the total contents of N-6 and N-Q increased significantly to 42% and 74% from 0 and 42% respectively when temperature reached 1000°C. Table 5-5 shows that the surface oxygen contents remained stable at 8.1-10.4 at%, so nitrogen contents increased as an expense of carbon contents. With the significant decrease of C sp^2, it can suggest that under plasma treatment, nitrogen ions/ radicals fused into carbon ring structures to form N-5, N-6, and N-Q species. No evidence to support the formation of amine after DBD cold plasma treatment was found from XPS analysis in the range of tested conditions.

Holding time had no effect in nitrogen contents in DBD cold plasma-treated biochar, indicating that the equilibrium state reaches after the first hour. Total nitrogen content measurement of DBD cold plasma-treated biochar at 20 W at 30 min, 1 h and 2 h with NH_3 flow rate 20 mL min^{-1} increased from 0.69 to 0.91 and 1.06 wt% respectively. This is in agreement with the study of Wang *et al.* (Wang *et al.* 2010). The nitrogen content increased slowly from 0.11-0.18 at% to 1.35-1.26 at% with increasing treating time from 20 to 100 min. Study of Rybin *et al.* showed that increasing treatment time up to 20 min at 10, 20 and 50 W did not change nitrogen contents on graphene (up to 3 at%). Therefore, holding time of 1 h in this study is sufficient to reach maximum nitrogen contents in the nitrogen incorporation.

Surface elemental contents of NH_3 heat-treated AC

In Table 5-5 and Table 5-7, they also show the effect of temperature on conventional heat treatment of biochar in NH_3. NH_3 heat treatment did not influence the total oxygen contents but decreased surface oxygen content sharply (from 8.1 at% in biochar precursor N_2/800-1 to 1.8 at% N_2/800-1-NH_3/800 as shown in Table 5-7). Total oxygen contents of NH_3 heat-treated AC were similar to the oxygen content of biochar precursor (Table 5-4). Furthermore, from Table 5-7, XPS O 1s spectra reduced C=O at temperature 600°C and removed most of the C-O/O-H at 800°C. The carbon content of NH_3 heat-treated AC remained almost the same precursor (N_2/800-1). The differences between XPS C 1s and O 1s profiles of biochar N_2/800-1, DBD cold plasma-treated biochar from N_2/800-1 and NH_3 heat-treated N_2/800-1-NH_3/800 are shown in Figure 5-5.

Increasing pre-treatment temperature for precursor reduced nitrogen content for NH_3 heat-treated AC. Table 5-5 showed that nitrogen contents of N_2/600-1-NH_3/800 and N_2/800-1-NH_3/800 were also higher than N_2/1000-1-NH_3/800 with 5.6 and 4.9 at% compared to 3.1 at%. XRD and Raman spectroscopy analysis (Table 4-7 and Table 4-8) showed that N_2/1000-1 had higher degree of ordered carbonaceous structure compared to N_2/600-1 and N_2/800-1, so it was more difficult to incorporate more nitrogen onto N_2/1000-1 compared to N_2/800-1 and N_2/600-1, with both total and surface nitrogen contents of N_2/1000-1-NH_3/800 lower than N_2/800-1-NH_3/800 and N_2/600-1-NH_3/800 respectively (Table 5-4 and Table 5-7). Pyridinic and pyrrolic groups were two dominant forms of nitrogen with similar N-6/N-5 ratios (~2:1), and surface oxygen being removed from biochar (Table 5-7 and Figure 5-4).

Further examination of XPS N 1s spectra of NH_3 heat-treated AC showed a clearer split between the peak of pyridinic-N and pyrrolic-N (Figure 5-4), but for DBD cold plasma-treated biochar, these two peaks merged without any clear division. Further analysis including FTIR and TPD was conducted to understand the difference in nitrogen species in biochar obtained from these two functionalisation methods.

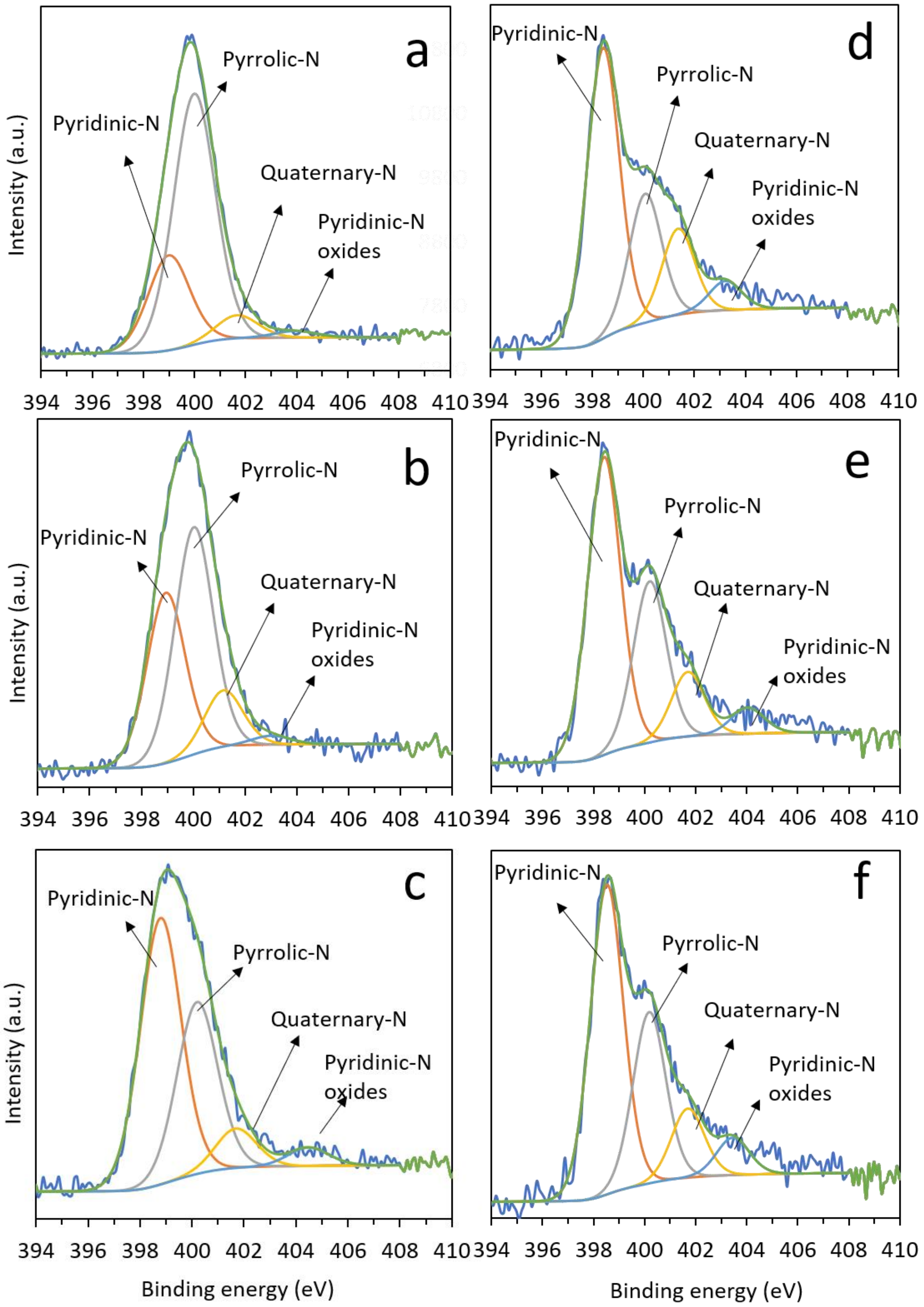

Figure 5-4 (Left) XPS N 1s peaks of DBD cold plasma-treated biochar in NH_3 (40 mL min^{-1}) using biochar N_2/800-1 (walnut shell pyrolysed in N_2 at 800°C) as the precursor: (a) N_2/800-1-H20W2: treatment at 20 W, (b) N_2/800-1-H40W2: treatment at 40 W, (c) N_2/800-1-H80W2: treatment at 80 W. (Right) Heat-treated AC in NH_3 (40 mL min^{-1}) at 800°C (d) N_2/600-1-NH_3/800 (using N_2/600-1 as the precursor), (e) N_2/800-1-NH_3/800 (using N_2/800-1 as the precursor) and (f) N_2/1000-1-NH_3/800 (using N_2/1000-1 as the precursor)

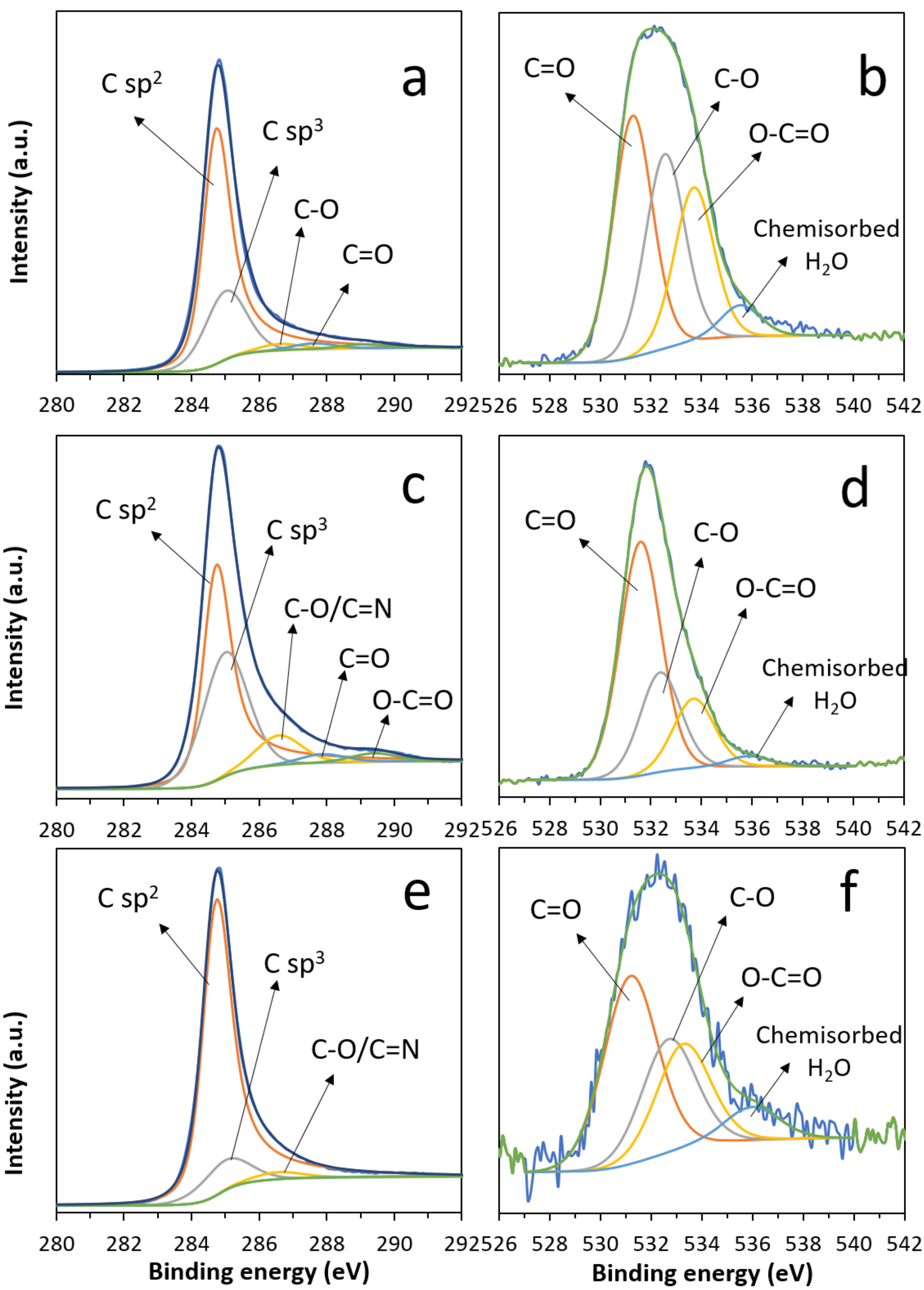

Figure 5-5 XPS C 1s (on the left) and O 1s (on the right) spectra of (a-b) biochar N_2/800-1, (c-d) DBD cold plasma-treated biochar at 40 W for 2 h (N_2/800-1-H40W2) and (e-f) NH_3 heat-treated AC at 800°C (N_2/800-1-NH_3/800)

5.2.3 Fourier Transform-Infrared Spectroscopy

FTIR was performed to help reveal more insight of functional groups in DBD cold plasma biochar and heat-treated AC in NH_3 environment. From literature (Jia *et al.* 2002, Xiao and Thomas 2005), the change in adsorption peaks at 1512, 1541 and 1570 cm^{-1} on coconut shell AC indicates the present of pyridinic, pyridonic, and pyrrolic (or indolic) structures, respectively. However, Figure 5-6 shows that there was little difference in FTIR spectra of N_2/800-1 and DBD cold plasma-treated biochar in the wavenumber region of 1500-1600 cm^{-1}. This indicates little change in nitrogen functional groups in DBD cold plasma-treated biochar samples. FTIR analysis results contrasted with XPS elemental analysis (Table 5-5, Table 5-7, Figure 5-4 and Figure 5-5), in which XPS N 1s illustrated high nitrogen functional group contents on the surface of DBD cold plasma-treated biochar. The difference is because the thickness allowance in FTIR *i.e.* adsorption depth up to 11 μm (De Haseth *et al.* 2007) and in XPS *i.e.* 5 nm (Konno 2016). Therefore, most nitrogen functional groups in XPS resided on surface of biochar rather than in bulk. High nitrogen content on surface in DBD cold plasma treated biochar samples agreed well with other reports (Saka 2018) where cold plasma treatment on CNTs (DBD, radio frequency, microwave, *etc.*) is effective in functionalising the surface of carbon rather than in bulk . In the review of Saka, different cold plasma sources such as DBD, corona discharge, pulsed corona, microwave, and radio frequency plasma creates acid and basic functional groups depending on gas sources, in which using Ar/O_2 mixture paves a way to form C-O, C=O and O-C=O groups from oxygen radicals on C-C and C=C bonds, and

Furthermore, the similarity of FTIR spectra of N_2/800-1 and DBD cold plasma-treated biochar also showed that oxygen groups was also not influenced during cold plasma treatment. This is in agreement with XPS and elemental analysis data as discussed in sections 5.2.1 and 5.2.2.

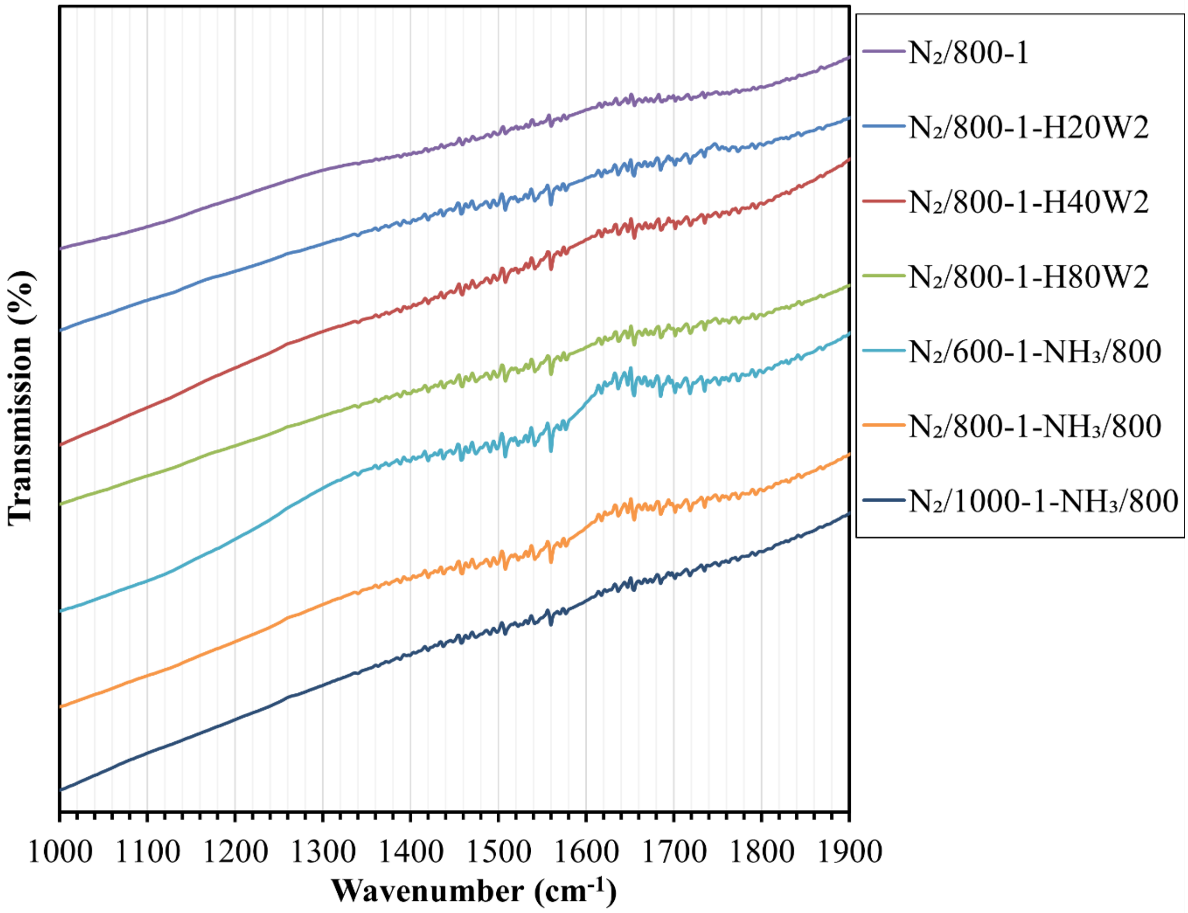

Figure 5-6 FTIR spectra of DBD cold plasma-treated biochar at 20 W, 40 W and 80 W for 2 h holding time in NH_3 (40 mL min^{-1}) (N$_2$/800-1-H20W2, N$_2$/800-1-H40W2 and N$_2$/800-1-H80W2) and NH_3 heat-treated AC at 800°C in NH_3 (40 mL min^{-1}) for 2 h

FTIR spectrum of N$_2$/600-1-NH$_3$/800 showed a clearer adsorption peak in the region of 1500-1600 cm^{-1} (Figure 5-6) compared to N$_2$/800-1-NH$_3$/800 and N$_2$/1000-1-NH$_3$/800, indicating the incorporation of nitrogen into this biochar in the form of pyridinic, pyridonic, and pyrrolic. The adsorption in the region 1500-1600 cm^{-1} of N$_2$/800-1-NH$_3$/800 reduced gradually compared to N$_2$/600-1-NH$_3$/800, and completely diminished in N$_2$/1000-1-NH$_3$/800. The only difference factor between these three samples was the pre-treatment or pyrolysis temperature (600, 800 and 1000°C). This indicated the decrease in nitrogen content among three NH_3 heat-treated AC, given that FTIR spectra of their precursors N$_2$/600-1, N$_2$/800-1 and N$_2$/100-1 were similar (Figure 5-7). Lower temperatures (600°C compared to 800 and 1000°C) created more flexible carbon structure and allowed more nitrogen to be incorporated. This result is in line with the decrease of nitrogen content from 5.6 at% in N$_2$/600-1-NH$_3$/800 to 3.1 at% in N$_2$/1000-1-NH$_3$/800 as detected from XPS (Table 5-5). However, no considerable information regarding oxygen functional groups was obtained from FTIR.

It is important to notice that XPS analysis presented lower nitrogen contents of NH_3 heat-treated AC (2.6-5.6 at%) compared to DBD cold plasma-treated biochar (3.9-8.1 at%). However, XPS N 1s peaks of NH_3 heat-treated AC showed a clearer distinction between N-6 and N-5 peaks, and NH_3 heat-treated AC also showed clearer adsorption in FTIR for nitrogen functional groups compared to DBD cold plasma-treated biochar.

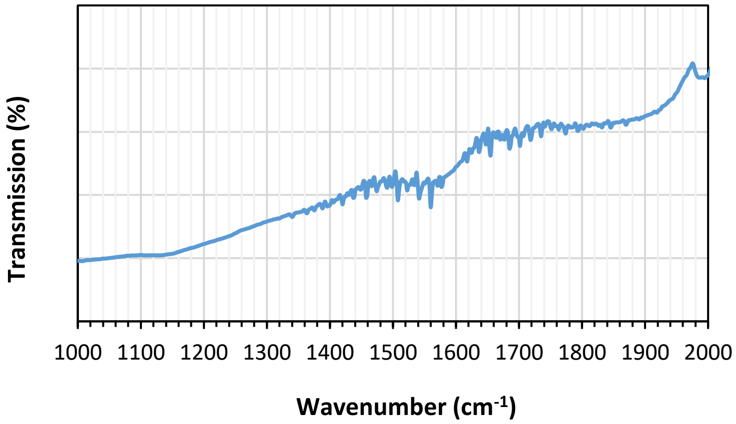

a)

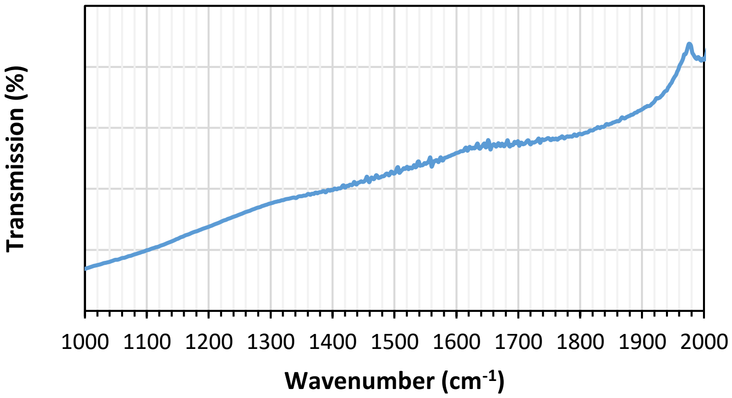

b)

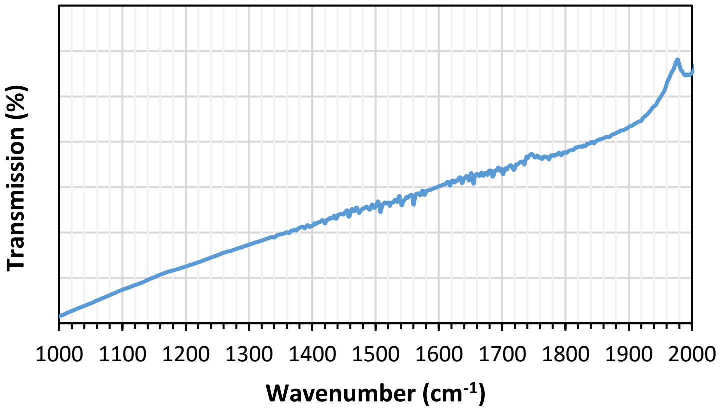

c)

Figure 5-7 FTIR profiles of biochar pyrolysed in N_2 (a) biochar N_2/600-1, (b) biochar N_2/800-1 (c) biochar N_2/1000-1

5.2.4 Temperature programmed desorption (TPD)

Functional groups in DBD cold plasma-treated biochar (N_2/800-1-H20W2, N_2/800-1-H40W2 and N_2/800-1-H80W2) were examined using TPD. The H_2O desorption in the temperature range of 240-800°C, coupled with the release of CO_2, indicated the release of different oxygen functional groups in biochar, including carboxylic acid and lactone/lactol (Jia and Thomas 2000, Jia *et al.* 2002, Xiao and Thomas 2005). The CO desorption (m/z 28) coincided with H_2O release at 800-1000°C can be due to hydroquinone/ semiquinone and ethers (Zielke *et al.* 1996, Figueiredo *et al.* 1999, Turner and Thomas 1999). Furthermore, TPD profiles of CO_2, CO, and H_2O of the precursor N_2/800-1 and DBD cold plasma-treated biochar were similar, indicating that cold plasma treatment had no effect on oxygen functional groups. This agreed with total surface oxygen functional groups as discussed in XPS (Table 5-5 and Table 5-7).

Figure 5-8 shows a significant release of NO (m/z = 30) from DBD cold plasma-treated biochar in the temperature range of 240-800°C compared to N_2/800-1. Although there was no considerable amount of N-X detected in XPS N 1s (Table 5-7), this NO desorption suggested surface reaction of nitrogen and oxygen species to form NO even at this temperature range. The intensive NO release can also explain for the depletion of N_2 desorption in the temperature range of 900-1300°C. The TPD profiles at m/z 14 and m/z 28 showed that most CO emerged in temperature range of 800-950°C and only a small proportion of N_2 evolved up to 1200°C. However, the intensity of N_2 released at 1200°C reduced with increasing cold plasma power *e.g.* N_2 evolution at 1200°C clearly observed at 20 W (N_2/800-1-H20W2), but less distinctive at 80 W (N_2/800-1-H80W2). N_2 desorption at high temperatures was due to surface reactions between mobile nitrogen species at high temperatures (Pels *et al.* 1995, Xiao *et al.* 2005). The desorption of N_2 at such high temperature could be the result of nitrogen functional groups gradually transforming from N-5 to N-6 and subsequently to N-Q, then being released as N_2 at high temperatures, following thermal stability order N-X < N-5 < N-6 < N-Q (Pels *et al.* 1995, Xiao *et al.* 2005). Moreover, the TPD profiles did not record any NH_3 desorption because of no noticeable difference between m/z 17 (NH_3 and OH) and m/z 18 (H_2O), so NO is the main nitrogen-contained desorption product for DBD cold plasma-treated biochar.

The TPD profiles of DBD cold plasma-treated biochar also recorded HCN desorption (m/z 27) in the temperature range of 200-400°C, especially for N_2/800-1-H20W2 (Figure 5-9). This low desorption temperatures suggested the formation of unstable nitrogen groups such as nitriles (-C≡N) or amines ($-NH_2$). NH_3 could react with COOH groups to form $-CO-NH_2$ and then dehydrate to form -C≡N, and this hypothesis can be supported by a small H_2O desorption in the range of 200-400°C. On the other hand, amine ($-NH_2$) could be formed by reaction between phenolic groups and NH_3 (Kundu *et al.* 2010). Amine/ amide groups were found as the main nitrogen group formed on corn starch at 160°C but then were transformed into N-5, N-6 and N-Q when temperature was raised to 400 and 600°C (Li *et al.* 2019). Cold plasma treatment must have allowed the reactions of NH_3 and oxygen surface functional groups or attachment of NH_3 into the C=C sp^2 to form $-C-NH_2$ groups. This release of HCN at this low temperature range, however, was different from the release of HCN stemming from cyanoacetylene groups (-C≡C−C≡N) at high temperature range of 830-970°C (Ikeda and Mackie 1995).

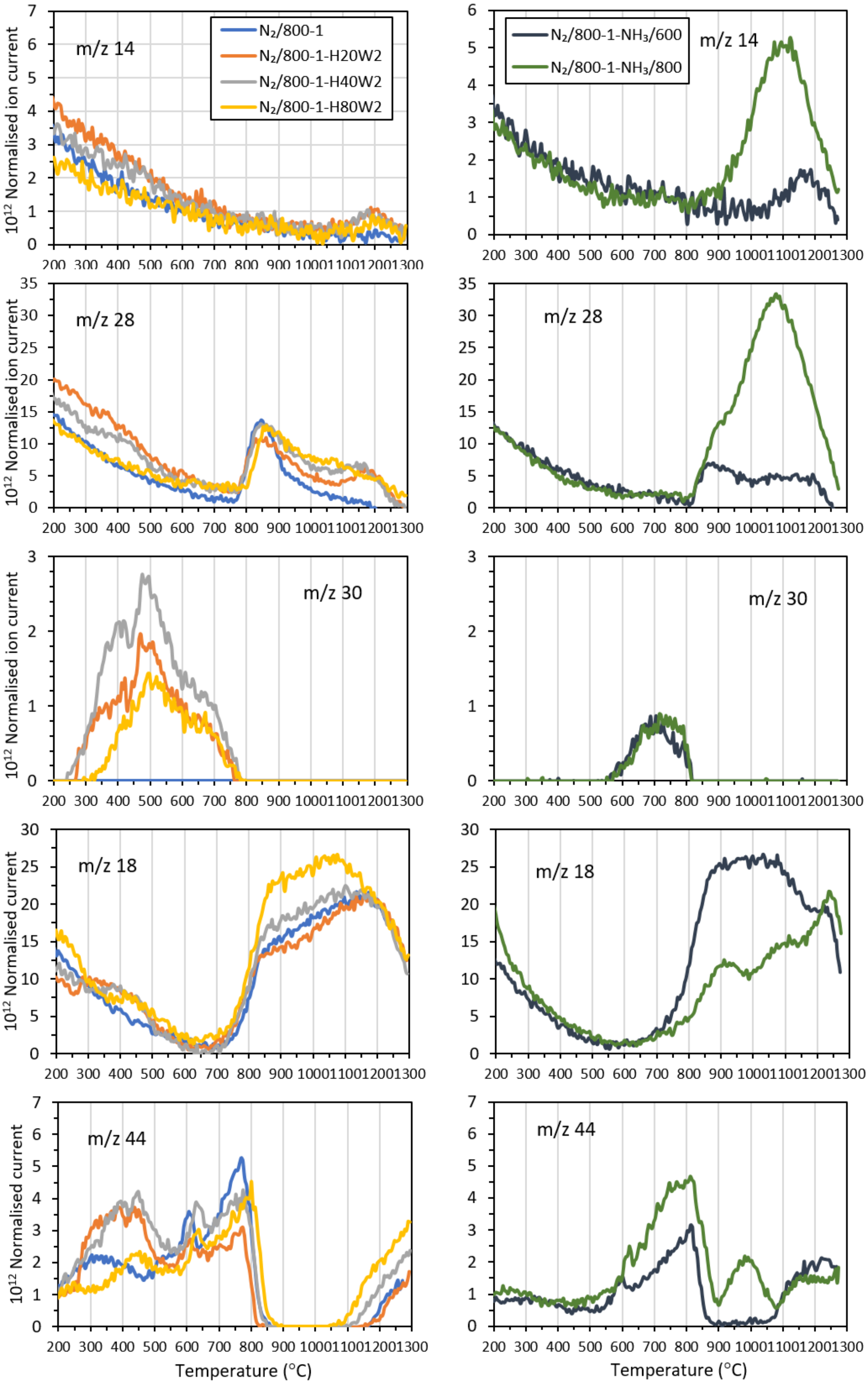

Figure 5-8 TPD profiles of biochar pyrolysed at 800°C (N_2/800-1) and DBD cold plasma-treated biochar at 20, 40 and 80 W in NH_3 (40 mL min^{-1}) (N_2/800-1-H20W2, N_2/800-1-H40W2 and N_2/800-1-H80W2) (left) and NH_3 heat-treated biochar at 800°C in NH_3 (40 mL min^{-1}) (right)

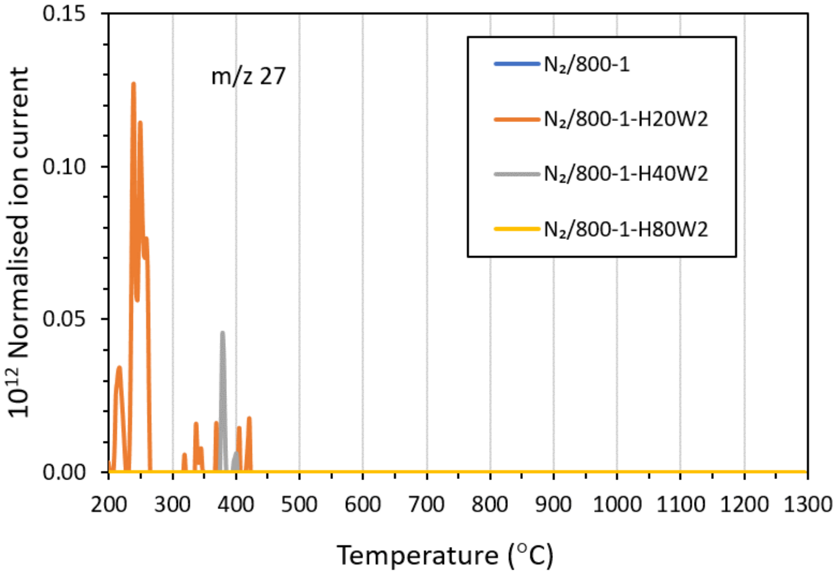

Figure 5-9 HCN desorption from TPD profile of DBD cold plasma-treated biochar N_2/800-1-H20W2, N_2/800-1-H40W2 and N_2/800-1-H80W2

Figure 5-8 showed TPD profiles of NH_3 heat-treated biochar showed distinctive behaviours compared to DBD cold plasma-treated biochar. Comparing m/z 14 and m/z 28 TPD profiles of AC N_2/800-1-NH_3/800, it showed small CO desorption peaks at ~850-900°C and then released N_2 up to 1200°C as shown by the similarity in m/z 14 and 28 peaks (Figure 5-8). Nitrogen surface functional groups in carbon react on the surface to form N_2 (Xiao *et al.* 2005). The proportion of N_2 desorbed from carbon N_2/800-1-NH_3/800 was much higher than any other DBD cold plasma-treated biochar (Figure 5-8), indicating higher N-5 and N-6 contents incorporated in biochar. However, the NO desorption from pyridine N-oxides of N_2/800-1-NH_3/800 desorbed much lower NO compared to DBD cold plasma-treated biochar. This NO desorption at 550-820°C coincided with CO_2 release (Figure 5-8). It can be due to the shortage of oxygen after NH_3 treatment as proven in XPS data (Table 5-5), and nitrogen in the form of pyridinic and pyrrolic were stable at temperatures below 800°C and only became reactive at above 800°C. There is no difference between the TPD profiles of m/z 17 and m/z 18 of these carbons indicating negligible NH_3 desorption, so N_2 is the major nitrogen-contained desorption product. The thermal stability of nitrogen functional groups in carbon has been shown previously shown as pyridine N-oxide < pyrrolic-N < pyrridinic-N < quaternary-N with pyrrolic-N gradually transforming into pyridinic-N, and subsequently into quaternary-N with increasing temperatures (Pels *et al.* 1995, Xiao *et al.* 2005). At high temperatures, mobile nitrogen surface species reacted to form N_2 through reaction: $-C(N)_m + -C(N)_{f\text{ or }m} \rightarrow N_2 + 2C_f$, in which $-C(N)_m$ is the mobile surface nitrogen functional group and $–C(N)_f$ is the fixed nitrogen functional group. These nitrogen-contained desorption products coincided with the nitrogen species detected in XPS (Table 5-7 and Figure 5-4) discussed previously.

5.3 Functionalisation of hydrochar

5.3.1 Total elemental CHNO analysis

Table 5-8 shows the total elemental CHNO analysis content for hydrochar HY250, HY290, DBD cold plasma-treated hydrochar and NH_3 heat-treated hydrochar. There is similarity in total and surface oxygen content in hydrochar as discussed later in XPS section 5.3.2. The surface oxygen content varied in the range 15.5-17.8 at% (see Table 5-9), similar to surface oxygen content in the range 18.32-22.70 wt% (see Table 5-8). This indicates that oxygen is distributed in and outside of spherical structures in hydrochar as shown through the formation mechanism of Sevilla and Fuertes (Sevilla and Fuertes 2009).

Table 5-8 Total elemental CHNO contents

Carbon sample	**Elemental content (wt%, dry ash free)**			
	C	**H**	**N**	**O**
HY250	72.33 ± 0.10	4.97 ± 0.08	0.00	22.70 ± 0.02
HY290	76.96 ± 0.07	4.72 ± 0.03	0.00	18.32 ± 0.03
HY250-H80W2	76.79 ± 0.12	3.91 ± 0.01	4.31 ± 0.01	14.99 ± 0.12
HY250-NH_3/800	69.87 ± 0.15	3.08 ± 0.01	7.46 ± 0.01	19.59 ± 0.13
HY290-H80W2	74.77 ± 0.13	4.46 ± 0.02	3.39 ± 0.02	17.38 ± 0.15
HY290-NH_3/800	70.96 ± 0.11	3.16 ± 0.02	7.10 ± 0.02	18.78 ± 0.14

NH_3 heat-treated hydrochar showed high total oxygen contents of 18.78-19.59 wt% contrast to low surface oxygen content 0.9-3.1 at% (see XPS O 1s Table 5-9). Therefore, NH_3 heat treatment at 800°C only removed oxygen on the hydrochar surface, which is similar to AC heat treated in NH_3 (see XPS O 1s Table 5-5). Furthermore, nitrogen contents increased to 7.10-7.46 wt%, indicating the successful incorporation of nitrogen into hydrochar. The range of nitrogen content is similar to nitrogen content of N_2/600-1-NH_3/800 (8.28 wt% in Table 5-4, but much higher than nitrogen content of NH_3 heat-treated AC N_2/800-1-NH_3/800 (4.76 wt%) and N_2/1000-1-NH_3/800 (2.70 wt%). Therefore, as discussed in section 5.1 about PXRD molecular structure of hydrochar, highly amorphous structure of hydrochar allowed more alteration during heat treatment with NH_3 and resulted in higher total nitrogen contents.

In contrast to NH_3 heat treatment, DBD cold plasma treatment in NH_3 only increased nitrogen contents to 3.39-4.41 wt% (Table 5-8), so DBD cold plasma treatment is not as effective as heat treatment method to incorporate nitrogen hydrochar. Furthermore, the range of nitrogen contents 3.39-4.41 wt% is also lower than surface nitrogen contents detected in XPS (6.1-8.9 at%, see XPS N 1s Table 5-9). Furthermore, oxygen contents in the range of 14.99-17.38 wt% is also higher than surface oxygen contents of HY250-H80W2 and HY290-H80W2 (see XPS O 1s Table 5-9). The two opposite trends of nitrogen and oxygen on surface and in bulk of DBD cold plasma are evidence that DBD cold plasma in NH_3 only influenced surface of hydrochar, replacing surface oxygen with nitrogen from NH_3.

5.3.2 X-ray photoelectron spectroscopy

Table 5-9 shows that DBD cold plasma-treated hydrochar at 80 W for 2 h in NH_3 (40 mL min^{-1}) significant reduced oxygen content from 15.5-17.8 at% to 6.6-7.2 at% but increased nitrogen content to 6.1-8.9 at%. The total carbon content slightly increased from 82.2-84.5 to 84.5-87.0 at% after cold plasma treatment. The same peak deconvolution of XPS C 1s, O 1s and N 1s peaks were applied to nitrogen-incorporated hydrochar to understand how functional groups were influenced. Figure 5-10 illustrates the XPS C 1s and O 1s peaks of HY250 and HY250-H80W2.

XPS C 1s of DBD cold plasma-treated hydrochar revealed an increase in C sp^2 content from 13.3-25 at% to 34.0-52.8 at% compared to hydrochar, and the total percentage of oxygen functional groups (C-O/OH, C=O and O-C=O) reduced significantly 61.1, 49.4 and 17.1 at% in HY200, HY250 and HY290 to 10.4, 19.4, and 7.9 at% in HY200-H80W2, HY250-H80W2 and HY290-H80W2 respectively (Table 5-10). Hydrochar was highly amorphous carbon, and at 200°C most lignocellulosic matters remained in hydrochar (HY200) and only a part of lignin decomposed at higher temperature at 290°C (HY290). The temperature of carbon sample during radio frequency cold plasma could be increased up to 200°C (Merenda *et al.* 2016). Although hydrochar was treated in DBD cold plasma in this study, temperature of hydrochar should be increased, together with NH_3 environment containing several ions/radicals, so hydrochar could undergo different decompose processes similar to liquefaction and improve its ordered structure. This explained the increase of C sp^2 contents and decrease of total oxygen contents (Table 5-9). Moreover, although the hydrogen contents could not be evaluated in XPS, the high content of C sp^3 showed that a proportion of hydrogen was not removed from hydrochar during DBD cold plasma process.

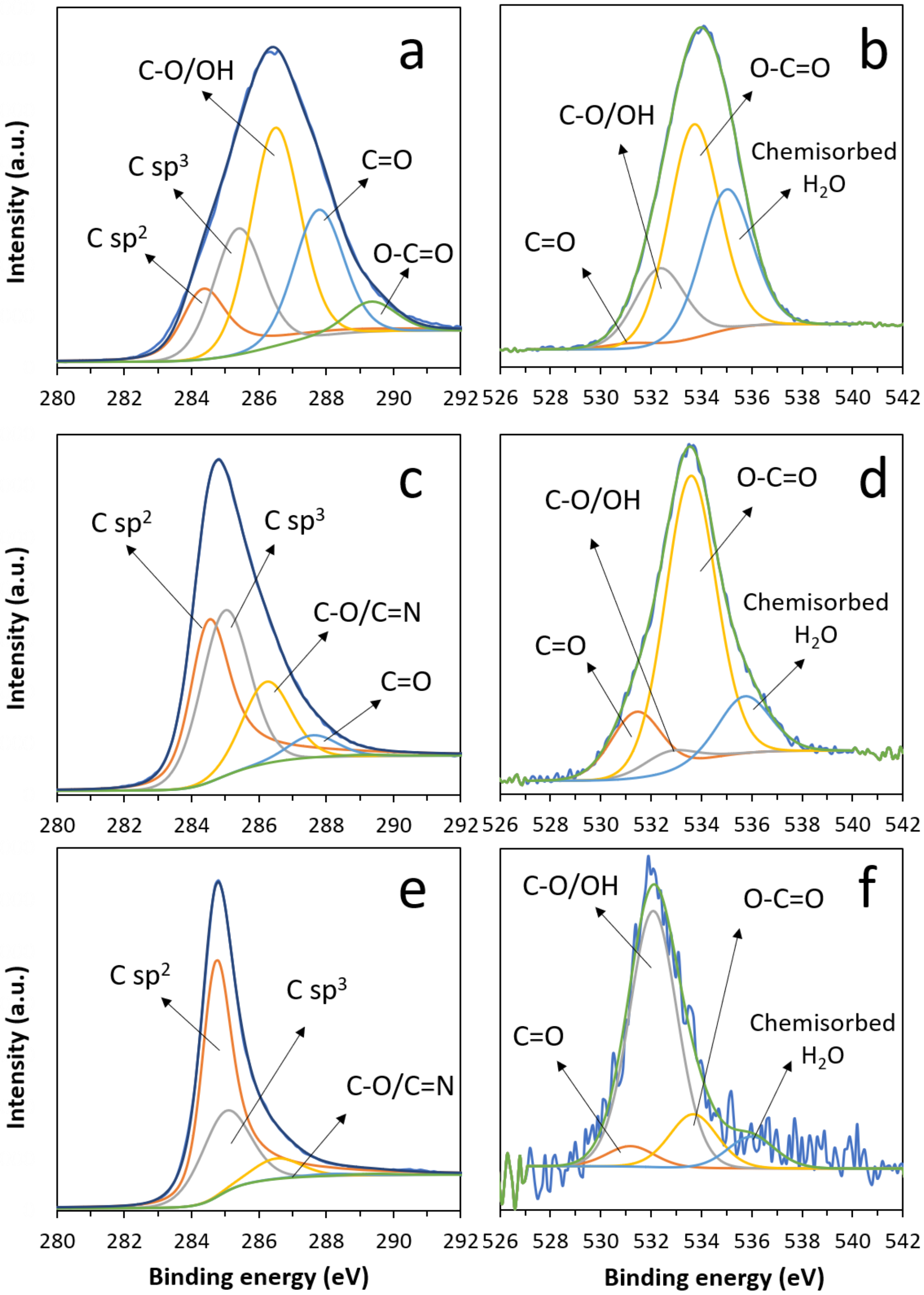

Figure 5-10 XPS C 1s (on the left) and O 1s (on the right) spectra of (a-b) hydrochar obtained from HTC at 250°C (HY250), (c-d) DBD cold plasma-treated of HY250 at 80 W (NH_3 40 mL min^{-1}) (HY250-H80W2) and (e-f) NH_3 heat-treated hydrochar in NH_3 at 800°C (HY250-NH_3/800)

Further details on oxygen functional groups were explored from XPS O 1s peaks of HY200-H80W2, HY250-H80W2 and HY290-H80W2, and carboxylic groups dominated other two oxygen components with O-C=O content varying in the range of 4.0-4.9 at% while the contents of C-OH and C=O were lower than 1.5 at% (Table 5-10). The formation of O-C=O groups could be favoured during DBD treatment after the formation of C-OH and C=O bonds as suggested by Chen *et al.* (Chen *et al.* 2009), in the study of MWCNTs treated in O_2 or Ar/O_2 plasma. The breakage of π bonds in C sp^2 created active sites reacting with active oxygen atoms to form C-O bonds, but the new C-O bonds could also rearrange intramolecular to form C=O bonds and subsequently rearrange to O-C=O thanks to proton transfers. Highly amorphous structure of hydrochar allowed more alteration to their surface functionalities compared to biochar, and abundant oxygen contents in original hydrochar also permitted the creation of many oxygen active ions/ radicals to form carboxylic groups. The low contents of both C-O and C=O in these DBD cold plasma-treated hydrochar also supported the mechanism of C-O and C=O groups being converted into O-C=O proposed by Chen *et al.* (Chen *et al.* 2009). The heat treatment of these hydrochar in NH_3 at 800°C, on the other hand, effectively removed almost oxygen functional groups on the surface of hydrochar with surface oxygen contents being only in the range of 0.9-3.1 at% (Table 5-5) as discussed in section 5.3.1 about total CHNO results.

Regarding nitrogen functional groups, XPS N 1s spectra of DBD cold plasma-treated hydrochar also showed the considerable nitrogen contents of 6.1-8.9 at%. Following the discussion of nitrogen species formed on biochar in DBD cold plasma in section 5.2.2, it appears that pyridinic-N is the main nitrogen-containing pieces, following by pyrrolic-N (N-6/N-5 ratio ~ 1.04-1.64) (see Table 5-9 and Figure 5-11). N-Q and N-X also accounts for small percentages (< 1.0 at%) in all DBD cold plasma-treated hydrochar samples. Figure 5-11 also presents the XPS N 1s of NH_3 heat-treated hydrochar (HY200-NH_3/800, HY250-NH_3/800 and HY290-NH_3/800), and these profiles are similar to XPS N 1s of NH_3 heat-treated AC (Figure 5-4). The surface nitrogen contents in NH_3 heat-treated hydrochar was in the range of 6.0-8.3 at%, similar to DBD cold plasma-treated hydrochar (6.1-8.9 at%) but higher than NH_3 heat-treated AC (2.6-6.1 at% see Table 5-9). This was due to highly amorphous structure of hydrochar, allowing more alteration during heat treatment and more nitrogen incorporation into carbon structure of hydrochar compared to biochar. High temperature at 800°C also allowed the rearrangement of carbon amorphous structure and removal of hydrogen, leading to high C sp^2 content (59.3-83.8 at%) compared to C sp^3 (0.4-

24.6 at%). This contrasted to the high C sp^3 contents in DBD cold plasma-treated hydrochar (26.3-36.6 at%) (Table 5-9).

Comparison of DBD cold plasma treatment and NH_3 heat treatment on two different biomass-derived carbon series, namely biochar and hydrochar, in terms of surface and total functional groups shows that both DBD cold plasma and NH_3 heat treatment alter surface of amorphous carbon materials rather than in bulk. The reaction mechanism for NH_3 heat treatment has been studied thoroughly (Stöhr *et al.* 1991, Jansen and van Bekkum 1995, Pels *et al.* 1995), with compelling evidence through a series of analysis to prove that pyrrolic-N, pyridinic-N, and quaternary-N being main nitrogen-containing species. The results of DBD cold plasma treatment in NH_3 explained in other studies such as (Chetty *et al.* 2009, Chen *et al.* 2010, Shao *et al.* 2010, Wang *et al.* 2010) and discussed in section 2.4.1.3 also assigned pyrrolic-N and pyridinic-N being main nitrogen-containing species. However, they did not explain the difference between XPS N 1s of carbon materials treated in DBD cold plasma and heat treatment, where there is no clear division between N-6 and N-5 peaks from XPS N 1s profiles of DBD cold plasma-treated compared to NH_3 heat-treated samples.

Table 5-9 Elemental analysis and oxygen functional analysis of hydrochar obtained from X-ray photoelectron spectroscopy

Carbon sample	**Atomic content (at%)**				**Components from C 1s profiles (at%)**					**C sp^2/ C sp^3 ratio**
	C	**N**	**O**	**K, Ca and Si**	**C sp^2**	**C sp^3**	**C-O/OH**	**C=O**	**O-C=O**	
HY200	82.4 ± 1.2	0.0	17.6 ± 1.2	0.0	19.4 ± 1.2	1.9 ± 1.3	25.0 ± 1.6	23.3 ± 1.2	12.8 ± 3.1	10.2
HY250	82.2 ± 0.1	0.0	17.8 ± 0.1	0.0	13.3 ± 1.5	19.5 ± 1.7	28.3 ± 2.4	16.9 ± 0.9	4.2 ± 0.1	0.7
HY290	84.5 ± 0.2	0.0	15.5 ± 0.2	0.0	25.0 ± 2.6	42.4 ± 2.8	13.3 ± 3.2	3.2 ± 2.0	0.6 ± 0.2	0.6
HY200-NH_3/800	89.7 ± 0.2	8.3 ± 0.4	2.0 ± 0.1	0.0	75.5 ± 4.0	5.8 ± 0.3	5.8 ± 0.6	1.1 ± 0.2	1.5 ± 0.1	13.0
HY250-NH_3/800	91.1 ± 0.2	8.0 ± 0.4	0.9 ± 0.1	0.0	59.3 ± 3.1	24.6 ± 1.4	6.1 ± 0.6	0.6 ± 0.1	0.5 ± 0.1	2.4
HY290-NH_3/800	90.9 ± 0.2	6.0 ± 0.3	3.1 ± 0.2	0.0	83.8 ± 4.4	0.4 ± 0.1	4.7 ± 0.5	0.7 ± 0.1	1.3 ± 0.1	209
HY200-H80W2	84.5 ± 0.2	8.9 ± 0.4	6.6 ± 0.4	0.0	37.5 ± 0.2	36.6 ± 1.0	8.0 ± 0.8	1.4 ± 0.3	1.0 ± 0.3	1.0
HY250-H80W2	86.7 ± 0.1	6.1 ± 0.3	7.2 ± 0.4	0.0	34.0 ± 0.2	33.6 ± 1.3	14.6 ± 1.3	3.8 ± 0.5	0.7 ± 0.5	1.0
HY290-H80W2	87.0 ± 0.2	6.2 ± 0.3	6.8 ± 0.4	0.0	52.8 ± 0.3	26.3 ± 1.2	6.4 ± 0.6	0.8 ± 1.3	0.7 ± 0.2	2.0

Table 5-10 Nitrogen and oxygen functional analysis of carbons obtained from X-ray photoelectron spectroscopy

Carbon sample	**Component from N 1s profiles (at%)**				**N-6/N-5 ratio**	**Components from O 1s profile (at%)**			
	N-6	**N-5**	**N-Q**	**N-X**		**C-O/OH**	**C=O**	**COOH**	**Chemisorbed H_2O**
HY200	ND	ND	ND	ND		4.4 ± 2.4	0.0	6.6 ± 0.8	6.6 ± 2.8
HY250	ND	ND	ND	ND		3.7 ± 0.6	0.1 ± 0.1	8.7 ± 0.1	5.3 ± 0.4
HY290	ND	ND	ND	ND		10.8 ± 0.8	3.1 ± 0.1	1.5 ± 0.8	0.1 ± 0.1
HY200-NH_3/800	4.0 ± 0.3	2.6 ± 0.2	1.1 ± 0.3	0.6 ± 0.2	1.54	1.5 ± 0.1	0.2 ± 0.1	0.2 ± 0.1	0.1 ± 0.1
HY250-NH_3/800	4.0 ± 0.3	2.5 ± 0.2	1.0 ± 0.3	0.5 ± 0.2	1.60	0.6 ± 0.1	0.1 ± 0.1	0.1 ± 0.1	0.1 ± 0.1
HY290-NH_3/800	2.9 ± 0.2	1.7 ± 0.1	1.0 ± 0.3	0.4 ± 0.2	1.71	2.2 ± 0.2	0.1 ± 0.1	0.6 ± 0.2	0.2 ± 0.1
HY200-H80W2	4.8 ± 0.4	3.6 ± 0.3	0.3 ± 0.1	0.2 ± 0.1	1.33	1.5 ± 0.1	1.0 ± 0.1	4.0 ± 0.4	0.1 ± 0.1
HY250-H80W2	2.6 ± 0.2	2.5 ± 0.1	0.8 ± 0.1	0.2 ± 0.1	1.04	0.2 ± 0.2	1.3 ± 0.1	4.9 ± 0.2	0.8 ± 0.2
HY290-H80W2	3.6 ± 0.3	2.2 ± 0.1	0.2 ± 0.1	0.2 ± 0.1	1.64	0.5 ± 0.1	1.4 ± 0.2	4.8 ± 0.5	0.1 ± 0.1

Table note: ND: not detected

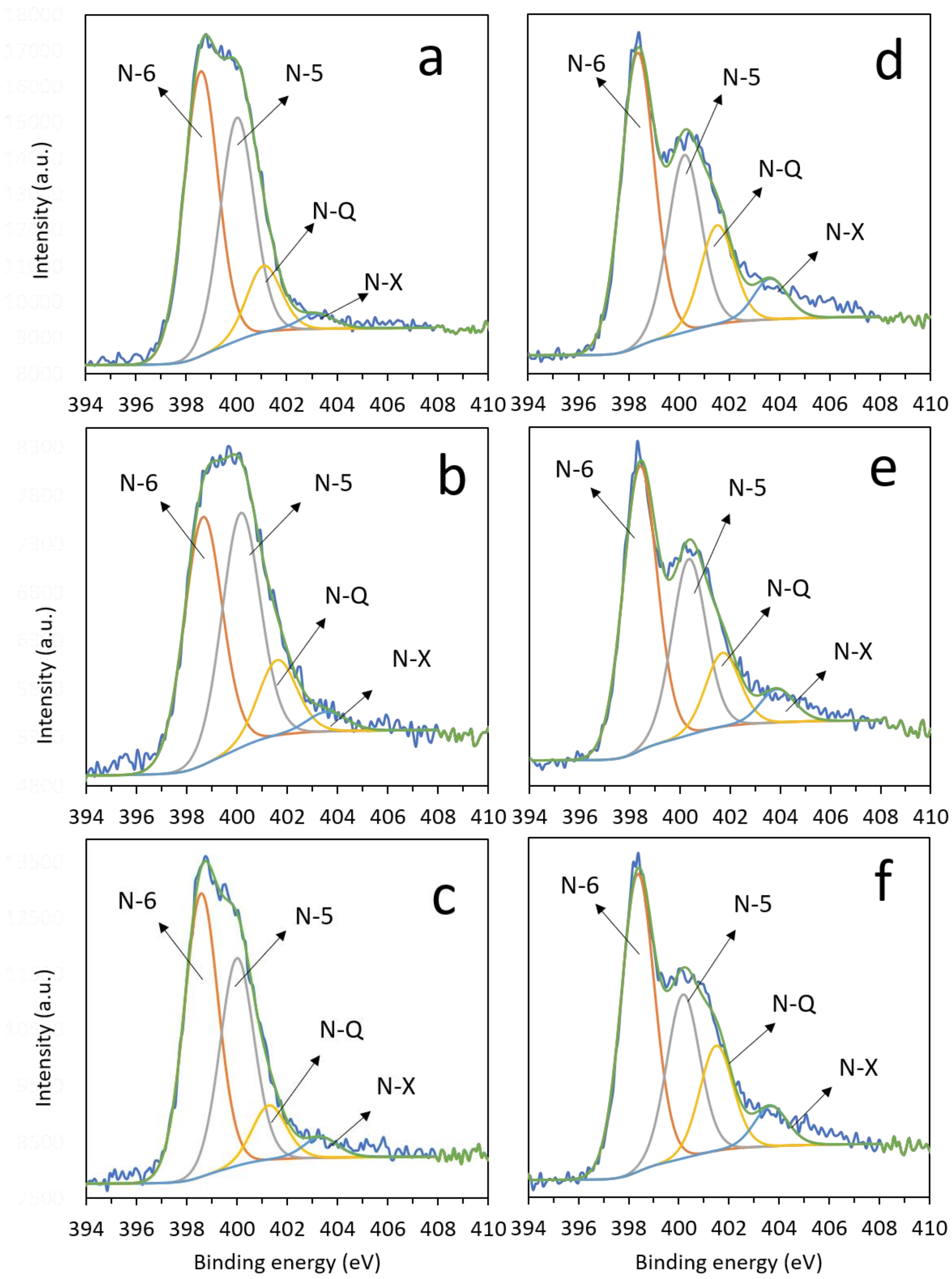

Figure 5-11 XPS N 1s peaks of DBD cold plasma-treated hydrochar at 80 W in NH_3 (40 mL min^{-1}) (left): (a) HY200-H80W2, (b) HY250-H80W2, (c) HY290-H80W2, and NH_3 heat-treated hydrochar at 800°C in NH_3 (40 mL min^{-1}) (right): (d) HY200-NH_3/800, (e) HY250-NH_3/800 and (f) HY250-NH_3/800

5.3.3 Fourier Transform-Infrared Spectroscopy (FTIR)

DBD cold plasma resulted in the removal of several oxygen functional groups in hydrochar HY250 (Figure 5-12). FTIR spectrum of HY250-H80W2 only showed a small peak in the wavenumber region 1500-1600 cm^{-1} indicating only a small proportion of nitrogen presented in the biochar, and this peak also overlapped by the peak at 1600 cm^{-1}. This could be due to the C=O asymmetric vibration of O-C=O which is in line with 4.9 at% of O-C=O groups detected by XPS (Table 5-7) (Jia and Thomas 2000). For example, the reduction of the adsorption intensity at 3400 cm^{-1} and the depletion of C-O stretching and O-H bending bands at 1211 and 1111 cm^{-1} (Jia and Thomas 2000, Xiao and Thomas 2005) of HY250-H80W2 were due to the removal of C-OH group, which was in agreement of C-OH content decrease from 3.7 to 0.2 at% as detected by XPS analysis (see Table 5-5). The band at 1701 cm^{-1} responsible for C=O in carboxylic acid of hydrochar HY250 was also reduced (Jia and Thomas 2000), which was also in agreement with the reduction of O-C=O from 8.7 to 4.9 at% in XPS O 1s (Table 5-5). Furthermore, carbon aliphatic symmetric stretching at ~2840 cm^{-1} and asymmetric stretching at ~2920 cm^{-1} (Yan *et al.* 2020) observed in HY250 were retained after cold plasma process, indicating the remain of some C sp^3 content in HY250-H80W2.

NH_3 heat treatment at 800°C also removed most of oxygen functional groups from hydrochar samples. FTIR spectra of NH_3 heat-treat hydrochar only showed adsorption in the wavenumber region of 1500-1600 cm^{-1}, indicating the presence of nitrogen functional groups in the form of pyridinic, pyridonic, and pyrrolic (see Figure 5-7 and Figure 5-12) (Jia *et al.* 2002, Xiao and Thomas 2005). It is noticeable that the adsorption of nitrogen functional groups in HY250-NH_3/800 in FTIR were stronger than other NH_3 heat-treated AC (N_2/600-1-NH_3/800, N_2/800-1-NH_3/800 and N_2/1000-1-NH_3/800 – Figure 5-6), indicating the higher nitrogen contents of NH_3 heat-treated hydrochar compared to NH_3 heat-treated AC. Therefore, the versatile structure of the precursor such as hydrochar allows better nitrogen incorporation than the rigid carbon structure such as biochar.

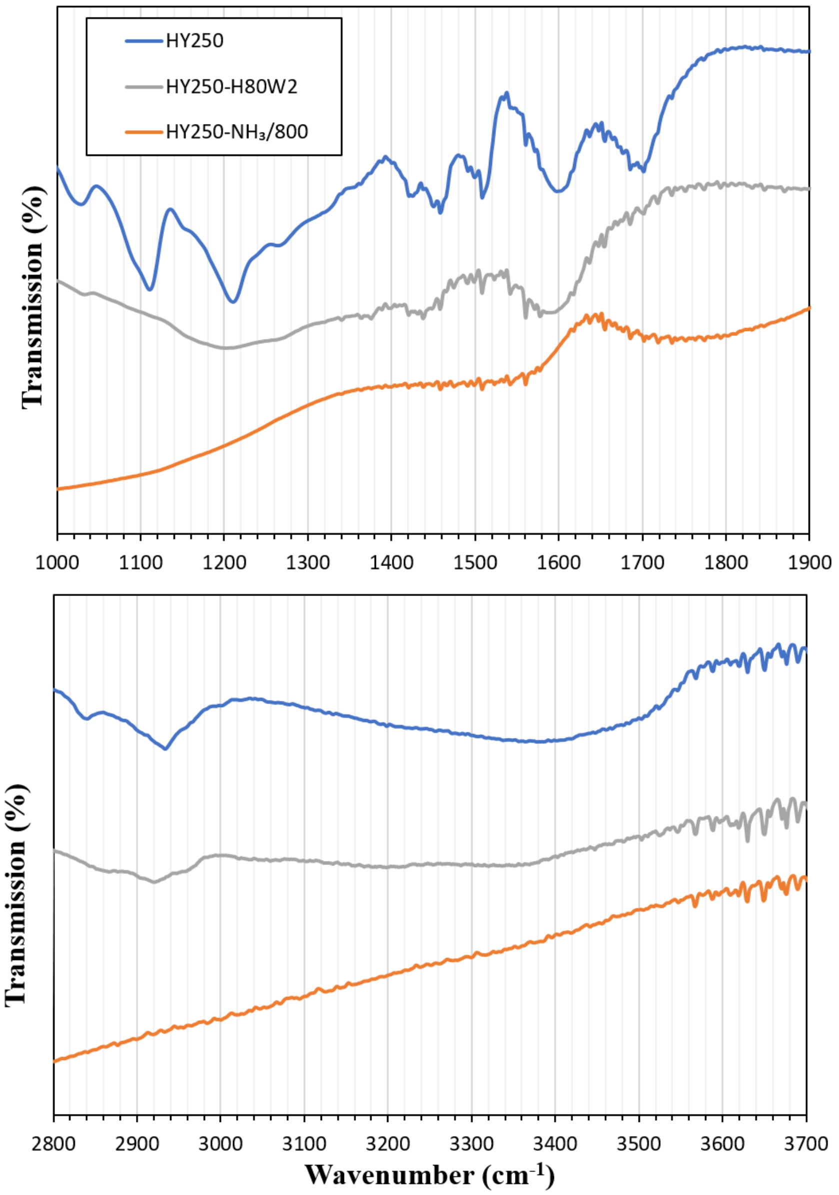

Figure 5-12 FTIR spectra of HY250, HY250-H80W2 and HY250-NH_3/800

5.4 Carbonaceous structure

5.4.1 Raman spectroscopy

Raman spectroscopy was performed on DBD cold plasma-treated biochar in order to understand how operating conditions of cold plasma influenced the carbonaceous structure. The I_D/I_G ratio (intensity ratio between D and G peaks) is widely used to assess the carbonaceous structure of biochar (Arkhipova *et al.* 2017, Kierkowicz *et al.* 2018). Table 5-11 shows no significant change in I_D/I_G ratios in the range of 0.87-0.95 over the tested plasma power, holding times and gas flow rates. The full width at half maximum of D peaks (W_D) for all DBD cold plasma-treated biochar also remained constant with varying cold plasma power

(20-80 W), flow rates (20-40 mL min^{-1}) and treating time (1-2 h) (73.2-87.2 cm^{-1}). The stable I_D/I_G ratios and W_D can be concluded that tested cold plasma operating conditions had no influence on the carbonaceous structure.

DBD cold plasma-treated hydrochar had similar structure as hydrochar. Raman spectroscopy profiles of hydrochar and DBD cold plasma-treated hydrochar were not recorded due to highly amorphous carbon content, and microscope images during Raman spectroscopy analysis showed the colour of these samples were changed after applying laser beam on Raman analysis although DBD cold plasma-treated hydrochar has gone through significant change in functional groups. Therefore, DBD cold plasma is not an effective method to modify molecular structure of both biochar and hydrochar. On the other hand, NH_3 heat-treated hydrochar showed considerable increase of I_D/I_G ratio to 0.96-0.97 and low G peak full width at half maximum (69 cm^{-1}) (see Table 5-11). Heat treatment temperature (HTT) of 800°C allowed the transition from amorphous carbon structure to more ordered carbonaceous structure.

The results from DBD cold plasma-treated biochar and hydrochar is in agreement with others (Fang *et al.* 2019, Hoque *et al.* 2020). In the study of Fang *et al.*, carbon nanotubes were modified using microwave plasma power of 120 W at 2 kPa in N_2, and I_D/I_G ratio remained in the range 0.85-0.86 when increasing treatment time from 10 to 60 min. I_D/I_G ratio of carbon thin film annealed at 900°C also remained in the range 0.74-0.85 after radio frequency cold plasma treatment (10 W, 13.56 MHz and N_2 20 mL min^{-1}) (Hoque *et al.* 2020). As discussed in sections 5.2 about the incorporation of nitrogen into biochar through DBD cold plasma, there is increase in nitrogen contents up to 8.7 at% (see Table 5-5), and C sp^3 contents also increased from 8.8 at% to 20.9-32.9 at% for biochar followed by the decrease of C sp^2 contents (see Table 5-5). It is suggested that DBD cold plasma treatment reactively modifies C sp^2 regions (graphene edges/defects) by incorporating heteroatoms such as nitrogen and hydrogen into carbon structure. However, DBD cold plasma only influences surface of biochar rather than in bulk, so Raman spectroscopy could not detect this level of change and did not result in any change to I_D/I_G ratio. This also explained why full width at half maximum of D (W_D) and G peaks (W_G) only fluctuated in the narrow range of 230.3-256.0 cm^{-1} and 73.2-87.2 cm^{-1} without significant change (see Table 5-11).

Table 5-11 Raman spectroscopy parameters I_D/I_G (Intensity ratio between D and G peaks), A_D/A_G (Area ratio between D and G peaks), full-width at half maximum of D peak (W_D) and G peak (W_G), and D and G peak positions of biochar and hydrochar

Carbon sample	**I_D/I_G**	**A_D/A_G**	**W_D (cm^{-1})**	**W_G (cm^{-1})**	**D-peak position (cm^{-1})**	**G-peak position (cm^{-1})**
N_2/800-1	0.90 ± 0.02	2.83 ± 0.09	250.6 ± 5.8	79.9 ± 0.6	1341.1 ± 0.2	1596.2 ± 1.3
N_2/800-1-H20W1	0.95 ± 0.02	2.80 ± 0.09	251.4 ± 5.8	85.5 ± 0.6	1342.3 ± 0.2	1595.9 ± 1.3
N_2/800-1-H20W2	0.90 ± 0.02	2.91 ± 0.09	246.3 ± 5.7	76.2 ± 0.6	1337.2 ± 0.2	1596.5 ± 1.3
N_2/800-1-L20W1	0.94 ± 0.02	2.80 ± 0.09	247.9 ± 5.7	83.5 ± 0.6	1338.1 ± 0.2	1594.1 ± 1.3
N_2/800-1-L20W2	0.94 ± 0.02	2.63 ± 0.08	243.0 ± 5.6	87.2 ± 0.7	1341.0 ± 0.2	1595.8 ± 1.3
N_2/800-1-H40W1	0.93 ± 0.02	2.84 ± 0.09	244.1 ± 5.6	79.7 ± 0.6	1339.3 ± 0.2	1596.5 ± 1.3
N_2/800-1-H40W2	0.88 ± 0.02	2.84 ± 0.09	242.9 ± 5.6	75.7 ± 0.6	1337.9 ± 0.2	1597.7 ± 1.3
N_2/800-1-L40W1	0.91 ± 0.02	2.84 ± 0.09	230.3 ± 5.3	74.0 ± 0.6	1337.4 ± 0.2	1599.6 ± 1.3
N_2/800-1-L40W2	0.93 ± 0.02	2.86 ± 0.09	247.1 ± 5.7	80.5 ± 0.6	1340.6 ± 0.2	1596.8 ± 1.3
N_2/800-1-H80W1	0.87 ± 0.02	2.87 ± 0.09	241.3 ± 5.6	73.2 ± 0.5	1339.0 ± 0.2	1599.4 ± 1.3
N_2/800-1-H80W2	0.93 ± 0.02	2.87 ± 0.09	252.7 ± 5.8	81.4 ± 0.6	1342.5 ± 0.2	1597.6 ± 1.3
N_2/800-1-L80W1	0.94 ± 0.02	2.98 ± 0.09	254.7 ± 5.9	78.9 ± 0.6	1341.2 ± 0.2	1597.3 ± 1.3
N_2/800-1-L80W2	0.92 ± 0.02	2.91 ± 0.09	256.0 ± 5.9	78.9 ± 0.6	1341.2 ± 0.2	1595.5 ± 1.3
N_2/600-1-NH_3/800	0.90 ± 0.02	3.09 ± 0.09	220.6 ± 5.1	70.6 ± 0.5	1333.6 ± 0.2	1597.1 ± 1.3
N_2/800-1-NH_3/800	0.99 ± 0.02	3.19 ± 0.05	220.6 ± 5.1	68.2 ± 0.5	1337.7 ± 0.3	1602.6 ± 1.3
HY200-NH_3/800	0.96 ± 0.02	3.21 ± 0.10	231.7 ± 5.3	69.1 ± 0.5	1340.3 ± 0.2	1600.4 ± 1.3
HY250-NH_3/800	0.97 ± 0.02	3.23 ± 0.10	229.0 ± 5.3	69.0 ± 0.5	1339.3 ± 0.2	1600.6 ± 1.3

5.4.2 X-ray diffraction

Powder X-ray diffraction (PXRD) profiles of biochar and hydrochar showed broad peaks at ~22-23° and ~43° presenting for (002) and (100) carbon crystallites respectively. Crystal thickness, crystal diameter and interlayer distance of DBD cold plasma-treated biochar (N_2/800-1-H20W2, N_2/800-1-H40W2 and N_2/800-1-H80W2) were similar compared to their precursor N_2/800-1 (Figure 5-13 and Table 5-12). L_c, d_{002}, and L_a of these samples slightly decreased with increasing plasma powers. This slightly decrease of crystal thickness was in conjunction with the decrease in interlayer distance. It appears that high plasma power allowed the removal of other atoms rather than carbon residing inside carbon layers, resulting in the reduce of crystal thickness from 10.44 ± 0.05 Å of N_2/800-1-H20W2 to 9.08 ± 0.05 Å of N_2/800-1-H80W2. DBD cold plasma treatment also allowed NH_3 to react with carbon atoms on edge sites of carbon crystal, leading to the decrease of L_a from 24.65 ± 0.34 to 20.52 ± 0.28 Å when increasing plasma power from 20 W to 80 W. The study of García *et al.* on influence of microwave plasma on pine wood biochar in O_2 atmosphere (2.45 GHz, 150 W power, 0.1 kPa) also suggested that the bulk carbonaceous structure remained stable during the oxygen plasma treatment through XRD result (García *et al.* 1998). NH_3 heat-treated AC (N_2/600-1-NH_3/800, N_2/800-1-NH_3/800, N_2/1000-1-NH_3/800) slightly increase the crystal diameter L_a from 22.47 Å to 23.00-27.96 Å compared to biochar N_2/800-1.

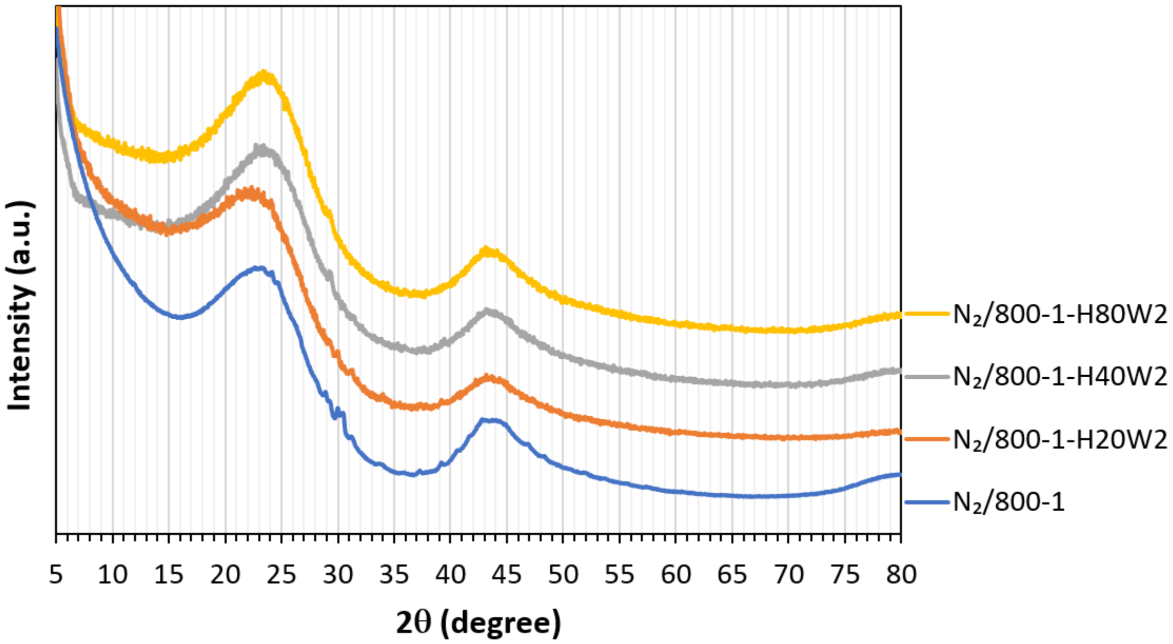

Figure 5-13 XRD patterns of DBD cold plasma-treated biochar at 20, 40 and 80 W for 2 h in NH_3 (40 mL min^{-1}) (N_2/800-1-H20W2, N_2/800-1-H40W2 and N_2/800-1-H80W2) and biochar precursor N_2/800-1

Table 5-12 Crystallite thickness L_c, interlayer distance d_{002}, and crystal diameter L_a from XRD

Carbon sample	Crystal thickness, L_c (Å)	Interlayer distance, d_{002} (Å)	Crystal diameter, L_a (Å)
N_2/800-1	10.29 ± 0.05	3.86 ± 0.02	22.47 ± 0.31
N_2/800-1-H20W2	10.44 ± 0.05	3.97 ± 0.02	24.65 ± 0.34
N_2/800-1-H40W2	10.25 ± 0.05	3.91 ± 0.02	23.54 ± 0.33
N_2/800-1-H80W2	9.08 ± 0.05	3.79 ± 0.02	20.52 ± 0.28
N_2/600-1-NH_3/800	11.75 ± 0.05	3.51 ± 0.02	25.82 ± 0.36
N_2/800-1-NH_3/800	10.24 ± 0.05	3.76 ± 0.01	26.99 ± 0.37
N_2/1000-1-NH_3/800	10.59 ± 0.05	3.65 ± 0.02	27.96 ± 0.39
HY200	ND	ND	ND
HY250	ND	ND	ND
HY290	ND	ND	ND
HY200-NH_3/800	12.05 ± 0.06	3.51 ± 0.02	25.17 ± 0.35
HY250-NH_3/800	12.41 ± 0.06	3.57 ± 0.02	26.40 ± 0.37
HY290-NH_3/800	12.16 ± 0.06	3.56 ± 0.02	25.48 ± 0.35
HY200-H80W2	9.95 ± 0.05	4.06 ± 0.02	15.10 ± 0.21
HY250-H80W2	10.29 ± 0.05	4.12 ± 0.02	14.39 ± 0.20
HY290-H80W2	12.23 ± 0.06	3.90 ± 0.02	14.62 ± 0.20

Table note: L_c, L_a and d_{002} of HY200, HY250 and HY290 were not calculated due to amorphous carbon structure. ND: not detected

Crystallite dimensions of hydrochar were not calculated due to very broad peak at 10-30° and no peak of ~43° recorded, indicating that hydrochar was highly amorphous and the conditions of HTC treatment was not intensive enough to alter lignocellulosic contents in walnut shells into multi-layered carbonaceous structure (Figure 5-1). The structure of DBD cold plasma treated hydrochar showed enhancement in carbonaceous structure, but their PXRD patterns still presented broad peaks at ~43°, indicating very small carbon crystal being distributed randomly in these samples. The d_{002} values remaining high (3.9-4.12 Å) revealed that many heteroatoms including oxygen and nitrogen residing between these carbon layers. Moreover, the peak at ~11° of DBD cold plasma-treated hydrochar, which is distinctive for (002) on graphene oxide, was also detected in XRD patterns of DBD cold plasma-treated hydrochars (Figure 5-14) (Stobinski *et al.* 2014). The evolution of the peak ~11° in PXRD profiles of DBD cold plasma-treated hydrochar and the laser sensitivity of these samples under Raman spectroscopy indicated that cold plasma treatment did not intensively alter the structure of hydrochar. Together with the decrease in oxygen content as seen in XPS O 1s (Table 5-9), it is reasonably assumed that cold plasma only influences layers on the surface of hydrochar, which agrees with other studies (Chetty *et al.* 2009, Su *et al.* 2020). This is different from PXRD diameters recorded for NH_3 heat-treated hydrochar. High temperatures allowed rearrangement of carbon structure to create highly ordered carbon structure with higher L_c and L_a values (12.05-12.41 and 25.17-26.40 Å respectively) and small interlayer distance (3.51-3.57 Å) (Table 5-12).

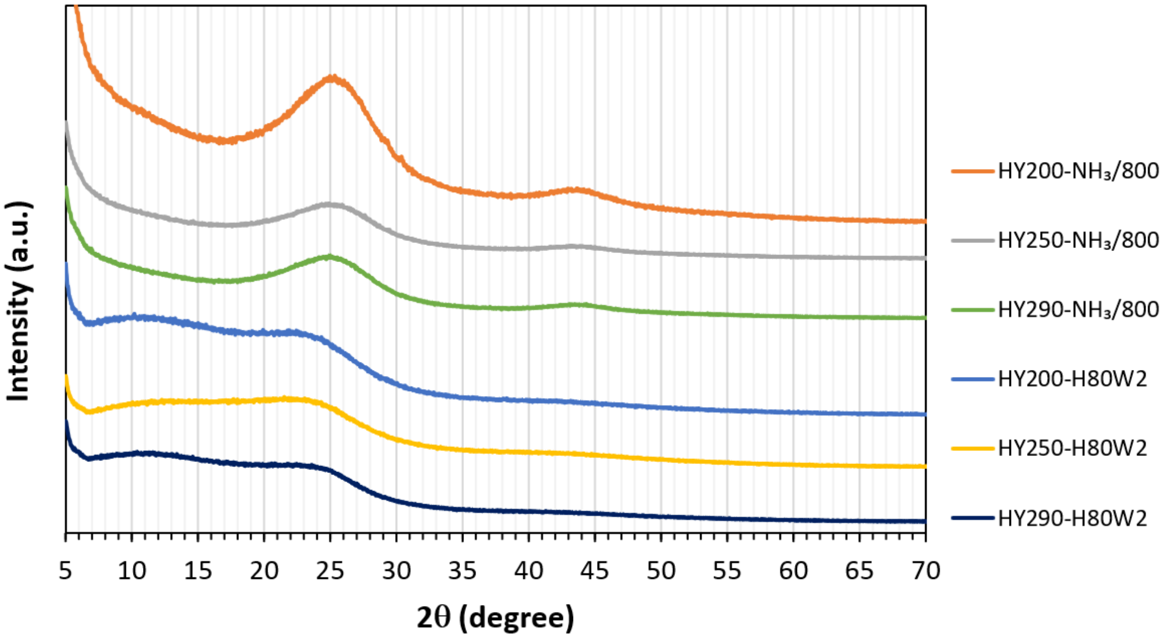

Figure 5-14 XRD patterns of DBD cold plasma-treated hydrochar at 80 W in NH_3 (40 mL min^{-1}) and NH_3 heat-treated hydrochar at 800°C for 2 h in NH_3 (40 mL min^{-1})

5.5 Gas sorption-desorption behaviours of functionalized biochar and hydrochar

DBD cold plasma treatment had little influence on the development of porosity in biochar N_2/800-1. Ultramicropore surface area S_{CO2} reduced from 591 m^2 g^{-1} in N_2/800-1 to 487-529 m^2 g^{-1} in DBD cold plasma-treated biochar (N_2/800-1-H20W2, N_2/800-1-H40W2 and N_2/800-1-H80W2) (Table 5-13), and S_{BET} of these biochar samples also reduced to ~1-2 m^2 g^{-1} after the treatment. The remarkable difference of S_{CO2} and S_{BET} can be attributed to activated diffusion effect due to sintering effect of plasma (Marsh 1987, Mian *et al.* 2018).

DBD cold plasma treatment on hydrochar slightly improved S_{CO2}, from 77 m^2 g^{-1} in HY200 to 261 m^2 g^{-1} HY200-H80W2, and 100 m^2 g^{-1} in HY250 to 247 m^2 g^{-1} in HY250-H80W2. These

DBD cold plasma-treated hydrochar samples also presented activated diffusion effect, with S_{BET} varying at extremely low value at 4-6 m^2 g^{-1}. SEM images of hydrochar (HY200, HY250, HY290) do not show porous structure but many spheres on the surface (see Figure 5-2), so DBD cold plasma treatment did not improve porous structure of hydrochar.

The negligible influence of DBD cold plasma treatment on surface area and porosity on both biochar and hydrochar in this study is in agreement with study of Ning *et al.* (Ning *et al.* 2018). In the study of Ning *et al.*, S_{BET} and total pore volumes of walnut shell AC (pyrolysed in N_2 at 700°C for 1 h and activated with KOH at 700°C for 1 h) only varied in the range of 526-640 m^2 g^{-1} and 0.247-0.295 cm^3 g^{-1} respectively after treated in DBD cold plasma in NH_3 for 10 min at various output voltages of 5.6-8.0 kV.

NH_3 heat-treated hydrochar showed a significant improvement in ultramicropore volume with S_{CO2} increasing up to 811 and 775 m^2 g^{-1} in HY200-NH_3/800 and HY250-NH_3/800. Heat treatment in NH_3 at 800°C, on the other hand, fostered gasification reactions with carbon and increase S_{BET} significantly as discussed in section 4.1. This is evident that DBD cold plasma is not suitable to modify the surface area of carbon materials.

Table 5-13 Pore structure characterization by CO_2 and N_2 adsorption-desorption

Carbon sample	**S_{CO2} (m^2 g^{-1})**	**V_{CO2} (cm^3 g^{-1})**	**S_{BET} (m^2 g^{-1})**	**V_{N2} (cm^3 g^{-1})**	**V_{micro} (cm^3 g^{-1})**	**V_{meso} (cm^3 g^{-1})**
N_2/800-1	591 ± 4	0.220 ± 0.001	29 ± 1	0.050 ± 0.001	0.009	0.041
N_2/800-1-H20W2	529 ± 3	0.197 ± 0.001	1.5 ± 1	0.023 ± 0.001	0.001	0.022
N_2/800-1-H40W2	487 ± 2	0.181 ± 0.001				
N_2/800-1-H80W2	519 ± 2	0.193 ± 0.001	1.1 ± 1	0.021 ± 0.001	0.001	0.020
N_2/600-1-NH_3/800			869 ± 18	0.395 ± 0.004	0.328	0.067
N_2/800-1-NH_3/800	686 ± 4	0.256 ± 0.001	720 ± 15	0.337 ± 0.003	0.273	0.064
N_2/1000-1-NH_3/800	732 ± 5	0.273 ± 0.001	541 ± 11	0.292 ± 0.003	0.205	0.087
HY200	77 ± 1	0.029 ± 0.001				
HY250	100 ± 1	0.037 ± 0.001				
HY290	92 ± 1	0.034 ± 0.001				
HY200-NH_3/800	811 ± 6	0.302 ± 0.001				
HY250-NH_3/800	775 ± 5	0.289 ± 0.001	785 ± 16	0.403 ± 0.004	0.302	0.101
HY290-NH_3/800			748 ± 15	0.369 ± 0.003	0.286	0.083
HY200-H80W2	261 ± 2	0.097 ± 0.001				
HY250-H80W2	247 ± 2	0.092 ± 0.001	6 ± 1	0.070 ± 0.001	0.002	0.068
HY290-H80W2			4 ± 1	0.030 ± 0.001	0.001	0.029

Note: S_{CO2}: ultramicropore surface area, determined by using DR plot and CO_2 adsorption at 0°C; V_{CO2}: ultramicropore volume determined using DR plot on CO_2 adsorption at 0°C; S_{BET}: total surface area determined by BET plot ($p/p° = 1\times10^{-3}$-0.06) and N_2 adsorption at -196°C; V_{N2}: total pore volume determined by N_2 adsorption at -196°C at $p/p° = 0.995$; V_{micro}: micropore volume (0.3-2 nm) determined by using DR plot on N_2 adsorption at -196°C; V_{meso}: subtraction of V_{micro} from V_{N2}.

5.6 Discussion on mechanism of nitrogen incorporation into biomass-derived carbon under DBD cold plasma and heat treatment in NH_3

Functionalisation using DBD cold plasma and heat treatment in NH_3 environment on two different precursors: biochar pyrolysed at 600-1000°C and hydrochar obtained from HTC at 200-290°C) allows to reveal some insights on the mechanism of nitrogen incorporation. First, as discussed about the bulk and surface functional groups (see sections 5.2.1, 5.2.2, 5.3.1, and 5.3.2), both DBD cold plasma and heat treatment alter functional groups on the surface of both biochar and hydrochar. The surface nitrogen contents varied in the range of 2.6-8.9 at% (see Table 5-5 and Table 5-9) depending on precursors and operating conditions, while total nitrogen contents also increased up to 8.28 wt% (see Table 5-4 and Table 5-8). However, while the mechanism of nitrogen incorporation to carbon materials has been studied thoroughly (Stöhr *et al.* 1991, Jansen and van Bekkum 1995, Pels *et al.* 1995), it could not explain the differences in XPS N 1s peaks of DBD cold plasma-treated biochar and hydrochar.

However, TPD results did not fully support the XPS data. Most of nitrogen in DBD cold plasma-treated biochar were in the forms of N-6 and N-5 with little content of N-X, but the TPD profiles of these samples yielded significant NO desorption at low temperature range (300-800°C) and limited N_2 desorption at 1200°C (Figure 5-8). This contrasted with the N_2 evolution at 900-1200°C of both NH_3 heat-treated AC (Figure 5-8). Furthermore, HCN were also found in TPD profiles of two DBD cold plasma-treated biochar (N_2/800-1-H20W2 and N_2/800-1-H40W2), but not in other NH_3 heat-treated AC and hydrochar.

Heat treatment of biochar in NH_3 effectively introduced high nitrogen content to carbons through decomposition and condensation reactions between carbon and NH_3 to form pyrrolic-N, pyridinic-N and quaternary-N. HTT ranges of 600-1000°C is sufficient to transform nitrogen in NH_3 into carbon ring structures, and increased nitrogen content to 12.7-13.9 wt% for anthralur char (Stöhr *et al.* 1991), 6.5-7.3 wt% for bituminous coals (Pietrzak *et al.* 2010), and 8.56 wt% for corn straw biochar (Lian *et al.* 2016). It is evident that N_2 desorption at temperatures > 950°C is due to reactions of mobile surface nitrogen atoms in which most of nitrogen was in the form of N-5, N-6 and N-Q (Xiao *et al.* 2005). XPS data of NH_3 heat-treated AC and hydrochar in this study supported TPD data of these carbon samples, and most of nitrogen should be in the forms of N-5 and N-6.

Therefore, it is not suitable to interpret XPS data of DBD cold plasma-treated biochar into N-5, N-6, and N-Q due to the unusual behaviours of TPD profiles of these samples. It has been noticed that XPS N 1s peaks could also been deconvoluted into thermally unstable nitrogen groups such as amine, nitrile, and amide/ lactam-N functional groups. First, XPS N1s binding energy of amine groups C-$NH_{x=1,2}$ is ~399.0-399.4 eV (Pels *et al.* 1995, Manakhov *et al.* 2014), close to binding energies of pyridinic-N (398.7 ± 0.3 eV) (Pels *et al.* 1995, Chen *et al.* 2018). Second, binding energy of amide/lactam N-C=O is ~400.3 eV, close to pyrrolic-N (400.3 ± 0.3 eV) used in this study (Pels *et al.* 1995, Chen *et al.* 2018). Finally, XSP N 1s binding energy of nitrile group -C≡N is ~399.5-399.7 eV, between binding energies values of amine and amide/lactam (Pels *et al.* 1995, Manakhov *et al.* 2014).

As discussed in section 5.2.4 on TPD profiles of DBD cold plasma-treated and NH_3 heat-treated biochar, DBD cold plasma-treated biochar released majority of NO at 300-800°C and only a small amount of N_2 at high temperatures (900-1200°C) (see Figure 5-8). DBD cold plasma-treated biochar N_2/800-1-H20W2 and N_2/800-1-H40W2 also showed a small desorption of HCN at temperatures < 400°C (see Figure 5-9). Comparison to significant desorption of N_2 at 900-1200°C of N_2/800-1-NH_3/800 shows that nitrogen groups in DBD cold plasma-treated biochar are thermally unstable nitrogen groups (amine, nitrile, and amide).

This is in line with some studies on NH_3 treatment in low temperature range of 200-400°C. For example, the study of Shafeeyan *et al.* showed that the nitrogen contents of palm shell biochar after two steps activation with air (at 400°C) and NH_3 (at 400 and 800°C) introduced more nitrogen to biochar (3.7-4.6 wt%) compared to AC heat treated with NH_3 only (2.1-3.1 wt%) (Shafeeyan *et al.* 2011) due to the carboxylic and hydroxyl groups presented on the surface of carbon, and these oxygen functional groups reacted with NH_3 to incorporate more nitrogen:

$$-COO^-NH_4^+ \rightarrow -CO\text{-}NH_2 + H_2O$$

$$-CO\text{-}NH_2 \rightarrow C\equiv N + H_2O$$

$$-OH + NH_3 \rightarrow -NH_2 + H_2O$$

Furthermore, it is also suggested that C-N bonds can be formed due to the C-C bond rupture and nitrogen ion bombardment on the surface of carbon material to create C-NH_x (Yook *et al.* 2010). The presence of these nitrogen functional groups could also influence the determination of oxygen components from XPS O 1s. XPS O 1s binding energy of oxygen in amide group N-C=O is ~531.2 eV, and this is as the same as the binding energy of C=O (531.4 ± 0.2 eV) (Wang *et al.* 2001, Yang *et al.* 2009, Huang *et al.* 2018). Therefore, the XPS O 1s peak at 531.4 eV could not be strictly interpreted as C=O content in the case of DBD cold plasma-treated biochar and hydrochar.

These results show that XPS could not effectively distinguish pyridinic-N and pyrrolic-N from amine, nitrile and amide/lactam-N functional groups. Other analysis such as TPD should be performed to ascertain XPS result.

The mechanism of reactions between biochar/hydrochar and NH_3 in DBD cold plasma treatment is suggested as followed: NH_3 molecule is split into radicals and ions, then these radicals and ions react with carbons to form thermally unstable nitrogen functional groups such as amide ($-CO-NH_2$), nitrile ($-C\equiv N$) and amine ($-NH_2$). During cold plasma, NH_2, NH, H, excited NH_3 radicals and ions NH_4^+, NH_3^+, H^+ are formed due to collisions of NH_3 molecules with the energetic electrons produced in the discharge. Table 5-14 summarises major chemical reactions for NH_3 in cold plasma. These nitrogen-containing ions and radicals react with carbon free radicals in biochar and hydrochar, which are produced in DBD cold plasma to form covalent C-N bonds and/or substitute C atoms in graphene structures.

Table 5-14 Major chemical reactions for NH_3 in cold plasma

No.	**Reaction**	**Reaction rate coefficient**	**Reference**
1	$NH_3 + e \rightarrow NH_3^+ + 2e$	-	(Bavafa *et al.* 2008)
2	$NH_3 + e \rightarrow NH_2^+ + H^\bullet + 2e$	-	(Bavafa *et al.* 2008)
3	$NH_3 + e \rightarrow NH_2^+ + H^\bullet + e$	-	(Bavafa *et al.* 2008)
4	$NH_3 + e \rightarrow NH^+ + 2H^\bullet + 2e$	-	(Bavafa *et al.* 2008)
5	$NH_2^\bullet + H^\bullet \rightarrow NH_3$	10^{-13}	(Dollet *et al.* 1995)
6	$NH_2^\bullet + NH_2^\bullet \rightarrow NH^\bullet + NH_3$	1.4×10^{-12}	(Dollet *et al.* 1995)
7	$NH_3 + NH_3^+ \rightarrow NH_2^\bullet + NH_4^+$	2.2×10^{-9}	(Rybin *et al.* 2016)
8	$NH_3 + NH_2^+ \rightarrow NH_2^\bullet + NH_3^+$	10^{-9}	(Rybin *et al.* 2016)

Although reactions (7) and (8) have high reaction rate coefficients, but they are limited by NH_x^+ (x = 2,3). NH_4^+ is unreactive towards NH_3, since the reactions between NH_x^+ (x = 2,3) and NH_3 are fast, it can be suggested that the dominant ions in the discharge will be NH_4^+. Dominant ions in the discharge will be NH_4^+ (Dollet *et al.* 1995). $NH_2^\bullet$ is considered as an important radical in NH_3 plasma system.

Low DBD plasma power (20 W) favours the formation of amide groups, and some amide groups can react to form nitrile (-C≡N) but high powers (40 W and 80 W) mainly favour the formation of amine groups (-NH_2) (Figure 5-15). It is reasonably assumed that these groups were then furtherly converted into thermally stable groups including N-5, N-6 and N-X through rearrangement reactions. This result and explanation, however, contrasted with the study of Yook *et al.* with increasing source power from 25-200W reducing the percentage of amino/total nitrogen from 25 to 15% (Yook *et al.* 2010). The difference may be stemmed from difference in analysis technique. In this study, the transition from amide to amine groups with increasing DBD cold plasma power was observed directly through the change in XPS binding energies, and XPS is a non-destructive analysis which does not influence the chemical states of samples. However, the amine and total nitrogen contents in the study of Yook *et al.* was determined from optical emission spectroscopy. During the optical emission spectroscopy, nitrogen species can react with each other to increase the yield of N_2 and C≡N and decreased the ratio of amino/total nitrogen.

The results from this study also show that DBD cold plasma power could not convert amine, nitrile and amide groups into pyridinic-N, pyrrolic-N and quaternary-N. The study of Li *et al.* on pyrolysis of penicillin presented pathway to convert tyrosine (containing NH_2 group) is converted to indole (containing pyrrolic-N) through a series of isomerisation, decomposition and cyclization reactions (Zhang *et al.* 2020). This suggests there is a possible pathway to transform amine, nitrile, and amide groups into pyridinic-N, pyrrolic-N and quaternary-N (see Figure 5-16). However, to the best of my knowledge, there has been no thorough study about the influence of cold plasma on the transformation of amine, nitrile, and amide groups into pyridinic-N, pyrrolic-N and quaternary-N.

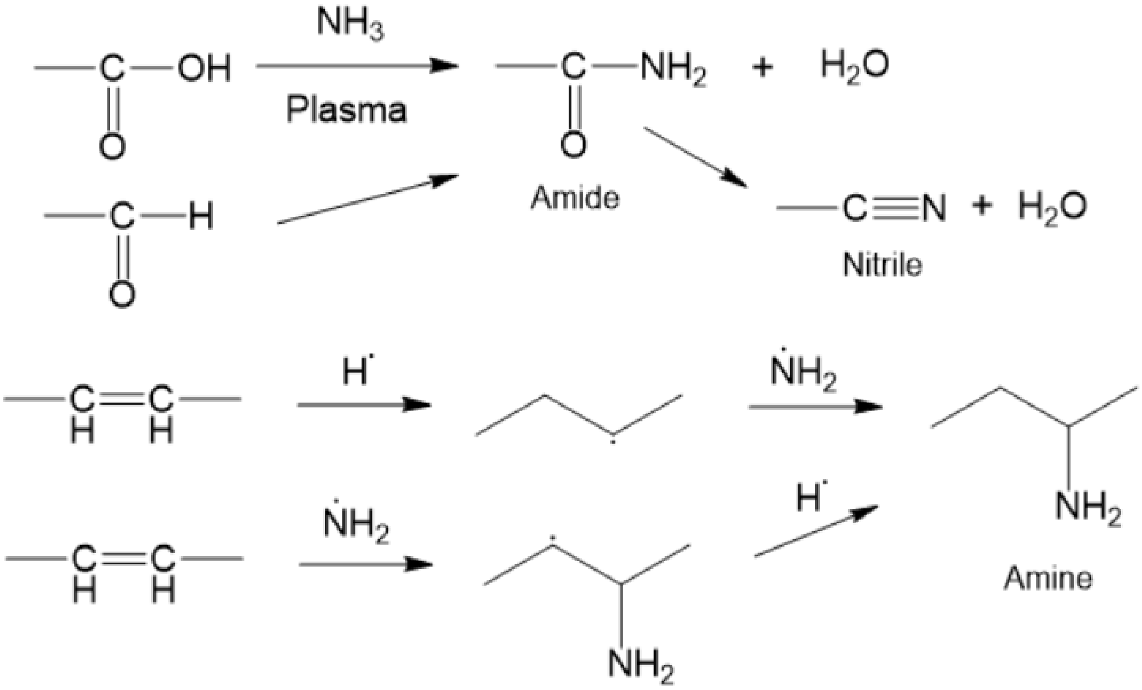

Figure 5-15 Suggested reaction mechanism of NH_3 with carbon in DBD treatment

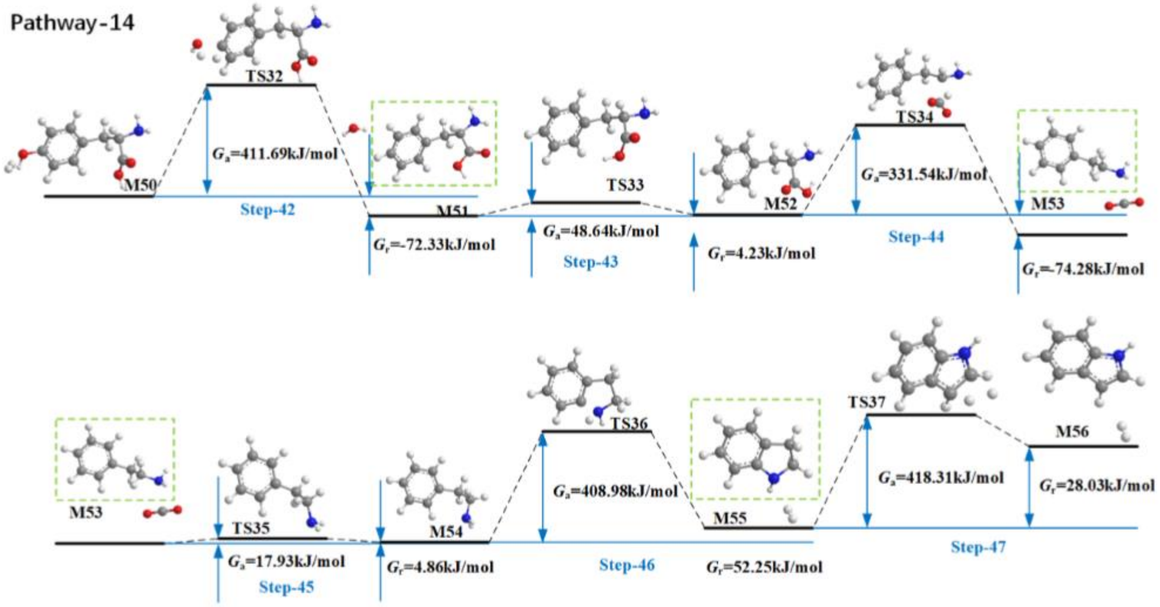

Figure 5-16 Suggested mechanism for formation of indole from tyrosine through pyrolysis (Zhang *et al.* 2020)

Further peak deconvolution of XPS N 1s peaks after being adjusted to amine and amide groups for some DBD cold plasma-treated biochar is presented in Table 5-15. Due to the similar binding energies between amine groups ($-NH_x$) and N-6 and between amide and N-5, the N-6 contents from Table 5-7 can be interpreted as amine groups ($-NH_x$), and the N-5 contents from Table 5-7 can be interpreted as amide groups (N-C=O).

Table 5-15 Nitrogen content of some DBD-treated biochar after being adjusted to new fitting for amine and amide groups to XPS N 1s peaks

Carbon sample	**Component from N 1s profiles (at%)**			
	Amine C-NH$_x$	**Amide N-C=O**	**N-Q**	**N-X**
N_2/800-1-H20W2	1.8	4.4	0.4	0.1
N_2/800-1-H40W2	2.0	2.2	0.6	0.1
N_2/800-1-H80W2	4.3	1.7	0.2	0.3

Carbonaceous structure analysis from XRD, Raman spectroscopy, surface area and pore structure analysis from gas sorption-desorption also revealed that DBD cold plasma in NH_3 atmosphere only influences functional groups regardless of significant differences in carbonaceous amorphous structure and functional groups of biochar and hydrochar. Heat treatment in NH_3, however, enhanced both carbonaceous structure and porous structure of biochar and hydrochar.

5.7 Cyclic voltammetry

5.7.1 Functionalised biochar

As discussed in Chapter 4, carbonization at temperatures up to 800°C give the largest increase in the VO^{2+}/VO_2^+ couple in cyclic voltammetry while functional groups increase in the V^{2+}/V^{3+} and V^{3+}/VO^{2+} couples. Pyridinic and pyrrolic groups also enhance CV of PVDF/ walnut shell-derived carbon composite. Therefore, the influence of different nitrogen functional groups on VO^{2+}/VO_2^+ couple will be examined more thoroughly in this Chapter 5. NH_3 heat-treated AC provided a series of AC with pyridinic-N, pyrrolic-N and quaternary-N, and DBD cold plasma-treated biochar provided a series of biochar with amine, nitrile, and amide groups.

Figure 5-17 shows the cyclic voltammetry (CV) profiles of DBD cold plasma-treated biochar (N_2/800-1-H20W2, N_2/800-1-H40W2, and N_2/800-1-H80W2). Peak separation of the oxidation from VO^{2+} to VO_2^+ and the reduction from VO_2^+ to VO^{2+} of N_2/800-1-H20W2 and N_2/800-1-H80W2 were 0.98 V and 0.78 V compared to 0.28 V and 0.27 V of N_2/800-1 and N_2/800-1-H40W2. Furthermore, peak currents of VO^{2+}/VO_2^+ couple of N_2/800-1-H20W2 and N_2/800-1-H80W2 also lowered than those of N_2/800-1 and N_2/800-1-H40W2. This indicates higher irreversibility and lower electrochemical reactivity of VO^{2+}/VO_2^+ couple of biochar N_2/800-1-H40W2.

Increasing DBD cold plasma power from 20 W to 80 W did not change carbonaceous molecular structure as shown in Raman and PXRD profiles (see Table 5-11 and Table 5-12). Significant different in CO_2 DR micropore volume (0.181-0.197 cm^3 g^{-1}) and BET N_2 total pore volume (0.021-0.023 cm^3 g^{-1}) (see Table 5-13) is evident that there is severe activated diffusion effect in DBD cold plasma-treated biochar. Surface nitrogen content of this DBD cold plasma-treated biochar series varies in a narrow range of 4.9-6.5 at% (Table 5-5). Also, total nitrogen contents also fluctuate in a small range of 1.06-1.39 wt% (Table 5-4). These changes in nitrogen contents are also similar to surface and bulk oxygen contents. Therefore, both carbonaceous amorphous structure and porosity appear not to have marked effect on electrochemical behaviours of this biochar series.

For this DBD cold plasma-treated biochar, the main difference in this DBD cold plasma-treated biochar is the ratio of amine-N and amide-N groups. From Table 5-7 and Table 5-15, the ratio of amine-N/amide-N groups in N_2/800-1-H40W2 is ~0.91, while the ratios for N_2/800-1-H20W2 and N_2/800-1-H80W2 are ~0.41 and ~2.5 respectively. It is evident that the ratio of amine-N/amide-N groups close to 1.0 benefits for the reversibility and increase electrochemical reactivity of VO^{2+}/VO_2^+ couple, and both amine-N and amide-N groups contribute to conversion between VO^{2+} and VO_2^+ ions.

Figure 5-17, however, presents little change to reactivity VO^{2+}/VO_2^+ couple of N_2/800-1-H40W2 compared to precursor N_2/800-1 despite the incorporation of amine-N and amide-N groups. The peak separation of these two samples remained almost identical (0.27 and 0.28 V). This could be due to only a small layer of nitrogen incorporated on the surface of biochar as discussed in XPS and total CHNO data (sections 5.2.1 and 5.2.2).

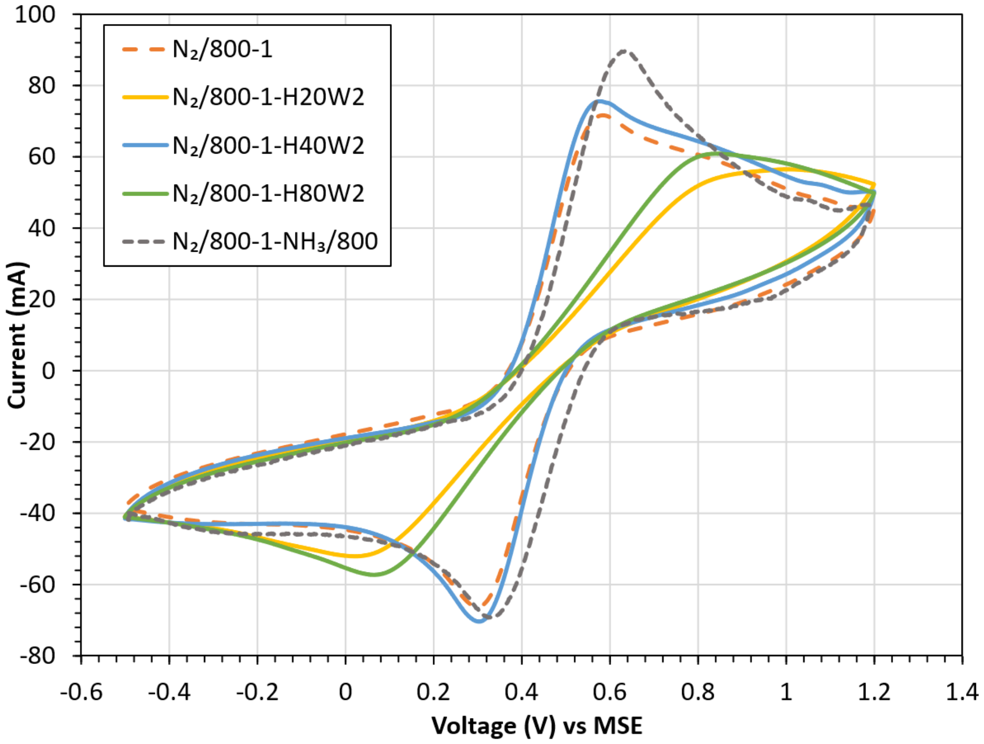

Figure 5-17 Cyclic voltammetry of biochar N_2/800-1 and DBD cold plasma-treated biochar in NH_3 (40 mL min^{-1}) at 20 W (N_2/800-1-H20W2), 40 W (N_2/800-1-H40W2) and 80 W (N_2/800-1-H80W2) in comparison with NH_3 heat-treated biochar at 800°C N_2/800-1-NH_3/800

The influence of pyridinic-N and pyrrolic-N on conversion between vanadium ions has been discussed in Chapter 4. Chapter 5 explores the impact of more biochar precursor prepared at different HTTs (600, 800, 1000°C) and corresponding NH_3 heat-treated AC at 800°C. From Figure 5-18, NH_3 heat-treated AC at 800°C samples (N_2/600-1-NH_3/800, N_2/800-1-NH_3/800 and N_2/1000-1-NH_3/800) increase peak currents of oxidation $VO^{2+} \rightarrow VO_2^+$ to 85, 90, and 85 mA, compared to 58, 71 and 67 mA of corresponding biochar precursor (N_2/600-1, N_2/800-1 and N_2/1000-1) respectively. However, there are less changes to reduction $VO_2^+ \rightarrow VO^{2+}$.

NH_3 heat-treated AC has similar CO_2 DR micropore volume (0.256-0.273 $cm^3\ g^{-1}$) and BET mesopore volume (0.064-0.067 $cm^3\ g^{-1}$) (see Table 5-13). NH_3 heat treatment increased N_2 DR micropore volume to 0.205-0.328 $cm^3\ g^{-1}$, which is 70-83% of total N_2 pore volume. BET mesopore volume of NH_3 heat-treated AC is also similar to mesopore volume of N_2/800-1 (0.041 to 0.064-0.067 $cm^3\ g^{-1}$). Some studies assigned the increase of surface area and porosity to the enhance of reactivity of VO^{2+}/ VO_2^+ (Xu *et al.* 2019), but the results from NH_3 heat-treated AC show that increase in surface area and pore volume of NH_3 heat-treated AC appears to have little influence on the conversion of VO^{2+} and VO_2^+. This agrees with the conclusions from electrochemical behaviours of two AC CO_2/800-1 and CO_2/800-1-K_2CO_3

discussed in Chapter 4, in which CO_2/800-1-K_2CO_3 has similar porous structure to CO_2/800-1, and the small increases in CV intensities are assigned to functional groups.

It is also little evident that carbon amorphous structure contributes to the conversion of VO^{2+}/VO_2^+ couple. The main change in carbon amorphous structure as shown Raman spectroscopy is the increase in I_D/I_G of N_2/600-1-NH_3/800 from 0.69 ± 0.02 to 0.90 ± 0.02 (see Table 4-7 and Table 5-11). PXRD also confirms the increase in L_c from 10.75 to 11.75 Å and L_a from 18.33 to 25.82 Å (see Table 4-8 and Table 5-12). However, this could not explain the increase in CV peak current of oxidation $VO^{2+} \rightarrow VO_2^+$ of N_2/600-1 and N_2/600-1-NH_3/800 (Figure 5-18). Comparison of carbonaceous amorphous structure of N_2/1000-1 and N_2/1000-1-NH_3/800 shows that L_c and L_a only vary in a very narrow range 9.99-10.59 and 26.85-27.96 Å (Table 4-8 and Table 5-12). After pyrolysed in N_2 at 1000°C, it is unlikely that NH_3 heat treatment at 800°C caused substantial change to amorphous structure of N_2/1000-1-NH_3/800. Despite that, both N_2/600-1-NH_3/800 and N_2/1000-1-NH_3/800 shows significant increase in CV peak of oxidation $VO^{2+} \rightarrow VO_2^+$. Therefore, carbon amorphous structure should not be the main factor influencing VO^{2+}/VO_2^+ couple.

This result indicates that nitrogen functional groups influence oxidation of $VO^{2+} \rightarrow VO_2^+$. Total nitrogen contents (see Table 5-4) and surface nitrogen content (see Table 5-5 and Table 5-7) confirm that NH_3 heat treatment replaces surface oxygen with nitrogen, and most nitrogen resides on surface of biochar. Significant surface nitrogen (3.1-5.6 at%) benefits for the oxidation of oxidation of $VO^{2+} \rightarrow VO_2^+$ with pyridinic-N/pyrrolic-N contents varying in the range of 1.78-2.00. NH_3 heat treatment may also increase the homogenous degree of surface of biochar.

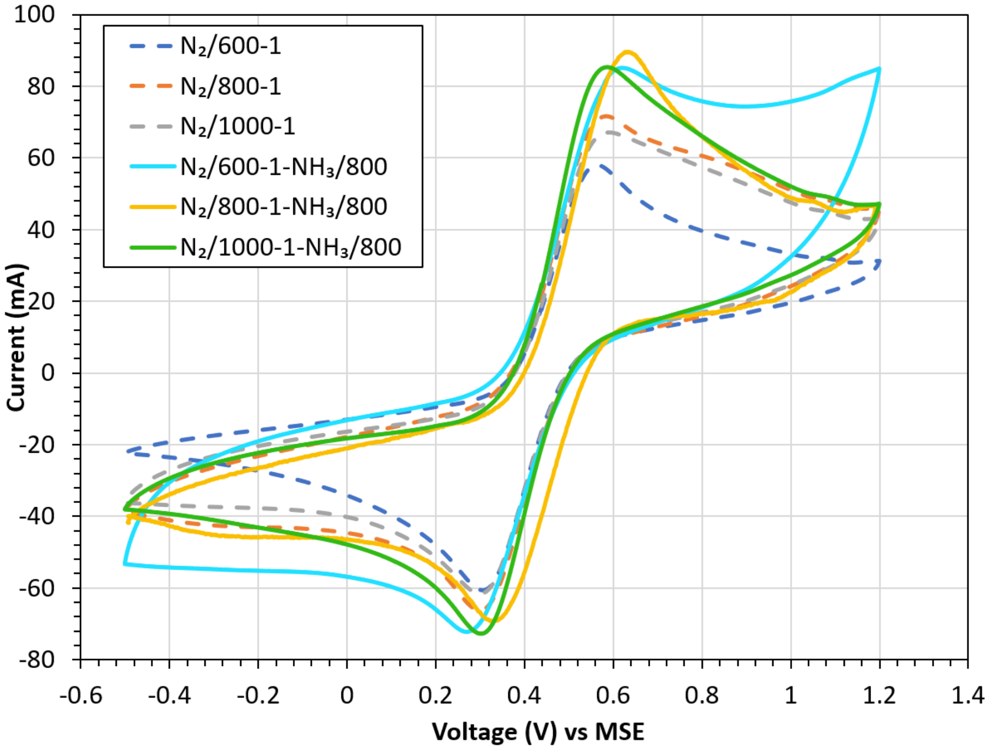

Figure 5-18 Cyclic voltammetry spectra of biochar N_2/600-1, N_2/800-1 and N_2/1000-1 and corresponding NH_3 heat-treated AC at 800°C N_2/600-1-NH_3/800, N_2/800-1-NH_3/800 and N_2/1000-1-NH_3/800

The confirmation on the influence of pyridinic-N and pyrrolic-N groups to the oxidation of $VO^{2+} \rightarrow VO_2^+$ is also evident explaining that pyridinic-N and pyrrolic-N groups are more effective than amine-N and amide-N groups in supporting the conversion from VO^{2+} to VO_2^+, in which CV peak current of N_2/800-1-NH_3/800 is higher than N_2/800-1-H40W2 (Figure 5-17).

5.7.2 Functionalised hydrochar

DBD cold plasma-treated and NH_3 heat-treated hydrochar also provide useful information related to the conversion of VO^{2+}/VO_2^+ couple (see Figure 5-19). CV peak currents of the oxidation $VO^{2+} \rightarrow VO_2^+$ of all DBD cold plasma-treated hydrochar were lower than those of NH_3 heat-treated hydrochar, from 56-63 mA to 70-84 mA. However, the reduction of VO_2^+ to VO^{2+} did not show any differences between hydrochar obtained from these two treatment processes. CV peak currents of reduction $VO_2^+ \rightarrow VO^{2+}$ of DBD cold plasma-treated hydrochar varied in the range 60-68 mA, close to 56-65 mA of NH_3 heat-treated hydrochar.

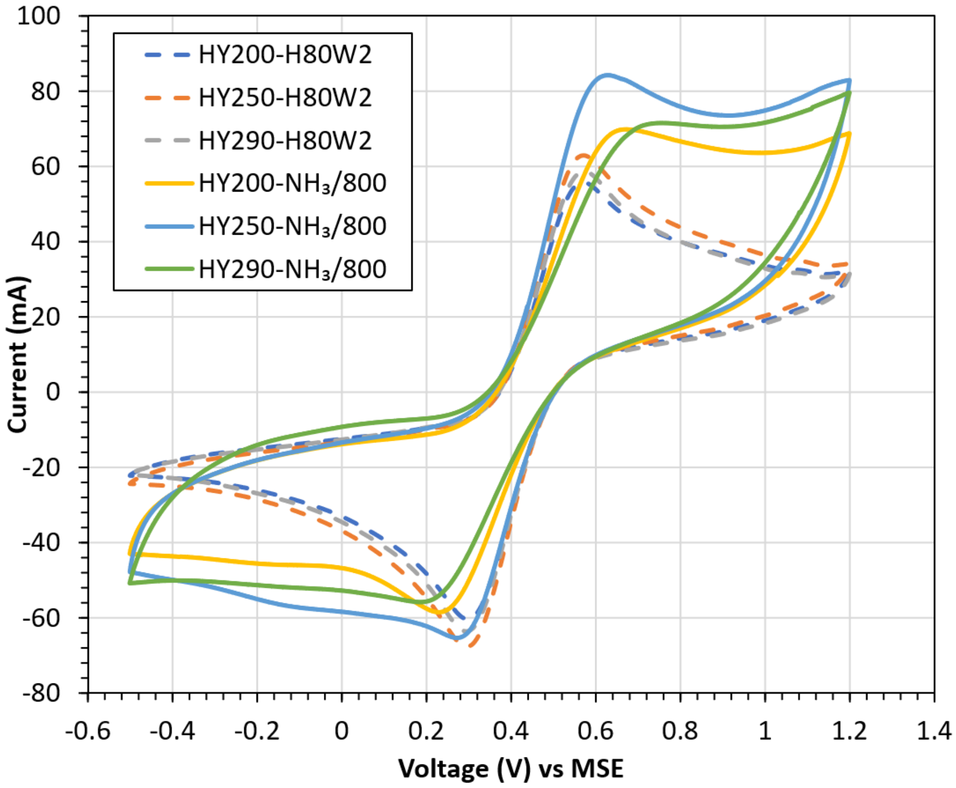

Figure 5-19 Cyclic voltammetry of DBD cold plasma-treated hydrochar in NH_3 (HY200-H80W2, HY250-H80W2 and HY290-H80W2) and NH_3 heat-treated hydrochar at 800°C (HY200-NH_3/800, HY250-NH_3/800 and HY290-NH_3/800

Regarding surface area and porosity, comparison of BET N_2 total volume and N_2 DR micropore volume of NH_3 heat-treated hydrochar shows that 75-77% of BET N_2 total pore volume is micropores (see Table 5-13). CO_2 DR micropore volume varied in the range 0.289-0.302 cm^3 g^{-1}, similar to 0.369-0.403 cm^3 g^{-1} of N_2 DR micropore volume, indicating that most pores in NH_3 heat-treated hydrochar is ultramicropores smaller than 1.4 nm. CO_2 and N_2 adsorption results of DBD cold plasma-treated hydrochar show that there is activated diffusion effect for these carbon samples. From the study of Meskinfam Langroudi *et al.*, the solvated VO^{2+} ($[VO(H_2O)_5]^{2+}$) ion has been shown to easily diffuse into carbon structure thanks to its smaller size compared to VO_2^+ ($[VO_2(H_2O)_4]^+$ or $[VO_2(H_2O)_3]^+$), so more VO^{2+} ions can access electrode surface and benefit the conversion from VO^{2+} to VO_2^+ (Meskinfam Langroudi *et al.* 2019). However, the majority of ultramicropores in NH_3 heat-treated hydrochar and activated diffusion effect in NH_3 heat-treated hydrochar are unlikely to influence the conversion of VO^{2+} and VO_2^+. The characteristics of porosity of these treated hydrochar is also similar to results of walnut shell-derived carbon discussed in Chapter 4 and functionalised carbon samples discussed in section 5.7.1.

There is evidence that carbonaceous structure influence the transformation of VO^{2+} and VO_2^+. Raman spectroscopy and PXRD show that there is significant increase in molecular structures due to heat treatment in NH_3 at 800°C (see Table 5-11 and Table 5-12). L_c and L_a of NH_3 heat-treated hydrochar increased to 12.05-12.41 Å and 25.17-25.48 Å respectively, and interlayer distance d_{002} reduced to 3.51-3.57 Å. DBD cold plasma treatment also improved carbon amorphous structure of hydrochar although d_{002} were still as high as 3.90-4.12 Å, so cold plasma treatment is not as effective as NH_3 heat treatment in modifying carbonaceous structure. As discussed in Chapter 4 on the influence of N_2 biochar series and CO_2 activated carbon series (also see Figure 4-12), increasing HTT to 800°C could enhance electrochemical activity of walnut shell-derived carbon. Therefore, NH_3 heat treatment at 800°C could contribute to the oxidation $VO_2^+ \rightarrow VO^{2+}$.

Furthermore, pyridinic-N and pyrrolic-N groups in NH_3 heat-treated hydrochar also help explain higher CV peak current of oxidation $VO_2^+ \rightarrow VO^{2+}$ compared to amine-N and amide-N groups of DBD cold plasma-treated hydrochar, which has been discussed in CV spectra of NH_3 heat-treated AC (section 5.7.1). XPS N 1s of NH_3 heat-treated hydrochar show nitrogen contents of 6.0-8.3 at% with pyridinic-N of 2.9-4.0 at% and pyrrolic-N of 1.7-2.6 at% (Table 5-10), and total nitrogen contents of NH_3 heat-treated hydrochar is in the range 7.10-7.46 wt% (Table 5-8). TPD profiles of HY250-NH_3/800 is similar to TPD profiles of other NH_3 heat-treated AC sample (see Figure 5-8), confirm the represent of pyridinic-N and pyrrolic-N groups.

CV peak currents (in mA) and peak voltages (in V) of biochar and hydrochar from DBD cold plasma and NH_3 heat treatment are summarised in Table 5-16. From Table 5-16, despite the enhancement in kinetic of the oxidation process from VO^{2+} to VO_2^+ on NH_3 heat-treated AC and hydrochar, these samples also showed lower reversibility with I_{pa}/I_{pc} ratio varying from 1. DBD cold plasma-treated biochar and hydrochar presented I_{pa}/I_{pc} ratio closer to 1, indicating better reversibility of VO^{2+} to VO_2^+ couple, even though cold plasma treatment did not favour the incorporation of pyridinic-N and pyrrolic-N groups. However, DBD cold plasma treatment did not remove oxygen functional groups compared to NH_3 heat treatment, so the increase in irreversibility of these carbon samples may be assigned to the elimination of oxygen functional groups.

Table 5-16 Peak current and peak voltage from cyclic voltammetry of different carbon samples for VO^{2+}/VO_2^+ couple

Carbon sample	**Peak current (mA)**			**Peak voltage (V) vs MSE**		
	Oxidation VO^{2+} to VO_2^+ (I_{pa})	Reduction VO_2^+ to VO^{2+} (I_{pc})	I_{pa}/I_{pc}	Oxidation VO^{2+} to VO_2^+ (E_{pa})	Reduction VO_2^+ to VO^{2+} (E_{pc})	ΔEp
N_2/600-1	58	61	0.96	0.56	0.31	0.26
N_2/800-1	72	66	1.08	0.58	0.30	0.28
N_2/1000-1	67	62	1.09	0.59	0.30	0.29
N_2/800-1-H20W2	56	52	1.08	1.00	0.02	0.98
N_2/800-1-H40W2	76	70	1.07	0.58	0.30	0.28
N_2/800-1-H80W2	61	57	1.06	0.84	0.07	0.78
N_2/600-1-NH_3/800	85	72	1.18	0.62	0.27	0.35
N_2/800-1-NH_3/800	90	69	1.29	0.63	0.32	0.31
N_2/1000-1-NH_3/800	85	73	1.17	0.59	0.30	0.29
HY200-H80W2	56	60	0.92	0.57	0.30	0.27
HY250-H80W2	63	68	0.93	0.57	0.30	0.27
HY290-H80W2	59	64	0.92	0.57	0.29	0.28
HY200-NH_3/800	70	59	1.19	0.67	0.23	0.44
HY250-NH_3/800	84	65	1.29	0.63	0.27	0.35
HY290-NH_3/800	80	56	1.43	1.20	0.19	1.01

5.8 Conclusions

DBD cold plasma treatment is an effective method to introduce nitrogen functional groups onto surface of biomass-derived carbon with surface nitrogen content up to 8.7 at% from 0.0 at% in original biochar/hydrochar precursor. Cold plasma power is a dominant factor affecting the nitrogen functionalisation process. Low DBD cold plasma power 20 W favours the formation of amide groups N-C=O whereas high plasma powers 40 W and 80 W produce amine $C-NH_x$. The ratio of amine-N/amide-N group increases from ~0.4 to ~2.5 with increasing DBD cold plasma power from 20 W to 80 W. DBD cold plasma incorporates surface nitrogen groups by attacking C sp^2 linkages. In this study, NH_3 heat treatment at 800°C has also been proved to modify surface functional groups with main nitrogen species being pyridinic-N, pyrrolic-N and quaternary-N, but this treatment replaces surface oxygen groups with nitrogen from NH_3. Therefore, DBD cold plasma treatment can retain more oxygen functional groups in biochar than NH_3 heat treatment in due to the near atmospheric environment. The similarity of XPS profile between amine-N and pyridinic-N, amide-N and pyrrolic-N requires other analysis such as TPD and FTIR to be performed to ascertain results from XPS. Cold plasma treatment, however, is not a suitable technique to modify surface area and porous structure and carbonaceous structure.

CV spectra of biochar treated at different DBD plasma powers show that amine-N and amide-N groups at amine-N/amide-N ratio of 0.91 benefits for the conversion of VO^{2+} and VO_2^+ ions, but amine-N/amide-N ratio at ~0.4 and ~2.5 decreases the electrochemical reactivity of VO^{2+}/VO_2^+ couple. However, pyridinic-N and pyrrolic-N groups are more effective than amine-N and amide-N groups in supporting the oxidation from VO^{2+} to VO_2^+. However, DBD cold plasma treated-carbon samples show higher reversibility of VO^{2+}/VO_2^+ couple due to the existence of various oxygen functional groups. NH_3 heat treatment removes surface oxygen functional groups and increases the irreversibility of VO^{2+}/VO_2^+ couple. Moreover, both nitrogen and oxygen functional groups, carbonaceous structure, and porosity have little influence on the reduction of VO_2^+ to VO^{2+}.

Chapter 6

Phosphorus incorporation on walnut shell-derived carbon using H_3PO_4

This chapter aims to look at the impact of phosphorus incorporation process on activated carbon (AC) using H_3PO_4 acid as a reagent. The influence of operating conditions, including activating temperatures, acid concentration and holding time, on properties of AC during the treatment are explored. There is no remarkable change in total and surface phosphorus contents on H_3PO_4-treated AC due to the ordered carbon molecular structure of the AC precursor, hindering the functionalisation effect of H_3PO_4. Nevertheless, both heat treatment temperatures (HTTs) and concentration of H_3PO_4 solution are the dominating factors controlling surface phosphorus species. Low H_3PO_4 solution concentration and low HTT promote the formation of C-O-P groups (C-O-PO_3/(C-O)$_3$PO) whereas increasing H_3PO_4 solution concentration and HTT incorporate C-P groups (C-PO_3/C_2-PO_2/C_3-PO).

6.1 Functional group characterisation

6.1.1 Total elemental CHNO analysis

Table 6-1 shows the total elemental CHNO contents of H_3PO_4-treated AC. The results in was normalised to CHNO contents without any moisture and ash contents reported. The total oxygen contents of H_3PO_4-treated AC only varied in a narrow range of 6.41-8.09 wt% compared to 7.54 wt% of precursor CO_2/800-1. Total carbon contents of H_3PO_4-treated AC also fluctuated in a small range of 90.86-92.41 wt% compared to 90.52 wt% of CO_2/800-1. Therefore, H_3PO_4 heat treatment does not modify total elemental contents with varying HTTs in the range of 600-1000°C (CO_2/800-1-H_3PO_4/600-2 to CO_2/800-1-H_3PO_4/1000-2). AC precursor CO_2/800-1 underwent heat treatment at 800°C, so the molecular structure of CO_2/800-1 has been modified significantly as discussed in Raman spectroscopy and PXRD results (see Table 4-7 and Table 4-8). This is similar to H_3PO_4 treatment on anthracite in the HTT range of 600-800°C (Ma *et al.* 2018) or sucrose derived AC at 900°C (Lysenko *et al.* 2012), where little effect of H_3PO_4 activation of elemental contents was observed.

Table 6-1 Total elemental CHNO analysis

Carbon sample	Elemental content (wt%, dry ash free)			
	C	H	N	O
CO_2/800-1	90.52 ± 0.21	1.63 ± 0.09	0.31 ± 0.01	7.54 ± 0.12
CO_2/800-1-H_3PO_4/600-2	92.41 ± 0.33	0.98 ± 0.01	0.21 ± 0.15	6.41 ± 0.16
CO_2/800-1-H_3PO_4/800-2	92.25 ± 0.37	0.88 ± 0.08	0.21 ± 0.16	6.65 ± 0.13
CO_2/800-1-H_3PO_4/1000-2	90.86 ± 0.96	0.49 ± 0.07	0.55 ± 0.01	8.09 ± 0.87
CO_2/800-1-H_3PO_4/NH_3-2	83.84 ± 0.88	1.02 ± 0.15	8.25 ± 0.10	6.89 ± 0.83

NH_3 heat treatment on CO_2/800-1 soaked in H_3PO_4 2 M achieved total nitrogen content of 8.25 wt% without little change in total hydrogen contents (1.02-1.63 wt%) and oxygen contents (6.89-7.54 wt%). This total nitrogen content is higher than nitrogen content of N_2/800-1-NH_3/800 (4.76 wt% – see Table 4-5), in which N_2/800-1 was also pyrolysed at 800°C and subsequently treated at 800°C in NH_3. Therefore, soaking CO_2/800-1 in H_3PO_4 2 M influences on the total nitrogen contents, in which H_3PO_4 should react with NH_3 to create more N-P bonds in AC.

6.1.2 X-ray photoelectron spectroscopy

The impact of phosphorus incorporation on AC using H_3PO_4 was investigated. As discussed in section 2.4.2.2, H_3PO_4 is an effective reagent to be used for phosphorus incorporation into AC. AC CO_2/800-1 was chosen due to high surface area (S_{BET} = 482 m^2 g^{-1} and S_{CO2} = 632 m^2 g^{-1} - Table 4-1), so H_3PO_4 ions were expected to easily adsorb into the AC. HTT, concentration of H_3PO_4 solution, holding time and carrier gases were varied to investigate how operating conditions influenced functional groups of AC. Phosphorus was introduced into CO_2/800-1 when varying HTTs in the range of 600-1000°C and H_3PO_4 concentration in the range of 0.5-5 M under N_2. A control sample (AC CO_2/800-1-H_3PO_4/800-0), which went through the same treatment without being soaked in H_3PO_4 solution, did not show any surface phosphorus through XPS spectrum, so the treatment successfully introduced phosphorus into surface of AC (see Table 6-2).

Table 6-2, however, also shows that the surface phosphorus contents in these AC samples were only in the range of 0.8-2.1 at% (Table 6-2). Increasing the H_3PO_4 concentration from 0.5 M to 5 M did not influence phosphorus contents in AC. Surface phosphorus contents of AC soaked in H_3PO_4 0.5 M varied in a narrow range 1.0-1.5 at%, similar to 1.1-2.1 at% of H_3PO_4-treated AC soaked in 5 M solution. Furthermore, varying HTTs at 600-1000°C under N_2 in all H_3PO_4 concentration 0.5-5 M also did not show significant impact of XPS C 1s and

O 1s contents with surface carbon contents in the range of 87.7-92.2 at% and oxygen in the range of 6.8-10.2 at%. Comparison of CO_2/800-1-H_3PO_4/800-2 to two AC samples CO_2/800-1-H_3PO_4/800-2-1h and CO_2/800-1-H_3PO_4/800-2-3h also presents little difference in surface functional groups, indicating holding times did not control surface functional groups. Furthermore, comparison of carbon and oxygen contents in bulk (see Table 6-1) and on the surface (see Table 6-2) shows that there is similarity of carbon and oxygen contents from both analysis methods. It is evident that H_3PO_4 treatment has little influence on carbon and oxygen functional groups, and phosphorus only resides on the surface of AC.

The low phosphorus contents in this study is in agreement with the study of Lysenko *et al.* on sucrose-derived AC (Lysenko *et al.* 2012). Sucrose-derived AC carbonised at 900°C for 2.5 h and activated in H_3PO_4 at 800°C showed a low phosphorus content of 2.03 wt%. Another study on anthracite also showed that phosphorus content also fluctuated in a small range of 0.3-1.1 % when temperatures varied in the range of 600-800°C (Ma *et al.* 2018). Pyrolysis of sucrose at 900°C in study of Lysenko *et al.* and pyrolysis of walnut shell at 800°C (AC CO_2/800-1) in this study should sufficiently remove all functional groups in sucrose and transform biomass carbonaceous structure, while anthracite is a well-known hard and highly compact coal with fewest impurities. Therefore, it is unlikely for H_3PO_4 to react to incorporate new functional groups into AC. The study of Lysenko *et al.* also showed that sucrose-derived AC going through one activation step at 800°C with H_3PO_4 had higher phosphorus content of 15.24 wt%, so biomass without underwent high temperature activation is likely to incorporate more phosphorus.

The interpretation of XPS O 1s peaks of H_3PO_4-treated AC becomes more complicated than other walnut shell-derived samples discusses in Chapter 4 due to cross linkages of carbon, oxygen, and phosphorus atoms (see Table 6-3). XPS O 1s peaks show similar binding energies for C=O and P=O (531.4 ± 0.2 eV), C-O and C-O-P (532.4 ± 0.3 eV), and O-C=O and P-O-P (533.4 ± 0.3 eV) (see Figure 6-1). In general, XPS O1s C=O/P=O contents remained stable in the range of 1.2-2.4 at%, XPS O1s C-O/C-O-P contents varied in the range 0-4.3 at%, and XPS O 1s COOH/P-O-P varied in the range 2.4-5.5 at%. This is similar to C=O, C-O and COOH contents of precursor CO_2/800-1. The change in surface oxygen functional groups of H_3PO_4-treated AC did not showed any specific pattern compared to AC CO_2/800-1. Phosphorus incorporation did not change surface oxygen content of H_3PO_4-treated AC, so there is a mixture of oxygen functional groups of oxygen and carbon and of oxygen and phosphorus on the surface of AC.

Table 6-2 Elemental analysis and oxygen functional analysis of carbons obtained from X-ray photoelectron spectroscopy

Carbon sample	**Elemental content (at%)**					**Components from C 1s profiles (at%)**				
	C	**O**	**N**	**P**	**K, Ca and Si**	**C sp^2**	**C sp^3**	**C-O/OH**	**C=O**	**O-C=O**
CO_2/800-1	90.0 ± 0.3	9.0 ± 0.2	0.0	0.0	1.7	50.5 ± 4.9	30.3 ± 8.6	5.4 ± 0.3	2.2 ± 0.4	1.6 ± 0.2
CO_2/800-1-H_3PO_4/600-0.5	90.1 ± 0.3	8.5 ± 0.3	0.0	1.4 ± 0.1	0.0	67.5 ± 3.1	14.7 ± 1.9	4.0 ± 0.1	1.8 ± 0.5	2.1 ± 0.2
CO_2/800-1-H_3PO_4/700-0.5	90.9 ± 0.3	8.0 ± 0.3	0.0	1.1 ± 0.1	0.0	80.9 ± 3.8	1.3 ± 0.2	4.9 ± 0.2	1.5 ± 0.1	2.3 ± 0.2
CO_2/800-1-H_3PO_4/800-0.5	92.2 ± 0.4	6.8 ± 0.2	0.0	1.0 ± 0.1	0.0	76.6 ± 3.6	9.3 ± 1.2	3.2 ± 0.1	1.5 ± 0.1	1.6 ± 0.2
CO_2/800-1-H_3PO_4/1000-0.5	89.4 ± 0.3	9.1 ± 0.3	0.0	1.5 ± 0.1	0.0	66.3 ± 2.8	13.7 ±1.8	4.9 ± 0.4	1.8 ± 0.2	2.7 ± 0.2
CO_2/800-1-H_3PO_4/600-2	90.0 ± 0.3	8.8 ± 0.3	0.0	1.2 ± 0.1	0.0	82.0 ± 3.4	2.2 ± 0.3	3.1 ± 0.1	0.7 ± 0.1	2.0 ± 0.2
CO_2/800-1-H_3PO_4/700-2	89.6 ± 0.3	9.3 ± 0.3	0.0	1.1 ± 0.1	0.0	65.3 ± 2.7	15.5 ± 2.0	4.5 ± 0.1	2.2 ± 0.1	2.1 ± 0.2
CO_2/800-1-H_3PO_4/800-2	89.7 ± 0.3	9.0 ± 0.3	0.0	1.3 ± 0.1	0.0	68.0 ± 3.2	13.1 ± 2.9	4.6 ± 0.4	1.7 ± 0.5	2.3 ± 0.2
CO_2/800-1-H_3PO_4/1000-2	90.2 ± 0.3	8.2 ± 0.3	0.0	1.6 ± 0.2	0.0	65.4 ± 2.7	16.2 ± 2.1	4.5 ± 0.1	2.1 ± 0.1	2.0 ± 0.2
CO_2/800-1-H_3PO_4/800-2-1h	90.4 ± 0.3	8.8 ± 0.4	0.0	0.8 ± 0.1	0.0	54.4 ± 2.2	23.3 ± 3.0	6.5 ± 0.2	3.2 ± 0.2	3.0 ± 0.3
CO_2/800-1-H_3PO_4/800-2-3h	90.1 ± 0.3	8.9 ± 0.3	0.0	1.0 ± 0.1	0.0	63.0 ± 2.6	18.0 ± 2.3	4.8 ± 0.1	1.8 ± 0.1	2.5 ± 0.2
CO_2/800-1-H_3PO_4/600-5	91.9 ± 0.3	7.0 ± 0.2	0.0	1.1 ± 0.1	0.0	71.6 ± 3.0	13.1 ± 1.7	3.5 ± 0.1	1.9 ± 0.1	1.8 ± 0.2
CO_2/800-1-H_3PO_4/700-5	89.1 ± 0.3	9.5 ± 0.3	0.0	1.4 ± 0.3	0.0	63.6 ± 3.4	15.7 ± 2.0	4.7 ± 0.2	1.9 ± 0.1	3.2 ± 0.3
CO_2/800-1-H_3PO_4/800-5	87.7 ± 0.2	10.2 ± 0.1	0.0	2.1 ± 0.1	0.0	62.5 ± 3.3	15.9 ± 2.8	4.9 ± 0.3	2.2 ± 0.3	2.3 ± 0.1
CO_2/800-1-H_3PO_4/1000-5	89.7 ± 0.3	8.5 ± 0.2	0.0	1.8 ± 0.1	0.0	55.6 ± 2.9	26.1 ± 3.4	2.6 ± 0.1	2.9 ± 0.3	2.5 ± 0.1
CO_2/800-1-H_3PO_4/NH_3-0.5	91.0 ± 0.4	4.3 ± 0.1	4.1 ± 0.1	0.6 ± 0.1	0.0	70.6 ± 3.7	12.0 ± 1.5	4.7 ± 0.3	1.8 ± 0.3	1.9 ± 0.1

Carbon sample	Elemental content (at%)					Components from C 1s profiles (at%)				
	C	O	N	P	K, Ca and Si	C sp^2	C sp^3	C-O/OH	C=O	O-C=O
CO_2/800-1-H_3PO_4/NH_3-2	86.2 ± 0.2	5.7 ± 0.2	6.4 ± 0.2	1.7 ± 0.2	0.0	79.9 ± 4.2	0	4.3 ± 0.2	0.7 ± 0.1	1.4 ± 0.1
CO_2/800-1-H_3PO_4/NH_3-5	81.5 ± 0.4	6.9 ± 0.2	7.4 ± 0.1	4.2 ± 0.3	0.0	55.2 ± 3.7	17.3 ± 3.6	5.3 ± 0.3	2.1 ± 0.1	1.6 ± 0.2
CO_2/800-1-H_3PO_4/800-0	90.7 ± 0.3	9.3 ± 0.3	0.0	0.0	0.0	69.0 ± 3.6	12.0 ± 1.5	5.1 ± 0.3	2.3 ± 0.2	2.3 ± 0.2
CO_2/800-1-H_3PO_4/CO_2-2	90.0 ± 0.4	8.8 ± 0.3	0.0	1.2 ± 0.1	0.0	74.5 ± 3.9	7.7 ± 1.0	4.1 ± 0.2	1.7 ± 0.1	2.0 ± 0.2

Table 6-3 Oxygen and phosphorus functional analysis of carbons obtained from X-ray photoelectron spectroscopy

Carbon sample	Components from O 1s (at%)				Components from P 2p (at%)		
	C=O/ P=O	C-O/C-O-P	COOH/ P-O-P	Chemisorbed H_2O	C-PO_3/ C_2-PO_2/ C_3-PO	C-O-P	Pentoxide
CO_2/800-1	2.5 ± 0.2	2.9 ± 0.2	2.7 ± 0.1	0.3 ± 0.1	0.0	0.0	0.0
CO_2/800-1-H_3PO_4/600-0.5	2.3 ± 0.1	1.3 ± 0.1	4.2 ± 0.4	0.7 ± 0.1	0.5 ± 0.1	0.8 ± 0.1	0.1 ± 0.1
CO_2/800-1-H_3PO_4/700-0.5	1.8 ± 0.1	2.0 ± 0.2	3.6 ± 0.2	0.6 ± 0.1	0.9 ± 0.1	0.1 ± 0.1	0.1 ± 0.1
CO_2/800-1-H_3PO_4/800-0.5	1.6 ± 0.1	1.8 ± 0.2	3.0 ± 0.2	0.4 ± 0.1	0.4 ± 0.1	0.5 ± 0.1	0.1 ± 0.1
CO_2/800-1-H_3PO_4/1000-0.5	1.7 ± 0.1	3.4 ± 0.3	3.6 ± 0.2	0.4 ± 0.1	1.2 ± 0.1	0.2 ± 0.1	0.1 ± 0.1
CO_2/800-1-H_3PO_4/600-2	1.9 ± 0.1	4.1 ± 0.4	2.4 ± 0.3	0.4 ± 0.1	0.5 ± 0.1	0.6 ± 0.1	0.1 ± 0.1
CO_2/800-1-H_3PO_4/700-2	1.9 ± 0.1	3.9 ± 0.4	3.2 ± 0.2	0.3 ± 0.1	0.6 ± 0.1	0.5 ± 0.1	0.1 ± 0.1
CO_2/800-1-H_3PO_4/800-2	1.6 ± 0.1	4.2 ± 0.4	2.9 ± 0.2	0.3 ± 0.1	1.0 ± 0.1	0.2 ± 0.1	0.1 ± 0.1
CO_2/800-1-H_3PO_4/1000-2	1.9 ± 0.1	1.6 ± 0.1	4.0 ± 0.3	0.7 ± 0.1	1.2 ± 0.1	0.3 ± 0.1	0.1 ± 0.1
CO_2/800-1-H_3PO_4/800-2-1h	0.9 ± 0.1	3.0 ± 0.3	4.5 ± 0.3	0.4 ± 0.1	0.7 ± 0.1	0.0	0.1 ± 0.1
CO_2/800-1-H_3PO_4/800-2-3h	1.6 ± 0.1	0.2 ± 0.1	6.5 ± 0.4	0.6 ± 0.1	0.7 ± 0.1	0.2 ± 0.1	0.1 ± 0.1

Carbon sample	**Components from O 1s (at%)**				**Components from P 2p (at%)**		
	C=O/ P=O	**C-O/C-O-P**	**COOH/ P-O-P**	**Chemisorbed H_2O**	**C-PO_3/ C_2-PO_2/ C_3-PO**	**C-O-P**	**Pentoxide**
CO_2/800-1-H_3PO_4/600-5	1.8 ± 0.1	0.0	4.7 ± 0.4	0.5 ± 0.1	0.7 ± 0.1	0.4 ± 0.1	0.0
CO_2/800-1-H_3PO_4/700-5	1.2 ± 0.1	2.2 ± 0.2	5.5 ± 0.4	0.5 ± 0.1	1.1 ± 0.1	0.2 ± 0.1	0.1 ± 0.1
CO_2/800-1-H_3PO_4/800-5	2.0 ± 0.1	4.3 ± 0.4	3.4 ± 0.4	0.5 ± 0.1	1.7 ± 0.1	0.3 ± 0.1	0.1 ± 0.1
CO_2/800-1-H_3PO_4/1000-5	2.4 ± 0.1	1.6 ± 0.1	3.9 ± 0.3	0.6 ± 0.1	1.4 ± 0.1	0.3 ± 0.1	0.1 ± 0.1
CO_2/800-1-H_3PO_4/NH_3-0.5	1.3 ± 0.1	0.4 ± 0.1	2.4 ± 0.2	0.2 ± 0.1	0.5 ± 0.1	0.1 ± 0.1	0.0
CO_2/800-1-H_3PO_4/NH_3-2	2.1 ± 0.1	0.8 ± 0.1	2.6 ± 0.2	0.2 ± 0.1	1.2 ± 0.1	0.4 ± 0.1	0.1 ± 0.1
CO_2/800-1-H_3PO_4/NH_3-5	1.7 ± 0.1	2.7 ± 0.1	2.1 ± 0.3	0.4 ± 0.1	1.7 ± 0.1	1.9 ± 0.5	0.6 ± 0.1
CO_2/800-1-H_3PO_4/800-0	0.0	3.2 ± 0.1	4.4 ± 0.4	1.7 ± 0.1	0.0	0.0	0.0
CO_2/800-1-H_3PO_4/CO_2-2	2.0 ± 0.1	2.1 ± 0.1	4.1 ± 0.4	0.6 ± 0.1	0.8 ± 0.1	0.4 ± 0.1	0.0

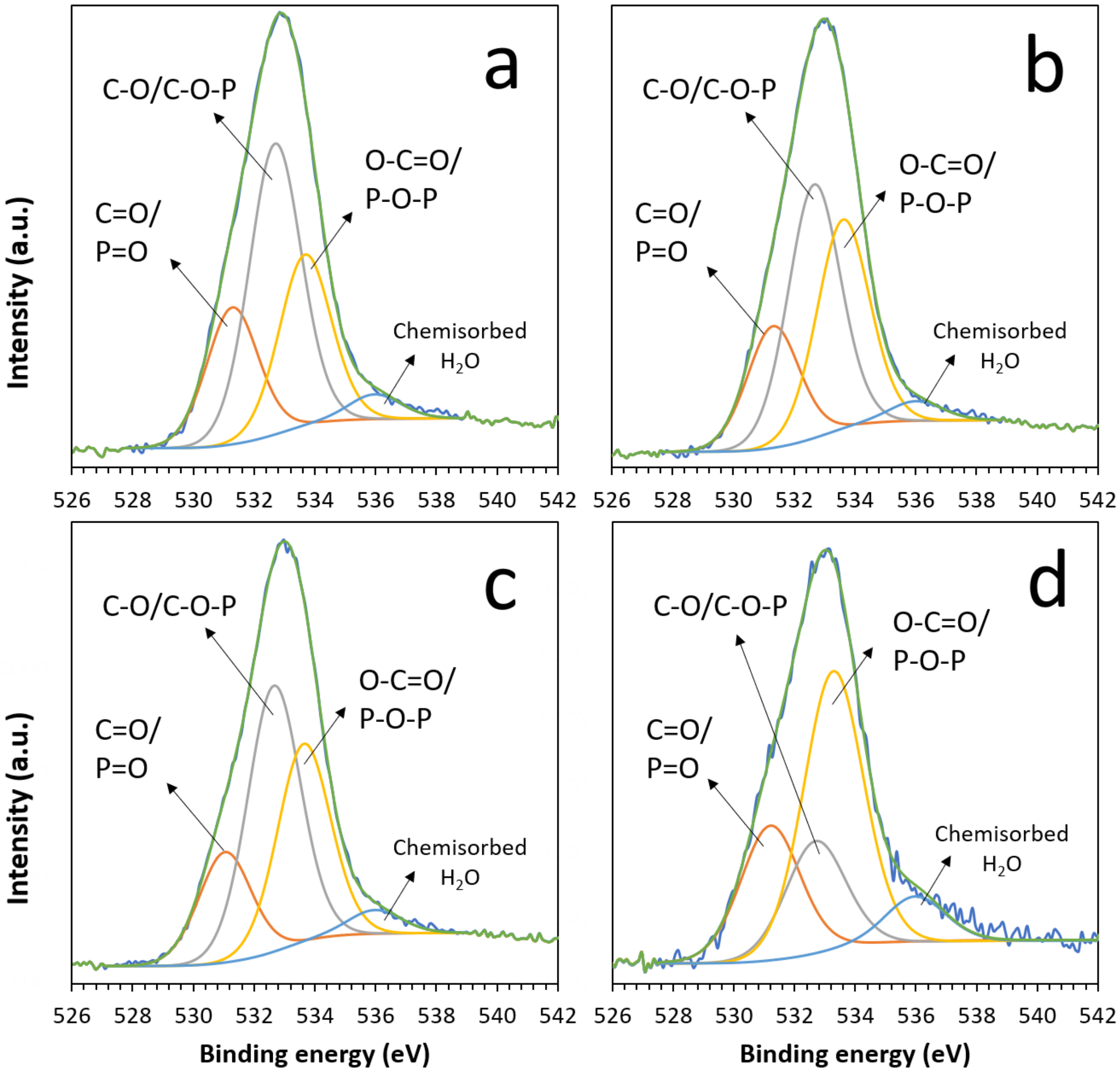

Figure 6-1 XPS O 1s peaks of AC soaked in H_3PO_4 2 M solution and treated in N_2 at 600-1000°C: (a) CO_2/800-1-H_3PO_4/600-2 (600°C), (b) CO_2/800-1-H_3PO_4/700-2 (700°C), (c) CO_2/800-1-H_3PO_4/800-2 (800°C) and (d) CO_2/800-1-H_3PO_4/1000-2 (1000°C)

XPS C 1s peaks of AC CO_2/800-1 treated in H_3PO_4 2 M from 600-1000°C is illustrated in Figure 6-2. Table 6-2 shows that H_3PO_4 heat treatment influenced surface carbon C sp^2 and C sp^3 species contents of AC. XPS C1s C sp^2 contents of H_3PO_4-treated AC increased from 50.5 at% (AC CO_2/800-)1 to 55.6-82.0 at% depending on HTTs and H_3PO_4 concentration. C sp^3 contents of H_3PO_4-treated AC decreased from 30.3 at% to 1.3-26.1 at%. High temperatures (600-1000°C) and the presence of H_3PO_4 could foster the elimination of hydrogen in AC, so it enhanced the conversion of C sp^3 into C sp^2. However, there was no clear trend in the conversion between C sp^2 and C sp^3 regarding HTT and H_3PO_4 solution concentrations. HTT and H_3PO_4 solution concentrations also did not show any clear trend related to surface oxygen species as seen in Table 6-2.

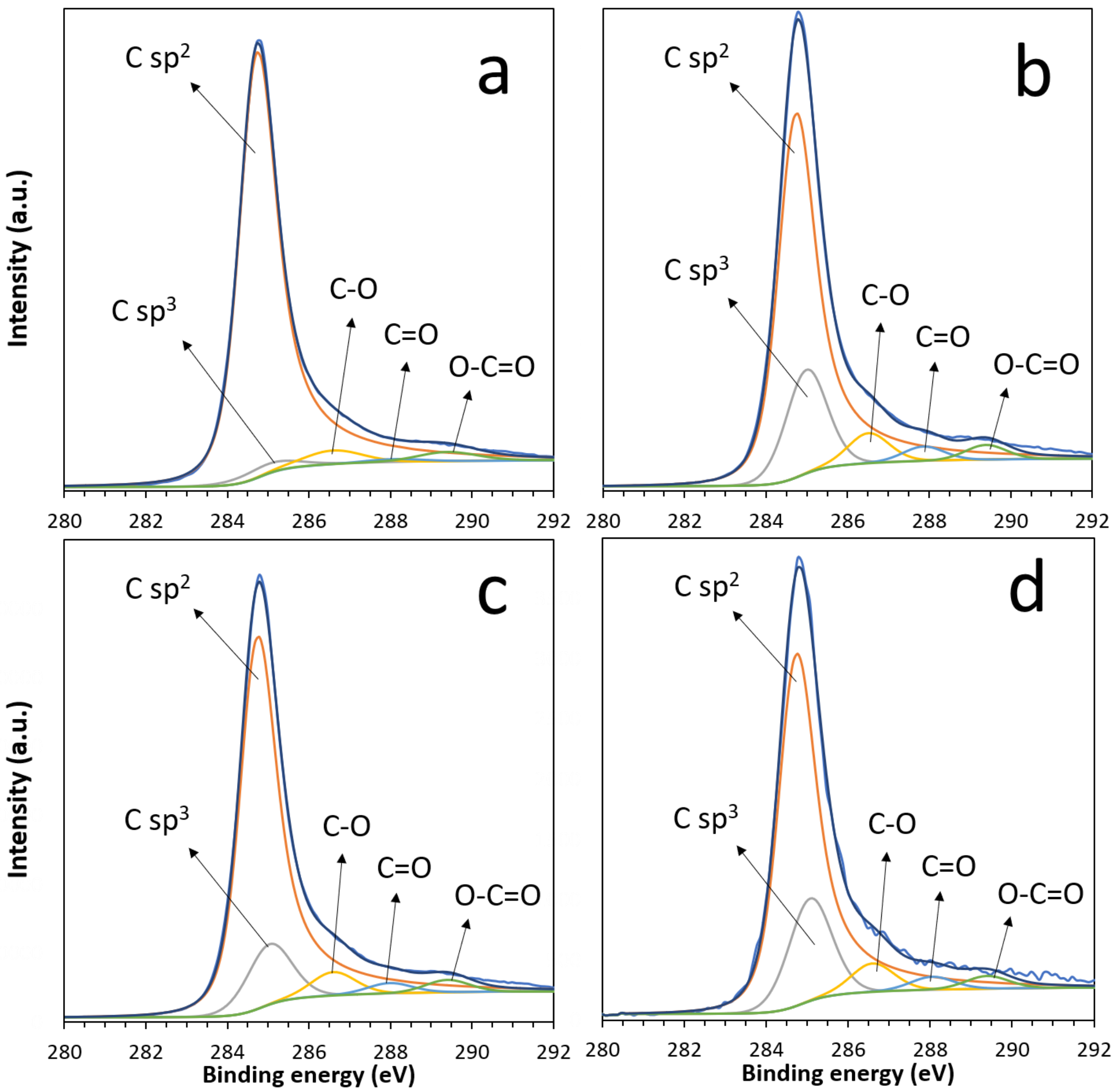

Figure 6-2 XPS C 1s peaks of AC soaked in H_3PO_4 2 M solution and treated in N_2 at 600-1000°C: (a) CO_2/800-1-H_3PO_4/600-2 (600°C), (b) CO_2/800-1-H_3PO_4/700-2 (700°C), (c) CO_2/800-1-H_3PO_4/800-2 (800°C) and (d) CO_2/800-1-H_3PO_4/1000-2 (1000°C)

XPS P 2p peaks were deconvoluted into three peaks, including C-P groups ($C\text{-}PO_3/C_2\text{-}PO_2/C_3\text{-}PO$) at 133.0 ± 0.3 eV, C-O-P at 134.6 ± 0.3 eV and pentoxide P_4O_{10} (136 ± 0.4 eV) (Wu and Radovic 2006, Rosas *et al.* 2012, Ma *et al.* 2018). Table 6-2 and Table 6-3 shows phosphorus functional species from XPS P 2p. Figure 6-3 also illustrates XPS P 2p peaks of H_3PO_4-treated AC. Varying temperatures and H_3PO_4 solution concentrations did not impact surface phosphorus contents, but these operating conditions influenced phosphorus functional group species. Increasing both HTTs and H_3PO_4 solution concentration favoured the formation of C-P linkages (including C-PO_3/ C_2-PO_2/ C_3-PO), while decreasing temperatures and H_3PO_4 solution concentration resulted in more C-O-P groups:

- The surface content of C-P groups remained at 0.4-0.5 at% when using H_3PO_4 0.5 M in HTT range 600-800°C (AC CO_2/800-1-H_3PO_4/600-0.5 to CO_2/800-1-H_3PO_4/800-0.5). However, surface content of C-P groups increased to 1.2 at% (AC CO_2/800-1-H_3PO_4/1000-0.5) with increasing HTT to 1000°C, and C-O-P content reduced to 0.2 at% (see Table 6-3).
- With H_3PO_4 2 M solution, the surface contents of both C-P and C-O-P group varies in the same range of 0.5-0.6 at% at 600-700°C. However, C-P groups is the dominant form of phosphorus functional species at HTT of 800-1000°C, varying in the range of 1.0-1.2 at% compared to 0.2-0.3 at% of C-O-P groups.
- At extremely high H_3PO_4 solution concentration of 5 M, most phosphorus groups are in the form of C-P groups 0.7-1.7 at% in the whole HTT range of 600-1000 °C compared to 0.2-0.4 at% of C-O-P groups.
- In all AC samples, pentoxide only accounted for around 0.1 at%.

The transformation of C-O-P into C-P groups is suggested to follow this mechanism: hydrogen atoms in H_3PO_4 are first removed with heat treatment and then react with carbon to form C-O-P groups, but increasing HTT allows rearrangement reactions for C and P to react and form C-P groups. H_3PO_4 could decompose into radicals such as PO*, P* and O_2P* with increasing heat treatment temperatures (Ding *et al.* 2017), and then react with carbon in AC to form C-P groups (C-PO_3/ C_2-PO_2/ C_3-PO). The transformation from C-O-P into C-P groups was also observed in the study of Bedia *et al.* (Bedia *et al.* 2011). Increasing temperatures from 400 to 800°C shifted C-O-PO_3/$(C\text{-}O)_3$PO to C-PO_3/C_2PO_2 for olive stone-derived AC. In this study, it is revealed that both HTT and H_3PO_4 solution concentration determine the relative content of C-P groups (C-PO_3/C_2-PO_2/C_3-PO) and C-O-P groups (C-O-PO_3/$(C\text{-}O)_3$PO). It is evident that increasing HTT and H_3PO_4 concentration fostered the transformation of C-O-P groups (C-O-PO_3/$(C\text{-}O)_3$PO) to C-P groups (C-PO_3/C_2-PO_2/C_3-PO).

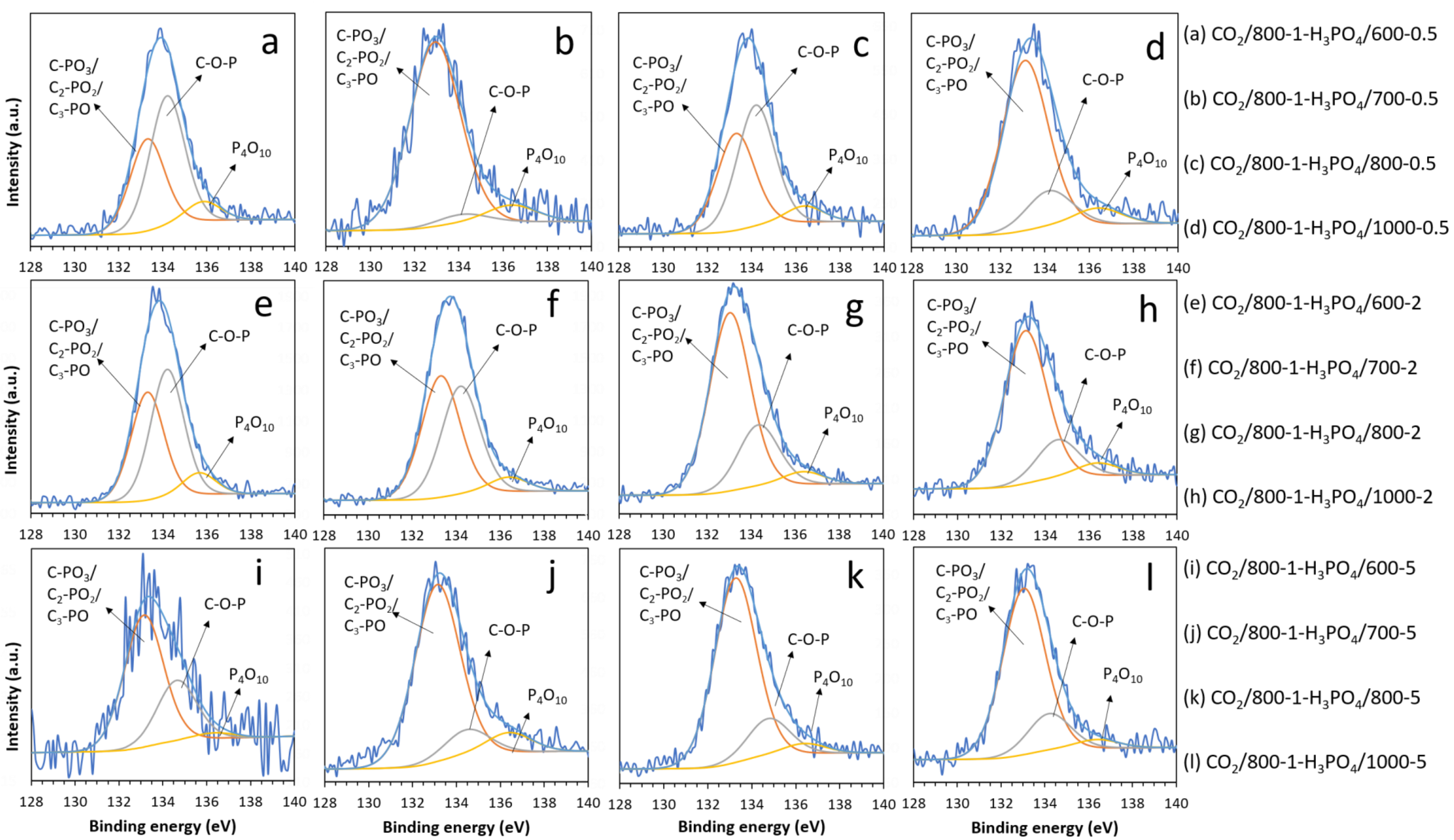

Figure 6-3 XPS P 2p spectra of AC treated at different heat treatment temperatures (600-1000°C) and H_3PO_4 concentration (0.5-5 M)

AC CO_2/800-1 soaked into H_3PO_4 solution 0.5, 2 and 5 M was heat treated under NH_3 to incorporate nitrogen into AC (CO_2/800-1-H_3PO_4/NH_3-0.5, CO_2/800-1-H_3PO_4/NH_3-2 and CO_2/800-1-H_3PO_4/NH_3-5 respectively). Changing heat treatment environment from N_2 to NH_3 increased surface nitrogen contents to 4.1-7.4 at% with increasing H_3PO_4 solution concentration from 0.5 to 5 M compared to null in AC CO_2/800-1 (see Table 6-2 and Table 6-4). The surface nitrogen contents were higher than surface nitrogen content of AC thermally treated under NH_3 only (only 4.9 at% for AC N_2/800-1-NH_3/800 – see Table 4-2).

In the study of Ding *et al.*, increasing HTTs decomposes both H_3PO_4 and NH_3 into several different radicals including PO*, P*, O_2P*, NH*, NH_2* (Ding *et al.* 2017). After that, these radicals react with AC to form nitrogen and phosphorus functional groups. Nitrogen-containing radicals from NH_3 atmosphere also reacted with H_3PO_4 at high HTTs to incorporate not only nitrogen groups but also phosphorus groups compared to AC treated with H_3PO_4 or NH_3 separately, leading to nitrogen content of 7.4 at% and phosphorus content of 4.2 at% in AC CO_2/800-1-H_3PO_4/NH_3-5. In terms of nitrogen functional groups, heat treatment at 800°C mainly promoted the formation of N-6 over N-5, which is similar as other NH_3 heat-treated AC as discussed in XPS section 4.2.1 of Chapter 4, section 5.2.2 of Chapter 5 and NH_3 heat-treated hydrochar in section 5.3.2. Total nitrogen content of CO_2/800-1-H_3PO_4/NH_3-2 was 8.25 wt% (Table 6-1) higher than the surface nitrogen 6.4 at%, indicating more nitrogen functional groups integrated into the structure of AC.

Table 6-4 Nitrogen functional groups from XPS N 1s of AC soaked in H_3PO_4 0.5, 2 and 5 M solution and heat treated in NH_3 at 800°C

Carbon sample	**Components from N 1s profile (at%)**				**N-6/N-5 ratio**
	N-6	**N-5**	**N-Q**	**N-X**	
CO_2/800-1-H_3PO_4/NH_3-0.5	1.9 ± 0.2	1.5 ± 0.1	0.4 ± 0.1	0.3 ± 0.1	1.27
CO_2/800-1-H_3PO_4/NH_3-2	3.6 ± 0.3	2.4 ± 0.1	0.0	0.4 ± 0.1	1.50
CO_2/800-1-H_3PO_4/NH_3-5	3.4 ± 0.3	3.1 ± 0.1	0.6 ± 0.2	0.3 ± 0.1	1.10

AC CO_2/800-1 soaked in H_3PO_4 2 M was treated in CO_2 at 800°C for 2 h to obtain CO_2/800-1-H_3PO_4/CO_2-2. Table 6-2 and Table 6-3 show that surface composition of CO_2/800-1-H_3PO_4/CO_2-2 was similar to CO_2/800-1-H_3PO_4/800-2. C sp^2 and C sp^3 content of CO_2/800-1-H_3PO_4/CO_2-2 were 74.5 at% and 7.7 at%, respectively. XPS P 2p spectrum of this AC also shows that C-P groups at 0.8 at% was also the main phosphorus functional group compared to 0.4 at% of C-O-P groups. The similarity of surface functional groups between CO_2/800-1-H_3PO_4/CO_2-2 and CO_2/800-1-H_3PO_4/800-2 indicates that changing from N_2 to CO_2

atmosphere does not modify surface carbon and phosphorus composition of H_3PO_4-treated AC.

6.1.3 Fourier Transform-Infrared Spectroscopy

FTIR were performed to further examine functional groups of H_3PO_4-treated AC. FTIR profiles of H_3PO_4-treated AC at different HTTs and H_3PO_4 concentration solutions are illustrated in Figure 6-4, Figure 6-5 and Figure 6-6. The surface phosphorus contents in H_3PO_4-treated AC varied only in the range of 0.8-2.1 at% compared to AC precursor CO_2/800-1 and blank sample CO_2/800-1-H_3PO_4/800-0 as discussed in XPS analysis (see Table 6-2 and Table 6-3), so there was little change to adsorption bands at around 1140-1320 cm^{-1}, indicating that there is no presence of P=O stretching (Figure 6-4, Figure 6-5 and Figure 6-6) (Larkin 2011).

Despite changes in operating conditions of functionalising process and new phosphorus functional groups on the surface of AC, there was only slightly difference in FTIR profiles of these samples compared to precursor CO_2/800-1. FTIR provided more in-depth analysis, up to 1 µm compared to XPS, so lack of peaks of phosphorus and oxygen functional groups in FTIR showed that H_3PO_4 heat treatment procedure only introduced and altered functional groups on surface of AC rather than in bulk. This is in agreement with the low phosphorus contents of AC as seen in XPS analysis (see Table 6-2 and Table 6-3). Other biomass-derived AC, which were activated directly from biomass rather than the underwent through a pre-pyrolysis stage at high temperatures, could rise phosphorus contents up to 15.24 at% for sucrose-derived AC treated at 800°C (Lysenko *et al.* 2012) or 4.7 wt% for corncob-derived AC at 400°C (Sych *et al.* 2012).

Moreover, there was no significant evidence for P-H stretching in the region of 2270-2450 cm^{-1} and P-OH stretching in the region of 2100-2800 cm^{-1} in these AC samples (Larkin 2011). The characterised peaks for phosphorus including the band at 1050 cm^{-1} for aliphatic phosphate C-O-P vibration, and 980 cm^{-1} for P-O-P vibration were also not observed in FTIR profiles of H_3PO_4-treated AC. Also, the phosphorus incorporation process did not influence significantly on oxygen functional groups. There were no clear peaks on the oxygen functional groups such as COOH and OH groups in FTIR.

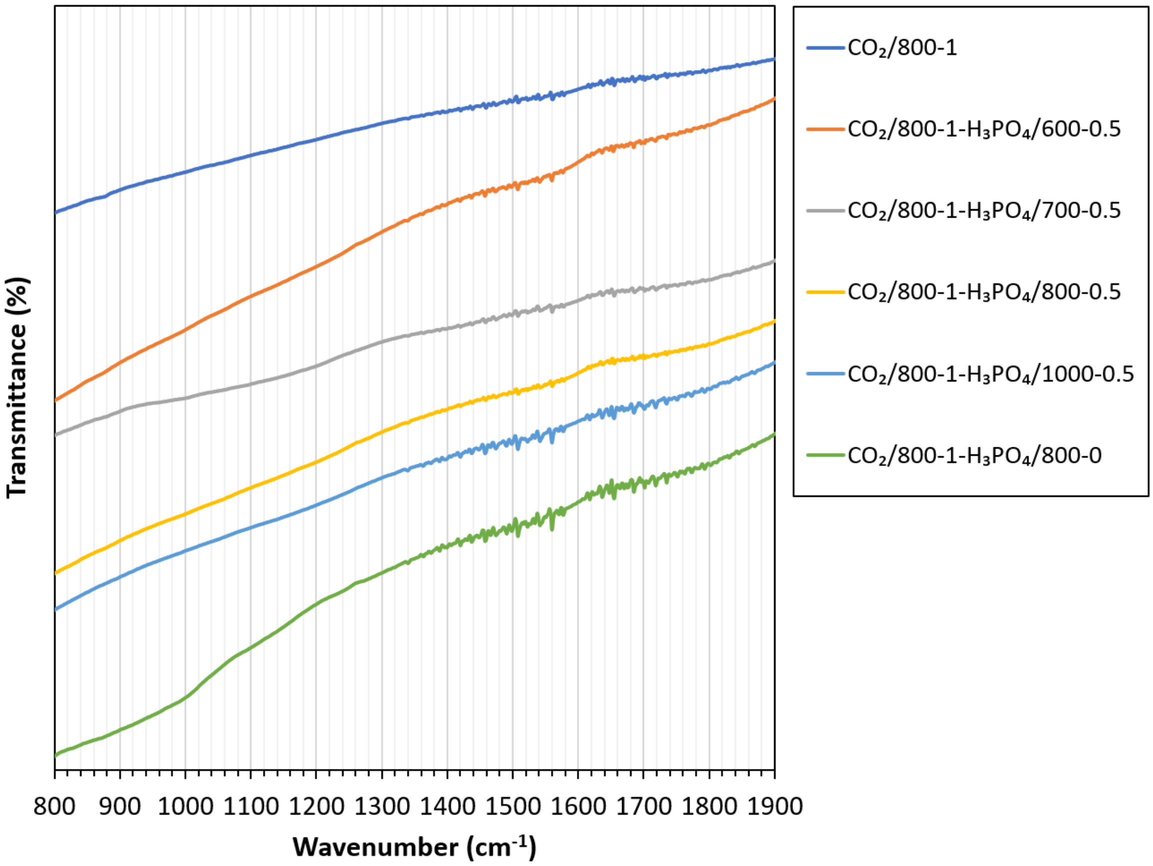

Figure 6-4 FTIR spectra of AC treated in H_3PO_4 0.5 M at 600-1000°C in N_2: CO_2/800-1-H_3PO_4/600-0.5, CO_2/800-1-H_3PO_4/700-0.5, CO_2/800-1-H_3PO_4/800-0.5, and CO_2/800-1-H_3PO_4/1000-0.5

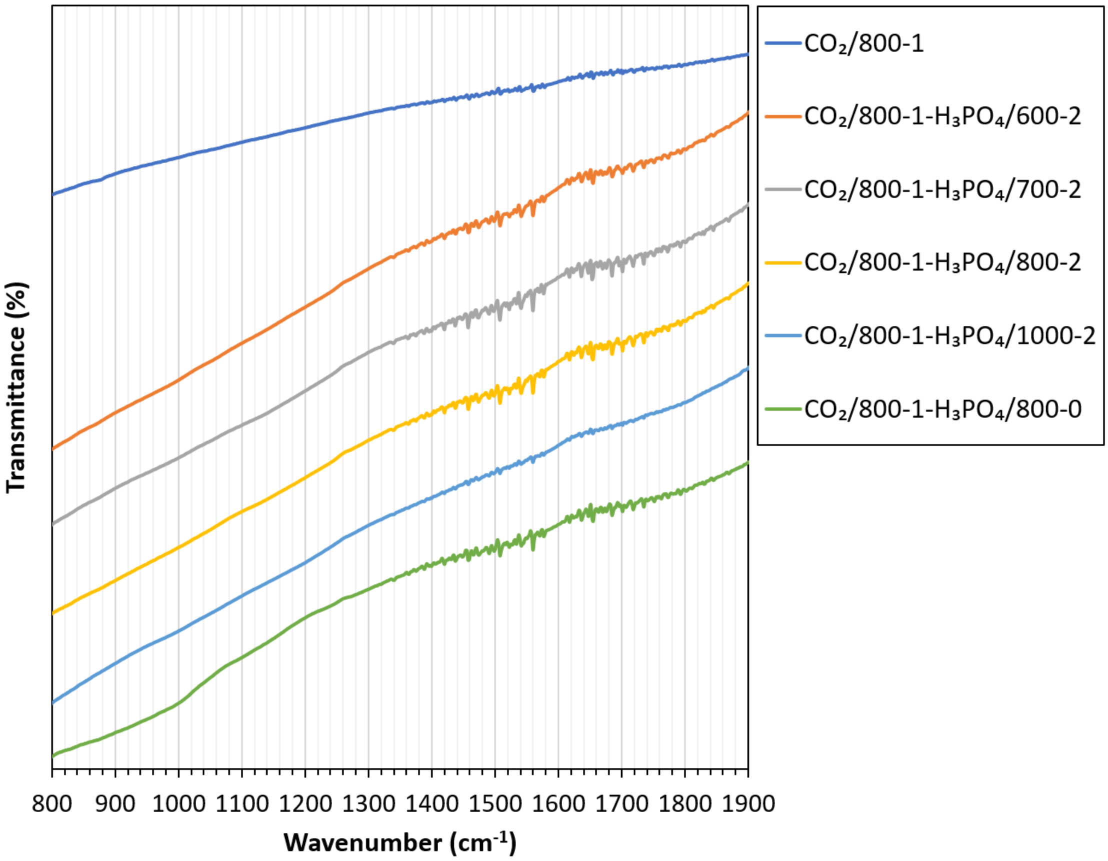

Figure 6-5 FTIR spectra of AC treated in H_3PO_4 2 M at 600-1000°C in N_2: CO_2/800-1-H_3PO_4/600-2, CO_2/800-1-H_3PO_4/700-2, CO_2/800-1-H_3PO_4/800-2, and CO_2/800-1-H_3PO_4/1000-2

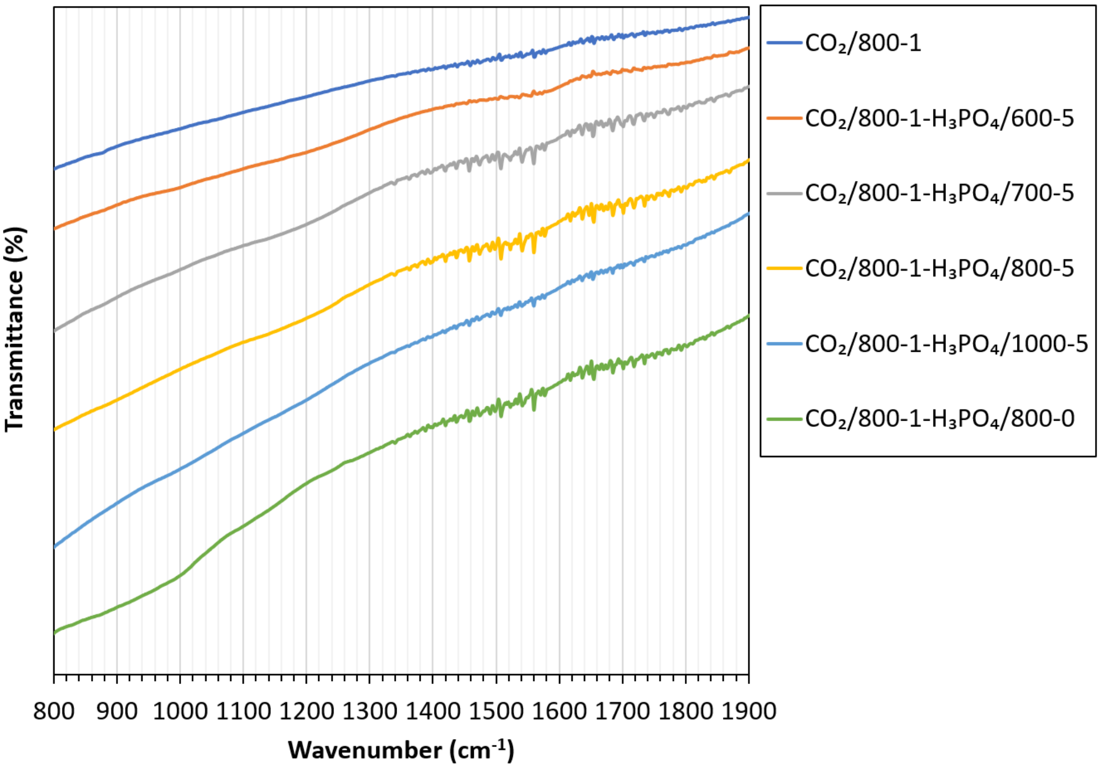

Figure 6-6 FTIR spectra of AC treated in H_3PO_4 5 M at 600-1000°C in N_2: CO_2/800-1-H_3PO_4/600-5, CO_2/800-1-H_3PO_4/700-5, CO_2/800-1-H_3PO_4/800-5, and CO_2/800-1-H_3PO_4/1000-5

FTIR spectra of AC soaked in H_3PO_4 solutions 0.5, 2 and 5 M and heat treated under NH_3 at 800°C are illustrated in Figure 6-7. Small adsorption peaks at 1500-1600 cm^{-1} in FTIR profiles of these NH_3 heat-treated AC samples indicated the existence of surface nitrogen functional groups as detected by XPS (see Table 6-3) and bulk nitrogen content analysis (see Table 6-1). The band at 1500-1600 cm^{-1} characterised pyridinic, pyridonic, and pyrrolic (or indolic) as studied in the study of Xiao and Thomas and Jia *et al.* (Jia *et al.* 2002, Xiao and Thomas 2005). This is also similar to NH_3 heat-treated AC and hydrochar as discussed in FTIR sections 5.2.3 and 5.3.3. Therefore, switching carrier gas from N_2 to NH_3 successfully incorporated nitrogen functional groups into AC. Furthermore, increasing concentration of H_3PO_4 solution also increased phosphorus group content. A small peak of P=O stretching at 1140-1320 cm^{-1} was observed in FTIR spectra of CO_2/800-1-H_3PO_4/NH_3-5 (Figure 6-7) but not in the profile CO_2/800-1-H_3PO_4/NH_3-0.5 (Larkin 2011). However, even with high H_3PO_4 solution concentration 5 M, it did not significantly increase the total phosphorus functional groups in AC. Ordered carbonaceous structure of AC CO_2/800-1 as discussed by Raman spectroscopy and PXRD (see Table 4-7 and Table 4-8) hindered the modification of H_3PO_4 on functional groups of AC during heat treatment. FTIR profiles of AC CO_2/800-1-H_3PO_4/CO_2-2 is also included in Figure 6-7, but changing gas environment from N_2 to CO_2 did not induce remarkable change in functional groups compared to CO_2/800-1.

FTIR profiles of AC treated at 1, 2 and 3 h holding time are also presented in Figure 6-8. Even though the holding time at 800°C increased from 1 h to 3 h, there was no significant change in any adsorption peaks in these profiles, indicating that holding time had negligible influence on phosphorus and oxygen functional group contents of H_3PO_4-treated AC.

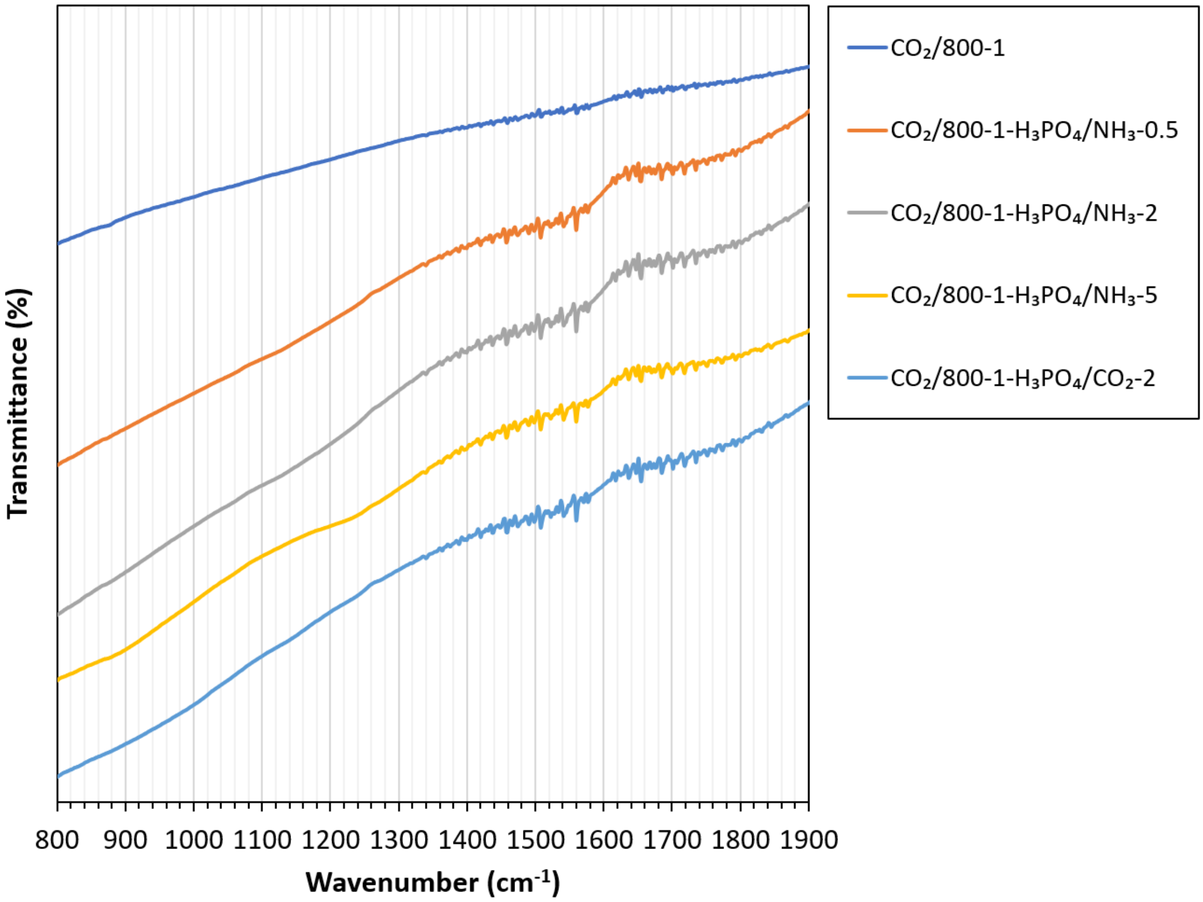

Figure 6-7 FTIR spectra of AC soaked in H_3PO_4 and treated at 800°C under NH_3: CO_2/800-1-H_3PO_4/NH_3-0.5 (H_3PO_4 0.5 M), CO_2/800-1-H_3PO_4/NH_3-2 (H_3PO_4 2 M) and CO_2/800-1-H_3PO_4/NH_3-5 (H_3PO_4 5 M) and under CO_2: CO_2/800-1-H_3PO_4/CO_2-2

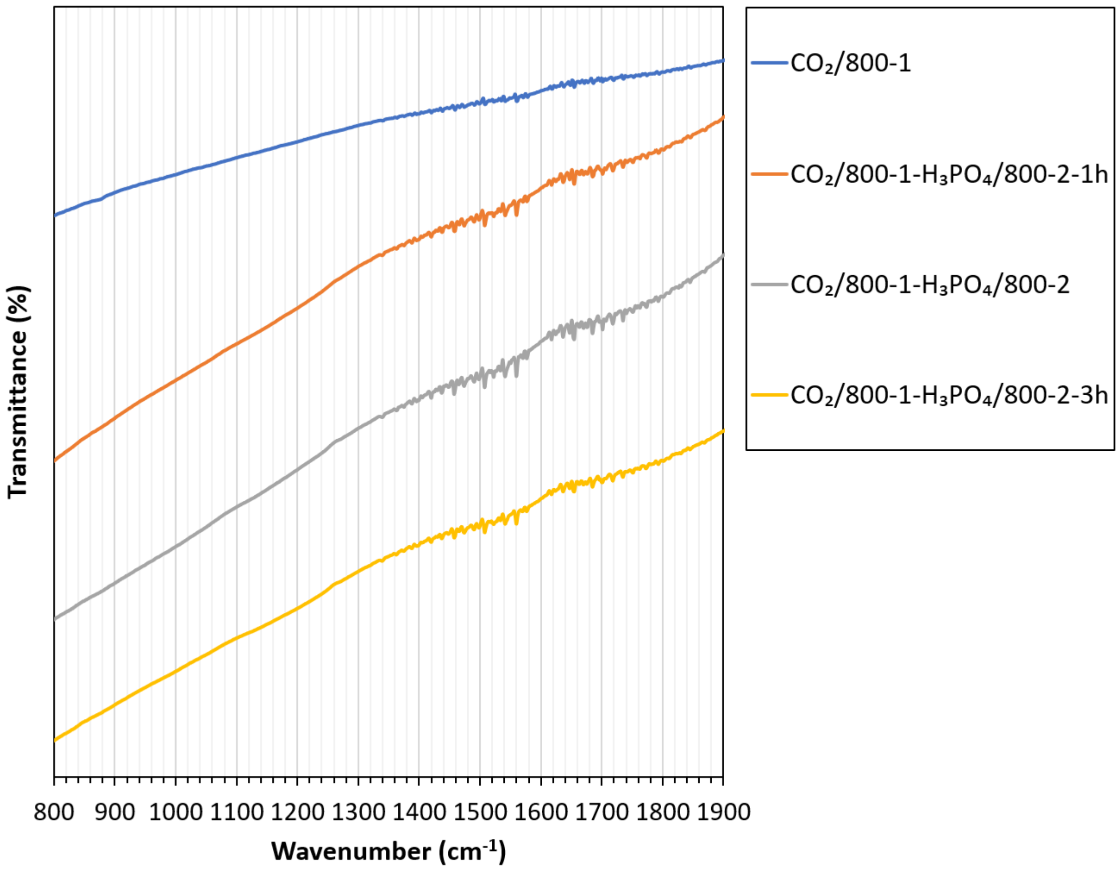

Figure 6-8 FTIR spectra of AC treated in H_3PO_4 2 M at 800°C in N_2 at 1, 2 and 3 h holding time: CO_2/800-1-H_3PO_4/800-2-1h, CO_2/800-1-H_3PO_4/800-2 and CO_2/800-1-H_3PO_4/800-2-3h.

6.1.4 Inductively coupled plasma mass spectrometry

One of the difficulties in characterising phosphorus in AC is to determine the total phosphorus content. The phosphorus content could not be determined directly by using elemental analysis technique in determining bulk CHNO contents. Therefore, inductively coupled plasma mass spectrometry (ICP-MS) was performed to examine the phosphorus content of AC. Table 6-5 illustrates the phosphorus content of several H_3PO_4-treated AC samples.

The phosphorus contents obtained from ICP-MS analysis were generally ten times lower than the surface phosphorus contents recorded from XPS (Table 6-3). The most significant increase in phosphorus content was observed when increasing H_3PO_4 solution concentration from 0.5 M to 2 M. This increased the phosphorus content detected in ICP-MS of CO_2/800-1-H_3PO_4/NH_3-0.5 from 0.06 wt% to 0.16 wt% in CO_2/800-1-H_3PO_4/NH_3-2 (Table 6-5). However, increasing H_3PO_4 solution concentration from 2 M to 5 M only results in small increase of phosphorus content from 0.13 to 0.18 wt% (for CO_2/800-1-H_3PO_4/800-2 and CO_2/800-1-H_3PO_4/800-5). Increasing H_3PO_4 concentration from 0.5 to 2 M could lead to the increase of phosphorus content incorporated into the solid, but reach saturation point where no more H_3PO_4 molecules could be incorporated during soaking preparation step, so it is not possible for more H_3PO_4 molecules to be incorporated into AC. On the other hand, increasing temperatures from 600 to 1000°C only varied phosphorus contents in the range of 0.09-0.14 wt% for AC CO_2/800-1-H_3PO_4/600-2 and CO_2/800-1-H_3PO_4/1000-2, so HTTs did not affect phosphorus contents in AC.

Table 6-5 Phosphorus content in H_3PO_4-treated AC obtained from ICP

Carbon sample	**Phosphorus concentration (μg g^{-1} AC)**	**Phosphorus content in AC (wt%)**	**Phosphorus content from XPS (at%)**
CO_2/800-1-H_3PO_4/600-2	1135.5	0.11	1.2 ± 0.1
CO_2/800-1-H_3PO_4/700-2	883.5	0.09	1.1 ± 0.1
CO_2/800-1-H_3PO_4/800-2	1285.5	0.13	1.3 ± 0.1
CO_2/800-1-H_3PO_4/1000-2	1437.5	0.14	1.6 ± 0.2
CO_2/800-1-H_3PO_4/800-5	1840.5	0.18	2.1 ± 0.1
CO_2/800-1-H_3PO_4/NH_3-2	1575.5	0.16	1.7 ± 0.2
CO_2/800-1-H_3PO_4/NH_3-0.5	560.5	0.06	0.6 ± 0.1

Low phosphorus contents detected from ICP-MS, together with FTIR analysis and surface phosphorus contents measured by XPS supported the hypothesis that phosphorus incorporation using H_3PO_4 with heat treatment on AC mainly modified the surface of AC and introduced phosphorus into its surface rather than in bulk. However, there was some undissolved sediment after AC was diluted in strong acid during ICP sample preparation, so there might be some phosphorus contents left in sediments and not all phosphorus was detected in ICP-MS.

6.2 Carbonaceous structure by powder X-ray diffraction

Powder X-ray diffraction (PXRD) was performed to analyse carbonaceous structure of H_3PO_4-treated AC (Table 6-6 and Figure 6-9). Being similar to biochar pyrolysed under N_2 and treated under CO_2 (as discussed in Chapter 4) and NH_3 heat-treated AC and hydrochar (as discussed in Chapter 5), PXRD patterns of H_3PO_4-treated AC showed two main peaks at ~22-23° and ~43° presenting for (002) and (100) carbon crystallites. Crystallite dimensions, including crystallite thickness L_c, interlayer distance d_{002}, and crystal diameter L_a of H_3PO_4-treated AC were calculated and shown in Table 6-6. Increasing HTTs from 600 to 1000°C increased L_a from 24.34-29.26 Å and reduced L_c significantly from 10.63-9.80 Å (AC CO_2/800-1-H_3PO_4/600-2 to CO_2/800-1-H_3PO_4/1000-2) while d_{002} remained unchanged with HTTs. The change in crystal dimensions with increasing HTTs is similar to biochar pyrolysed under N_2 and AC treated under CO_2 (see Table 4-8), in which HTT is the dominating operating condition over the holding time and carrier gas in controlling carbonaceous structure. Increasing heating temperatures allows the removal of other heteroatoms and the rearrangement of carbons in biochar, so it leads to higher ordered carbonaceous structure of H_3PO_4-treated AC.

Table 6-6 Crystallite thickness L_c, interlayer distance d_{002}, and crystal diameter L_a from XRD

Carbon sample	**Crystal thickness, L_c (Å)**	**Interlayer distance, d_{002} (Å)**	**Crystal diameter, L_a (Å)**
CO_2/800-1	9.91 ± 0.05	3.86 ± 0.02	23.15 ± 0.32
CO_2/800-1-H_3PO_4/600-2	10.63 ± 0.05	3.94 ± 0.02	24.34 ± 0.34
CO_2/800-1-H_3PO_4/700-2	10.29 ± 0.05	3.95 ± 0.02	26.32 ± 0.36
CO_2/800-1-H_3PO_4/800-2	10.14 ± 0.05	4.06 ± 0.02	24.59 ± 0.34
CO_2/800-1-H_3PO_4/1000-2	9.80 ± 0.05	3.97 ± 0.02	29.26 ± 0.40
CO2/800-1-H_3PO_4/800-0.5	9.59 ± 0.05	3.89 ± 0.02	24.60 ± 0.34
CO_2/800-1-H_3PO_4/800-5	9.40 ± 0.05	3.96 ± 0.02	24.90 ± 0.34
CO_2/800-1-H_3PO_4/NH_3-0.5	10.57 ± 0.05	3.74 ± 0.02	27.62 ± 0.38
CO_2/800-1-H_3PO_4/NH_3-2	10.53 ± 0.05	3.77 ± 0.02	26.23 ± 0.36
CO_2/800-1-H_3PO_4/NH_3-5	9.93 ± 0.05	3.89 ± 0.02	28.79 ± 0.40

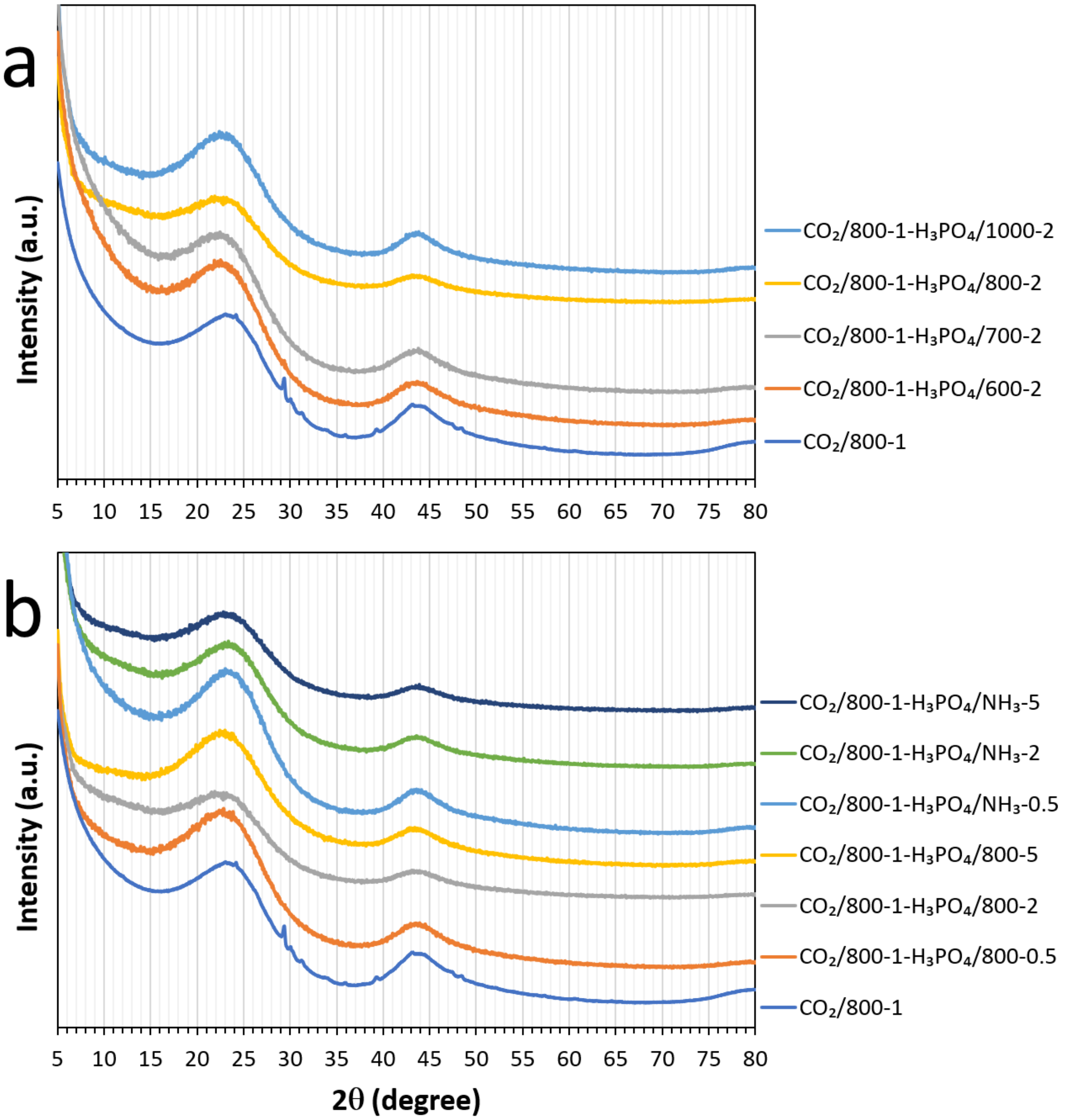

Figure 6-9 XRD patterns of (a) AC CO_2/800-1 and H_3PO_4-treated AC using H_3PO_4 solution 2 M at 600-1000°C under N_2 and (b) H_3PO_4-treated AC using H_3PO_4 solution 0.5-5 M at 800°C under N_2 and NH_3 atmosphere

The impact of increasing H_3PO_4 solution concentration from 0.5 M to 5 M can be seen for AC CO_2/800-1-H_3PO_4/800-0.5, CO_2/800-1-H_3PO_4/800-2 and CO_2/800-1-H_3PO_4/800-5. Table 6-6 shows that L_a remained constant in the range of 24.59-24.90 Å, and d_{002} only fluctuated in the range of 3.89-3.96 Å. However, L_c of CO_2/800-1-H_3PO_4/800-2 was slightly higher than the other two samples, 10.14 Å compared to 9.59 and 9.40 Å (Table 6-6). PXRD patterns of AC soaked in H_3PO_4 0.5, 2 and 5 M and heat treated in NH_3 were also examined. There was no compelling evidence for the influence of NH_3 gas atmosphere and H_3PO_4 concentration on L_a, L_c and d_{002} of AC CO_2/800-1-H_3PO_4/NH_3-0.5, CO_2/800-1-H_3PO_4/NH_3-2 and CO_2/800-1-

H_3PO_4/NH_3-5. *L_c* slightly varied in the range of 10.53-10.57 Å with increasing H_3PO_4 concentration from 0.5 to 5 M, and *L_a* fluctuated in the range of 26.23-28.79 Å. Based on PXRD carbon crystallite parameters of these samples, H_3PO_4 solution concentration appears to have negligible influence on carbonaceous structure of H_3PO_4-treated AC.

6.3 Gas adsorption-desorption behaviours

Surface area and porosity of H_3PO_4-treated AC were characterised using CO_2 adsorption-desorption at 0°C and N_2 adsorption-desorption at -196°C (Table 6-7). Phosphorus incorporation impacted negatively on surface area and porosity of AC. After AC CO_2/800-1 was soaked in H_3PO_4 2 M solution and annealed with temperatures in the range of 600-1000°C, S_{BET} of H_3PO_4-treated AC decreased significantly from 482 m^2 g^{-1} (CO_2/800-1) to 303 m^2 g^{-1} of CO_2/800-1-H_3PO_4/800-2. S_{BET} decreased further to 107 m^2 g^{-1} at 600°C (AC CO_2/800-1-H_3PO_4/600-2) but increasing temperature up to 1000°C severely reduced S_{BET} of CO_2/800-1-H_3PO_4/1000-2 to 9 m^2 g^{-1} which was similar to low BET N_2 surface area of N_2/1000-1 (Table 4-1). High pyrolysis temperatures annealed and corrupted carbon structure, leading to collapse of carbonaceous structure and extremely low S_{BET}. However, S_{CO2} of these H_3PO_4-treated AC samples only decreased from 632 m^2 g^{-1} from CO_2/800-1 to 482-567 m^2 g^{-1} for H_3PO_4-treated AC using H_3PO_4 2 M, so phosphorus incorporating procedure did not significantly modify ultramicropore surface area of these samples. The considerable difference between CO_2 DR micropore surface area and BET N_2 surface area of these H_3PO_4-treated AC samples indicated that there is significant activated diffusion effect.

Table 6-7 shows that changing N_2 to NH_3 atmosphere improved surface area of AC. S_{BET} of NH_3 heat-treated AC at 800°C using H_3PO_4 at 0.5, 2 and 5 M (CO_2/800-1-H_3PO_4/NH_3-0.5, CO_2/800-1-H_3PO_4/NH_3-2 and CO_2/800-1-H_3PO_4/NH_3-5) were in the range of 353-753 m^2 g^{-1}, higher than 303 m^2 g^{-1} of CO_2/800-1-H_3PO_4/800-2. NH_3 at 800°C reacted with AC through gasification/ pyrolysis reactions, so it enhanced the surface area of AC compared to N_2 atmosphere. However, comparison of N_2 DR micropore volume (0.140-0.298 cm^3 g^{-1}) to BET N_2 total pore volume (0.156-0.336 cm^3 g^{-1}) shows that 89-90% of pores of NH_3 heat-treated AC is micropore, indicating that NH_3 heat treatment only fostered the development of micropore. Mesopore volume of NH_3 heat-treated AC varied in a narrow range of 0.016-0.038 cm^3 g^{-1} (Table 6-7), similar to mesopore volume of CO_2/800-1 0.084 cm^3 g^{-1}. This is similar to other NH_3 heat-treated AC and hydrochar in Chapter 4 and Chapter 5 (see Table 4-1 and Table 5-13). Nevertheless, S_{BET} of AC soaked in H_3PO_4 and heat treated in NH_3 decreased with increasing H_3PO_4 solution concentration from 0.5 to 5 M, from 753 to 353 m^2 g^{-1} for AC

CO_2/800-1-H_3PO_4/NH_3-0.5 and CO_2/800-1-H_3PO_4/NH_3-5 respectively. Increasing H_3PO_4 concentration could enhance the annealed effect of NH_3 at 800°C, resulted in more pore collapse and lower surface porosity.

Changing carrier gas from NH_3 to CO_2 only increase the surface area from 604 to 755 m^2 g^{-1} (Table 6-7) (AC CO_2/800-1-H_3PO_4/NH_3-2 and CO_2/800-1-H_3PO_4/CO_2-2 respectively), so it is reasonably assumed that ordered carbon structure of AC inhibited the modifying effect of carrier gas on surface area of AC. The surface area of CO_2/800-1-H_3PO_4/CO_2-2 was as the same as CO_2/1000-1, 755 to 704 m^2 g^{-1}, respectively. Similar to NH_3 heat-treated AC, N_2 DR micropore volume accounts to 81% of total pore volume, indicating that CO_2 gasification only enhances micropore volume.

Table 6-7 Pore structure characterization by CO_2 and N_2 adsorption-desorption

Carbon sample	**S_{CO2} (m^2 g^{-1})**	**V_{CO2} (cm^3 g^{-1})**	**S_{BET} (m^2 g^{-1})**	**V_{N2} (cm^3 g^{-1})**	**V_{micro} (cm^3 g^{-1})**	**V_{meso} (cm^3 g^{-1})**
CO_2/800-1	632 ± 4	0.235 ± 0.001	482 ± 10	0.299 ± 0.003	0.181	0.084
CO_2/800-1-H_3PO_4/600-2	482 ± 5	0.179 ± 0.001	107 ± 2	0.084 ± 0.001	0.026	0.058
CO_2/800-1-H_3PO_4/800-2	567 ± 5	0.211 ± 0.001	303 ± 6	0.188 ± 0.002	0.122	0.066
CO_2/800-1-H_3PO_4/1000-2	551 ± 5	0.205 ± 0.001	9 ± 1	0.046 ± 0.001	0.003	0.043
CO_2/800-1-H_3PO_4/800-0.5			343 ± 7	0.166 ± 0.002	0.136	0.030
CO_2/800-1-H_3PO_4/800-5			117 ± 3	0.069 ± 0.001	0.046	0.023
CO_2/800-1-H_3PO_4/NH_3-0.5			753 ± 16	0.336 ± 0.003	0.298	0.038
CO_2/800-1-H_3PO_4/NH_3-2	641 ± 6	0.239 ± 0.001	636 ± 13	0.280 ± 0.003	0.251	0.029
CO_2/800-1-H_3PO_4/NH_3-5			353 ± 8	0.156 ± 0.002	0.140	0.016
CO_2/800-1-H_3PO_4/CO_2-2			755 ± 16	0.366 ± 0.004	0.297	0.069

Note: S_{CO2}: ultramicropore surface area, determined by using DR plot and CO_2 adsorption at 0°C; V_{CO2}: ultramicropore volume determined using DR plot and CO_2 adsorption at 0 °C; S_{BET}: total surface area determined by BET plot ($p/p° = 1\times10^{-3}$-0.06) and N_2 adsorption at -196°C; V_{N2}: total pore volume determined by N_2 adsorption at -196 °C at $p/p° = 0.995$; V_{micro}: micropore volume (0.3-2 nm) determined by using DR plot and N_2 adsorption at -196 °C; V_{meso}: subtraction of V_{micro} from V_{N2}.

6.4 Cyclic voltammetry

Figure 6-10 illustrates cyclic voltammetry (CV) profiles of several H_3PO_4-treated AC using H_3PO_4 2 M solution at 600-1000°C (CO_2/800-1-H_3PO_4/600-2, CO_2/800-1-H_3PO_4/800-2, and CO_2/800-1-H_3PO_4/1000-2). Peak currents of V^{2+}/V^{3+}, V^{3+}/VO^{2+} and VO^{2+}/VO^{2+} of H_3PO_4-treated AC did not show any significant change compared to AC precursor CO_2/800-1. Characterisation of H_3PO_4-treated AC from total CHNO analysis, XPS and ICP-MS only show that surface phosphorus contents only increase in the range of 1.1-1.6 at% (Table 6-2). The study of Gao *et al.* shows that phosphorus functional groups with the phosphorus content up to 13.0 at% on pristine polyaniline graphite felt (a smooth and non-porous structure with very low surface area (< 1 m^2 g^{-1})) was shown to demonstrate catalytic effects towards both VO^{2+}/VO_2^+, V^{3+}/VO^{2+}, and V^{2+}/V^{3+} (Gao *et al.* 2019). Therefore, low surface phosphorus contents in this study is unlikely to influence the conversion of vanadium redox reactions although there is difference of the contents of C-P group and C-O-P group CO_2/800-1-H_3PO_4/600-2 and CO_2/800-1-H_3PO_4/1000-2 as discussed in XPS (see Table 6-2).

The study of Kim *et al.* reveals that the low phosphorus content on carbon felt using NH_4PF_6 2 M (activated at 800°C for 2 h in Ar) at 2.0 at% could benefit the conversion of V^{2+}/V^{3+} and VO^{2+}/VO_2^+ through several oxygen-rich phosphate group couples (Kim *et al.* 2016). This surface phosphorus content is similar to phosphorus content in this study 1.1-1.6 at%. AC in this study was applied on bipolar plate instead of carbon felt in the study of Kim *et al.*, and this may explain why influence of surface phosphorus groups on V^{2+}/V^{3+}, V^{3+}/VO^{2+} and VO^{2+}/VO^{2+} was not observed in this study. As discussed in Chapter 4, AC was treated in HNO_3 to significantly modify surface oxygen functional groups, but it only slightly changed the electrochemical behaviours of vanadium redox reactions. Therefore, the result in this study does not rule out the positive impact of phosphorus functional groups on vanadium redox reactions found in other studies, and higher phosphorus contents are important to examine the influence of phosphorus to vanadium redox reactions.

CV spectrum of NH_3-heat treated AC CO_2/800-1-H_3PO_4/NH_3-2 shows enhancement in V^{3+}/VO^{2+} couple and slightly increase in V^{2+}/V^{3+} compared to precursor CO_2/800-1 and H_3PO_4-treated AC CO_2/800-1-H_3PO_4/800-2. NH_3 heat-treated AC CO_2/800-1-H_3PO_4/NH_3-2 contained both surface nitrogen and phosphorus (6.4 at% and 1.7 at% respectively – see Table 6-2). PXRD results (see Table 6-6) and porosity characterisation (see Table 6-7) show that NH_3 heat treatment at 800°C coupled with using H_3PO_4 2 M solution did not influence carbon amorphous structure and porosity. Phosphorus contents of CO_2/800-1-H_3PO_4/NH_3-2 and

CO_2/800-1-H_3PO_4/800-2 were also similar, 1.3 at% and 1.7 at%, respectively (see Table 6-2). This is evident that the nitrogen content enhances electrochemical activity of V^{2+}/V^{3+} and V^{3+}/VO^{2+}, similar to other NH_3 heat-treated AC discussed in Chapter 4 and Chapter 5. This also agrees with the result of Xu *et al.* that nitrogen functional groups could support the activity of vanadium redox reactions.

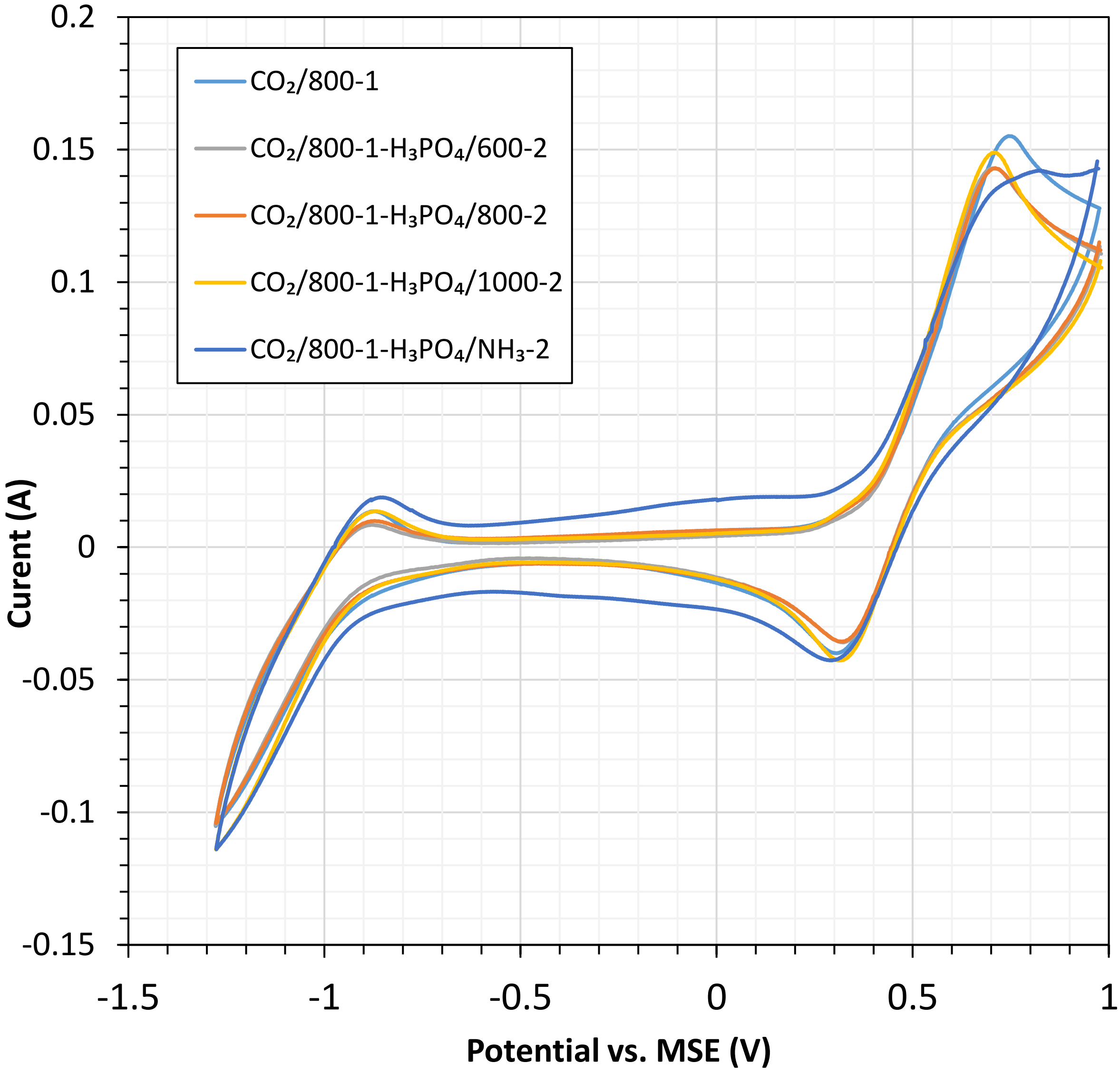

Figure 6-10 Cyclic voltammetry profiles of H_3PO_4-treated AC using H_3PO_4 2 M solution at 600-1000°C (CO_2/800-1-H_3PO_4/600-2, CO_2/800-1-H_3PO_4/800-2, and CO_2/800-1-H_3PO_4/1000-2) and H_3PO_4-treated AC under NH_3 (CO_2/800-1-H_3PO_4/NH_3-2)

6.5 Conclusions

H_3PO_4 heat treatment on AC has been conducted. It is shown that both heat treatment temperatures and H_3PO_4 solution concentration influence surface phosphorus group species.

Low H_3PO_4 solution concentration and low HTT promote the formation of C-O-P groups (C-O-PO_3/(C-O)$_3$PO) whereas increasing H_3PO_4 solution concentration and HTT incorporate C-P groups (C-PO_3/C_2-PO_2/C_3-PO). Surface phosphorus content in this study only increases up to 1.0-2.1 at% due to ordered carbonaceous structure of AC used in this study. H_3PO_4 heat treatment also does not influence carbonaceous amorphous structure and porosity of AC precursor. The low surface phosphorus functional groups, therefore, do not influence electrochemical behaviours of vanadium redox couples. The NH_3 heat-treated AC in this study, containing both nitrogen and phosphorus functional groups, shows positive impact on V^{2+}/V^{3+} and V^{3+}/VO^{2+} couples, which is in line with results obtained in Chapter 4 and Chapter 5.

Chapter 7 Conclusions and further perspectives

7.1 General conclusions

The depletion of non-renewable energy (*i.e.* fossil fuels) requires the replacement by environmentally-friendly energy sources such as solar energy, wind, geothermal and tidal energy, together with the use of energy storage to increase the incorporation of these renewable energies into grid system. As discussed in Chapter 1 and 2, VRFB has been considered as a potential energy storage which facilitates large-scale storage for renewables to increase the accessibility of renewables to all end-user demands, but high capital and maintenance cost, coupling with low energy density compared to other energy storages such as lithium-ion battery still hinders the application of VRFB. Furthermore, a significant amount of biomass (which is considered as renewable carbon source) is disposed in landfill or burn for energy. Therefore, the potential of walnut shell-derived carbon as a precursor for bipolar plates in VRFB has been studied in this thesis. This aims to make VRFB an economical energy storage by reducing the use of non-renewable graphite by biomass-derived carbon, also utilising porosity, functional groups, and carbonaceous structure in biomass-derived carbon to improve the performance of VRFB.

However, until now, only a few studies of biomass-derived carbons as a precursor for bipolar plate in VRFB from Nanyang Technological University, Singapore, using AC derived from orange peel (Maharjan *et al.* 2017), coconut shell (Ulaganathan *et al.* 2015), and Sal wood sawdust (Maharjan *et al.* 2019) have been conducted. The results in these studies, as discussed in section 2.2.2 about carbon components in VRFB, show contradicting results on how porosity, functional groups, and carbonaceous structure influence the electrochemical behaviours of vanadium redox reactions. Therefore, the work in Chapter 4 is dedicated to exploring in a systematically way how porosity, functional groups, and carbonaceous structure could influence vanadium redox reactions. Although pyrolysis under N_2 and CO_2, oxidising in concentrated HNO_3 solution, heat treatment with K_2CO_3 and HNO_3 are not novel functionalisation methods, these functionalisation methods provide a clear changing in porosity, oxygen functional groups and carbonaceous of biomass-derived carbon. A systematic change in these biomass-derived carbon properties was used to explain the change in electrochemical behaviours of vanadium redox reactions. Based on that, the role of oxygen functional groups in V^{2+}/V^{3+} and V^{3+}/VO^{2+} couples were determined, and surface area and porosity did not play significant roles in vanadium redox couples. Compared to the study of

Ulaganathan *et al.* (Ulaganathan *et al.* 2015), pores in coconut shell-derived carbon is predominantly mesoporous, which is significantly different from microporous walnut shell-derived carbon in this study. This supports the explanation that oxygen functional groups enhance the conversion of V^{2+}/V^{3+} and V^{3+}/VO^{2+} couples as observed in the study of Ulaganathan *et al.* (cyclic voltammetry spectrum of this coconut shell-derived AC is presented in Figure 2-4, section 2.2.2 page 18). Functionalisation of nitrogen groups in this study also shows that nitrogen could benefit for the conversion of VO^{2+}/VO_2^+ couple. This is in agreement with the study of Schnucklake *et al.* in which nitrogen functional groups (up to 4.2 at%) were deemed to improve the reversibility of VO^{2+}/VO_2^+ couple and reduce the charge transfer resistance (Schnucklake *et al.* 2019). The systematic change in porosity, functional groups, and carbonaceous structure used in Chapter 4 was also used in Chapter 5 to assess the impact of these parameters on VO^{2+}/VO_2^+ couple. Unfortunately, functionalisation of phosphorus groups in Chapter 6 did not show any specific influence on vanadium redox reactions. Despite that, the positive results from Chapter 4 and Chapter 5 prove that the impact of functional groups in walnut shell-derived carbon (or PVDF/walnut shell-derived carbon composite) as precursor for bipolar plate is similar to the impact of functional groups on carbon/graphite felt in other studies. Therefore, results from modification of carbon/graphite felt can be transposed to other studies on composite bipolar plate in VRFB in the future. Furthermore, it is also shown that a systematic change in characteristics of carbon precursors is crucial to understand the influence of those parameters on vanadium redox reactions.

7.2 Conclusions arising from the experimental context

- Heat treatment temperature is a dominating factor in controlling properties of walnut shell-derived carbon carbonised under N_2 and CO_2. Both suites of walnut shell-derived carbon prepared under N_2 and CO_2 are ultramicroporous with similar gas adsorption characteristics in which N_2 DR micropore volume accounts for 57-78% of total pores. CO_2 DR micropore volume characterization of biochar pyrolysed in N_2 atmosphere shows there is activated diffusion effect in this suite of biochar. Most walnut shell-derived carbons prepared under N_2 and CO_2 at 800-1000°C are basic carbons as shown by acid/base titrations. PXRD analysis shows that crystal diameter L_a of these walnut shell-derived carbon samples increase from 18.33 to 26.85-28.71 Å whereas I_D/I_G ratio from Raman spectroscopy increases from 0.69-0.72 at 600°C to 0.95-1.02 at 1000°C.

- Oxidising AC in concentrated HNO_3 solution increases both bulk and surface oxygen contents to 23.84 wt% and 13.5 at% respectively, and incorporates a mixture of acidic carboxylic, lactone, lactol anhydride functional groups into AC. Heat treatment of oxidized AC to 400°C decomposes mainly carboxylic groups, while increasing heat treatment temperature (HTT) to 800°C decompose more oxygen functional groups. Heat treatment AC with K_2CO_3 results to little change in carbon molecular structure, and this AC is amphoteric with mainly phenolic groups.
- Properties of carbon materials carbonised under N_2 and CO_2, oxidised in HNO_3 and treated in K_2CO_3 give evident that carbonization at temperatures up to 800°C give the largest increase in the VO^{2+}/VO_2^+ couple in cyclic voltammetry while functional groups increase in the V^{2+}/V^{3+} and V^{3+}/VO^{2+} couples. Majority of pores of walnut shell-derived carbon in this study is micropores which does not influence the electrochemical behaviours of the vanadium redox reactions.
- Dielectric barrier discharge (DBD) cold plasma and conventional heat treatment under NH_3 are effective to incorporate surface nitrogen functional groups. Cold plasma power is a dominant factor affecting the nitrogen functionalisation process. In DBD cold plasma treatment, amine-N and amide-N groups are incorporated to surface of biochar up to 8.7 at% with amine-N/amide-N ratio increasing from ~0.4 to ~2.5 when cold plasma power increases from 20 W to 80 W. NH_3 heat treatment also modifies surface functional groups by replacing oxygen with pyridinic-N, pyrrolic-N and quaternary-N.
- The similarity of XPS profile between amine-N and pyridinic-N, amide-N and pyrrolic-N requires other analysis such as TPD and FTIR to be performed to ascertain results from XPS. Cold plasma treatment, however, is not a suitable technique to modify surface area and porous structure and carbonaceous structure.
- Pyridinic-N and pyrrolic-N groups enhance reactivity of V^{2+}/V^{3+} and V^{3+}/VO^{2+} couples. Also, pyridinic-N and pyrrolic-N groups are more effective than amine-N and amide-N groups in supporting the oxidation from VO^{2+} to VO_2^+. For amine-N and amide-N, amine-N/amide-N ratio of 0.9 rather 0.4 and 2.5 positively influences the conversion of VO^{2+}/VO_2^+. Due to the removal of surface functional groups during NH_3 heat treatment, it increases the irreversibility of VO^{2+}/VO_2^+ couple. It is also revealed that nitrogen and oxygen functional groups, carbonaceous structure, and porosity have little influence on the reduction of VO_2^+ to VO^{2+}.

- H_3PO_4 heat treatment on AC shows that low H_3PO_4 solution concentration and low HTT (*i.e.* 0.5 M and 600-700°C) promote the formation of C-O-P groups (C-O-PO_3/$(C\text{-}O)_3PO$) whereas increasing H_3PO_4 solution concentration and HTT (*i.e.* 2 M and 800-1000°C) incorporate C-P groups (C-PO_3/C_2-PO_2/C_3-PO).
- Due to ordered carbonaceous structure of walnut shell-derived carbon precursor, phosphorus content only increases up to 1.0-2.1 at%, and phosphorus only resides on the surface of AC. Therefore, the influence of phosphorus functional groups to vanadium redox reactions are not observed in this study.

7.3 Further perspectives and recommendation for future works

- Biomass-derived carbon shows potential to become a precursor for bipolar plate in vanadium redox flow battery. Further research on the influence of various contents of biomass-derived carbon in the PVDF/biomass-derived carbon composite would be beneficial, and developing method to prepare PVDF/biomass-derived carbon composite without applying on commercial bipolar plate is crucial to ensure the sustainable application of bipolar plate into vanadium redox flow battery.
- The impact of porosity, carbonaceous structure, and functional groups of biomass-derived carbon on vanadium redox reactions has been assessed, and positive changes in electrochemical behaviours of vanadium redox couples in accordance with systematic change in properties of biomass-derived carbon have been observed. However, the impact of biomass-derived carbon on vanadium redox reactions is considered to be small in this study. Therefore, it is important to understand how to increase the positive impact of functional groups on biomass-derived carbon to vanadium redox couples. Further testing of biomass-derived carbon as bipolar plate material in model vanadium redox flow battery is crucial to assess how properties of biomass-derived carbon can influence electrochemical characteristics.
- DBD cold plasma treatment could incorporate amine-N and amide-N functional groups into biomass-derived carbon, but it is unclear how DBD cold plasma treatment does not support the transition from amine-N and amide-N functional groups into pyridinic-N, pyrrolic-N and quaternary-N. Being similar to conventional NH_3 heat treatment, DBD cold plasma treatment also impact surface of biochar, but it is evident from this study that the depth level of nitrogen incorporation into biochar is different from these two methods. Therefore, further research in incorporating mechanism of nitrogen into biomass-derived carbon and how to convert amine-N and amide-N

groups into pyridinic-N, pyrrolic-N and quaternary-N would be beneficial for DBD cold plasma to replace NH_3 heat treatment.

- The study in H_3PO_4 heat treatment on AC shows that phosphorus functional groups could be altered using different heat treatment temperatures and H_3PO_4 solution concentrations. Therefore, further study in how to increase phosphorus content in biomass-derived carbon and how different phosphorus functional groups influence kinetics of vanadium redox reactions would be beneficial for applying phosphorus-incorporated carbon as precursor for vanadium redox flow battery.
- There is still a gap between material characterisations and electrochemical experiment. Material characterisations are applied on biomass-derived carbon whereas electrochemical experiment is conducted on PVDF/biomass-derived carbon composite in which PVDF is used as a binder. Therefore, further studies on other important factors such as electrical resistivity, area-specific resistance, tensile strength, and thermal conductivity of both biomass-derived carbon and PVDF/biomass-derived carbon are important to understand how biomass-derived carbon can be used in bipolar plate.
- Thermochemical processes (pyrolysis, heat treatment in oxidation atmosphere such as CO_2, NH_3, activation with K_2CO_3, *etc.*) are conventional processes and have been studied for a long time. Therefore, it is possible to use these for mass production of biomass-derived carbon. However, the main challenge hindering the scale-up process fall into the characteristics of biomass feedstock. Lignin accounts up to 50% of total feedstock mass, and the structure of lignin can vary significantly among different biomass feedstock. Lignin can influence the characteristics of biomass-derived carbon, such as electrical resistivity, area-specific resistance, tensile strength, and thermal conductivity. Further study of how the structure of lignin influences these properties is important for the scale-up process of biomass-derived carbon in bipolar plate manufacturing. Another challenge would be the optimisation of surface are, porosity and functional groups during mass production of biomass-derived carbon.

References

(1980). "Redox flow cell development and demonstration project." Journal of Power Sources **5**(4): 382-384.

(2001). Appendix 2 - Isotopic Composition of the Elements. Inductively Coupled Plasma-Mass Spectrometry. H. E. Taylor. San Diego, Academic Press**:** 167-173.

Ahmad, M., A. U. Rajapaksha, J. E. Lim, M. Zhang, N. Bolan, D. Mohan, M. Vithanage, S. S. Lee and Y. S. Ok (2014). "Biochar as a sorbent for contaminant management in soil and water: A review." Chemosphere **99**: 19-33.

Al-Wabel, M. I., A. Al-Omran, A. H. El-Naggar, M. Nadeem and A. R. A. Usman (2013). "Pyrolysis temperature induced changes in characteristics and chemical composition of biochar produced from conocarpus wastes." Bioresource technology **131**: 374-379.

Álvarez-Murillo, A., S. Román, B. Ledesma and E. Sabio (2015). "Study of variables in energy densification of olive stone by hydrothermal carbonization." Journal of Analytical and Applied Pyrolysis **113**: 307-314.

Arkhipova, E. A., A. S. Ivanov, N. E. Strokova, S. A. Chernyak, A. V. Shumyantsev, K. I. Maslakov, S. V. Savilov and V. V. Lunin (2017). "Structural evolution of nitrogen-doped carbon nanotubes: From synthesis and oxidation to thermal defunctionalization." Carbon **125**: 20-31.

Aziz, M. A. and S. Shanmugam (2017). "Zirconium oxide nanotube–Nafion composite as high performance membrane for all vanadium redox flow battery." Journal of Power Sources **337**: 36-44.

Baek, J., H.-S. Shin, D. C. Chung and B.-J. Kim (2017). "Studies on the correlation between nanostructure and pore development of polymeric precursor-based activated hard carbons: II. Transmission electron microscopy and Raman spectroscopy studies." Journal of Industrial and Engineering Chemistry **54**: 324-331.

Basso, D., F. Patuzzi, D. Castello, M. Baratieri, E. C. Rada, E. Weiss-Hortala and L. Fiori (2016). "Agro-industrial waste to solid biofuel through hydrothermal carbonization." Waste Management **47**: 114-121.

Basso, D., E. Weiss-Hortala, F. Patuzzi, D. Castello, M. Baratieri and L. Fiori (2015). "Hydrothermal carbonization of off-specification compost: A byproduct of the organic municipal solid waste treatment." Bioresource technology **182**: 217-224.

Bavafa, M., H. Ilati and B. Rashidian (2008). "Comprehensive simulation of the effects of process conditions on plasma enhanced chemical vapor deposition of silicon nitride." Semiconductor Science and Technology **23**(9): 095023.

Bayu, A., A. Abudula and G. Guan (2019). "Reaction pathways and selectivity in chemo-catalytic conversion of biomass-derived carbohydrates to high-value chemicals: A review." Fuel Processing Technology **196**: 106162.

Bedia, J., R. Barrionuevo, J. Rodríguez-Mirasol and T. Cordero (2011). "Ethanol dehydration to ethylene on acid carbon catalysts." Applied Catalysis B: Environmental **103**(3): 302-310.

Bedia, J., J. M. Rosas, J. Márquez, J. Rodríguez-Mirasol and T. Cordero (2009). "Preparation and characterization of carbon based acid catalysts for the dehydration of 2-propanol." Carbon **47**(1): 286-294.

Benaddi, H., T. J. Bandosz, J. Jagiello, J. A. Schwarz, J. N. Rouzaud, D. Legras and F. Béguin (2000). "Surface functionality and porosity of activated carbons obtained from chemical activation of wood." Carbon **38**(5): 669-674.

Bian, R., B. Ma, X. Zhu, W. Wang, L. Li, S. Joseph, X. Liu and G. Pan (2016). "Pyrolysis of crop residues in a mobile bench-scale pyrolyser: Product characterization and environmental performance." Journal of Analytical and Applied Pyrolysis **119**: 52-59.

Bobleter, O. (1994). "Hydrothermal degradation of polymers derived from plants." Progress in Polymer Science **19**(5): 797-841.

Boehm, H. P. (2002). "Surface oxides on carbon and their analysis: a critical assessment." Carbon **40**(2): 145-149.

Boudou, J. P., M. Chehimi, E. Broniek, T. Siemieniewska and J. Bimer (2003). "Adsorption of H_2S or SO_2 on an activated carbon cloth modified by ammonia treatment." Carbon **41**(10): 1999-2007.

Brunauer, S., P. H. Emmett and E. Teller (1938). "Adsorption of Gases in Multimolecular Layers." Journal of the American Chemical Society **60**(2): 309-319.

Burhenne, L. and T. Aicher (2014). "Benzene removal over a fixed bed of wood char: The effect of pyrolysis temperature and activation with CO_2 on the char reactivity." Fuel Processing Technology **127**: 140-148.

Burrell, M. C. (2001). Chemical Analysis, Electron Spectroscopy. Encyclopedia of Materials: Science and Technology. K. H. J. Buschow, R. W. Cahn, M. C. Flemings et al. Oxford, Elsevier**:** 1142-1149.

Calo, J. M., D. Cazorla-Amorós, A. Linares-Solano, M. C. Román-Martínez and C. S.-M. De Lecea (1997). "The effects of hydrogen on thermal desorption of oxygen surface complexes." Carbon **35**(4): 543-554.

Cao, X., F. Xiao, P. Duan, J. J. Pignatello, J. Mao and K. Schmidt-Rohr (2019). "Effects of post-pyrolysis air oxidation on the chemical composition of biomass chars investigated by solid-state nuclear magnetic resonance spectroscopy." Carbon **153**: 173-178.

Cha, J. S., J.-C. Choi, J. H. Ko, Y.-K. Park, S. H. Park, K.-E. Jeong, S.-S. Kim and J.-K. Jeon (2010). "The low-temperature SCR of NO over rice straw and sewage sludge derived char." Chemical Engineering Journal **156**(2): 321-327.

Chen, C., B. Liang, A. Ogino, X. Wang and M. Nagatsu (2009). "Oxygen Functionalization of Multiwall Carbon Nanotubes by Microwave-Excited Surface-Wave Plasma Treatment." The Journal of Physical Chemistry C **113**(18): 7659-7665.

Chen, D., X. Chen, J. Sun, Z. Zheng and K. Fu (2016). "Pyrolysis polygeneration of pine nut shell: Quality of pyrolysis products and study on the preparation of activated carbon from biochar." Bioresource Technology **216**: 629-636.

Chen, J., Z. H. Zhu, S. Wang, Q. Ma, V. Rudolph and G. Q. Lu (2010). "Effects of nitrogen doping on the structure of carbon nanotubes (CNTs) and activity of Ru/CNTs in ammonia decomposition." Chemical Engineering Journal **156**(2): 404-410.

Chen, M.-m. (2016). Chapter 12 - Thermal Analysis. Materials Science and Engineering of Carbon. M. Inagaki and F. Kang, Butterworth-Heinemann**:** 249-272.

Chen, W., R. Wei, L. Yang, Y. Yang, G. Li and J. Ni (2019). "Characteristics of wood-derived biochars produced at different temperatures before and after deashing: Their different potential advantages in environmental applications." Science of The Total Environment **651**: 2762-2771.

Chen, W., L. Xu, Y. Tian, H. Li and K. Wang (2018). "Boron and nitrogen co-doped graphene aerogels: Facile preparation, tunable doping contents and bifunctional oxygen electrocatalysis." Carbon **137**: 458-466.

Cheng, P., S. Gao, P. Zang, X. Yang, Y. Bai, H. Xu, Z. Liu and Z. Lei (2015). "Hierarchically porous carbon by activation of shiitake mushroom for capacitive energy storage." Carbon **93**: 315-324.

Chetty, R., S. Kundu, W. Xia, M. Bron, W. Schuhmann, V. Chirila, W. Brandl, T. Reinecke and M. Muhler (2009). "PtRu nanoparticles supported on nitrogen-doped multiwalled carbon nanotubes as catalyst for methanol electrooxidation." Electrochimica Acta **54**(17): 4208-4215.

Cho, E. J., L. T. P. Trinh, Y. Song, Y. G. Lee and H.-J. Bae (2020). "Bioconversion of biomass waste into high value chemicals." Bioresource Technology **298**: 122386.

Chowdhury, Z. Z., M. Ziaul Karim, M. A. Ashraf and K. Khalid (2016). "Influence of carbonization temperature on physicochemical properties of biochar derived from slow pyrolysis of durian wood (Durio zibethinus) sawdust." BioResources **11**(2): 3356-3372.

Ciuta, S., D. Tsiamis and M. J. Castaldi (2018). Chapter Two - Fundamentals of Gasification and Pyrolysis. Gasification of Waste Materials. S. Ciuta, D. Tsiamis and M. J. Castaldi, Academic Press**:** 13-36.

Claesson, P. M., A. van der Wal and A. Fogden (2007). 8 - New Techniques for Optimization of Particulate Cleaning. Handbook for Cleaning/Decontamination of Surfaces. I. Johansson and P. Somasundaran. Amsterdam, Elsevier Science B.V.**:** 885-927.

Cuesta, A., P. Dhamelincourt, J. Laureyns, A. Martínez-Alonso and J. M. D. Tascón (1994). "Raman microprobe studies on carbon materials." Carbon **32**(8): 1523-1532.

Darling, R. M. and M. L. Perry (2014). "The influence of electrode and channel configurations on flow battery performance." Journal of The Electrochemical Society **161**(9): A1381.

Das, P., M. Dinda, N. Gosai and S. Maiti (2015). "High Energy Density Bio-oil via Slow Pyrolysis of Jatropha curcas Shells." Energy & Fuels **29**(7): 4311-4320.

Das, S. K., G. K. Ghosh and R. Avasthe (2020). "Application of biochar in agriculture and environment, and its safety issues." Biomass Conversion and Biorefinery: 1-11.

Dastgheib, S. A., T. Karanfil and W. Cheng (2004). "Tailoring activated carbons for enhanced removal of natural organic matter from natural waters." Carbon **42**(3): 547-557.

De Haseth, J. A., J. D. Winefordner, P. R. Griffiths and J. A. De Haseth (2007). Fourier Transform Infrared Spectrometry. Hoboken, UNITED STATES, John Wiley & Sons, Incorporated.

Del Bubba, M., B. Anichini, Z. Bakari, M. C. Bruzzoniti, R. Camisa, C. Caprini, L. Checchini, D. Fibbi, A. El Ghadraoui, F. Liguori and S. Orlandini (2020). "Physicochemical properties and sorption capacities of sawdust-based biochars and commercial activated carbons towards ethoxylated alkylphenols and their phenolic metabolites in effluent wastewater from a textile district." Science of The Total Environment **708**: 135217.

Demirbas, A. (2004). "Effects of temperature and particle size on bio-char yield from pyrolysis of agricultural residues." Journal of Analytical and Applied Pyrolysis **72**(2): 243-248.

Diaz-Silvarrey, L. S., K. Zhang and A. N. Phan (2018). "Monomer recovery through advanced pyrolysis of waste high density polyethylene (HDPE)." Green Chemistry **20**(8): 1813-1823.

Ding, H., K. Huang, S. Li, L. Xu, J. Xia and M. Li (2017). "Flame retardancy and thermal degradation of halogen-free flame-retardant biobased polyurethane composites based on ammonium polyphosphate and aluminium hypophosphite." Polymer Testing **62**: 325-334.

Ding, Y., O. A. Ezekoye, S. Lu, C. Wang and R. Zhou (2017). "Comparative pyrolysis behaviors and reaction mechanisms of hardwood and softwood." Energy Conversion and Management **132**: 102-109.

Doe, U. S. (2007). "Basic Research Needs for Electrical Energy Storage." DOE Report.

Doetsch, C. and J. Burfeind (2016). Chapter 12 - Vanadium Redox Flow Batteries A2 - Letcher, Trevor M. Storing Energy. Oxford, Elsevier**:** 227-246.

Dollet, A., J. P. Couderc and B. Despax (1995). "Analysis and numerical modelling of silicon nitride deposition in a plasma-enhanced chemical vapour deposition reactor. I. Bidimensional modelling." Plasma Sources Science and Technology **4**(1): 94-106.

Donar, Y. O., E. Çağlar and A. Sınağ (2016). "Preparation and characterization of agricultural waste biomass based hydrochars." Fuel **183**: 366-372.

Dong, S., P. Alvarez, N. Paterson, D. R. Dugwell and R. Kandiyoti (2009). "Study on the Effect of Heat Treatment and Gasification on the Carbon Structure of Coal Chars and Metallurgical Cokes using Fourier Transform Raman Spectroscopy." Energy & Fuels **23**(3): 1651-1661.

Dubinin, M. M. and H. F. Stoeckli (1980). "Homogeneous and heterogeneous micropore structures in carbonaceous adsorbents." Journal of Colloid and Interface Science **75**(1): 34-42.

Fang, J., B. Gao, A. R. Zimmerman, K. S. Ro and J. Chen (2016). "Physically (CO_2) activated hydrochars from hickory and peanut hull: preparation, characterization, and sorption of methylene blue, lead, copper, and cadmium." RSC Advances **6**(30): 24906-24911.

Fang, Z., T. Sato, R. L. Smith, H. Inomata, K. Arai and J. A. Kozinski (2008). "Reaction chemistry and phase behavior of lignin in high-temperature and supercritical water." Bioresource Technology **99**(9): 3424-3430.

Fang, Z., H. Zhao, L. Xiong, F. Zhang, Q. Fu, Z. Ma, C. Xu, Z. Lin, H. Wang, Z. Hu and S. Yao (2019). "Enhanced ferromagnetic properties of N_2 plasma-treated carbon nanotubes." Journal of Materials Science **54**(3): 2307-2314.

Ferrari, A. C., J. C. Meyer, V. Scardaci, C. Casiraghi, M. Lazzeri, F. Mauri, S. Piscanec, D. Jiang, K. S. Novoselov and S. Roth (2006). "Raman spectrum of graphene and graphene layers." Physical review letters **97**(18): 187401.

Ferrari, A. C. and J. Robertson (2000). "Interpretation of Raman spectra of disordered and amorphous carbon." Physical Review B **61**(20): 14095-14107.

Ferrari, A. C. and J. Robertson (2001). "Resonant Raman spectroscopy of disordered, amorphous, and diamondlike carbon." Physical Review B **64**(7): 075414.

Ferrari, A. C. and J. Robertson (2004). "Raman spectroscopy of amorphous, nanostructured, diamond–like carbon, and nanodiamond." Philosophical Transactions of the Royal Society of London A: Mathematical, Physical and Engineering Sciences **362**(1824): 2477-2512.

Figueiredo, J. L., M. F. R. Pereira, M. M. A. Freitas and J. J. M. Órfão (1999). "Modification of the surface chemistry of activated carbons." Carbon **37**(9): 1379-1389.

Forner-Cuenca, A. and F. R. Brushett (2019). "Engineering porous electrodes for next-generation redox flow batteries: recent progress and opportunities." Current Opinion in Electrochemistry **18**: 113-122.

Fridman, A. (2008). Plasma chemistry, Cambridge university press.

Friedl, J., C. M. Bauer, A. Rinaldi and U. Stimming (2013). "Electron transfer kinetics of the VO^{2+}/VO_2^+ – Reaction on multi-walled carbon nanotubes." Carbon **63**: 228-239.

Fritz, O. W. and K. J. Hüttinger (1993). "Active sites and intrinsic rates of carbon-gas reactions—a definite confirmation with the carbon-carbon dioxide reaction." Carbon **31**(6): 923-930.

Gao, Y., H. Wang, Q. Ma, A. Wu, W. Zhang, C. Zhang, Z. Chen, X.-X. Zeng, X. Wu and Y. Wu (2019). "Carbon sheet-decorated graphite felt electrode with high catalytic activity for vanadium redox flow batteries." Carbon **148**: 9-15.

García-Mateos, F. J., R. Berenguer, M. J. Valero-Romero, J. Rodríguez-Mirasol and T. Cordero (2018). "Phosphorus functionalization for the rapid preparation of highly nanoporous submicron-diameter carbon fibers by electrospinning of lignin solutions." Journal of Materials Chemistry A **6**(3): 1219-1233.

García, A. B., A. Martínez-Alonso, C. A. Leon y Leon and J. M. D. Tascón (1998). "Modification of the surface properties of an activated carbon by oxygen plasma treatment." Fuel **77**(6): 613-624.

Garlapalli, R. K., B. Wirth and M. T. Reza (2016). "Pyrolysis of hydrochar from digestate: Effect of hydrothermal carbonization and pyrolysis temperatures on pyrochar formation." Bioresource Technology **220**: 168-174.

Garrido, J., A. Linares-Solano, J. M. Martin-Martinez, M. Molina-Sabio, F. Rodriguez-Reinoso and R. Torregrosa (1987). "Use of nitrogen vs. carbon dioxide in the characterization of activated carbons." Langmuir **3**(1): 76-81.

Geng, Z., Q. F. Xiao, H. Lv, B. Li, H. B. Wu, Y. F. Lu and C. M. Zhang (2016). "One-Step Synthesis of Microporous Carbon Monoliths Derived from Biomass with High Nitrogen Doping Content for Highly Selective CO2 Capture." Scientific Reports **6**.

Gong, Y., H. Wang, Z. Wei, L. Xie and Y. Wang (2014). "An efficient way to introduce hierarchical structure into biomass-based hydrothermal carbonaceous materials." ACS Sustainable Chemistry & Engineering **2**(10): 2435-2441.

González, Z., C. Botas, C. Blanco, R. Santamaría, M. Granda, P. Álvarez and R. Menéndez (2013). "Graphite oxide-based graphene materials as positive electrodes in vanadium redox flow batteries." Journal of Power Sources **241**: 349-354.

Gregg, S. and K. Sing (1982). Adsorption, surface area and porosity, London; New York : Academic Press.

Gu, D., R. Ma, Y. Zhou, F. Wang, K. Yan, Q. Liu and J. Wang (2017). "Synthesis of Nitrogen-Doped Porous Carbon Spheres with Improved Porosity toward the Electrocatalytic Oxygen Reduction." ACS Sustainable Chemistry & Engineering **5**(11): 11105-11116.

Guo, L., J. Yang, G. Hu, X. Hu, L. Wang, Y. Dong, H. DaCosta and M. Fan (2016). "Role of Hydrogen Peroxide Preoxidizing on CO_2 Adsorption of Nitrogen-Doped Carbons Produced from Coconut Shell." ACS Sustainable Chemistry & Engineering **4**(5): 2806-2813.

Guo, S., X. Dong, T. Wu, F. Shi and C. Zhu (2015). "Characteristic evolution of hydrochar from hydrothermal carbonization of corn stalk." Journal of Analytical and Applied Pyrolysis **116**: 1-9.

Guo, S., X. Dong, T. Wu and C. Zhu (2016). "Influence of reaction conditions and feedstock on hydrochar properties." Energy Conversion and Management **123**: 95-103.

Haerle, R., E. Riedo, A. Pasquarello and A. Baldereschi (2001). "sp^2/sp^3 hybridization ratio in amorphous carbon from C 1s core-level shifts: X-ray photoelectron spectroscopy and first-principles calculation." Physical Review B **65**(4): 045101.

Halim, S. A. and J. Swithenbank (2016). "Characterisation of Malaysian wood pellets and rubberwood using slow pyrolysis and microwave technology." Journal of Analytical and Applied Pyrolysis **122**: 64-75.

Hall, P. J. and J. M. Calo (1989). "Secondary interactions upon thermal desorption of surface oxides from coal chars." Energy & fuels **3**(3): 370-376.

Han, P., H. Wang, Z. Liu, X. Chen, W. Ma, J. Yao, Y. Zhu and G. Cui (2011). "Graphene oxide nanoplatelets as excellent electrochemical active materials for VO^{2+}/VO_2^+ and V^{2+}/V^{3+} redox couples for a vanadium redox flow battery." Carbon **49**(2): 693-700.

Harris, J., A. N. Phan and K. Zhang (2018). "Cold plasma catalysis as a novel approach for valorisation of untreated waste glycerol." Green Chemistry **20**(11): 2578-2587.

Hasegawa, T. (2017). Quantitative Infrared Spectroscopy for Understanding of a Condensed Matter, Springer.

Hayashi, J. i., T. Horikawa, I. Takeda, K. Muroyama and F. Nasir Ani (2002). "Preparing activated carbon from various nutshells by chemical activation with K_2CO_3." Carbon **40**(13): 2381-2386.

He, C., J. Zhao, Y. Yang and J. Y. Wang (2016). "Multiscale characteristics dynamics of hydrochar from hydrothermal conversion of sewage sludge under sub- and near-critical water." Bioresource Technology **211**: 486-493.

He, X., F. Zhang, R. Wang and W. Liu (2007). "Preparation of a carbon nanotube/carbon fiber multi-scale reinforcement by grafting multi-walled carbon nanotubes onto the fibers." Carbon **45**(13): 2559-2563.

Holzman, D. C. (2007). "The Vanadium Advantage: Flow Batteries Put Wind Energy in the Bank." Environmental Health Perspectives **115**(7): A358-A361.

Hoque, M. K., J. A. Behan, J. Creel, J. G. Lunney, T. S. Perova and P. E. Colavita (2020). "Reactive Plasma N-Doping of Amorphous Carbon Electrodes: Decoupling Disorder and Chemical Effects on Capacitive and Electrocatalytic Performance." Frontiers in Chemistry **8**(1020).

Huang, C., A. M. Puziy, O. I. Poddubnaya, D. Hulicova-Jurcakova, M. Sobiesiak and B. Gawdzik (2018). "Phosphorus, nitrogen and oxygen co-doped polymer-based core-shell carbon sphere for high-performance hybrid supercapacitors." Electrochimica Acta **270**: 339-351.

Huang, C., T. Sun and D. Hulicova-Jurcakova (2013). "Wide electrochemical window of supercapacitors from coffee bean-derived phosphorus-rich carbons." ChemSusChem **6**(12): 2330-2339.

Hutson, N. D. and R. T. Yang (1997). "Theoretical basis for the Dubinin-Radushkevitch (D-R) adsorption isotherm equation." Adsorption **3**(3): 189-195.

Ikeda, E. and J. C. Mackie (1995). "Thermal decomposition of two coal model compounds — pyridine and 2-picoline. Kinetics and product distributions." Journal of Analytical and Applied Pyrolysis **34**(1): 47-63.

Imamoglu, M., H. Şahin, Ş. Aydın, F. Tosunoğlu, H. Yılmaz and S. Z. Yıldız (2016). "Investigation of Pb (II) adsorption on a novel activated carbon prepared from hazelnut husk by K_2CO_3 activation." Desalination and Water Treatment **57**(10): 4587-4596.

Intani, K., S. Latif, A. K. M. R. Kabir and J. Müller (2016). "Effect of self-purging pyrolysis on yield of biochar from maize cobs, husks and leaves." Bioresource Technology **218**: 541-551.

International Nut and Dried Fruit Council (2018). "Nuts & Dried Fruits Statistical Yearbook 2017/2018." https://www.nutfruit.org/files/tech/1524481168_INC_Statistical_Yearbook_2017-2018.pdf.

Ishii, T. and T. Kyotani (2016). Chapter 14 - Temperature Programmed Desorption. Materials Science and Engineering of Carbon. M. Inagaki and F. Kang, Butterworth-Heinemann**:** 287-305.

Ishimaru, K., T. Hata, P. Bronsveld, D. Meier and Y. Imamura (2007). "Spectroscopic analysis of carbonization behavior of wood, cellulose and lignin." Journal of Materials Science **42**(1): 122-129.

Işıtan, S., S. Ceylan, Y. Topcu, C. Hintz, J. Tefft, T. Chellappa, J. Guo and J. L. Goldfarb (2016). "Product quality optimization in an integrated biorefinery: Conversion of pistachio nutshell biomass to biofuels and activated biochars via pyrolysis." Energy Conversion and Management **127**: 576-588.

Iwashita, N. (2016). Chapter 2 - X-ray Powder Diffraction. Materials Science and Engineering of Carbon. M. Inagaki and F. Kang, Butterworth-Heinemann**:** 7-25.

Iwashita, N., C. R. Park, H. Fujimoto, M. Shiraishi and M. Inagaki (2004). "Specification for a standard procedure of X-ray diffraction measurements on carbon materials." Carbon **42**(4): 701-714.

Jansen, R. J. J. and H. van Bekkum (1994). "Amination and ammoxidation of activated carbons." Carbon **32**(8): 1507-1516.

Jansen, R. J. J. and H. van Bekkum (1995). "XPS of nitrogen-containing functional groups on activated carbon." Carbon **33**(8): 1021-1027.

Jia, Y. F. and K. M. Thomas (2000). "Adsorption of Cadmium Ions on Oxygen Surface Sites in Activated Carbon." Langmuir **16**(3): 1114-1122.

Jia, Y. F., B. Xiao and K. M. Thomas (2002). "Adsorption of Metal Ions on Nitrogen Surface Functional Groups in Activated Carbons." Langmuir **18**(2): 470-478.

Johnson, C. A., J. W. Patrick and K. Mark Thomas (1986). "Characterization of coal chars by Raman spectroscopy, X-ray diffraction and reflectance measurements." Fuel **65**(9): 1284-1290.

Johnson, C. A. and K. M. Thomas (1987). "The thermal history of char samples taken from a gasifier." Fuel **66**(1): 17-21.

Jones, J. M., A. W. Harding, S. D. Brown and K. M. Thomas (1995). "Detection of reactive intermediate nitrogen and sulfur species in the combustion of carbons that are models for coal chars." Carbon **33**(6): 833-843.

Kaburagi, Y., A. Yoshida and Y. Hishiyama (2016). Chapter 7 - Raman Spectroscopy. Materials Science and Engineering of Carbon. M. Inagaki and F. Kang, Butterworth-Heinemann**:** 125-152.

Kahoush, M., N. Behary, A. Cayla, B. Mutel, J. Guan and V. Nierstrasz (2019). "Surface modification of carbon felt by cold remote plasma for glucose oxidase enzyme immobilization." Applied Surface Science **476**: 1016-1024.

Kakati, B. K., D. Sathiyamoorthy and A. Verma (2010). "Electrochemical and mechanical behavior of carbon composite bipolar plate for fuel cell." International Journal of Hydrogen Energy **35**(9): 4185-4194.

Kalra, Y. (1997). Handbook of reference methods for plant analysis, CRC press.

Kang, S., X. Li, J. Fan and J. Chang (2012). "Characterization of hydrochars produced by hydrothermal carbonization of lignin, cellulose, D-xylose, and wood meal." Industrial & engineering chemistry research **51**(26): 9023-9031.

Kawamoto, H. (2017). "Lignin pyrolysis reactions." Journal of Wood Science: 1-16.

Kazmierczak-Razna, J., P. Nowicki, M. Wiśniewska, A. Nosal-Wiercińska and R. Pietrzak (2017). "Thermal and physicochemical properties of phosphorus-containing activated carbons obtained from biomass." Journal of the Taiwan Institute of Chemical Engineers **80**: 1006-1013.

Keiluweit, M., P. S. Nico, M. G. Johnson and M. Kleber (2010). "Dynamic Molecular Structure of Plant Biomass-Derived Black Carbon (Biochar)." Environmental Science & Technology **44**(4): 1247-1253.

Khare, B., P. Wilhite, B. Tran, E. Teixeira, K. Fresquez, D. N. Mvondo, C. Bauschlicher and M. Meyyappan (2005). "Functionalization of Carbon Nanotubes via Nitrogen Glow Discharge." The Journal of Physical Chemistry B **109**(49): 23466-23472.

Kierkowicz, M., E. Pach, A. Santidrián, S. Sandoval, G. Gonçalves, E. Tobías-Rossell, M. Kalbáč, B. Ballesteros and G. Tobias (2018). "Comparative study of shortening and cutting strategies of single-walled and multi-walled carbon nanotubes assessed by scanning electron microscopy." Carbon **139**: 922-932.

Kim, J.-H., S. Y. Hwang, J. E. Park, G. B. Lee, H. Kim, S. Kim and B. U. Hong (2019). "Impact of the oxygen functional group of nitric acid-treated activated carbon on KOH activation reaction." Carbon Letters **29**(3): 281-287.

Kim, K. J., H. S. Lee, J. Kim, M. S. Park, J. H. Kim, Y. J. Kim and M. Skyllas-Kazacos (2016). "Superior Electrocatalytic Activity of a Robust Carbon-Felt Electrode with Oxygen-Rich Phosphate Groups for All-Vanadium Redox Flow Batteries." ChemSusChem **9**(11): 1329-1338.

Kim, K. J., M.-S. Park, Y.-J. Kim, J. H. Kim, S. X. Dou and M. Skyllas-Kazacos (2015). "A technology review of electrodes and reaction mechanisms in vanadium redox flow batteries." Journal of Materials Chemistry A **3**(33): 16913-16933.

Kirk, B. P. and H. C. Wilkinson (1970). "Application of the unterzaucher method to the determination of oxygen in coke." Talanta **17**(6): 475-482.

Konno, H. (2016). Chapter 8 - X-ray Photoelectron Spectroscopy. Materials Science and Engineering of Carbon. M. Inagaki and F. Kang, Butterworth-Heinemann**:** 153-171.

Köseoğlu, E. and C. Akmil-Başar (2015). "Preparation, structural evaluation and adsorptive properties of activated carbon from agricultural waste biomass." Advanced Powder Technology **26**(3): 811-818.

Kozlowski, C. and P. M. A. Sherwood (1986). "X-ray photoelectron spectroscopic studies of carbon fibre surfaces vii-electrochemical treatment in ammonium salt electrolytes." Carbon **24**(3): 357-363.

Krikstolaityte, V., O. E. Y. Joshua, A. Veksha, N. Wai, G. Lisak and T. M. Lim (2018). "Conversion of Spent Coffee Beans to Electrode Material for Vanadium Redox Flow Batteries." Batteries **4**(4): 56.

Kumar, M., R. C. Gupta and T. Sharma (1993). "X-ray diffraction studies of *Acacia* and *Eucalyptus* wood chars." Journal of Materials Science **28**(3): 805-810.

Kumar, R., T. Bhuvana and A. Sharma (2018). "Tire Waste Derived Turbostratic Carbon as an Electrode for a Vanadium Redox Flow Battery." ACS Sustainable Chemistry & Engineering **6**(7): 8238-8246.

Kumar, S. and S. Jayanti (2016). "Effect of flow field on the performance of an all-vanadium redox flow battery." Journal of Power Sources **307**: 782-787.

Kundu, S., W. Xia, W. Busser, M. Becker, D. A. Schmidt, M. Havenith and M. Muhler (2010). "The formation of nitrogen-containing functional groups on carbon nanotube surfaces: a quantitative XPS and TPD study." Physical Chemistry Chemical Physics **12**(17): 4351-4359.

Lahaye, J., G. Nansé, A. Bagreev and V. Strelko (1999). "Porous structure and surface chemistry of nitrogen containing carbons from polymers." Carbon **37**(4): 585-590.

Lahijani, P., Z. A. Zainal, M. Mohammadi and A. R. Mohamed (2015). "Conversion of the greenhouse gas CO_2 to the fuel gas CO via the Boudouard reaction: A review." Renewable and Sustainable Energy Reviews **41**: 615-632.

Larkin, P. (2011). Chapter 6 - IR and Raman Spectra-Structure Correlations: Characteristic Group Frequencies. Infrared and Raman Spectroscopy. P. Larkin. Oxford, Elsevier**:** 73-115.

Lee, D., S. H. Hong, K.-H. Paek and W.-T. Ju (2005). "Adsorbability enhancement of activated carbon by dielectric barrier discharge plasma treatment." Surface and Coatings Technology **200**(7): 2277-2282.

Lee, J., X. Yang, S. H. Cho, J. K. Kim, S. S. Lee, D. C. W. Tsang, Y. S. Ok and E. E. Kwon (2017). "Pyrolysis process of agricultural waste using CO2 for waste management, energy recovery, and biochar fabrication." Applied Energy **185**: 214-222.

Lee, N. J., S.-W. Lee, K. J. Kim, J.-H. Kim, M.-S. Park, G. Jeong, Y.-J. Kim and D. Byun (2012). "Development of carbon composite bipolar plates for vanadium redox flow batteries." Bull. Korean Chem. Soc **33**(11): 3589-3592.

Lee, W. H. and P. J. Reucroft (1999). "Vapor adsorption on coal- and wood-based chemically activated carbons: (I) Surface oxidation states and adsorption of H_2O." Carbon **37**(1): 7-14.

Lee, Y.-J. (2004). "The second order Raman spectroscopy in carbon crystallinity." Journal of Nuclear Materials **325**(2): 174-179.

Leung, P., X. Li, C. Ponce de Leon, L. Berlouis, C. T. J. Low and F. C. Walsh (2012). "Progress in redox flow batteries, remaining challenges and their applications in energy storage." RSC Advances **2**(27): 10125-10156.

Li, M., Z. Bi, L. Xie, G. Sun, Z. Liu, Q. Kong, X. Wei and C.-M. Chen (2019). "From Starch to Carbon Materials: Insight into the Cross-Linking Reaction and Its Influence on the Carbonization Process." ACS Sustainable Chemistry & Engineering **7**(17): 14796-14804.

Li, W., J. Liu and C. Yan (2011). "Multi-walled carbon nanotubes used as an electrode reaction catalyst for VO^{2+}/VO_2^+ for a vanadium redox flow battery." Carbon **49**(11): 3463-3470.

Li, X., J. Zhao, Y. Qin, W. Xu, J. Liu, J. Yang, Q. Xu and C. Yan (2017). "Investigation of the electrolyte properties for the vanadium redox flow battery (VI): Measurement and prediction of surface tension of aqueous VOSO4 at 283.15 to 313.15 K." Journal of Molecular Liquids **225**: 296-301.

Li, Y., J. Parrondo, S. Sankarasubramanian and V. Ramani (2019). "Impact of Surface Carbonyl- and Hydroxyl-Group Concentrations on Electrode Kinetics in an All-Vanadium Redox Flow Battery." The Journal of Physical Chemistry C **123**(11): 6370-6378.

Lian, F., G. Cui, Z. Liu, L. Duo, G. Zhang and B. Xing (2016). "One-step synthesis of a novel N-doped microporous biochar derived from crop straws with high dye adsorption capacity." Journal of Environmental Management **176**: 61-68.

Lillo-Ródenas, M. A., D. Cazorla-Amorós and A. Linares-Solano (2003). "Understanding chemical reactions between carbons and NaOH and KOH: An insight into the chemical activation mechanism." Carbon **41**(2): 267-275.

Lillo-Ródenas, M. A., J. Juan-Juan, D. Cazorla-Amorós and A. Linares-Solano (2004). "About reactions occurring during chemical activation with hydroxides." Carbon **42**(7): 1371-1375.

Lim, D. G., K. Kim, M. Razdan, R. Diaz, S. Osswald and V. G. Pol (2017). "Lithium storage in structurally tunable carbon anode derived from sustainable source." Carbon **121**: 134-142.

Linden, D. (2010). Linden's Handbook of batteries, McGraw-Hill.

Liu, B., X. Zhou, H. Chen, Y. Liu and H. Li (2016). "Promising porous carbons derived from lotus seedpods with outstanding supercapacitance performance." Electrochimica Acta **208**: 55-63.

Liu, F., R. Yu and M. Guo (2016). "Hydrothermal carbonization of forestry residues: influence of reaction temperature on holocellulose-derived hydrochar properties." Journal of Materials Science: 1-11.

Liu, G., X. Pan, X. Ma, S. Xin and Y. Xin (2020). "Effects of feedstock and inherent mineral components on oxidation resistance of biochars." Science of The Total Environment **726**: 138672.

Lourenssen, K., J. Williams, F. Ahmadpour, R. Clemmer and S. Tasnim (2019). "Vanadium redox flow batteries: A comprehensive review." Journal of Energy Storage **25**: 100844.

Lu, P., P. J. Cullen and K. Ostrikov (2016). Chapter 4 - Atmospheric Pressure Nonthermal Plasma Sources. Cold Plasma in Food and Agriculture. N. N. Misra, O. Schlüter and P. J. Cullen. San Diego, Academic Press**:** 83-116.

Lysenko, N. D., P. S. Yaremov, M. V. Ovcharova and V. G. Ilyin (2012). "Highly acidic phosphorus-containing porous carbons: synthesis and physicochemical properties." Journal of Materials Science **47**(7): 3089-3095.

Ma, W., L. Xie, L. Dai, G. Sun, J. Chen, F. Su, Y. Cao, H. Lei, Q. Kong and C.-M. Chen (2018). "Influence of phosphorus doping on surface chemistry and capacitive behaviors of porous carbon electrode." Electrochimica Acta **266**: 420-430.

Ma, Z., Y. Yang, Q. Ma, H. Zhou, X. Luo, X. Liu and S. Wang (2017). "Evolution of the chemical composition, functional group, pore structure and crystallographic structure of bio-char from palm kernel shell pyrolysis under different temperatures." Journal of Analytical and Applied Pyrolysis **127**(Supplement C): 350-359.

Maharjan, M., A. Bhattarai, M. Ulaganathan, N. Wai, M. O. Oo, J.-Y. Wang and T. M. Lim (2017). "High surface area bio-waste based carbon as a superior electrode for vanadium redox flow battery." Journal of Power Sources **362**: 50-56.

Maharjan, M., N. Wai, A. Veksha, A. Giannis, T. M. Lim and G. Lisak (2019). "Sal wood sawdust derived highly mesoporous carbon as prospective electrode material for vanadium redox flow batteries." Journal of Electroanalytical Chemistry **834**: 94-100.

Mäkelä, M., V. Benavente and A. Fullana (2015). "Hydrothermal carbonization of lignocellulosic biomass: Effect of process conditions on hydrochar properties." Applied Energy **155**: 576-584.

Manakhov, A., L. Zajíčková, M. Eliáš, J. Čechal, J. Polčák, J. Hnilica, Š. Bittnerová and D. Nečas (2014). "Optimization of cyclopropylamine plasma polymerization toward enhanced layer stability in contact with water." Plasma Processes and Polymers **11**(6): 532-544.

Marchon, B., J. Carrazza, H. Heinemann and G. A. Somorjai (1988). "TPD and XPS studies of O_2, CO_2, and H_2O adsorption on clean polycrystalline graphite." Carbon **26**(4): 507-514.

Marsh, H. (1987). "Adsorption methods to study microporosity in coals and carbons—a critique." Carbon **25**(1): 49-58.

Marsh, H. (1991). "A TRIBUTE TO WALKER,PHILIP,L." Carbon **29**(6): 703-704.

Marsh, H. and B. Rand (1970). "The characterization of microporous carbons by means of the dubinin-radushkevich equation." Journal of Colloid and Interface Science **33**(1): 101-116.

Marsh, H. and F. Rodríguez-Reinoso (2006). CHAPTER 2 - Activated Carbon (Origins). Activated Carbon. H. Marsh and F. Rodríguez-Reinoso. Oxford, Elsevier Science Ltd**:** 13-86.

Mašek, O., V. Budarin, M. Gronnow, K. Crombie, P. Brownsort, E. Fitzpatrick and P. Hurst (2013). "Microwave and slow pyrolysis biochar—Comparison of physical and functional properties." Journal of Analytical and Applied Pyrolysis **100**: 41-48.

Mather, P. and K. Thomas (1997). "Carbon black/high density polyethylene conducting composite materials: Part I Structural modification of a carbon black by gasification in carbon dioxide and the effect on the electrical and mechanical properties of the composite." Journal of materials science **32**(2): 401-407.

Meng, F. and D. Wang (2020). "Effects of vacuum freeze drying pretreatment on biomass and biochar properties." Renewable Energy **155**: 1-9.

Merenda, A., E. Des Ligneris, K. Sears, T. Chaffraix, K. Magniez, D. Cornu, J. A. Schütz and L. F. Dumée (2016). "Assessing the temporal stability of surface functional groups introduced by plasma treatments on the outer shells of carbon nanotubes." Scientific reports **6**: 31565.

Meskinfam Langroudi, M., C. S. Pomelli, R. Giglioli, C. Chiappe, M. Aysla Costa de Oliveira, B. Mecheri, S. Licoccia and A. D'Epifanio (2019). "Interaction of vanadium species with a functionalized graphite electrode: A combined theoretical and experimental study for flow battery applications." Journal of Power Sources **420**: 134-142.

Mestre, A. S., F. Hesse, C. Freire, C. O. Ania and A. P. Carvalho (2019). "Chemically activated high grade nanoporous carbons from low density renewable biomass (Agave sisalana) for the removal of pharmaceuticals." Journal of Colloid and Interface Science **536**: 681-693.

Mian, M. M., G. Liu, B. Yousaf, B. Fu, H. Ullah, M. U. Ali, Q. Abbas, M. A. Mujtaba Munir and L. Ruijia (2018). "Simultaneous functionalization and magnetization of biochar via NH3 ambiance pyrolysis for efficient removal of Cr (VI)." Chemosphere **208**: 712-721.

Minke, C., T. Hickmann, A. R. dos Santos, U. Kunz and T. Turek (2016). "Cost and performance prospects for composite bipolar plates in fuel cells and redox flow batteries." Journal of Power Sources **305**: 182-190.

Minke, C. and T. Turek (2018). "Materials, system designs and modelling approaches in techno-economic assessment of all-vanadium redox flow batteries – A review." Journal of Power Sources **376**: 66-81.

Mireles, S., J. Parsons, T. Trad, C. L. Cheng and J. Kang (2019). "Lead removal from aqueous solutions using biochars derived from corn stover, orange peel, and pistachio shell." International Journal of Environmental Science and Technology **16**(10): 5817-5826.

Montoya, J., B. Pecha, D. Roman, F. C. Janna and M. Garcia-Perez (2017). "Effect of temperature and heating rate on product distribution from the pyrolysis of sugarcane bagasse in a hot plate reactor." Journal of Analytical and Applied Pyrolysis **123**: 347-363.

Moreno-Castilla, C., M. A. Ferro-Garcia, J. P. Joly, I. Bautista-Toledo, F. Carrasco-Marin and J. Rivera-Utrilla (1995). "Activated Carbon Surface Modifications by Nitric Acid, Hydrogen Peroxide, and Ammonium Peroxydisulfate Treatments." Langmuir **11**(11): 4386-4392.

Mori, Y., T. Enomae and A. Isogai (2009). "Preparation of pure vaterite by simple mechanical mixing of two aqueous salt solutions." Materials Science and Engineering: C **29**(4): 1409-1414.

Muradov, N., B. Fidalgo, A. C. Gujar, N. Garceau and A. T-Raissi (2012). "Production and characterization of Lemna minor bio-char and its catalytic application for biogas reforming." Biomass and Bioenergy **42**: 123-131.

Nagel, K., N. O. Hoilett, M. A. Mottaleb, M. J. Meziani, J. Wistrom and M. Bellamy (2019). "Physicochemical Characteristics of Biochars Derived From Corn, Hardwood, Miscanthus, and Horse Manure Biomasses." Communications in Soil Science and Plant Analysis **50**(8): 987-1002.

NASA TM-79067, National Aeronautics and Space Administration and U.S. Dept. of Energy (1979). "Redox Flow Cell Development and Demonstration Project."

Nemanich, R. J. and S. A. Solin (1979). "First- and second-order Raman scattering from finite-size crystals of graphite." Physical Review B **20**(2): 392-401.

Ning, P., S. J. Liu, C. Wang, K. Li, X. Sun, L. H. Tang and G. Liu (2018). "Adsorption-oxidation of hydrogen sulfide on Fe/walnut-shell activated carbon surface modified by NH3-plasma." Journal of Environmental Sciences **64**: 216-226.

Nishi, Y. and M. Inagaki (2016). Chapter 11 - Gas Adsorption/Desorption Isotherm for Pore Structure Characterization. Materials Science and Engineering of Carbon. M. Inagaki and F. Kang, Butterworth-Heinemann**:** 227-247.

Niu, X., J. Zhou, T. Qian, M. Wang and C. Yan (2017). "Confined silicon nanospheres by biomass lignin for stable lithium ion battery." Nanotechnology **28**(40): 405401.

Nizamuddin, S., N. S. Jaya Kumar, J. N. Sahu, P. Ganesan, N. M. Mubarak and S. A. Mazari (2015). "Synthesis and characterization of hydrochars produced by hydrothermal carbonization of oil palm shell." Canadian Journal of Chemical Engineering **93**(11): 1916-1921.

Noack, J., L. Wietschel, N. Roznyatovskaya, K. Pinkwart and J. Tübke (2016). "Techno-economic modeling and analysis of redox flow battery systems." Energies **9**(8): 627.

Noh, J. S. and J. A. Schwarz (1990). "Effect of HNO_3 treatment on the surface acidity of activated carbons." Carbon **28**(5): 675-682.

Ouyang, C. and X. Wang (2020). "Recent progress in pyrolyzed carbon materials as electrocatalysts for the oxygen reduction reaction." Inorganic Chemistry Frontiers **7**(1): 28-36.

Overend, R. P., E. Chornet and J. A. Gascoigne (1987). "Fractionation of lignocellulosics by steam-aqueous pretreatments." Philosophical Transactions of the Royal Society of London A: Mathematical, Physical and Engineering Sciences **321**(1561): 523-536.

Paethanom, A. and K. Yoshikawa (2012). "Influence of pyrolysis temperature on rice husk char characteristics and its tar adsorption capability." Energies **5**(12): 4941-4951.

Park, J., I. Hung, Z. Gan, O. J. Rojas, K. H. Lim and S. Park (2013). "Activated carbon from biochar: Influence of its physicochemical properties on the sorption characteristics of phenanthrene." Bioresource Technology **149**: 383-389.

Park, J. H., J. J. Park, O. O. Park and J. H. Yang (2016). "Capacity Decay Mitigation by Asymmetric Positive/Negative Electrolyte Volumes in Vanadium Redox Flow Batteries." ChemSusChem **9**(22): 3181-3187.

Park, M., I. Y. Jeon, J. Ryu, J. B. Baek and J. Cho (2015). "Exploration of the Effective Location of Surface Oxygen Defects in Graphene-Based Electrocatalysts for All-Vanadium Redox-Flow Batteries." Advanced Energy Materials **5**(5).

Pels, J. R., F. Kapteijn, J. A. Moulijn, Q. Zhu and K. M. Thomas (1995). "Evolution of nitrogen functionalities in carbonaceous materials during pyrolysis." Carbon **33**(11): 1641-1653.

Pena, J., A. Villot and C. Gerente (2020). "Pyrolysis chars and physically activated carbons prepared from buckwheat husks for catalytic purification of syngas." Biomass and Bioenergy **132**: 105435.

Picard, M., S. Thakur, M. Misra and A. K. Mohanty (2019). "Miscanthus grass-derived carbon dots to selectively detect Fe^{3+} ions." RSC Advances **9**(15): 8628-8637.

Pietrzak, R., K. Jurewicz, P. Nowicki, K. Babeł and H. Wachowska (2010). "Nitrogen-enriched bituminous coal-based active carbons as materials for supercapacitors." Fuel **89**(11): 3457-3467.

Polaki, S. R., N. Kumar, N. Gopala Krishna, T. R. Ravindran, M. Kamruddin, S. Dash and A. K. Tyagi (2015). "Tribological properties of chemically modified diamond like carbon films in hydrogen plasma." Tribology International **81**: 283-290.

Prakash, P. and K. N. Sheeba (2016). "Prediction of pyrolysis and gasification characteristics of different biomass from their physico-chemical properties." Energy Sources, Part A: Recovery, Utilization and Environmental Effects **38**(11): 1530-1536.

Puri, B. R. and R. C. Bansal (1964). "Studies in surface chemistry of carbon blacks Part II. Surface acidity in relation to chemisorbed oxygen." Carbon **1**(4): 457-464.

Puziy, A. M., O. I. Poddubnaya, A. Martínez-Alonso, F. Suárez-García and J. M. D. Tascón (2005). "Surface chemistry of phosphorus-containing carbons of lignocellulosic origin." Carbon **43**(14): 2857-2868.

Qiao, Z.-j., M.-m. Chen, C.-y. Wang and Y.-c. Yuan (2014). "Humic acids-based hierarchical porous carbons as high-rate performance electrodes for symmetric supercapacitors." Bioresource technology **163**: 386-389.

Qu, G.-Z., J. Li, D.-L. Liang, D.-L. Huang, D. Qu and Y.-M. Huang (2013). "Surface modification of a granular activated carbon by dielectric barrier discharge plasma and its effects on pentachlorophenol adsorption." Journal of Electrostatics **71**(4): 689-694.

Rauda, I. E., V. Augustyn, B. Dunn and S. H. Tolbert (2013). "Enhancing pseudocapacitive charge storage in polymer templated mesoporous materials." Accounts of chemical research **46**(5): 1113-1124.

Reddy, T. B. (2010). Linden’s handbook of batteries 4th edition, McGraw-Hill, New York.

Reich, S. and C. Thomsen (2004). "Raman spectroscopy of graphite." Philosophical Transactions of the Royal Society of London. Series A: Mathematical, Physical and Engineering Sciences **362**(1824): 2271-2288.

Renewable Energy Policy Network for the 21st Century (2020). "Global Status Report 2020."

Rexer, T. F., E. J. Mathia, A. C. Aplin and K. M. Thomas (2014). "High-Pressure Methane Adsorption and Characterization of Pores in Posidonia Shales and Isolated Kerogens." Energy & Fuels **28**(5): 2886-2901.

Reza, M. T., B. Wirth, U. Lüder and M. Werner (2014). "Behavior of selected hydrolyzed and dehydrated products during hydrothermal carbonization of biomass." Bioresource Technology **169**: 352-361.

Rodby, K. E., T. J. Carney, Y. A. Gandomi, J. L. Barton, R. M. Darling and F. R. Brushett (2020). "Assessing the levelized cost of vanadium redox flow batteries with capacity fade and rebalancing." Journal of Power Sources: 227958.

Romero-Anaya, A. J., M. Ouzzine, M. Lillo-Ródenas and A. Linares-Solano (2014). "Spherical carbons: Synthesis, characterization and activation processes." Carbon **68**: 296-307.

Ronsse, F., S. van Hecke, D. Dickinson and W. Prins (2013). "Production and characterization of slow pyrolysis biochar: Influence of feedstock type and pyrolysis conditions." GCB Bioenergy **5**(2): 104-115.

Rosas, J. M., R. Ruiz-Rosas, J. Rodríguez-Mirasol and T. Cordero (2012). "Kinetic study of the oxidation resistance of phosphorus-containing activated carbons." Carbon **50**(4): 1523-1537.

Rueda-Ordóñez, Y. J. and K. Tannous (2016). "Thermal decomposition of sugarcane straw, kinetics and heat of reaction in synthetic air." Bioresource Technology **211**: 231-239.

Rui, X., M. O. Oo, D. H. Sim, S. c. Raghu, Q. Yan, T. M. Lim and M. Skyllas-Kazacos (2012). "Graphene oxide nanosheets/polymer binders as superior electrocatalytic materials for vanadium bromide redox flow batteries." Electrochimica Acta **85**: 175-181.

Rybin, M., A. Pereyaslavtsev, T. Vasilieva, V. Myasnikov, I. Sokolov, A. Pavlova, E. Obraztsova, A. Khomich, V. Ralchenko and E. Obraztsova (2016). "Efficient nitrogen doping of graphene by plasma treatment." Carbon **96**: 196-202.

Saha, P., M. K. Datta, O. I. Velikokhatnyi, A. Manivannan, D. Alman and P. N. Kumta (2014). "Rechargeable magnesium battery: Current status and key challenges for the future." Progress in Materials Science **66**: 1-86.

Saka, C. (2018). "Overview on the surface functionalization mechanism and determination of surface functional groups of plasma treated carbon nanotubes." Critical reviews in analytical chemistry **48**(1): 1-14.

Schmiers, H., J. Friebel, P. Streubel, R. Hesse and R. Köpsel (1999). "Change of chemical bonding of nitrogen of polymeric N-heterocyclic compounds during pyrolysis." Carbon **37**(12): 1965-1978.

Schnucklake, M., L. Eifert, J. Schneider, R. Zeis and C. Roth (2019). "Porous N- and S-doped carbon–carbon composite electrodes by soft-templating for redox flow batteries." Beilstein Journal of Nanotechnology **10**: 1131-1139.

Sekirifa, M. L., M. Hadj-Mahammed, S. Pallier, L. Baameur, D. Richard and A. H. Al-Dujaili (2013). "Preparation and characterization of an activated carbon from a date stones variety by physical activation with carbon dioxide." Journal of Analytical and Applied Pyrolysis **99**: 155-160.

Seredych, M., D. Hulicova-Jurcakova, G. Q. Lu and T. J. Bandosz (2008). "Surface functional groups of carbons and the effects of their chemical character, density and accessibility to ions on electrochemical performance." Carbon **46**(11): 1475-1488.

Seung Kim, Y. and C. Rae Park (2016). Chapter 13 - Titration Method for the Identification of Surface Functional Groups. Materials Science and Engineering of Carbon. M. Inagaki and F. Kang, Butterworth-Heinemann**:** 273-286.

Sevilla, M. and A. B. Fuertes (2009). "Chemical and structural properties of carbonaceous products obtained by hydrothermal carbonization of saccharides." Chemistry–A European Journal **15**(16): 4195-4203.

Sevilla, M. and A. B. Fuertes (2009). "The production of carbon materials by hydrothermal carbonization of cellulose." Carbon **47**(9): 2281-2289.

Sevilla, M., J. A. Maciá-Agulló and A. B. Fuertes (2011). "Hydrothermal carbonization of biomass as a route for the sequestration of CO2: Chemical and structural properties of the carbonized products." Biomass and Bioenergy **35**(7): 3152-3159.

Sha'rani, S. S., E. A. Lotf, A. Ahmad, W. A. W. Ibrahim, M. M. Nasef and R. R. Ali (2016). "Stability and performance evaluation of ion-exchange membranes for vanadium redox flow battery." Jurnal Teknologi **78**(12): 7-12.

Shafeeyan, M. S., W. M. A. W. Daud, A. Houshmand and A. Arami-Niya (2011). "Ammonia modification of activated carbon to enhance carbon dioxide adsorption: Effect of pre-oxidation." Applied Surface Science **257**(9): 3936-3942.

Shao, Y., X. Wang, M. Engelhard, C. Wang, S. Dai, J. Liu, Z. Yang and Y. Lin (2010). "Nitrogen-doped mesoporous carbon for energy storage in vanadium redox flow batteries." Journal of Power Sources **195**(13): 4375-4379.

Shao, Y., S. Zhang, M. H. Engelhard, G. Li, G. Shao, Y. Wang, J. Liu, I. A. Aksay and Y. Lin (2010). "Nitrogen-doped graphene and its electrochemical applications." Journal of Materials Chemistry **20**(35): 7491-7496.

Sharma, R. K., J. B. Wooten, V. L. Baliga, X. Lin, W. Geoffrey Chan and M. R. Hajaligol (2004). "Characterization of chars from pyrolysis of lignin." Fuel **83**(11): 1469-1482.

Shi, L., S. Liu, Z. He and J. Shen (2014). "Nitrogen-Doped Graphene: Effects of nitrogen species on the properties of the vanadium redox flow battery." Electrochimica Acta **138**: 93-100.

Shirley, D. A. (1972). "High-Resolution X-Ray Photoemission Spectrum of the Valence Bands of Gold." Physical Review B **5**(12): 4709-4714.

Skyllas-Kazacos, M., M. H. Chakrabarti, S. A. Hajimolana, F. S. Mjalli and M. Saleem (2011). "Progress in flow battery research and development." Journal of The Electrochemical Society **158**(8): R55-R79.

Skyllas-Kazacos, M. and J. McCann (2015). Vanadium redox flow batteries (VRBs) for medium-and large-scale energy storage. Advances in batteries for medium and large-scale energy storage, Elsevier**:** 329-386.

Skyllas-Kazacos, M., C. Menictas and T. Lim (2013). 12 - Redox flow batteries for medium- to large-scale energy storage A2 - Melhem, Ziad. Electricity Transmission, Distribution and Storage Systems, Woodhead Publishing**:** 398-441.

Skyllas-Kazacos, M., M. Rychick and R. Robins (1988). All-vanadium redox battery, Google Patents.

Smith, M. W., I. Dallmeyer, T. J. Johnson, C. S. Brauer, J.-S. McEwen, J. F. Espinal and M. Garcia-Perez (2016). "Structural analysis of char by Raman spectroscopy: Improving band assignments through computational calculations from first principles." Carbon **100**: 678-692.

Smith, M. W., B. Pecha, G. Helms, L. Scudiero and M. Garcia-Perez (2017). "Chemical and morphological evaluation of chars produced from primary biomass constituents: Cellulose, xylan, and lignin." Biomass and Bioenergy **104**: 17-35.

Solum, M. S., R. J. Pugmire, M. Jagtoyen and F. Derbyshire (1995). "Evolution of carbon structure in chemically activated wood." Carbon **33**(9): 1247-1254.

Stańczyk, K., R. Dziembaj, Z. Piwowarska and S. Witkowski (1995). "Transformation of nitrogen structures in carbonization of model compounds determined by XPS." Carbon **33**(10): 1383-1392.

Stein, I. Y., A. J. Constable, N. Morales-Medina, C. V. Sackier, M. E. Devoe, H. M. Vincent and B. L. Wardle (2017). "Structure-mechanical property relations of non-graphitizing pyrolytic carbon synthesized at low temperatures." Carbon **117**: 411-420.

Stobinski, L., B. Lesiak, A. Malolepszy, M. Mazurkiewicz, B. Mierzwa, J. Zemek, P. Jiricek and I. Bieloshapka (2014). "Graphene oxide and reduced graphene oxide studied by the XRD, TEM and electron spectroscopy methods." Journal of Electron Spectroscopy and Related Phenomena **195**: 145-154.

Stöhr, B., H. P. Boehm and R. Schlögl (1991). "Enhancement of the catalytic activity of activated carbons in oxidation reactions by thermal treatment with ammonia or hydrogen cyanide and observation of a superoxide species as a possible intermediate." Carbon **29**(6): 707-720.

Su, Y., K. Li and J. Wang (2020). "Microstructures, mechanical properties and corrosion resistance of sprayed Ca–P coating for micropatterning carbon/carbon substrate surface." Ceramics International **46**(6): 7374-7387.

Sun, B. and M. Skyllas-Kazacos (1992). "Chemical modification of graphite electrode materials for vanadium redox flow battery application—part II. Acid treatments." Electrochimica Acta **37**(13): 2459-2465.

Sun, H., W. C. Hockaday, C. A. Masiello and K. Zygourakis (2012). "Multiple Controls on the Chemical and Physical Structure of Biochars." Industrial & Engineering Chemistry Research **51**(9): 3587-3597.

Sych, N. V., S. I. Trofymenko, O. I. Poddubnaya, M. M. Tsyba, V. I. Sapsay, D. O. Klymchuk and A. M. Puziy (2012). "Porous structure and surface chemistry of phosphoric acid activated carbon from corncob." Applied Surface Science **261**: 75-82.

Tang, S., N. Lu, J. K. Wang, S.-K. Ryu and H.-S. Choi (2007). "Novel Effects of Surface Modification on Activated Carbon Fibers Using a Low Pressure Plasma Treatment." The Journal of Physical Chemistry C **111**(4): 1820-1829.

Tay, T., S. Ucar and S. Karagöz (2009). "Preparation and characterization of activated carbon from waste biomass." Journal of Hazardous Materials **165**(1): 481-485.

Taylor, H. E. (2001). Chapter 1 - Introduction. Inductively Coupled Plasma-Mass Spectrometry. H. E. Taylor. San Diego, Academic Press**:** 1-5.

Taylor, S. M., A. Pătru, E. Fabbri and T. J. Schmidt (2017). "Influence of surface oxygen groups on V(II) oxidation reaction kinetics." Electrochemistry Communications **75**: 13-16.

Thomas, P., C. W. Lai and M. R. Bin Johan (2019). "Recent developments in biomass-derived carbon as a potential sustainable material for super-capacitor-based energy storage and environmental applications." Journal of Analytical and Applied Pyrolysis **140**: 54-85.

Thommes, M., K. Kaneko, A. V. Neimark, J. P. Olivier, F. Rodriguez-Reinoso, J. Rouquerol and K. S. Sing (2015). "Physisorption of gases, with special reference to the evaluation of surface area and pore size distribution (IUPAC Technical Report)." Pure and applied chemistry **87**(9-10): 1051-1069.

Tougaard, S. (1988). "Quantitative analysis of the inelastic background in surface electron spectroscopy." Surface and Interface Analysis **11**(9): 453-472.

Tripathi, N., C. D. Hills, R. S. Singh and C. J. Atkinson (2019). "Biomass waste utilisation in low-carbon products: harnessing a major potential resource." npj Climate and Atmospheric Science **2**(1): 1-10.

Tsaneva, V. N., W. Kwapinski, X. Teng and B. A. Glowacki (2014). "Assessment of the structural evolution of carbons from microwave plasma natural gas reforming and biomass pyrolysis using Raman spectroscopy." Carbon **80**: 617-628.

Turner, J. A. and K. M. Thomas (1999). "Temperature-Programmed Desorption of Oxygen Surface Complexes on Acenaphthylene-Derived Chars: Comparison with Oxygen K-Edge XANES Spectroscopy." Langmuir **15**(19): 6416-6422.

U.S. Energy Information Administration (2016). "International Energy Outlook 2016."

Uchimiya, M., L. H. Wartelle, K. T. Klasson, C. A. Fortier and I. M. Lima (2011). "Influence of pyrolysis temperature on biochar property and function as a heavy metal sorbent in soil." Journal of Agricultural and Food Chemistry **59**(6): 2501-2510.

Ulaganathan, M., A. Jain, V. Aravindan, S. Jayaraman, W. C. Ling, T. M. Lim, M. P. Srinivasan, Q. Yan and S. Madhavi (2015). "Bio-mass derived mesoporous carbon as superior electrode in all vanadium redox flow battery with multicouple reactions." Journal of Power Sources **274**: 846-850.

Uzun, B. B., E. Apaydin-Varol, F. Ateş, N. Özbay and A. E. Pütün (2010). "Synthetic fuel production from tea waste: Characterisation of bio-oil and bio-char." Fuel **89**(1): 176-184.

Vassilev, S. V., C. G. Vassileva, Y.-C. Song, W.-Y. Li and J. Feng (2017). "Ash contents and ash-forming elements of biomass and their significance for solid biofuel combustion." Fuel **208**: 377-409.

Viswanathan, V., A. Crawford, D. Stephenson, S. Kim, W. Wang, B. Li, G. Coffey, E. Thomsen, G. Graff, P. Balducci, M. Kintner-Meyer and V. Sprenkle (2014). "Cost and performance model for redox flow batteries." Journal of Power Sources **247**: 1040-1051.

Volperts, A., A. Plavniece, G. Dobele, A. Zhurinsh, I. Kruusenberg, K. Kaare, J. Locs, L. Tamasauskaite-Tamasiunaite and E. Norkus (2019). "Biomass based activated carbons for fuel cells." Renewable Energy **141**: 40-45.

Wang, G., H. Peng, X. Qiao, L. Du, X. Li, T. Shu and S. Liao (2016). "Biomass-derived porous heteroatom-doped carbon spheres as a high-performance catalyst for the oxygen reduction reaction." International Journal of Hydrogen Energy **41**(32): 14101-14110.

Wang, G., J. Zhang, J. Zhang, J. Chen, S. Zhu, X. Liu and R. Wang (2016). "Sulfonated poly(ether ether ketone)/poly(vinylidene fluoride)/graphene composite membrane for a vanadium redox flow battery." Journal of Solid State Electrochemistry: 1-10.

Wang, M., X. Lei, L. Hu, P. Zhang, H. Hu and J. Fang (2017). "High-performance Waste Biomass-derived Microporous Carbon Electrocatalyst with a Towel-like Surface for Alkaline Metal/air batteries." Electrochimica Acta **250**: 384-392.

Wang, S. and Z. Luo Chapter 1 Biomass components and characteristics. Pyrolysis of Biomass, De Gruyter.

Wang, S., X. Zhao, T. Cochell and A. Manthiram (2012). "Nitrogen-Doped Carbon Nanotube/Graphite Felts as Advanced Electrode Materials for Vanadium Redox Flow Batteries." The Journal of Physical Chemistry Letters **3**(16): 2164-2167.

Wang, T., Y. Zhai, Y. Zhu, C. Li and G. Zeng (2018). "A review of the hydrothermal carbonization of biomass waste for hydrochar formation: Process conditions, fundamentals, and physicochemical properties." Renewable and Sustainable Energy Reviews **90**: 223-247.

Wang, Y.-Q., F.-Q. Zhang and P. M. A. Sherwood (2001). "X-ray Photoelectron Spectroscopic Studies of Carbon Fiber Surfaces. 25. Interfacial Interactions between PEKK Polymer and Carbon Fibers Electrochemically Oxidized in Nitric Acid and Degradation in a Saline Solution." Chemistry of Materials **13**(3): 832-841.

Wang, Y., D. C. Alsmeyer and R. L. McCreery (1990). "Raman spectroscopy of carbon materials: structural basis of observed spectra." Chemistry of Materials **2**(5): 557-563.

Wang, Y., Y. Shao, D. W. Matson, J. Li and Y. Lin (2010). "Nitrogen-Doped Graphene and Its Application in Electrochemical Biosensing." ACS Nano **4**(4): 1790-1798.

Wang, Y., S. Zuo, M. Miao, Y. Liu, Z. Gu and Y. Jin (2019). "Cost-effective preparation of metal-free electrocatalysts by phosphoric acid activation of lignocellulosic materials for oxygen reduction reaction." International Journal of Hydrogen Energy **44**(5): 2811-2822.

Wang, Z., J. Wu, T. He and J. Wu (2014). "Corn stalks char from fast pyrolysis as precursor material for preparation of activated carbon in fluidized bed reactor." Bioresource Technology **167**: 551-554.

Wannapeera, J. and N. Worasuwannarak (2015). "Examinations of chemical properties and pyrolysis behaviors of torrefied woody biomass prepared at the same torrefaction mass yields." Journal of Analytical and Applied Pyrolysis **115**: 279-287.

Wei, L., T. S. Zhao, G. Zhao, L. An and L. Zeng (2016). "A high-performance carbon nanoparticle-decorated graphite felt electrode for vanadium redox flow batteries." Applied Energy **176**: 74-79.

Whitehead, J. C. (2016). Chapter 3 - The Chemistry of Cold Plasma. Cold Plasma in Food and Agriculture. N. N. Misra, O. Schlüter and P. J. Cullen. San Diego, Academic Press**:** 53-81.

Williams, P. T. and S. Besler (1996). "The influence of temperature and heating rate on the slow pyrolysis of biomass." Renewable energy **7**(3): 233-250.

Windeatt, J. H., A. B. Ross, P. T. Williams, P. M. Forster, M. A. Nahil and S. Singh (2014). "Characteristics of biochars from crop residues: Potential for carbon sequestration and soil amendment." Journal of Environmental Management **146**: 189-197.

Wu, F.-C., R.-L. Tseng and R.-S. Juang (2005). "Preparation of highly microporous carbons from fir wood by KOH activation for adsorption of dyes and phenols from water." Separation and Purification Technology **47**(1): 10-19.

Wu, L., Y. Shen, L. Yu, J. Xi and X. Qiu (2016). "Boosting vanadium flow battery performance by nitrogen-doped carbon nanospheres electrocatalyst." Nano Energy **28**: 19-28.

Wu, X. and L. R. Radovic (2006). "Inhibition of catalytic oxidation of carbon/carbon composites by phosphorus." Carbon **44**(1): 141-151.

Wutscher, A., T. Eckhard, D. Hiltrop, K. Lotz, W. Schuhmann, C. Andronescu and M. Muhler (2019). "Nitrogen-Doped Metal-Free Carbon Materials Derived from Cellulose as Electrocatalysts for the Oxygen Reduction Reaction." Chemelectrochem **6**(2): 514-521.

Xia, S., K. Li, H. Xiao, N. Cai, Z. Dong, C. xu, Y. Chen, H. Yang, X. Tu and H. Chen (2019). "Pyrolysis of Chinese chestnut shells: Effects of temperature and Fe presence on product composition." Bioresource Technology **287**: 121444.

Xiao, B., J. P. Boudou and K. M. Thomas (2005). "Reactions of Nitrogen and Oxygen Surface Groups in Nanoporous Carbons under Inert and Reducing Atmospheres." Langmuir **21**(8): 3400-3409.

Xiao, B. and K. M. Thomas (2005). "Adsorption of aqueous metal ions on oxygen and nitrogen functionalized nanoporous activated carbons." Langmuir **21**(9): 3892-3902.

Xiao, S., L. Yu, L. Wu, L. Liu, X. Qiu and J. Xi (2016). "Broad temperature adaptability of vanadium redox flow battery—Part 1: Electrolyte research." Electrochimica Acta **187**: 525-534.

Xu, A., L. Shi, L. Zeng and T. S. Zhao (2019). "First-principle investigations of nitrogen-, boron-, phosphorus-doped graphite electrodes for vanadium redox flow batteries." Electrochimica Acta **300**: 389-395.

Xu, Q., T. S. Zhao and P. K. Leung (2013). "Numerical investigations of flow field designs for vanadium redox flow batteries." Applied Energy **105**: 47-56.

Yan, J., Z. Lei, Z. Li, Z. Wang, S. Ren, S. Kang, X. Wang and H. Shui (2020). "Molecular structure characterization of low-medium rank coals via XRD, solid state ^{13}C NMR and FTIR spectroscopy." Fuel **268**: 117038.

Yan, W., S. K. Hoekman, A. Broch and C. J. Coronella (2014). "Effect of hydrothermal carbonization reaction parameters on the properties of hydrochar and pellets." Environmental Progress and Sustainable Energy **33**(3): 676-680.

Yang, D.-S., J. Y. Lee, S.-W. Jo, S. J. Yoon, T.-H. Kim and Y. T. Hong (2018). "Electrocatalytic activity of nitrogen-doped CNT graphite felt hybrid for all-vanadium redox flow batteries." International Journal of Hydrogen Energy **43**(3): 1516-1522.

Yang, D., A. Velamakanni, G. Bozoklu, S. Park, M. Stoller, R. D. Piner, S. Stankovich, I. Jung, D. A. Field, C. A. Ventrice and R. S. Ruoff (2009). "Chemical analysis of graphene oxide films after heat and chemical treatments by X-ray photoelectron and Micro-Raman spectroscopy." Carbon **47**(1): 145-152.

Yang, H., R. Yan, H. Chen, D. H. Lee and C. Zheng (2007). "Characteristics of hemicellulose, cellulose and lignin pyrolysis." Fuel **86**(12): 1781-1788.

Yang, Z., J. Zhang, M. C. W. Kintner-Meyer, X. Lu, D. Choi, J. P. Lemmon and J. Liu (2011). "Electrochemical energy storage for green grid." Chemical reviews **111**(5): 3577-3613.

Yook, J. Y., J. Jun and S. Kwak (2010). "Amino functionalization of carbon nanotube surfaces with NH_3 plasma treatment." Applied Surface Science **256**(23): 6941-6944.

Yu, J., N. Paterson, J. Blamey and M. Millan (2017). "Cellulose, xylan and lignin interactions during pyrolysis of lignocellulosic biomass." Fuel **191**: 140-149.

Yuan, T., W. He, G. Yin and S. Xu (2020). "Comparison of bio-chars formation derived from fast and slow pyrolysis of walnut shell." Fuel **261**: 116450.

Yue, Z. R., W. Jiang, L. Wang, S. D. Gardner and C. U. Pittman (1999). "Surface characterization of electrochemically oxidized carbon fibers." Carbon **37**(11): 1785-1796.

Zeng, K., D. P. Minh, D. Gauthier, E. Weiss-Hortala, A. Nzihou and G. Flamant (2015). "The effect of temperature and heating rate on char properties obtained from solar pyrolysis of beech wood." Bioresource Technology **182**(Supplement C): 114-119.

Zeng, L., T. S. Zhao, L. Wei, Y. K. Zeng and Z. H. Zhang (2016). "Highly stable pyridinium-functionalized cross-linked anion exchange membranes for all vanadium redox flow batteries." Journal of Power Sources **331**: 452-461.

Zhang, B., S. Zhang, Z. Weng, G. Wang, E. Zhang, P. Yu, X. Chen and X. Wang (2016). "Quaternized adamantane-containing poly(aryl ether ketone) anion exchange membranes for vanadium redox flow battery applications." Journal of Power Sources **325**: 801-807.

Zhang, G., Y. Sun, Y. Xu and R. Zhang (2018). "Catalytic performance of N-doped activated carbon supported cobalt catalyst for carbon dioxide reforming of methane to synthesis gas." Journal of the Taiwan Institute of Chemical Engineers **93**: 234-244.

Zhang, J., Y. Duan, Q. Zhou, C. Zhu, M. She and W. Ding (2016). "Adsorptive removal of gas-phase mercury by oxygen non-thermal plasma modified activated carbon." Chemical Engineering Journal **294**: 281-289.

Zhang, J., J. Shao, D. Huang, Y. Feng, X. Zhang, S. Zhang and H. Chen (2020). "Influence of different precursors on the characteristic of nitrogen-enriched biochar and SO_2 adsorption properties." Chemical Engineering Journal **385**: 123932.

Zhang, S.-Y., J.-F. Lu, J.-S. Zhang and G.-X. Yue (2008). "Effect of Pyrolysis Intensity on the Reactivity of Coal Char." Energy & Fuels **22**(5): 3213-3221.

Zhang, T., W. P. Walawender, L. T. Fan, M. Fan, D. Daugaard and R. C. Brown (2004). "Preparation of activated carbon from forest and agricultural residues through CO_2 activation." Chemical Engineering Journal **105**(1): 53-59.

Zhang, Y., M. Yin, L. Li, B. Fan, Y. Liu, R. Li, X. Ren, T.-S. Huang and I. S. Kim (2020). "Construction of aerogels based on nanocrystalline cellulose and chitosan for high efficient oil/water separation and water disinfection." Carbohydrate Polymers **243**: 116461.

Zhao, B., D. O'Connor, J. Zhang, T. Peng, Z. Shen, D. C. W. Tsang and D. Hou (2018). "Effect of pyrolysis temperature, heating rate, and residence time on rapeseed stem derived biochar." Journal of Cleaner Production **174**: 977-987.

Zhou, J.-H., Z.-J. Sui, J. Zhu, P. Li, D. Chen, Y.-C. Dai and W.-K. Yuan (2007). "Characterization of surface oxygen complexes on carbon nanofibers by TPD, XPS and FT-IR." Carbon **45**(4): 785-796.

Zhou, X. L., T. S. Zhao, L. An, Y. K. Zeng and L. Wei (2017). "Critical transport issues for improving the performance of aqueous redox flow batteries." Journal of Power Sources **339**: 1-12.

Zhu, Q., K. Grant and K. M. Thomas (1995). "The incorporation of nitrogen into isotropic carbons and its release during temperature-programmed combustion." Carbon **33**(1): 35-46.

Zhu, Q., S. L. Money, A. E. Russell and K. M. Thomas (1997). "Determination of the Fate of Nitrogen Functionality in Carbonaceous Materials during Pyrolysis and Combustion Using X-ray Absorption Near Edge Structure Spectroscopy." Langmuir **13**(7): 2149-2157.

Zhu, X., Y. Liu, F. Qian, S. Zhang and J. Chen (2015). "Investigation on the Physical and Chemical Properties of Hydrochar and Its Derived Pyrolysis Char for Their Potential Application: Influence of Hydrothermal Carbonization Conditions." Energy and Fuels **29**(8): 5222-5230.

Zhuang, Q., T. Kyotani and A. Tomita (1994). "DRIFT and TK/TPD analyses of surface oxygen complexes formed during carbon gasification." Energy & fuels **8**(3): 714-718.

Zickler, G. A., B. Smarsly, N. Gierlinger, H. Peterlik and O. Paris (2006). "A reconsideration of the relationship between the crystallite size L_a of carbons determined by X-ray diffraction and Raman spectroscopy." Carbon **44**(15): 3239-3246.

Zielke, U., K. J. Hüttinger and W. P. Hoffman (1996). "Surface-oxidized carbon fibers: I. Surface structure and chemistry." Carbon **34**(8): 983-998.

Appendix A Gas sorption-desorption models

Appendix A.1 Dubinin-Radushkevich model

In 1947, Dubinin and Radushkevich introduced a new approach to measure micropore volume based on the earlier theory of adsorption of Polanyi (Dubinin and Stoeckli 1980, Gregg and Sing 1982, Hutson and Yang 1997). According to Dubinin, adsorption in micropores involved the fill up process by adsorbate molecules rather than layer-by-layer forming on surface of the adsorbent. The essential parameter of Dubinin-Radushkevich (DR) model is the adsorption potential A (as referred by Polanyi) being defined as

$$A = RT\,ln\left(\frac{p^{\circ}}{p}\right) \tag{A-1}$$

in which p is the equilibrium pressure at temperature T, p° is the saturated vapour pressure. The adsorption potential A is referred by Dubinin and Radushkevich as the differential molar work of adsorption and expressed as the negative differential free energy of adsorption:

$$A = -\Delta G = RT\,ln\left(\frac{p^{\circ}}{p}\right) \tag{A-2}$$

The degree of micropores being filled in is defined as

$$\theta = \frac{W}{W^{\circ}} \tag{A-3}$$

in which W° is the total volume of the micropore system and W is the volume that has been filled when the relative pressure is p/p°. A fundamental postulate in this model is that θ is a function of A such that

$$\theta = f\left(\frac{A}{E}\right) = f\left(\frac{A}{E_0\beta}\right) \tag{A-4}$$

where E is the characteristic energy of adsorption, E_0 is the characteristic energy of adsorption for a reference vapour, and β is termed the similarity constant (where $\beta = 1$ for the reference vapour). One the assumption that the pore size distribution is Gaussian, Dubinin and Radushkevich arrived at the following expression

$$\theta = exp\left[-\left(\frac{A}{E_0\beta}\right)^2\right]$$

(A-5)

which is the commonly used form of the DR equation. Combine equation

(A-2),

(A-3) and $\theta = exp\left[-\left(\frac{A}{E_0\beta}\right)^2\right]$

(A-5) to obtain

$$W = W_0 \exp\left[-\left(\frac{RT\ln\frac{p^\circ}{p}}{E_0\beta}\right)^2\right] = W_0 \exp\left[-B\left(\frac{T}{\beta}\right)^2 \log_{10}^2\left(\frac{p^\circ}{p}\right)\right]$$

(A-6)

where E_0 and B are related by the following expression $E_0 = 0.001915\sqrt{(1/B)}$

For plotting, equation (A-6) can be transformed into

$$\log W = \log W_0 - D\log^2\left(\frac{P^\circ}{P}\right)$$

(A-7)

in which $D = B\left(\frac{T}{\beta}\right)^2$. W is simply the amount adsorbed expressed as a liquid volume and is given by $W = n/\rho*$ where $\rho*$ is the density of adsorbate in the micropores. In DR equation, plotting log W against $\log^2(p^\circ/p)$ for micropores following an ideal Gaussian type distribution should form an absolute straight line, but variations could be observed in many cases, from a partial straight line to a full curvature. Such variations can be linked to the lack of some micropore ranges, more micropores with specific dimensions presenting in the material or the pore size distribution completely not following Gaussian distribution. demonstrates several common types of DR plot deviations:

- The DR plot is a complete straight line if micropores follows Gaussian type distribution with adsorbate starting to fill in smallest pores first, and continuing to filling the last of the porosity at a relative pressure of unity [$\log^2(p^\circ/p) = 0$] (a).

- The DR plot presented in b is usually observed for microporous materials. The straight line forming from high $\log^2(p°/p)$ values to the cut-off position reveals micropore distribution with the inflection point indicating the width of the micropore. The lower the cut-off point, the more the anomaly may stem from the missing of larger pore sizes of the micropore, or the entire distribution is filled at relative pressure lower than unity.
- c demonstrates other common microporous materials. More ultra-micropores and super-micropores, existence of mesoporosity or multilayer formation of adsorbate molecules on non-porous surfaces may cause the upward curve at the low $\log^2(p°/p)$ values in the DR plot. The intercept between the linear part of the DR plot and y-axis indicates the content of micropores inside materials.
- Adsorbate molecules being unable to access very small micropores can result in the deviation at high $\log^2(p°/p)$ values in DR plot of d. Activated diffusion and/or molecular sieve effects may restrict adsorbate to enter these small micropores, so increasing temperature of adsorption can avoid these effects and return DR plot back to linear form.
- e presents a curve DR plot being associated with narrow pores. Adsorbate molecules are difficult to fill up narrow pores and unable to reach equilibrium. This phenomenon can be found with adsorbent is either just developing or closing (Marsh 1987). The isotherm is not an equilibrium isotherm and DR plot cannot be used in this case.

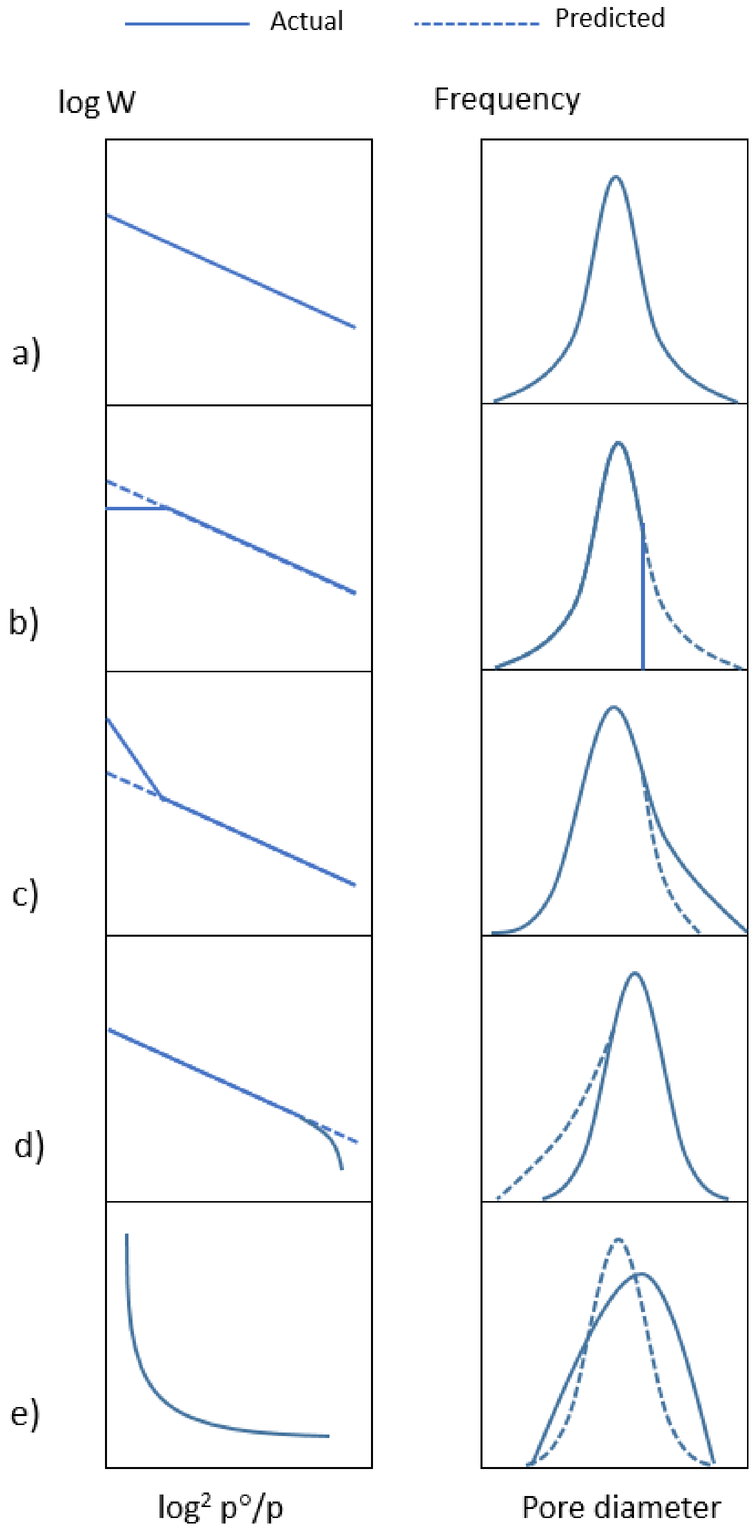

Figure A-1 Diagrammatic representation of the variations in Dubinin-Radushkevich plots of adsorption isotherms with associated pore size distributions (Marsh 1987)

DR model has been frequently used to interpret CO_2 adsorption isotherm at 0°C to describe microporosity in carbonaceous adsorbents or activated carbons (Dubinin and Stoeckli 1980) where BET model fails to be applied. Besides, DR model can also be used to obtain microporosity information from N_2 adsorption at -196°C (Marsh and Rand 1970, Rexer *et al.* 2014).

Appendix A.2 Brunauer-Emmett-Teller model

The multimolecular adsorption model was first introduced by Brunauer, Emmett and Teller (BET) in 1938 (Brunauer *et al.* 1938). The BET model adopted Langmuir's theory for unimolecular layers and successfully interpreted the multimolecular adsorption isotherm based on the theory with some reasonable assumptions. Many has used BET model to interpret N_2 adsorption at -196°C for surface area and pore volume.

First, the surface area being covered by 0, 1, 2, …, *i*, … layers of adsorbate molecules is called s_0, s_1, s_2, ... s_i, …. The surface area s_0 is the surface area of adsorbent, so it shall remain constant during the whole adsorption, so the rate of condensation of adsorbate molecules on the surface s_0 should be equal to the rate of evaporation from the first layer:

$$a_1 p s_0 = b_1 s_1 e^{-E1/RT} \tag{A-8}$$

in which p is the pressure, E_1 is the heat of adsorption of the first layer, and a_1 and b_1 are constant, given that a_1, b_1 and E_1 are independent of the number of molecules already in the first layer.

The surface area s_1 at equilibrium can be influenced by these four procedures simultaneously: adsorbate condenses on s_0, adsorbate evaporate from s_1, adsorbate condenses on s_1, and adsorbate evaporates from s_2. Therefore, we have

$$a_2 p s_1 + b_1 s_1 e^{-E1/RT} = b_2 s_2 e^{-E2/RT} + a_1 p s_0 \tag{A-9}$$

Applying (A-8) into (A-9), we obtain that

$$a_2 p s_1 = b_2 s_2 e^{-E2/RT} \tag{A-10}$$

the rate of condensation on top of the first layer is equal to the rate of evaporation from the second layer. Extending the same argument to the second and consecutive layers we have

$$\begin{aligned} a_3 p s_2 &= b_3 s_3 e^{-E3/RT} \\ \vdots \quad & \quad \vdots \\ a_i p s_{i-1} &= b_i s_i e^{-Ei/RT} \end{aligned}$$

The total surface area of the adsorbent is expressed as

$$A = \sum_{i=0}^{\infty} s_i$$

(A-11)

and the total volume of adsorbate adsorbed is

$$v = v_0 \sum_{i=0}^{\infty} i s_i$$

(A-12)

in which v_0 is the volume of gas adsorbed on one square centimetre of the adsorbed surface when it is covered with a complete unimolecular layer gas. It follows that

$$\frac{v}{Av_0} = \frac{v}{v_m} = \frac{\sum_{i=0}^{\infty} i s_i}{\sum_{i=0}^{\infty} s_i}$$

(A-13)

in which v_m is the volume of gas adsorbed when the entire adsorbent surface is covered with a complete unimolecular layer. If the heats of adsorption of second and consecutive layers are equal

$$E_2 = E_3 = \ldots = E_i = E_L$$

(A-14)

where E_L is the heat of liquefaction, and

$$\frac{b_2}{a_2} = \frac{b_3}{a_3} = \ldots = \frac{b_i}{a_i} = g$$

g being an appropriate constant. This is equivalent to saying that the evaporation-condensation properties of the molecules in the second and higher adsorbed layers are the same as those of the liquid state. We can express $s_1, s_2, s_3, \ldots s_i$ in terms of s_0:

$$s_1 = y s_0 \; where \; y = (a_1/b_1) p e^{E1/RT}$$

(A-15)

$$s_2 = x s_1 \; where \; x = (p/g) p e^{EL/RT}$$

(A-16)

$$s_3 = x s_2 = x^2 s_1$$

(A-17)

$$s_i = x s_{i-1} = x^{i-1} s_1 = y x^{i-1} s_0 = c x_i s_0$$

(A-18)

$$where\ c = \frac{y}{x} = \frac{a_1 g}{b_1} e^{(E_1 - E_L)/RT}$$

(A-19)

Substituting into equation (A-13) we have

$$\frac{v}{v_m} = \frac{cs_0 \sum_{i=1}^{\infty} ix_i}{s_0 \left\{ 1 + c \sum_{i=1}^{\infty} x_i \right\}}$$

(A-20)

with the summation in denominator is merely the sum of infinite geometric progression

$$\sum_{i=1}^{\infty} x^i = \frac{x}{1-x}$$

(A-21)

and the numerator is

$$\sum_{i=1}^{\infty} ix^i = x \frac{d}{dx} \sum_{i=1}^{\infty} x^i = \frac{x}{(1-x)^2}$$

(A-22)

Therefore, we obtain

$$\frac{v}{v_m} = \frac{cx}{(1-x)(1-x+cx)}$$

(A-23)

If we start the adsorption with a free adsorbent surface, an infinite number of layers can build up on the adsorbent at saturation pressure $p°$. To make $v = \infty$, when $p = p°$, x must be equal to unity. Thus from

$$(p° / g) pe^{EL/RT} \ and \ x = p / p°$$

(A-24)

Substituting into (A-23), we have

$$v = \frac{v_m cp}{(p° - p)[1 + (c-1)(p / p°)]}$$

(A-25)

For the purpose of testing, the equation can be put in the form

$$\frac{p}{n(p° - p)} = \frac{1}{n_m c} + \frac{(c-1)}{n_m c} \cdot \frac{p}{p°}$$

(A-26)

in which $p°$ is the saturated pressure (kPa), n is gas uptake at pressure p (mmol g^{-1}), n_m is complete monolayer coverage (mmol g^{-1}), and c is a dimensionless constant in BET equation, related to adsorption energy where

$$c = exp\left(\frac{\Delta H_A - \Delta H_L}{RT}\right) \tag{A-27}$$

in which ΔH_A is heat of adsorption of the first adsorbed layer, and ΔH_L is heat of adsorption of second & subsequent multilayers (*i.e.* the molar heat of condensation).

In BET equation, plotting the $\frac{p}{n(p° - p)}$ against $\frac{p}{p°}$ should form a straight line, in which the intercept is $\frac{1}{n_m c}$ and the slope is $\frac{(c-1)}{n_m c}$. The n_m and c values can be evaluated based on the intercept and slope of BET plot, and the surface area based on BET equations can be calculated based on the complete monolayer value (n_m), Avogadro's number (N_A), and the cross sectional area of a single adsorbate molecule (A_M).

The BET model was based on the assumption of infinite layers of adsorbate molecules on the surface of adsorbent, which led to the simplified form presented in equation (A-26). However, micropores, cracks and capillaries in some materials does not allow infinite numbers of adsorbate layers on the surface of adsorbent, so the thickness of the adsorbed layers cannot exceed some finite number n. Thus, equation (A-20) would become:

$$v = \frac{v_m cx}{(1-x)}\left\{\frac{1-(n+1)x^n + nx^{n+1}}{1+(c-1)x - cx^{n+1}}\right\} \tag{A-28}$$

in which $x = p/p°$ and the constants v_m and c have the same meaning as in equation (A-26). Equation (A-28) reduces to Langmuir's model if n = 1 and turns into equation (A-26) if n = ∞.

This allows equation (A-26) of BET model to be applied unrestrictedly on type II and IV isotherms but not type I isotherm (Brunauer *et al.* 1938). However, BET method has been frequently used to interpret adsorption isotherms on many types of carbon, even though many of them have high extent of microporosity. Therefore, the BET surface areas obtained in these cases will certainly be a relative means of comparison between different samples, rather than an accurate value of surface area (Nishi and Inagaki 2016).

Appendix B Analytical techniques

Appendix B.1 X-ray photoelectron spectroscopy

Figure B-1 demonstrates a schematic of a XPS instrument, main components including an X-ray source, electron energy analyser, detector and sample holder with other accessories. All components are installed inside an ultrahigh-vacuum chamber to remove all adsorption gases on sample surface (Burrell 2001). Many commercial instruments use the generic Kα X-ray radiation from magnesium (1253.6 eV) or aluminium (1486.6 eV) and the X-ray monochromatic wavelength is ensured by a monochromator. Electron energy analyser analyses energies of electrons emitted from sample under X-ray, with the concentric hemispherical analyser being the common type (Figure B-1) (Haerle *et al.* 2001). The hemispherical shape allows photoelectrons with correct kinetic energies to go through the entrance slit to exit slit and then be counted by the detector. The kinetic energies are determined based on the potential difference maintained between the two hemispheres and their radii (typically 100-200 mm). Electron flood gun is used in analysing non-conductive samples to avoid accumulated positive charge on sample surfaces, which change kinetic energy of photoelectrons (Burrell 2001).

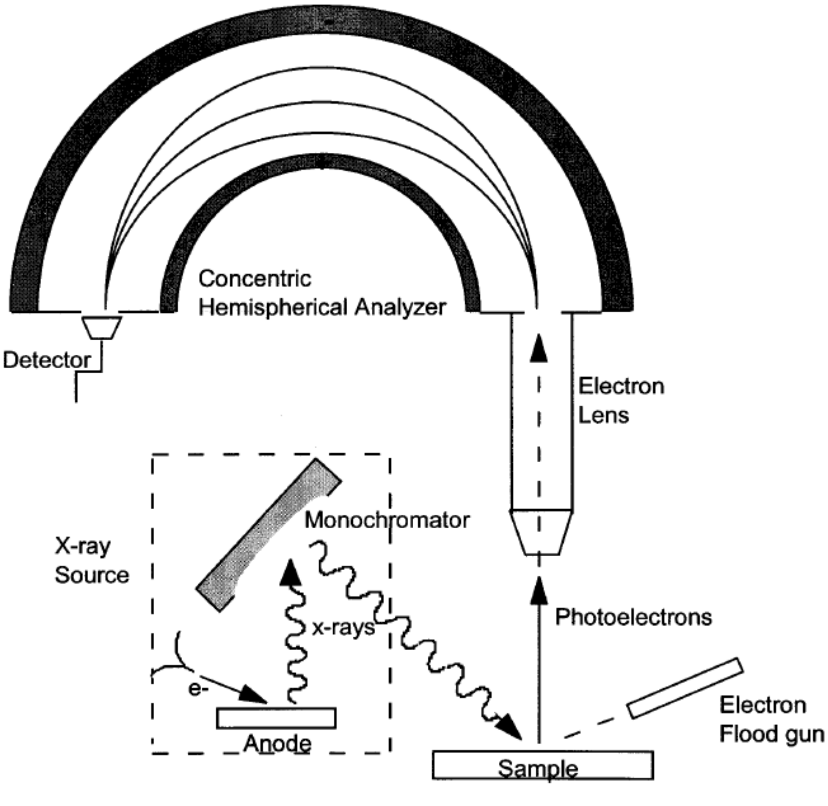

Figure B-1 Schematic of X-ray photoelectron spectroscopy (Burrell 2001)

XPS has been used to identify the state of carbon and other heterogeneous atoms such as oxygen and nitrogen. An elemental peak can combine different chemical bonding states of that element and peak fitting can be used to determine the semi-quantitative amount of those chemical bonding states. However, such interpretation procedure can yield various errors and reduce the accuracy of obtained data (Konno 2016) if important parameters in the peak fitting are not well-attended.

- **Background subtraction:** Shirley background subtraction for carbonaceous materials has been used for XPS for long time (Konno 2016). In Shirley's method, the starting binding energy and ending binding energy need determining manually, which requires carefulness every time the peak data is analysed (Shirley 1972). Tougaard's method can be used, but it requires much higher scanning spectra of binding energy (~50 eV), which is not applicable in most cases, and there are parameters that needs to be guessed prior doing the background subtraction (Tougaard 1988). In Shirley's method, the same binding energy values does not need to be exactly similar in all cases, but rather the average value of the background noise from both sides of the peak. For a peak with low signal-to-noise ratio, determining E_B values can alter the Shirley background significantly, so visual judgment is necessary to ensure the accuracy of this method.
- **Binding energy:** Although binding energies for chemical bonding states have been reported in literature, assigning a specific binding energy to a component can still be difficult because separation of binding energy values can be small and fall under instrument threshold. Therefore, choosing binding energy values for peak fitting should be done after considerable literature reviews and through a series of trials and errors to make sure the number of peaks chosen fully represent the chemical bonding states but at the same time not over interpret XPS peaks.
- **The full width at half maximum (FWHM)**: Different values for FWHMs of different chemical states can lead to errors and uncertainties in semiquantitative results. For carbonaceous materials, it is noticed that FWHMs should be restraint to a same value unless there are sufficient evidence proving the necessity to choose different FWHM values (Konno 2016) such as for sp^2/sp^3 hybridisation ratio in amorphous carbon (Haerle *et al.* 2001), AC (Seredych *et al.* 2008), carbon fibres (Yue *et al.* 1999), and CNTs (He *et al.* 2007).
- **Peak shape:** choosing suitable peak shape are important to ensure the quality of data interpretation, and the peak shape of Gaussian/ Lorentzian mixture (usually 70/30 or 80/20) are usually used for peak fitting. Being similar with FWHM, peak shape should be remained

the same for all component unless there are clear evidence for choosing a specific peak shape to ensure the consistency of data.

Appendix B.2 Temperature programmed desorption

Based on temperature profiles and desorbed gases, surface functional groups in carbon can be determined. Many oxygen functional groups directly decompose into CO, CO_2 and H_2O at various temperatures, and there are differences in decomposition temperatures for each specific functional group (as in Table 3-1). However, it is noticed that carboxylic groups give rise to the CO_2, followed by lactone/ lactol groups, phenol/ carbonyl/ quinone desorb to CO in TPD at higher temperatures, indicating the general thermal stability of oxygen functional groups as order: carboxylic < lactone/ lactol < phenol/ carbonyl/ quinone < pyrone. In general, the ending temperature of 1000-1200°C is sufficient to desorb all surface oxygen groups, but higher temperatures are required if investigating thermally stable functional groups is necessary.

The transformation of nitrogen species in carbon materials in TPD follows a more distinctive path than oxygen functional groups. Pyrrolic-N is converted into pyridinic-N at mild pyrolysis temperatures 460-800°C (Stańczyk *et al.* 1995, Lahaye *et al.* 1999), rather than desorb into nitrogen-containing gas/ vapour compounds, and pyridinic-N continues to be reconstructed into quaternary-N if higher temperatures are applied. The main decomposition product of pyridinic-N and quaternary-N is N_2 at > 927°C (1200 K) with only a small portion of HCN and NH_3 and even 10-40 % of nitrogen could stay in carbon materials after being heated at 1400°C (Xiao *et al.* 2005). Most N_2 resulted from surface reactions between nitrogen species rather than direct desorption, so the amount of some desorbed species such as NH_3 and HCN increases and less N_2 evolves if TPD run is conducted in H_2 atmosphere (Xiao *et al.* 2005). In general, nitrogen species are more thermal stable than oxygen functional groups with the thermal stability order as pyridinic-N oxides < pyrrolic-N < pyridinic-N < quaternary-N. Thus, it is necessary to use other analysis techniques to complement TPD information on nitrogen species.

On the other hand, phosphorus functional groups yields CO and CO_2 desorption at high temperatures at 907-947°C due to the breakage of C-O bonds in $C\text{-}O\text{-}PO_3$ (Wu and Radovic 2006). Other types of phosphorus functional groups seem to be resistant to high temperatures and do not desorb into gas compounds in TPD. Therefore, other characterisation techniques are required to understand about the phosphorus functional groups.

Appendix B.3 Electrochemical impedance spectroscopy model

This section explain the mathematical analysis of the EIS model shown in Figure 3-25.

Circuit 1: (Z1||Z2): $Z_1 = C_{dl0}$, $Z_2 = R_{dl0}$. The impedance of circuit 1:

$$\mathrm{Z} = \frac{Z_1 Z_2}{Z_1 + Z_2}$$

- $Z_1 = 1/(j\omega C) = -j/(\omega C)$
- $Z_2 = R$

Therefore,

$$Z = \frac{Z_1 Z_2}{Z_1 + Z_2} = \frac{\frac{-j}{\omega C}R}{R - \frac{j}{\omega C}} = \frac{\frac{-j}{\omega C}R\left(R + \frac{j}{\omega C}\right)}{\left(R - \frac{j}{\omega C}\right)\left(R + \frac{j}{\omega C}\right)} = \frac{\frac{-j}{\omega C}R^2 - \frac{j^2 R}{\omega^2 C^2}}{R^2 + \frac{1}{\omega^2 C^2}}$$

$$\mathrm{Z} = \frac{\frac{\mathrm{R}}{\omega^2 \mathrm{C}^2} - \mathrm{j}\frac{\mathrm{R}^2}{\omega \mathrm{C}}}{\mathrm{R}^2 + \frac{1}{\omega^2 \mathrm{C}^2}} = \frac{\mathrm{R}}{\mathrm{R}^2 \omega^2 \mathrm{C}^2 + 1} - \mathrm{j}\frac{\mathrm{R}\omega \mathrm{C}}{\mathrm{R}^2 \omega^2 \mathrm{C}^2 + 1}$$

Therefore, in the first circuit:

$$Resistance = Z_{real} = \frac{\mathrm{R}}{\mathrm{R}^2 \omega^2 \mathrm{C}^2 + 1}$$

$$Impedance = \mathrm{Z}_{\mathrm{imagine}} = \frac{\mathrm{R}\omega \mathrm{C}}{\mathrm{R}^2 \omega^2 \mathrm{C}^2 + 1}$$

Circuit 2: (Z1||Z2): $Z_1 = C_{dl}$, $Z_2 = R_{ct}$ + CPE1.

- $Z_1 = 1/(j\omega C) = -j/(\omega C)$
- $Z_2 = R_{ct} + \frac{Yinv}{\omega^{\varphi}}\left[\cos\left(\frac{\pi\varphi}{2}\right) - j\sin\left(\frac{\pi\varphi}{2}\right)\right] = R_{ct} + \frac{Yinv}{\omega^{\varphi}}cos\left(\frac{\pi\varphi}{2}\right) - j\frac{Yinv}{\omega^{\varphi}}\sin\left(\frac{\pi\varphi}{2}\right)$

Let $A = \frac{Yinv}{\omega^{\varphi}}cos\left(\frac{\pi\varphi}{2}\right)$ and $B = \frac{Yinv}{\omega^{\varphi}}\sin\left(\frac{\pi\varphi}{2}\right)$

Therefore, $Z_2 = R_{ct} + A - Bj = X - Bj$

The impedance of circuit 2: $\mathrm{Z} = \frac{Z_1 Z_2}{Z_1 + Z_2}$

- Numerator: $Z_1 Z_2 = \frac{-j}{\omega C}(X - Bj) = \frac{-jX - B}{\omega C}$
- Denominator: $Z_1 + Z_2 = X - Bj - \frac{j}{\omega C} = X - j\left(B + \frac{1}{\omega C}\right)$

Therefore,

$$Z = \frac{Z_1 Z_2}{Z_1 + Z_2} = \frac{\frac{-jX\ -\ B}{\omega C}}{X - j\left(B + \frac{1}{\omega C}\right)} = \frac{\frac{-jX\ -\ B}{\omega C}\left[X + j\left(B + \frac{1}{\omega C}\right)\right]}{\left[X - j\left(B + \frac{1}{\omega C}\right)\right]\left[X + j\left(B + \frac{1}{\omega C}\right)\right]}$$

Let $Y\ =\ \left(B + \frac{1}{\omega C}\right)$:

$$\mathrm{Z}\ =\ \frac{\frac{-jX\ -\ B}{\omega C}(X + jY)}{(X - jY)(X + jY)}\ =\ \frac{\frac{XY}{\omega C}\ -\ \frac{BX}{\omega C} - j\frac{X^2}{\omega C} - j\frac{B}{\omega C}\mathrm{Y}}{X^2 + Y^2}\ =\ \frac{\frac{1}{\omega C}(XY - BX)}{X^2 + Y^2} - j\frac{\frac{1}{\omega C}(X^2 + BY)}{X^2 + Y^2}$$

Therefore, in the second circuit:

$$Resistance\ =\ Z_{real} = \frac{\frac{1}{\omega C}(XY - BX)}{X^2 + Y^2}$$

$$Impedance\ =\ \mathrm{Z}_{imagine} = \frac{\frac{1}{\omega C}(X^2 + BY)}{X^2 + Y^2}$$

Circuit 3: ($Z_1||Z_2$). Z1 = CPE2, Z_2 = R_{ads} + C_{ads}

- $Z_1 = \frac{Yinv}{\omega^{\varphi}}\left[\cos\left(\frac{\pi\varphi}{2}\right) - j\sin\left(\frac{\pi\varphi}{2}\right)\right] = \frac{Yinv}{\omega^{\varphi}}cos\left(\frac{\pi\varphi}{2}\right) - j\frac{Yinv}{\omega^{\varphi}}\sin\left(\frac{\pi\varphi}{2}\right)\ =\ A\ -\ jB$
- $Z_2 = R_{ads} - j/(\omega C)$

The impedance of circuit 3: $\mathrm{Z} = \frac{Z_1 Z_2}{Z_1 + Z_2}$

- Numerator: $Z_1 Z_2 = (A - jB)\left(R_{ads} - j\frac{1}{\omega C}\right) = \left(AR_{ads}\ -\ \frac{B}{\omega C}\right) - j\left(BR_{ads}\ +\ \frac{A}{\omega C}\right)$
- Denominator: $Z_1 + Z_2 = (A + R_{ads}) - j\left(B\ +\ \frac{1}{\omega C}\right)$

Let $X\ =\ A\ +\ R_{ads}$ and $Y\ =\ B\ +\ \frac{1}{\omega C}$

Therefore,

$$Z = \frac{Z_1 Z_2}{Z_1 + Z_2} = \frac{\left(AR_{ads}\ -\ \frac{B}{\omega C}\right) - j\left(BR_{ads}\ +\ \frac{A}{\omega C}\right)}{X - j\,Y}$$

$$\mathrm{Z} = \frac{\left[\left(AR_{ads}\ -\ \frac{B}{\omega C}\right) - j\left(BR_{ads}\ +\ \frac{A}{\omega C}\right)\right](X + jY)}{(X - jY)(X + jY)}$$

$$Z = \frac{\left(AR_{ads}\ -\ \frac{B}{\omega C}\right)X\ +\ \left(BR_{ads}\ +\ \frac{A}{\omega C}\right)Y}{X^2 + Y^2} + \frac{-j\left(BR_{ads}\ +\ \frac{A}{\omega C}\right)X + j\left(AR_{ads}\ -\ \frac{B}{\omega C}\right)Y}{X^2 + Y^2}$$

$$Z = \frac{\left(AR_{ads}\ -\ \frac{B}{\omega C}\right)X\ +\ \left(BR_{ads}\ +\ \frac{A}{\omega C}\right)Y}{X^2 + Y^2} - j\frac{\left(BR_{ads}\ +\ \frac{A}{\omega C}\right)X\ -\left(AR_{ads}\ -\ \frac{B}{\omega C}\right)Y}{X^2 + Y^2}$$

Therefore, in the third circuit:

$$Resistance = Z_{real} = \frac{\left(AR_{ads} - \frac{B}{\omega C}\right)X + \left(BR_{ads} + \frac{A}{\omega C}\right)Y}{X^2 + Y^2}$$

$$Impedance = \mathrm{Z}_{imagine} = \frac{\left(BR_{ads} + \frac{A}{\omega C}\right)X - \left(AR_{ads} - \frac{B}{\omega C}\right)Y}{X^2 + Y^2}$$

The highly oxidized HNO_3 treated carbon samples (CO_2/800-1-HNO_3 and CO_2/800-1-HNO_3/400) gave low values of │ImZ│ and the capacitance behaviour of the samples was different from the other samples in the series. The only fit found for these samples involved taking the complex conjugate of the normal expression for Z given above.

$$Z = Yinv2[(j\omega)^{-\varphi}] = \frac{Yinv2}{\omega^{\varphi}}\left[\exp\left(\frac{-j\pi\varphi}{2}\right)\right] = \frac{Yinv2}{\omega^{\varphi}}\left[\cos\left(\frac{\pi\varphi}{2}\right) - j\,sin\left(\frac{\pi\varphi}{2}\right)\right]$$

The imaginary part of this is negative, but where a negative capacitance might be expected (usually where more complex chemical reactions or adsorption effects are seen) it is possible for the imaginary part of the expression above to become positive, corresponding to allowing the capacitance component to become negative. In this case, the equation for impedance of CPE2 and R_{ads} and C_{ads} is below:

$$Z_1 = \frac{Yinv2}{\omega^{\varphi}}\left[exp\left(\frac{j\pi\varphi}{2}\right)\right] = \frac{Yinv2}{\omega^{\varphi}}\left[\cos\left(\frac{\pi\varphi}{2}\right) + j\,sin\left(\frac{\pi\varphi}{2}\right)\right] = A + Bj$$

$$Z_2 = R_{ads} - j/(\omega C)$$

The impedance of circuit 3 becomes: $\mathrm{Z} = \frac{Z_1 Z_2}{Z_1 + Z_2}$

- Numerator: $Z_1 Z_2 = (A + jB)\left(R_{ads} - j\frac{1}{\omega C}\right) = \left(AR_{ads} + \frac{B}{\omega C}\right) + j\left(BR_{ads} - \frac{A}{\omega C}\right)$
- Denominator: $Z_1 + Z_2 = (A + R_{ads}) + j\left(B - \frac{1}{\omega C}\right)$

Let $X = A + R_{ads}$ and $Y* = B - \frac{1}{\omega C}$

Therefore,

$$Z = \frac{Z_1 Z_2}{Z_1 + Z_2} = \frac{\left(AR_{ads} + \frac{B}{\omega C}\right) + j\left(BR_{ads} - \frac{A}{\omega C}\right)}{X + j\,Y*} = \frac{\left[\left(AR_{ads} + \frac{B}{\omega C}\right) + j\left(BR_{ads} - \frac{A}{\omega C}\right)\right](X - jY*)}{(X + jY*)(X - jY*)}$$

$$Z = \frac{\left(AR_{ads} + \frac{B}{\omega C}\right)X + \left(BR_{ads} - \frac{A}{\omega C}\right)Y*}{X^2 + Y*^2} + \frac{j\left(BR_{ads} - \frac{A}{\omega C}\right)X - j\left(AR_{ads} + \frac{B}{\omega C}\right)Y*}{X^2 + Y*^2}$$

$$Z = \frac{\left(AR_{ads} + \frac{B}{\omega C}\right)X + \left(BR_{ads} - \frac{A}{\omega C}\right)Y*}{X^2 + Y*^2} + j\frac{\left(BR_{ads} + \frac{A}{\omega C}\right)X - \left(AR_{ads} - \frac{B}{\omega C}\right)Y*}{X^2 + Y*^2}$$

Therefore, in the third circuit:

$$Resistance = Z_{real} = \frac{\left(AR_{ads} + \frac{B}{\omega C}\right)X + \left(BR_{ads} - \frac{A}{\omega C}\right)Y*}{X^2 + Y*^2}$$

$$Impedance = \mathrm{Z}_{imagine} = \frac{\left(BR_{ads} + \frac{A}{\omega C}\right)X - \left(AR_{ads} - \frac{B}{\omega C}\right)Y*}{X^2 + Y*^2}$$

Appendix C Other figures and tables

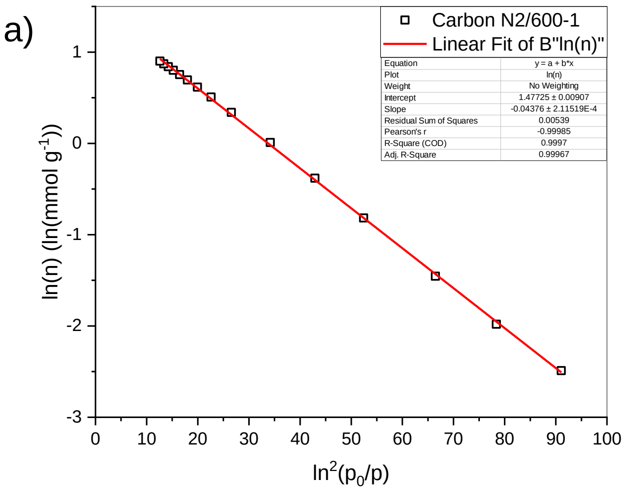

Equation	y = a + b*x
Plot	ln(n)
Weight	No Weighting
Intercept	1.47725 ± 0.00907
Slope	-0.04376 ± 2.11519E-4
Residual Sum of Squares	0.00539
Pearson's r	-0.99985
R-Square (COD)	0.9997
Adj. R-Square	0.99967

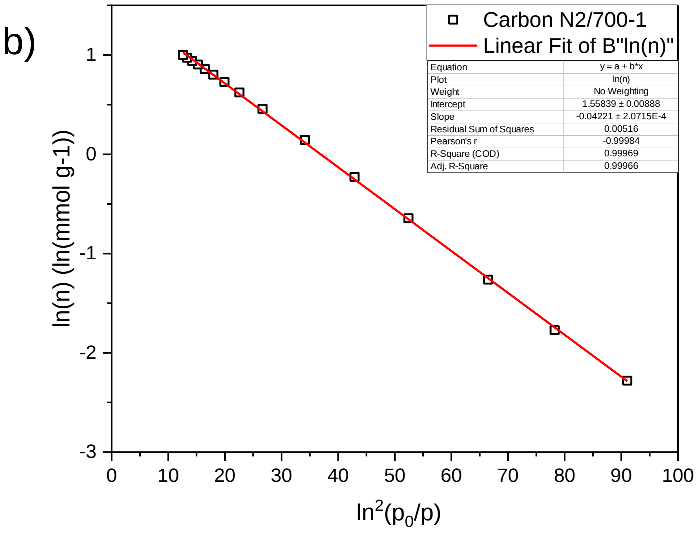

Equation	y = a + b*x
Plot	ln(n)
Weight	No Weighting
Intercept	1.55839 ± 0.00888
Slope	-0.04221 ± 2.0715E-4
Residual Sum of Squares	0.00516
Pearson's r	-0.99984
R-Square (COD)	0.99969
Adj. R-Square	0.99966

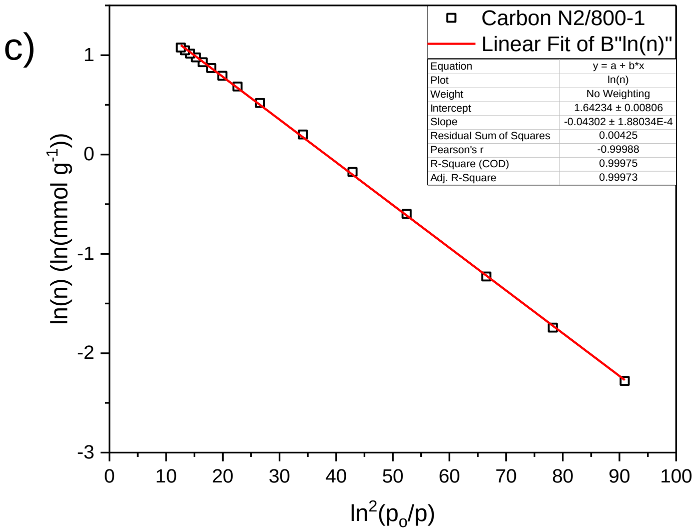

Figure C-1 DR plots for CO_2 adsorption at 0°C on biochar pyrolysed in N_2 atmosphere a) Biochar N_2/600-1, b) Biochar N_2/700-1 and c) Biochar N_2/800-1

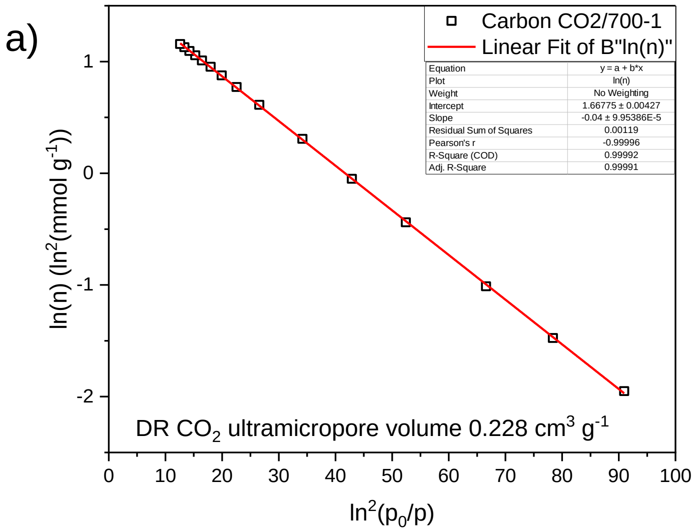

b)

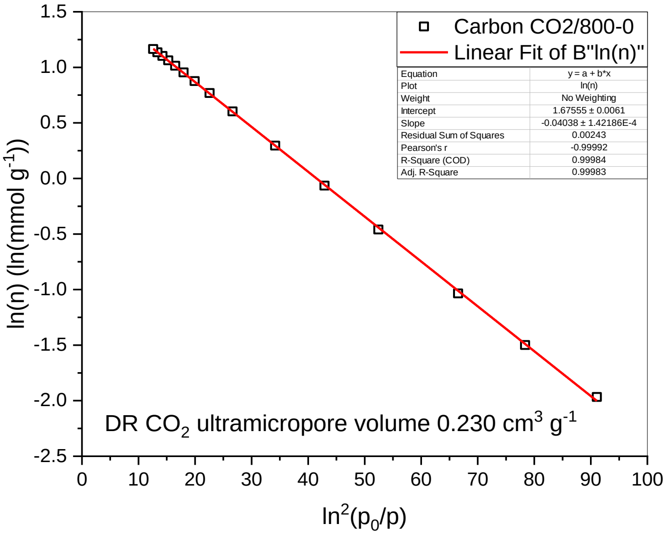
Carbon CO2/800-0
Linear Fit of B"ln(n)"
Equation | y = a + b*x
Plot | ln(n)
Weight | No Weighting
Intercept | 1.67555 ± 0.0061
Slope | -0.04038 ± 1.42186E-4
Residual Sum of Squares | 0.00243
Pearson's r | -0.99992
R-Square (COD) | 0.99984
Adj. R-Square | 0.99983
DR CO_2 ultramicropore volume 0.230 cm^3 g^{-1}
ln(n) (ln(mmol g^{-1}))
1.5
1.0
0.5
0.0
-0.5
-1.0
-1.5
-2.0
-2.5
0
10
20
30
40
50
60
70
80
90
100
$ln^2(p_0/p)$

c)

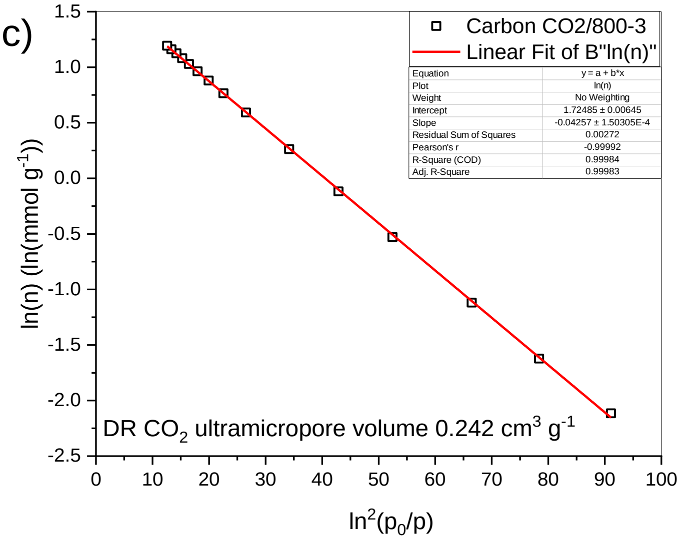
Carbon CO2/800-3
Linear Fit of B"ln(n)"
Equation | y = a + b*x
Plot | ln(n)
Weight | No Weighting
Intercept | 1.72485 ± 0.00645
Slope | -0.04257 ± 1.50305E-4
Residual Sum of Squares | 0.00272
Pearson's r | -0.99992
R-Square (COD) | 0.99984
Adj. R-Square | 0.99983
DR CO_2 ultramicropore volume 0.242 cm^3 g^{-1}
ln(n) (ln(mmol g^{-1}))
1.5
1.0
0.5
0.0
-0.5
-1.0
-1.5
-2.0
-2.5
0
10
20
30
40
50
60
70
80
90
100
$ln^2(p_0/p)$

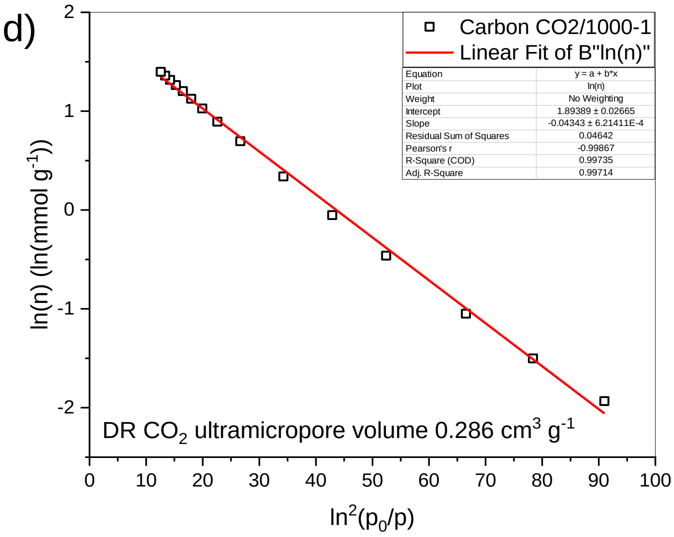

Figure C-2 DR plots for CO_2 adsorption at 0°C on AC treated under CO_2 atmosphere a) AC CO_2/700-1, b) AC CO_2/800-0, c) AC CO_2/800-3 and d) AC CO_2/1000-1

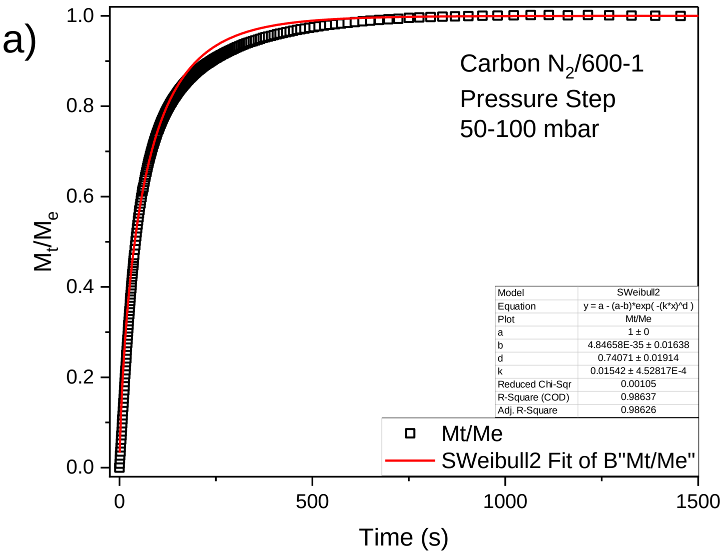

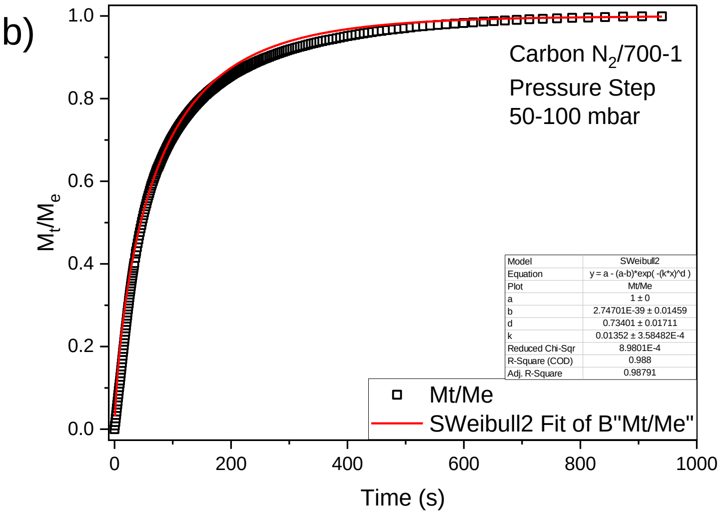

Model	SWeibull2
Equation	y = a - (a-b)*exp(-(k*x)^d)
Plot	Mt/Me
a	1 ± 0
b	2.74701E-39 ± 0.01459
d	0.73401 ± 0.01711
k	0.01352 ± 3.58482E-4
Reduced Chi-Sqr	8.9801E-4
R-Square (COD)	0.988
Adj. R-Square	0.98791

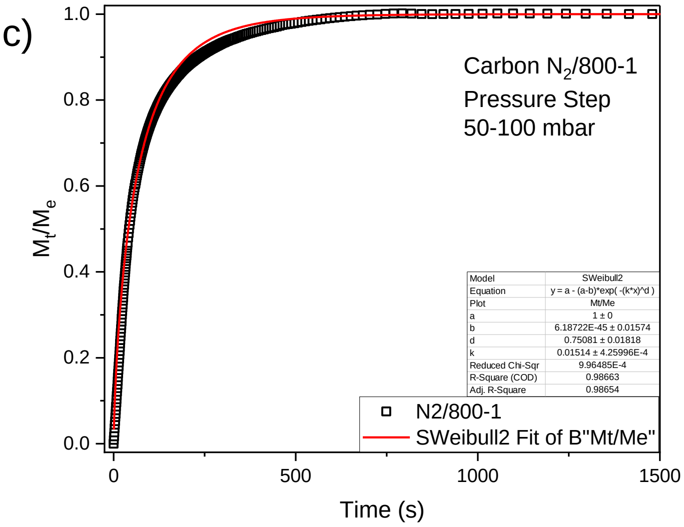

Model	SWeibull2
Equation	y = a - (a-b)*exp(-(k*x)^d)
Plot	Mt/Me
a	1 ± 0
b	6.18722E-45 ± 0.01574
d	0.75081 ± 0.01818
k	0.01514 ± 4.25996E-4
Reduced Chi-Sqr	9.96485E-4
R-Square (COD)	0.98663
Adj. R-Square	0.98654

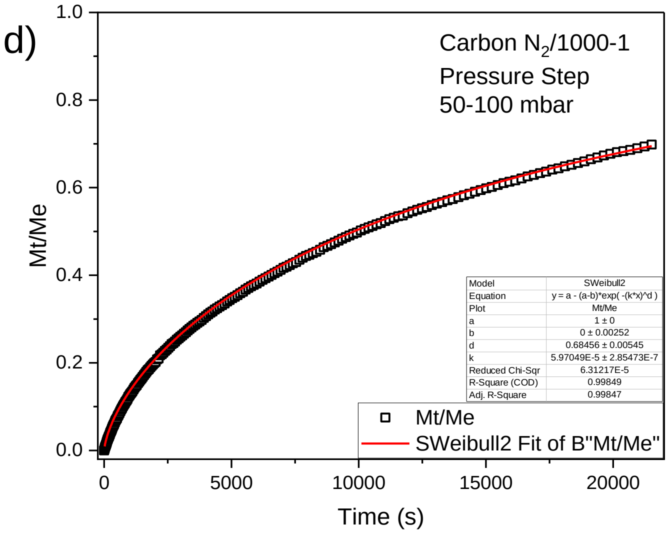

Figure C-3 Adsorption kinetics for pressure step 50-100 mbar for CO_2 adsorption on biochar a) biochar N_2/600-1 (0°C), b) biochar N_2/700-1 (0°C), c) biochar N_2/800-1 (0°C) and d) biochar N_2/1000-1 (30°C).

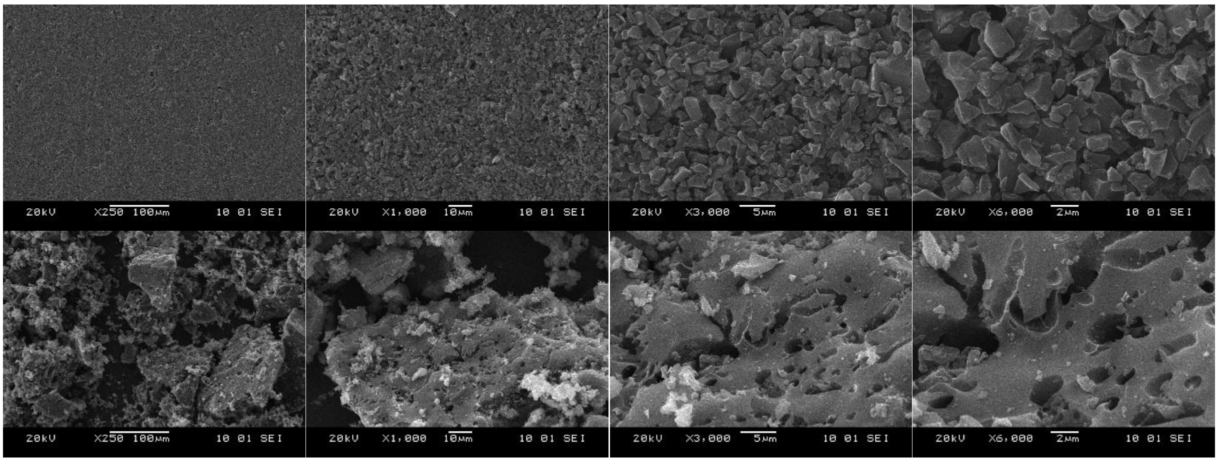

Figure C-4 Comparison of SEM images of PVDF/walnut shell-derived carbon composite N_2/600-1 (top row) and biochar N_2/600-1 (bottom row)

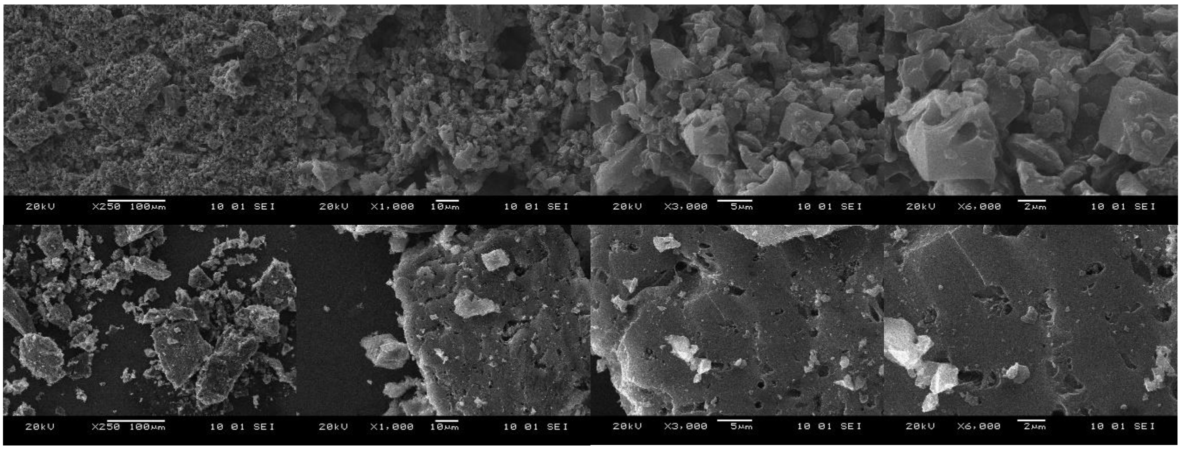

Figure C-5 Comparison of SEM images of PVDF/walnut shell-derived carbon composite N_2/800-1 (top row) and biochar N_2/800-1 (bottom row)

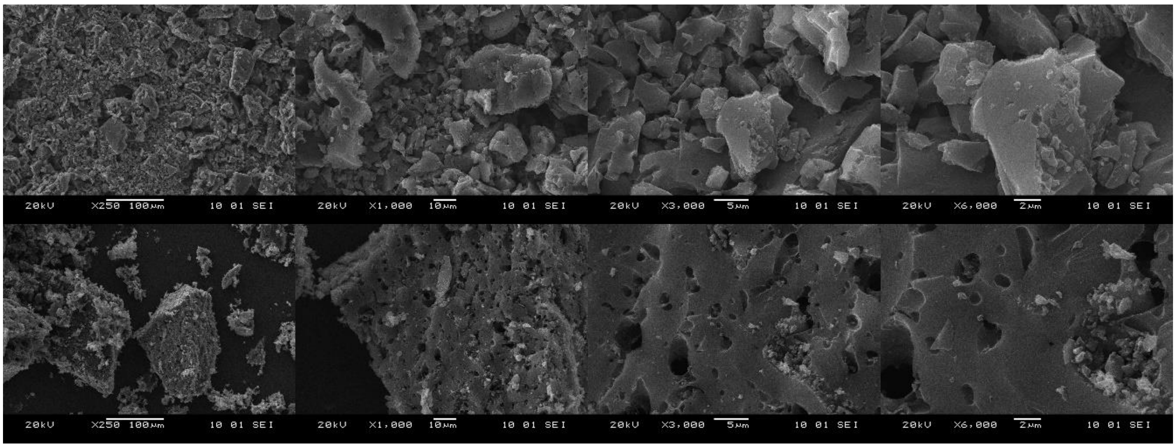

Figure C-6 Comparison of SEM images of PVDF/walnut shell-derived carbon composite N_2/1000-1 (top row) and biochar N_2/1000-1 (bottom row)

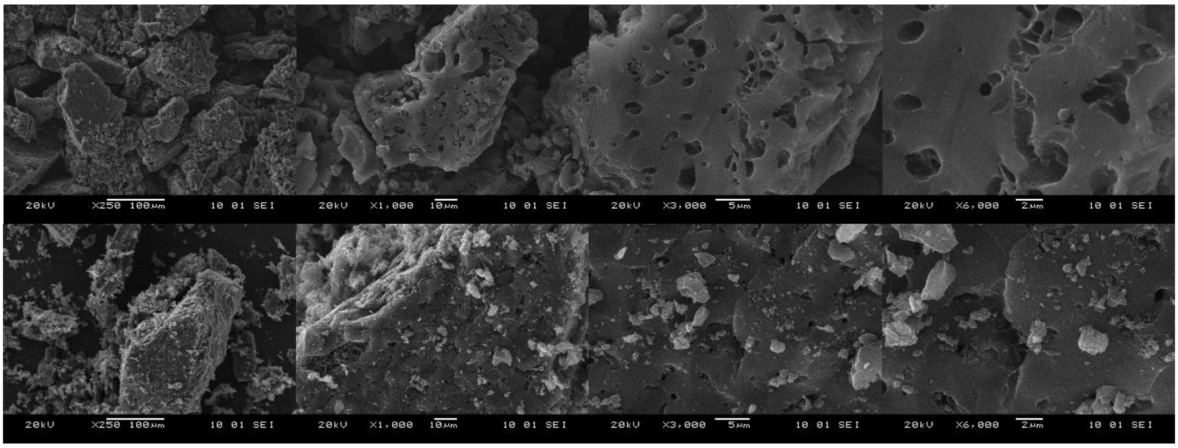

Figure C-7 Comparison of SEM images of PVDF/walnut shell-derived carbon composite CO_2/700-1 (top row) and AC CO_2/700-1 (bottom row)

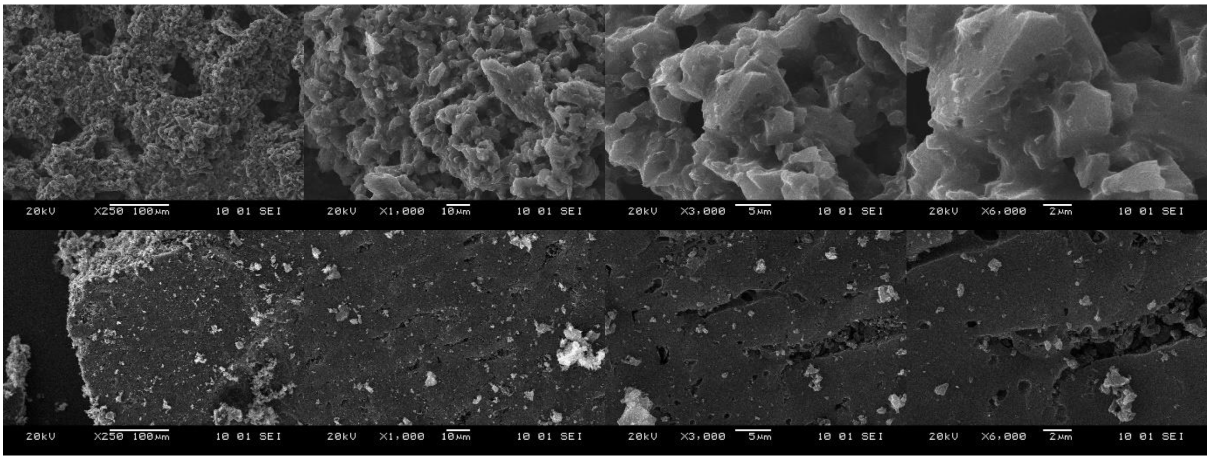

Figure C-8 Comparison of SEM images of PVDF/walnut shell-derived carbon composite CO_2/800-1 (top row) and AC CO_2/800-1 (bottom row)

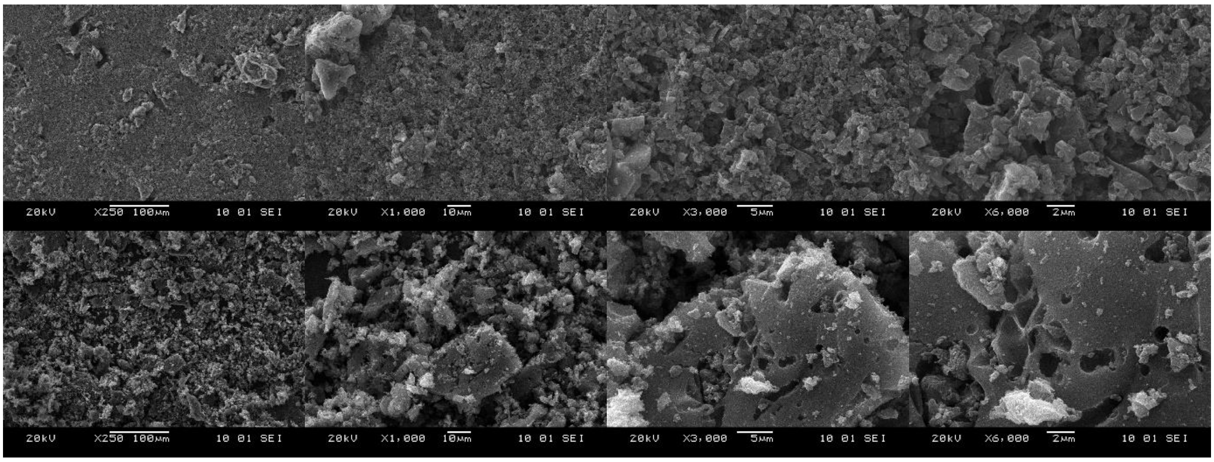

Figure C-9 Comparison of SEM images of PVDF/walnut shell-derived carbon composite CO_2/1000-1 (top row) and AC CO_2/1000-1 (bottom row)

a)

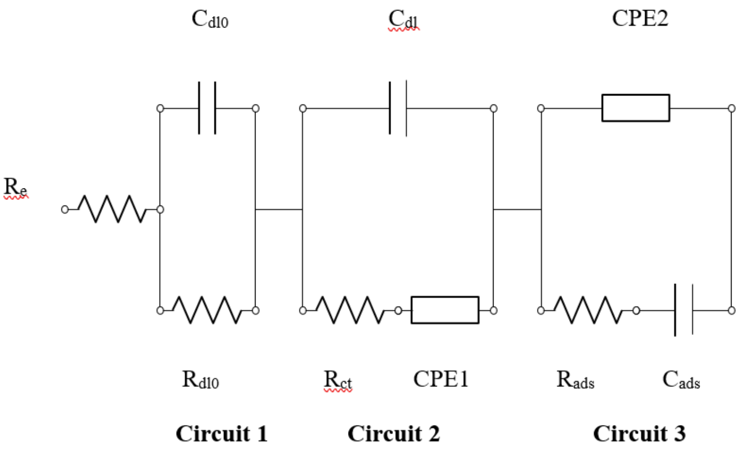

b)

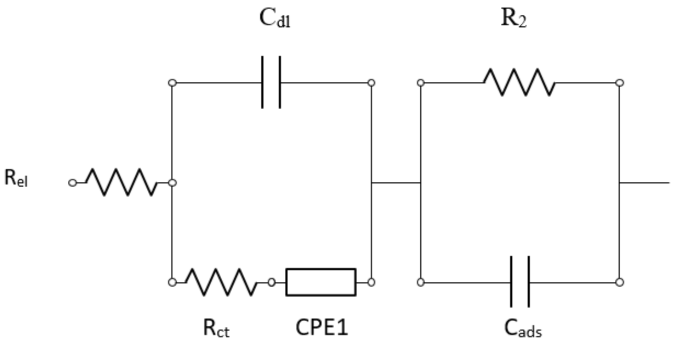

Figure C-10 EIS equivalent circuit model for a) walnut shell-derived carbon carbonised in N_2 and CO_2, HNO_3 treated CO_2/800-1 series, and K_2CO_3 treated CO_2/800-1 at 800°C b) NH_3 treated N_2/800-1 at 800°C

Table C-1 EIS model parameters a) Carbonization in N_2; b) Carbonization in CO_2; c) HNO_3 treated CO_2/800-1 series; d) NH_3 treated N_2/800-1 at 800°C e) K_2CO_3 treated CO_2/800-1 at 800°C

a) Carbonization in N_2

Electrode Carbon	**N_2/600-1**	**N_2/800-1**	**N_2/1000-1**
Parameter			
R_{el}	1.021 ± 0.006	0.9359 ± 0.0028	0.9825 ± 0.0055
C_{dl0}		$9.984 \pm 0.535 \times 10^{-5}$	$5.812 \pm 0.379 \times 10^{-5}$
R_{dl0}		0.1186 ± 0.0026	0.1858 ± 0.0056
R_{ct}	0.2729 ± 0.0051	0.0749 ± 0.0023	
C_{dl}	$3.282 \pm 0.136\ x10^{-5}$	$1.438 \pm 0.007 \times 10^{-3}$	$4.050 \pm 0.324 \times 10^{-4}$
$\phi 1$	0.2649 ± 0.0023	0.3105 ± 0.0031	0.1793 ± 0.0015
Yinv1	0.9352 ± 0.0071	0.5751 ± 0.0043	1.031 ± 0.0085
R_{ads}			
C_{ads}	0.4972 ± 0.0397	0.3344 ± 0.0399	0.5276 ± 0.0278
$\phi 2$			
Yinv2	0.08759 ± 0.00442	0.02911 ± 0.00265	0.9332 ± 0.00346

b) Carbonization in CO_2

Electrode Carbon	**CO_2/700-1**	**CO_2/800-1**	**CO_2/1000-1**
Parameter			

R_{el}	$7.992 \pm 0.073\times10^{-1}$	$5.767 \pm 0.014\times10^{-1}$	$8.661 \pm 0.038\times10^{-1}$
C_{dl0}		$1.951 \pm 0.084\times10^{-4}$	$1.697 \pm 0.184\times10^{-4}$
R_{dl0}		$7.271 \pm 0.128\times10^{-2}$	$7.962 \pm 0.352\times10^{-2}$
R_{ct}	$1.603 \pm 0.033\times10^{-1}$	$4.683 \pm 0.115\times10^{-2}$	$4.276 \pm 0.284\times10^{-2}$
C_{dl}	$6.268 \pm 0.266\times10^{-5}$	$4.644 \pm 0.257\times10^{-3}$	$4.018 \pm 0.536\times10^{-3}$
$\phi1$	$8.111 \pm 0.718\times10^{-1}$	$8.448 \pm 0.598\times10^{-1}$	$3.778 \pm 0.060\times10^{-1}$
Yinv1	$7.348 \pm 1.412\times10^{-2}$	$4.558 \pm 0.718\times10^{-2}$	$4.103 \pm 0.047\times10^{-1}$
R_{ads}	1.982 ± 0.106	Constrained zero	
C_{ads}	$3.761 \pm 0.254\times10^{-3}$	$4.714 \pm 0.223\times10^{-2}$	$1.510 \pm 0.13\times10^{-1}$
$\phi2$	$1.859 \pm 0.070\times10^{-1}$	$2.586 \pm 0.052\times10^{-1}$	
Yinv2	$8.537 \pm 0.080\times10^{-1}$	$3.528 \pm 0.082\times10^{-1}$	$6.308 \pm 0.365\times10^{-2}$

c) HNO_3 treated CO_2/800-1 series

Electrode Carbon	**CO_2/800-1-HNO_3**	**CO_2/800-1-HNO_3/400**
Parameter		
R_{el}	$5.469 \pm 0.043\times10^{-1}$	$6.047 \pm 0.045\times10^{-1}$
C_{dl0}	$2.476 \pm 0.21\times10^{-4}$	$1.840 \pm 0.248\times10^{-4}$
R_{dl0}	$5.305 \pm 0.225\times10^{-2}$	$6.443 \pm 0.389\times10^{-2}$
R_{ct}	$2.136 \pm 0.209\times10^{-2}$	$1.492 \pm 0.339\times10^{-2}$
C_{dl}	$2.848 \pm 0.471\times10^{-3}$	$3.035 \pm 0.956\times10^{-3}$
$\phi1$	$3.175 \pm 0.057\times10^{-3}$	$3.364 \pm 0.069\times10^{-1}$
Yinv1	$3.044 \pm 0.040\times10^{-1}$	$4.519 \pm 0.061\times10^{-1}$
R_{ads}	$1.534 \pm 0.183\times10^{-1}$	$2.298 \pm 0.396\times10^{-1}$
C_{ads}	$6.998 \pm 0.697\times10^{-2}$	$3.731 \pm 0.668\times10^{-2}$
$\phi2$	$1.025 \pm 0.056\times10^{-1}$	$2.413 \pm 0.064\times10^{-1}$
Yinv2	$1.337 \pm 0.048\times10^{-1}$	$2.247 \pm 0.050\times10^{-1}$

The complex conjugate was used to calculate Yinv2

d) NH_3 treated N_2/800-1 at 800°C

Electrode Carbon	**N_2/800-1-NH_3/800**
Parameter	
R_{el}	1.123 ± 0.003

R_{ct}	$8.892 \pm 0.28\times10^{-3}$
C_{dl}	$1.057 \pm 0.071\times10^{-4}$
$\phi1$	$3.134 \pm 0.022\times10^{-1}$
Yinv1	$5.719 \pm 0.038\times10^{-1}$
R_2	$4.913 \pm 0.278\times10^{-2}$
C_{ads}	1.726 ± 0.149

e) K_2CO_3 treated CO_2/800-1-K_2CO_3 at 800°C

Electrode Carbon	**CO_2/800-1-K_2CO_3**
Parameter	
R_{el}	$5.986 \pm 0.016\times10^{-1}$
C_{dl0}	$7.657 \pm 0.351\times10^{-5}$
R_{dl0}	$8.477 \pm 0.209\times10^{-2}$
R_{ct}	$1.518 \pm 0.192\times10^{-2}$
C_{dl}	$2.227 \pm 0.421\times10^{-3}$
$\phi1$	$3.425 \pm 0.040\times10^{-1}$
Yinv1	$4.466 \pm 0.041\times10^{-1}$
R_{ads}	
C_{ads}	$5.852 \pm 0.563\times10^{-1}$
$\phi2$	
Yinv2	$3.253 \pm 0.260\times10^{-2}$